Synchronization of 2D chiral active matter

Bruno Ventéjou Ventéjou

▶ **To cite this version:**

Bruno Ventéjou Ventéjou. Synchronization of 2D chiral active matter. Soft Condensed Matter [cond-mat.soft]. Université Paris-Saclay, 2021. English. NNT : 2021UPASP134 . tel-03559572

HAL Id: tel-03559572

https://theses.hal.science/tel-03559572v1

Submitted on 7 Feb 2022

HAL is a multi-disciplinary open access archive for the deposit and dissemination of scientific research documents, whether they are published or not. The documents may come from teaching and research institutions in France or abroad, or from public or private research centers.

L'archive ouverte pluridisciplinaire **HAL**, est destinée au dépôt et à la diffusion de documents scientifiques de niveau recherche, publiés ou non, émanant des établissements d'enseignement et de recherche français ou étrangers, des laboratoires publics ou privés.

université
PARIS-SACLAY

Synchronization of 2D chiral active matter

Synchronisation de la matière active chirale en 2D

Thèse de doctorat de l'Université Paris-Saclay

École doctorale n° 564, Physique de l'Ile-de-France (PIF)
Spécialité de doctorat: Physique
Unité de recherche: Université Paris-Saclay, CEA, CNRS, SPEC, 91191, Gif-sur-Yvette, France.
Référent: : Faculté des sciences d'Orsay

Thèse présentée et soutenue à Paris-Saclay, le 16 décembre 2021, par

Bruno VENTÉJOU

Composition du jury:

Vincent Hakim Directeur de recherche, PSL Université	Président
Éric Bertin Directeur de recherche, Université Grenoble-Alpes	Rapporteur & Examinateur
Sabine Klapp Professeure, TU Berlin	Rapporteur & Examinatrice
Leticia Cugliandolo Professeure, Sorbonne Université	Examinatrice
Francesco Ginelli Assitant Professeur , Università degli Studi dell'Insubria	Examinateur
Hugues Chaté Chercheur CEA, Université Paris-Saclay	Directeur

Thèse de doctorat

NNT: 2021UPASP134

Contents

Acknowledgements

Ma thèse s'est déroulée dans un contexte un peu particulier, puisque la Covid s'est invitée à la fête, et a annulé un certain nombre d'événements auxlesquels j'aurais dû participer. De plus, la situation m'a imposé un isolement, parfois difficile à vivre, et a rendu les interactions d'autant plus importantes. C'est pourquoi il est important à mes yeux de remercier les différentes personnes qui ont jalonné mon parcours.
Je remercie vivement Éric Bertin pour sa relecture attentive de mon rapport et ses commentaires. I would like to thank Sabine Klapp for her careful reading of this manuscript. Je tiens aussi à remercier Vincent Hakim pour avoir accepté de faire partie de mon jury de thèse et de mon comité de suivi de thèse. Ainsi, j'ai pu bénéficier de ses remarques pertinentes à différents moments. Also, I would like to thank the other members of the jury, Francesco Ginelli and Leticia Cugliandolo, for their interest in my work and accepting to evaluate it.
Ensuite, je souhaite remercier Hugues Chaté pour son accompagnement dans mon travail, la pertinence de ses remarques, et pour les opportunités qu'il m'a offertes. Il m'a permis d'étudier un sujet de façon très complète. J'ai beaucoup appris et progressé. Je souhaite remercier Aurelio Patelli, qui était présent au début de ma thèse. Il a joué un rôle important de par sa gentillesse et ses conseils techniques qui ont été très formateurs pour moi. Je souhaite aussi remercier Cesare Nardini pour ses remarques pertinentes sur mon sujet. I would like to thank Xiaqing Shi for the interactions we had and for guiding me during my trip to China. Je tiens à remercier Giordano pour toutes les discussions que l'on a pu avoir. Je tiens aussi à remercier Benoît Mahault pour tous les conseils à distance qu'il a pu me prodiguer. J'ai aussi pu voyager (un peu) et échanger avec différentes personnes que je souhaite remercier: Mathiew Turner, Hepeng Zhang et Yu Duan.
Je tiens à remercier le SPEC, notament son directeur François Daviaud, puis Patrice Roche pour leur accueil. Je tiens particulièrement à remercier son secrétariat et en particulier Nathalie Royer sans qui j'aurais été complétement perdu dans la partie administrative. Je tiens à remercier le CSRC de m'avoir accueilli lors de mon voyage en Chine. Je souhaite aussi remercier Daniel Bonamy, Caroline Raepsaet et Hervé Bercegol pour leur gentillesse et sans qui la soutenance n'aurait pas pu se dérouler aussi bien.
Cette thèse n'aurait pas eu la même saveur si vous n'aviez pas été là, Adel et Ludo. Je tiens aussi à remercier Alex et Lucile pour tous les bons moments passés au viaduc et ailleurs. Merci à tous mes amis qui m'ont accompagné durant toutes ces années! Enfin, je remercie Isa pour son aide. Je n'oublie pas ma famille et Sylvianne qui m'ont soutenu et sans qui rien n'aurait été possible.

Merci de m'accompagner durant toutes ces années, Élo! Il y aurait tant à dire...

Chapter 1

Introduction to active matter and synchronization

1.1 What is active matter?

The goal of physics is to understand and characterize the world around us. For centuries people have been trying to understand the interactions between a finite number of objects, with Newton and the gravitation interaction, or Coulomb and the electrostatic interaction. The wisdom was based on a deterministic point of view. On the other side, the later study of complex systems such as gas and liquid was based on thermodynamics, but in the XVII century, there was a change of paradigm with Boltzmann and Maxwell who provided a microscopic interpretation of thermodynamic quantities through a new approach based on a probabilistic point of view. Statistical physics was born, but it was limited to the study of equilibrium systems composed of passive materials like gas, liquid, and magnetic materials. Along the last decades, there is a renewal of the statistical physics through the study of out of equilibrium systems.
An equilibrium system is a system where all the quantities have the time to relax, and the behavior of such systems is governed by the law of large numbers. Thus, several properties have to be verified such as the fluctuation-dissipation theorem which does the link between the variance of the fluctuation and the linear response function, or the detailed balance which ensures the non-existence of flux inside the system. Unfortunately, the world of equilibrium system is a minority part of the variety of systems around us.
There are several ways for a system to be out-of-equilibrium. The first one is to take an equilibrium system and perturb it such as in the experiments of Ciliberto et al. [1] where they move a particle trap in an optical beam. Another possibility is to put a system in a stationary out of equilibrium state such as a system between two thermostats at different temperatures or a fluid between two moving plates. The last possibility is the relevant one for lots of living systems which are driven out of equilibrium by a flux of energy due to one chemical reaction which is often the transformation of ATP in ADP.

The most common definition of active matter is a matter which is driven out of equilibrium in the bulk by the fuel consumption to affect its movement. It means that the flux of energy is at the scale of all the constituents. Why this class of systems is interesting? The most interesting property is the ubiquity of collective motion in a wide range of active matter systems. It is very interesting because it occurs at all scales in different dimensions. We can make a non-exhaustive list of such collective motions such as flocks of birds [2], schools of fish [3] for collective motions in 3D. In 2D, there are herds of animals [4], colonies of bacteria [5, 6]. There is also collective motion at the proteins scale [7]. But the field of active matter is not reduced to living systems. Thus, there are also synthetic active matter systems with vibrated granular rods [8], colloids particles [9–11] or collections of robots [12]. What is interesting with this matter is, it shows new emergent structures, phase transition between order and disorder, and new nonequilibrium properties.
All these systems are composed of particles moving and surrounded by a fluid. In general, the fluid will mediate long-range interaction between particles, but sometimes this interaction is negligible compared to the local interaction between particles. In 2D, this can be due to interaction between particles and the medium which do not conserve the momentum. This type of system is named Dry system.
On the opposite side, systems, where the interaction between particles and fluid is strong, are named Wet system and they are usually called active fluids or active gels. In my thesis, I focus my work on dry systems.
If we look at the interaction between particles in a dry active matter system, there are two classes of minimal models. The first one is system where there is only repulsive interaction between particles and is referred to as Active Brownian Particles (ABP). In ABP particles are only subjected to external noise and to pairwise repulsion potential. These systems offer a motility-induced phase separation. It is due to the fact that particles slow down in dense regions and tend to accumulate. On the other side, the minimal models where the only ingredient is alignment are named DADAM for Dry, Aligning, Dilute, Active Matter [13]. There are several possible alignments: ferromagnetic or nematic as presented in Fig. 1.1. The ferromagnetic alignment corresponds to the case where particles synchronize their velocity. The nematic alignment is when particles try to align the direction of their polarization (with the same direction or a difference of π). The well-known Vicsek model corresponds to the case of polar particles with a ferromagnetic alignment and will be detailed later. This classification of active matter can be represented by the cube in Fig. 1.1.

Many living systems have internal degrees of freedom which may themselves try to synchronize or coupling between internal degrees of freedom and self-propulsion mechanism which leads to movement synchronization. This has been experimentally observed for myxobacteria [14, 15], who spontaneously reverse their walk from time to time: at high densities, large assemblies of them can synchronize the timing for the reversal of their velocities, leading to new collective effects in the displacement of groups. It is difficult to

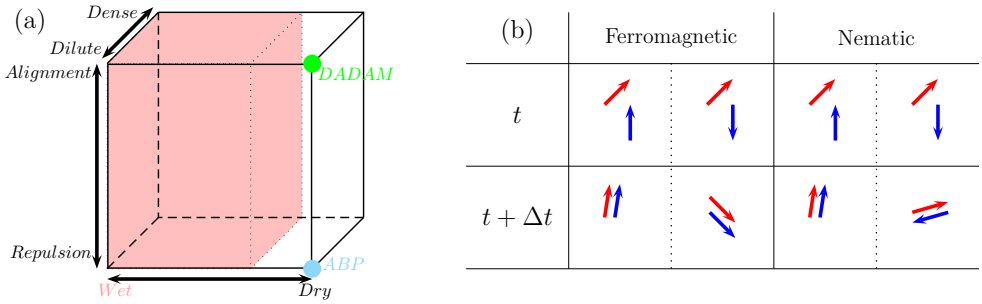

Figure 1.1: Classification of active matter. (a): Schematic view of the classification of active matter systems. Vicsek model belong to the DADAM class. (b) Scheme of the ferromagnetic alignment and the nematic alignment between two time step.

study situations where there is a two-way coupling between internal degrees of freedom and self-propulsion. Thus, we will start with a simpler situation where the direction of the particle's polarization is seen as the phase of an oscillator. Moreover, this oscillator has an intrinsic frequency and tries to synchronize with other oscillators. Due to the new link between polarization and intrinsic frequency, we are studying chiral active matter systems. This point will be detailed later. So the goal of this thesis is to describe the synchronization of chiral active matter systems.
The Vicsek model can be seen as a minimal model to provide a phase transition between a disordered phase and a phase where all the velocity of particles are identical. This model can be seen as a synchronization model because in one phase velocities show simultaneous behavior. Also, the Kuramoto model provides a minimal description of synchronization for random oscillators. So we will use these two minimal models as the starting point of my study.

1.2 Vicsek model

1.2.1 Presentation

The Vicsek model was introduced in 1995 [16] by *Vicsek et al.*. The goal was to study self-ordered motion in systems of particles. This work was motivated by the modeling of biological systems where collective motion occurs. The Vicsek model is a minimal model for self-propelled particles where there is only one simple local rule to describe alignment interaction and no repulsion. Thus, the Vicsek model is a borderline case of the classification of active matter as described in Fig. 1.2. The Vicsek model was introduced in 2D and considers a system with N point particles in a system with periodic boundaries. So it is possible to define the average density ρ_0 which is conserved. At each time step, particles will align with the average direction of the particles contain in a disk of radius r

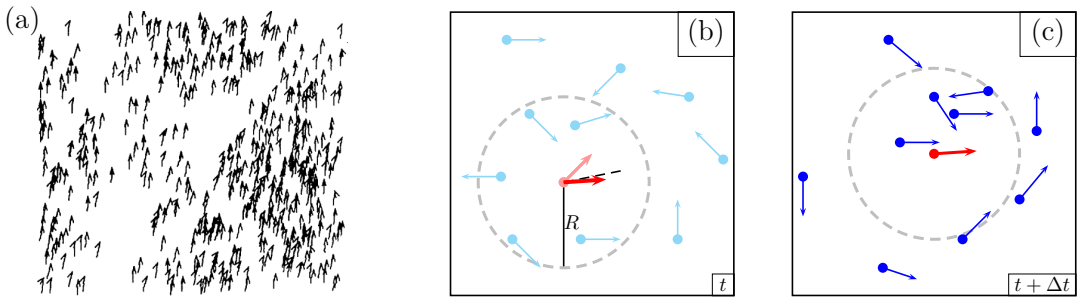

Figure 1.2: Presentation of the Vicsek model. (a): Snapshot of the order phase taken from [16]. (b): Scheme of the VM rules for alignment at time t. The dash line starting from the central particle represents the mean direction of the particles inside the disk of radius R. The bold red arrow is the direction of polarization at $t + \Delta t$, it is computed by taking the mean direction (dash line) plus a random noise. (c): Same population as panel (b) after one time step Δt.

with some random perturbation added. Thus, each particle follows the equations

$$\begin{aligned} \vec{x}_i(t + \Delta t) &= \vec{x}_i(t) + v_0 \vec{e}(\theta_i(t))\Delta t \\ \theta_i(t + \Delta t) &= \langle \theta(t) \rangle_r + \eta \xi_i \end{aligned} \tag{1.1}$$

where $\langle \theta(t) \rangle_r$ is the average direction of the particles in a disk of radius r and center on the position $\vec{x}_i$. One can compute the average direction by $\langle \theta(t) \rangle_r = \arctan[\langle \sin \theta(t) \rangle_r / \langle \cos \theta(t) \rangle_r]$, it corresponds to the direction of the polarisation vector given by the sum of polarisation vector of each particles in the neighborhood of particle i. Then ξ_i is a random number chosen with a uniform probability in $[-\pi/2, \pi/2]$. The first equation describes the self-propelled properties of the particles. The second equation contains two terms that are competing against each other. The first term, $\langle \theta(t) \rangle_r$ will align the direction of the particle with the mean direction of the neighbors including the central particle. The second term is a noise and will increase the angle disorder. In Eq. (1.1), there is no interaction between the particle and the media, which means that the system belongs to the class of dry models with no momentum conservation.

So there are three parameters v_0, ρ, and η to describe the system. v_0 is the distance between two updates for the particle, and it has been shown in [17] that the nature of the transition is not affected by the value of v_0. But the value of v_0 changes the value of the typical size where finite-size effects occur, and they can change the nature of the transition for too small system size. Then if we increase the density, we will increase in average the number of particles in interaction. To study the phase transition in the phase

space (ρ, η) we need to introduce the order parameter

$$m = \frac{1}{N}|\sum_{i=1}^{N} \vec{e}(\theta_i)| = |\vec{P}| \tag{1.2}$$

when the system is in the disordered phase the order parameter defined in 1.2 is zero. On the contrary, when the system is fully ordered (see Fig. 1.2 panel (a)), all the particles are pointing in the same direction, the order parameter m is almost one.

Now we can describe the phase transition of the Vicsek model, see Fig. 1.3. We have seen that ρ_0 and η compete. So to increase ρ is equivalent to decrease η. We consider the disordered phase of the Vicsek model at low ρ_0 or high η. In this phase, the order parameter Eq. (1.2) is zero $m = 0$ and the correlation function $C(t) = \langle m(t_0)m(t_0 + t)\rangle - \langle m(t_0)^2$ is decreasing exponentially according to [17]. It allows to compute a correlation time. It is also possible to compute the variance $Var(n)$ of a given number of particles n in a box. In the disordered phase, we get the standard central limit behavior for the variance.

Then one can increase the density or decrease the noise, at a given point a phase transition will occur and a homogeneous ordered phase will appear. It means that m will be non-zero and start to increase. Thus, a macroscopic number of particles starts to move in one direction, and it corresponds to a symmetry breaking. In this phase the variance of the density scale as a power of the density $Var(n) \sim \langle n\rangle^{\alpha} \quad \alpha > 1$, it means there are giant density fluctuations, see Fig. 1.3 panel (a). Moreover, Toner and Tu have shown in [18] the existence of a true polar long-range order. Numerically, it means that the polar order parameter converges to a non-zero value as a function of the system size. According to the Mermin-Wagner theorem [19], this is something impossible at equilibrium in 2D. Thus, this phase transition depends on the dynamical, nonequilibrium aspect of the model. The homogeneous ordered phase is also characterized by anomalously strong density fluctuations and superdiffusion [17, 18, 20].

In the beginning, the transition between the disordered phase and the homogeneous ordered phase was considered as a second-order phase transition [16]. This question was studied more precisely, and it has been shown that the transition is in fact discontinuous. First, particle-based simulations have shown that the transition is discontinuous [17, 21] at large scales, and due to finite-size effects, it could appear as continuous for small system size. Furthermore, hydrodynamic theories derived from the microscopic model also conclude with a discontinuous description of the transition [22–24].
At the transition between the disordered phase and the ordered phase, there is a coexistence between dilute disordered regions and dense ordered regions. These dense regions are called *bands*, see Fig. 1.3 panel (c), because they are elongated perpendicular to their polarization direction. These bands present a well-defined width. Thus, if we increase the density ρ, the order parameter will increase by feeding the band and keeping the gas

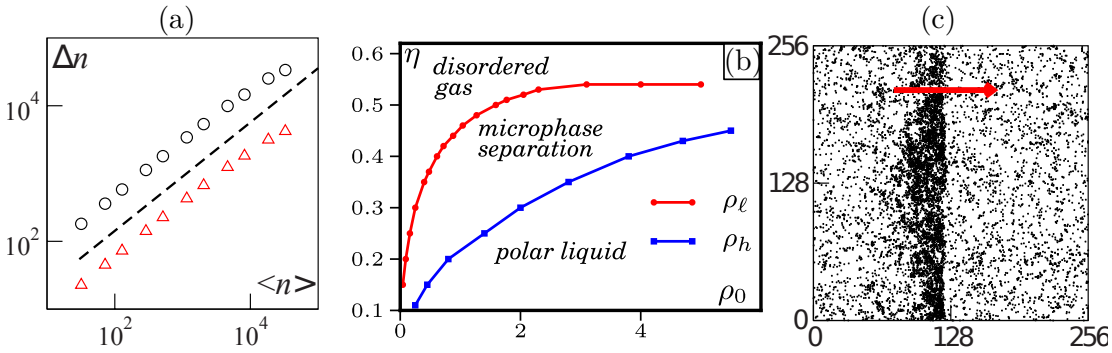

Figure 1.3: Results of the Vicsek model. (a): Figure extract from [17] and presents the giant density fluctuation in the ordered phase. Δn scales approximately as $n^{0.8}$. Black circle is for a 2D system of size $L = 256(\rho = 2,\ \eta = 0.25)$ and red triangle is a 3D system of size $L = 64$ $(\rho = 0.5,\ \eta = 0.1)$. (b): Phase diagram of the Vicsek model extract from [25]. $\rho_l(\eta)$ and $\rho_h(\eta)$ are the bimodal line and correspond to the limit of coexistence region between band and gas. (c): Figure extract from [17]. It represents a snapshot of a system in the coexistence region.

density constant. This will continue until it reaches the maximum width and then creates a new band. This scenario is called a microphase separation. When a system presents several bands they get into a smectic arrangement. The phase diagram of the Vicsek model, see Fig. 1.3 panel (b), contains three different phases: the disordered phase, the band phase (which corresponds to the coexistence of a disordered and an ordered phase), and the ordered phase. To understand the difference of symmetry of the ordered phase and the band phase, we can refer to [17]. The band phase is when the noise η is high enough to get percolation of the low-density regions and to get disconnected dense ordered patches. These patches self-organize in bands via the collection of particles and the superdiffusion in the direction perpendicular to the mean polarization.
This scenario of phase transition is similar to the liquid-gas phase transition. This is the reason why, in general, we refer to the disordered phase as the gas phase and the ordered phase as the liquid phase.
The band phase and the liquid phase do not present the same symmetries, so the existence of a supercritical regime is impossible. If we refer to the phase diagram of the Vicsek model, we can interpret this point as the critical point is sent to the infinity in density.
The Vicsek model is strongly affected by finite-size effects. Historically, this point made dispute about the nature of the transition because Vicsek was not able to see the band phase. There are some variations used to reduce these finite-size effects.

1.2.2 Forward Update rule

In this paragraph, we present the forward update rule. It reduces the dynamic's dependency to only one time step instead of two as explained in Fig. 1.2. The Vicsek model [16, 26] was initially introduced with the backward update rule. The Vicsek model with the forward update rule can be explicit as

$$\begin{aligned} \vec{x}_i(t+\Delta t) &= \vec{x}_i(t) + v_0\vec{e}(\theta_i(t+\Delta t))\Delta t \\ \theta_i(t+\Delta t) &= \langle\theta(t)\rangle_r + \eta\xi_i \end{aligned} \tag{1.3}$$

The difference between Eq. (1.1) and Eq. (1.3) is in the update rule for the position. Now the position takes into account the angle at time $t+\Delta t$ instead of angle at time t. In the backward update rule, the particle will align with a delay because the angle $\theta_i(t)$ is updated with the angle at time $t-\Delta t$. So the position at time t is updated with the information of the neighborhood at time $t-\Delta t$ which is introducing a delay. The forward update rule fixes this difference of time dependency, and the update rule for the position at time t depends on the position of neighborhood at time t. The meaning is that the particle aligns instantaneously with its neighbors.
The two update rules do not change the results in the limit of infinite size and infinite time. Moreover, they belong to the same universality class. But it will affect finite-size systems and this point was the main reason why Vicsek et al. do not see bands and claim for a continuous phase transition.
We will present later the continuous-time limit in 1.4.1 which takes into account that particles need time to align. Other variations of the Vicsek model exist, as metric free [27, 28] or vectorial noise [17], but they are not useful for this manuscript.

1.2.3 Hydrodynamic description of the Vicsek model

We have seen that the Vicsek model describes the transition between a disordered phase and an ordered phase in two dimensions and can be seen as a gas-liquid phase transition. To get a better insight on flocking model in active matter we can do a description with a hydrodynamic point of view. There are two ways to get hydrodynamic equations, the first way is to write terms allowed by symmetries. In this first way, there are several examples such as equations derived by Toner and Tu for the Vicsek model [18, 20, 29], by Csahók and Czirók [30] for anisotropic bacteria or Simha and Ramaswamy [31, 32] for elongated bacteria. The other way to get hydrodynamic equations is by coarse-graining a microscopic model. Thus, there are several ways to perform the coarse-graining based on different approximations. We will present the work of Bertin and collaborators which is based on the Boltzmann equation [22–24] and the work based on the Fokker-Planck equation, also called Smoluchovski equation when it is applied to particle distribution. The first type of hydrodynamic equations have coefficients without any link to the microscopic parameters.

1.2.3.1 Toner-Tu approach

In this part, we will present the first hydrodynamic description of the Vicsek model which is based on symmetries. This work has been done by Toner and Tu in [18, 20, 29, 33]. They write first Navier-Stokes equations and then add terms allowed by symmetries. The first symmetry is the rotational invariance and means there is no preference for the direction of polarization for the ordered phase. The second one is the conservation of the total number of particles. We notice that there is no Galilean invariance because a change of speed means a change of interaction between the particles. Following the previous consideration, they write the following equations for the density field $\rho(\vec{r},t)$ and the velocity field $\vec{v}(\vec{r},t)$

$$\partial_t \rho + \nabla \cdot (\rho \vec{v}) = 0 \tag{1.4a}$$

$$\begin{aligned} &\partial_t \vec{v} + \lambda_1 (\vec{v}\cdot\vec{\nabla})\vec{v} + \lambda_2 (\vec{\nabla}\cdot\vec{v})\vec{v} + \lambda_3 \vec{\nabla}(|\vec{v}^2|) \\ &= \alpha\vec{v} - \beta|\vec{v}|^2\vec{v} - \vec{\nabla}P + D_b\vec{\nabla}(\vec{\nabla}\cdot\vec{v}) + D_T\nabla^2\vec{v} + D_2(\vec{v}\cdot\vec{\nabla})^2\vec{v} + \vec{f} \end{aligned} \tag{1.4b}$$

where $P = \sum_{n=1}^{\infty} \sigma_n (\rho - \rho_0)^n$.

The first equation Eq. (1.4a) describes the advection of the density field by the velocity field and means that the total number of particles is conserved. The first line of the second equation Eq. (1.4b) describes the advection of the velocity field by itself. The part $\alpha - \beta|\vec{v}|^2$ describes a Ginzburg-Landau potential. For $\alpha < 0$ this is a damping term and for $\alpha > 0$ and $\beta > 0$ this is a saturation term which provide a typical value of velocity $v_0 = \sqrt{\frac{\alpha}{\beta}}$ for the ordered phase. The next term is a term of pressure which is the expansion around the average density. Then there are three terms of diffusion or viscosity. The last term $\vec{f}$ is a random driving force representing the noise.

To determine the stability of the ordered phase by using renormalization group methods, the authors consider a velocity field in one direction $v_\parallel$ with $|v_\parallel| = v_0$ and look at the variation of the fluctuation in the perpendicular direction $\vec{v}_\perp$. Then they rescale length, time, and fields as follow

$$\vec{x}_\perp \to b\vec{x}_\perp, \qquad x_\parallel \to b^\zeta x_\parallel, \qquad t \to b^z t, \qquad \vec{v}_\perp \to b^\chi \vec{v}_\perp, \qquad \delta\rho \to b^{\chi_\rho}\delta\rho \tag{1.5}$$

They choose the scaling exponent to keep the diffusion constants D_1, $D_\parallel = D_T + D_2 v_0^2$, $D_\perp = D_1 + D_b$ and the noise fixed. χ is the roughness exponent and measures how velocity fluctuations perpendicular to the direction of polarization decays with the system size. If $\chi < 0$ the fluctuation of velocity decay and the ordered phase is stable. ζ is the exponent that characterizes the anisotropy.
They claim to be able to determine the scaling exponent exactly in dimension $d = 2$ in the first papers [18, 20, 29] and found

$$z = \frac{2(d+1)}{5}, \qquad \zeta = \frac{d+1}{5}, \qquad \chi = \frac{3-2d}{5} \tag{1.6}$$

So for $d = 2$ we get $\chi = -1.5$, so the ordered phase is stable, and the system shows long-range order. The authors also show the existence of propagating sound modes. Then they determine the nature of diffusion in the ordered phase. They found an expression of the mean square displacement scaling as $\langle \Delta\vec{r}^2 \rangle \sim t^{4/3}$ that indicates an anomalous diffusion of the particles in the ordered phase.

Later, Toner reanalyzed the first model [33] and claimed that nonlinear terms were forgotten in the hydrodynamic equations Eq. (1.4) but the qualitative predictions of the first model remain.
Even if the first analysis by Toner and Tu provides good predictions of the long-range order, sound modes, and anomalous fluctuations it lacks the link between the parameters of the hydrodynamic equations and the microscopic parameters. Also, the renormalization group approach makes it difficult to explore the nature of the transition of the Vicsek model.

1.2.3.2 Boltzmann approach

In the previous section, the hydrodynamic equations were obtained from symmetry considerations, so it lacks parameters dependency to the microscopic parameters. Thus, Bertin et al. introduce a coarse-grained description of a microscopic model to fill this gap in [22, 23]. Here we provide a detailed description of this approach because it will be used in the main part.

Microscopic Model

The microscopic model is a bit different from the standard Vicsek model but belongs to the same class of self-propelled particles model. Bertin et al. consider self-propelled point-like particles moving on a continuous plane, with a velocity $\vec{v}$ such that $|\vec{v}| = v_0$. The velocity vector is then described only by the angle θ defined from an arbitrary direction. The particles evolve ballistically until they experience either a self-diffusion event or a binary collision that tends to align the velocity of the two particles. The self-diffusion process occurs with a probability λ per unit time and the change of the angle is given by $\theta' = \theta + \eta$ where η is drawn from a distribution $P_\sigma(\eta)$ Gaussian with variance σ. Moreover, binary collisions occur when the distance between two particles becomes less than d_0. Let consider a collision between a particle with a velocity angle θ_1 and the other particle with a velocity θ_2. The result angles are given by $\theta_1' = \bar{\theta} + \eta$ and $\theta_2' = \bar{\theta} + \eta$ where $\bar{\theta} = \frac{\theta_1 + \theta_2}{2}$ is the average angle, and η a noise with the same distribution $P_\sigma(\eta)$. It is possible to consider different noise distributions but for simplicity, they are assumed to be the same here.

Boltzmann equation

To go from the discrete world to the continuum description, we have to consider the one-body probability density function $f(\vec{r},\theta,t)$. It gives the number of particles at position $\vec{r}$ with a direction of polarization θ at time t. Then we write the Boltzmann equation which is a master equation for the temporal evolution of the one-body probability density function.

$$\partial_t f = I_{f.e.}[f] + I_{s.d.}[f] + I_{coll}[f] \tag{1.7}$$

The free evolution of the particles is governed by their displacement only so

$$I_{f.e.}[f(\vec{r},\theta,t)] = -v_0\vec{e}(\theta)\cdot\vec{\nabla}f(\vec{r},\theta,t) \tag{1.8}$$

The integral of self-diffusion part is given by

$$I_{s.d.}[f(\vec{r},\theta,t)] = -\lambda f(\vec{r},\theta,t) + \int \mathrm{d}\theta'\,\lambda \int \mathrm{d}\xi f(\vec{r},\theta',t)P_\sigma(\xi)\delta_{2\pi}(\theta-(\theta'+\xi)) = \lambda((P_\sigma * f)-1) \tag{1.9}$$

To give the collision integral we need to do some microscopic hypothesis. The condition to get two particles that collide is to get these particles close enough. The velocity of the second particle in the referential of the first particle is given by $v_2' = \vec{e}(\theta_2) - \vec{e}(\theta_1)$. To get a collision between the two particles, it needs to get the particle in a rectangle of length $|v_2'|dt$ and of width $2d_0$. It means that the frequency collision is given by the kernel $K(\theta_2-\theta_1) = 2d_0v_0||\vec{e}(\theta_2)-\vec{e}(\theta_1)|| = 4d_0v_0\sin|\frac{\theta_2-\theta_1}{2}|$.

Here, two approximations are needed. The typical distance of interaction is d_0 and the typical length between particles is of order $\frac{1}{\sqrt{\rho_0}}$ where ρ_0 is the average density of particles. To reduce collisions to two-body collisions, we need $d_0 \ll \frac{1}{\sqrt{\rho_0}}$ which implies $\rho_0 \to 0$, thus we are working in the dilute limit. The second assumption is to express the two-body distribution function as a product of the one-body distribution function such that $f_{2\mathrm{b}}(\vec{x},\vec{y},\theta,\theta',t) = f_{1\mathrm{b}}(\vec{x},\theta,t)f_{1\mathrm{b}}(\vec{y},\theta',t)$. This assumption is the molecular chaos and considers the correlation in space and orientation between two particles to be negligible. The validity of this second assumption has been discussed in [34–36]. The theoretical approach is inconclusive when the numerical simulations seem to invalidate this hypothesis. If we think about the problem, we can understand that two particles will stay aligned after a collision and it is hard to satisfy the hypothesis. So this approach seems to be questionable, but it provides a good qualitative agreement.

The integral of collision losses is given by

$$I_{coll}^{Loss}[f(\vec{r},\theta,t)] = \int \mathrm{d}\theta' K(\theta-\theta')f(\vec{r},\theta,t)f(\vec{r},\theta',t) \tag{1.10}$$

The integral of collision gain is given by

$$I_{coll}^{Gain}[f(\vec{r},\theta,t)] = \iint \mathrm{d}\theta_1\,\mathrm{d}\theta_2 K(\theta_1-\theta_2) f(\vec{r},\theta_1,t) f(\vec{r},\theta_2,t) \int \mathrm{d}\xi P_\sigma(\xi)\delta_{2\pi}(\tfrac{\theta_1+\theta_2}{2}+\xi-\theta) \tag{1.11}$$

It is possible to rescale the equation to reduce the dependency of this model to only two parameters by setting

$$t \to t/\lambda, \qquad \vec{r} \to v_0\vec{r}/\lambda, \qquad K \to 2d_0 v_0 K, \qquad f \to \rho_0 f \quad . \tag{1.12}$$

So the equation will only depend on the noise level η and the non-dimensional density $\tilde{\rho}_0 = 2d_0 v_0 \rho_0/\lambda$. Then we introduce the Fourier series expansion of $f(\vec{r},\theta,t)$ with respect to θ

$$\hat{f}_k(\vec{r},t) = \int_{-\pi}^{\pi} \mathrm{d}\theta f(\vec{r},\theta,t) e^{ik\theta} \tag{1.13}$$

Here we can notice the particular meaning of $\hat{f}_k$ for $k = 0, 1$

$$\hat{f}_0(\vec{r},t) = \int_{-\pi}^{\pi} \mathrm{d}\theta f(\vec{r},\theta,t) = \rho(\vec{r},t) \tag{1.14a}$$

$$\hat{f}_1(\vec{r},t) = \int_{-\pi}^{\pi} \mathrm{d}\theta f(\vec{r},\theta,t) e^{i\theta} = \rho(\vec{r},t)u(\vec{r},t) = p(\vec{r},t) \tag{1.14b}$$

which is respectively the density field and the momentum field. Also for all k, $\hat{f}_{-k} = \hat{f}_k^*$ where $\hat{f}^*$ is the complex conjugate.
By taking the Fourier transform along the angular coordinate of equation Eq. (1.7) we get the infinite hierarchy of PDE

$$\partial_t \hat{f}_k = -\frac{1}{2}(\nabla \hat{f}_{k-1} + \nabla^* \hat{f}_{k+1}) + (\hat{P}_k - 1)\hat{f}_k + \sum_{q=-\infty}^{\infty} \hat{f}_q \hat{f}_{k-q} J_{k,q} \tag{1.15}$$

with $I_{k,q} = \frac{1}{2\pi}\int \mathrm{d}\Delta e^{-i(2l-k)}|\sin\frac{\Delta}{2}|$, $J_{k,q} = \tilde{\rho_0}(\hat{P}_k I_{k,q} - I_{0,q})$ and $\hat{P}_k \equiv \hat{P}_k(\sigma) = \sum_{-\infty}^{\infty} \mathrm{d}\eta P_\sigma(\eta) e^{ik\eta}$.
This equation also introduces complex derivatives $\nabla = \partial_x + i\partial_y$ and the Laplacian $\Delta = \nabla\nabla^*$. One can notice that $P_k(\sigma) = e^{-\sigma^2 k^2/2}$ for a Gaussian distribution.
Then we will remove the hat, space, and time dependency in the following part to lighten notations.

Ginzburg-Landau truncation and closure scheme

To close the infinite hierarchy of PDE (1.15) we have to consider the homogeneous disordered isotropic state given by $f_0 = \rho_0$ and $f_k = 0$ for $(k \geq 1)$ which is a trivial solution. Then, if we study the linear stability of this solution, we get

$$\partial_t f_k = \mu_k(\rho_0,\sigma) f_k \tag{1.16}$$

where

$$\mu_k(f_0,\sigma) \equiv [(P_k - 1) + f_0(J_{k,k} + J_{k,0})] \tag{1.17}$$

So the linear stability of f_k is governed by the sign of the linear coefficient μ_k. We can express them for the first value of $k = 1, 2, 3, ...$

$$\mu_1 = P_1 - 1 + \frac{4\tilde{\rho}_0 f_0(3P_1 - 2)}{3\pi}\,, \tag{1.18a}$$

$$\mu_2 = P_2 - 1 - \frac{8\tilde{\rho}_0 f_0(7 + 5P_2)}{15\pi} \quad (< 0)\,, \tag{1.18b}$$

$$\mu_3 = P_3 - 1 - \frac{4\tilde{\rho}_0 f_0(35P_3 + 34)}{35\pi} \quad (< 0)\,, \tag{1.18c}$$

$$...$$

Now we can analyze the dependency of this μ_k for different values of noise and density. First, $0 \leq P_k \leq 1$ for all k so the left part of Eq. (1.18) is always negative. Then the sign of the numerator will determine the sign of μ_k, only for $k = 1$ the numerator will change its sign depending on the noise and density value. At this level, we expect that the first mode to become unstable in the vicinity of the transition line is f_1. So we assume $f_1 \sim \varepsilon$ is the relevant order parameter with $\varepsilon \ll 1$. If we use a Ginzburg-Landau approach it provides only one coherent scaling

$$f_1 \sim \varepsilon\,, \quad |f_0 - 1| \sim \varepsilon\,, \quad f_{k>0} \sim \epsilon^k\,, \quad \partial_t \sim \nabla \sim \varepsilon\,. \tag{1.19}$$

We use the scaling ansatz for the truncation of the infinite hierarchy of PDE (1.15). We stop the expansion for $k = 1$ at order ε^3, and at order ε^2 for $k = 2$.

$$\partial_t f_1 = -\frac{1}{2}\nabla\rho - \frac{1}{2}\nabla^* f_2 + \mu_1[f_0]f_1 + f_1^* f_2\left(J_{1,-1} + J_{1,2}\right) + \mathcal{O}(\varepsilon^4) \tag{1.20a}$$

$$\partial_t f_2 = -\frac{1}{2}\nabla f_1 + \mu_2[1]f_2 + f_1^2 J_{2,1} + \mathcal{O}(\varepsilon^3) \tag{1.20b}$$

This allows to neglect f_3 in the equation for $k = 2$, after comparing the different scaling we set $\partial_t f_2$ to zero. We get f_2 slaved to f_1 and ρ_0 through

$$f_2 = \frac{1}{2\mu_2[1]}\nabla f_1 - f_1^2\frac{J_{2,1}}{\mu_2} \tag{1.21}$$

Hydrodynamic equations

We use Eq. (1.21) to replace the expression of f_2 in Eq. (1.20a) and we get the following set of hydrodynamic equations

$$\partial_t\rho + \Re(\nabla^* f_1) = 0 \tag{1.22a}$$

$$\partial_t f_1 = -\frac{1}{2}\nabla\rho + \left(\mu_1[\rho] - \xi|f_1|^2\right)f_1 + \nu\Delta f_1 - \kappa_1 f_1^*\nabla f_1 - \kappa_2 f_1\nabla^* f_1 \tag{1.22b}$$

Here we recover the Toner-Tu Eq. (1.4) where $D_b = D_2 = 0$, but now the coefficients depend on the microscopic parameters via the moments of the noise distribution and the non-dimensional density $\tilde{\rho}_0$.
The coefficients are given by

$$\mu_1 \equiv P_1 - 1 + \frac{4\tilde{\rho}_0\rho(3P_1-2)}{3\pi} \qquad \xi \equiv \frac{16\tilde{\rho}_0^2(5P_1-2)(3P_2+1)}{\pi(15\pi(1-P_2)+8\tilde{\rho}_0(5P_2+7))}$$
$$\nu \equiv \frac{15\pi}{60\pi(P_2-1)+32\tilde{\rho}_0(7+5P_2)}$$
$$\kappa_1 \equiv \frac{20\tilde{\rho}_0(3P_2+1)}{8\tilde{\rho}_0(5P_2+7)-15\pi(P_2-1)} \qquad \kappa_2 \equiv \frac{6\tilde{\rho}_0(2-5P_1)}{8\tilde{\rho}_0(5P_2+7)-15\pi(P_2-1)}$$

with ξ and ν are positive. It means the Eq. (1.22) behave in a good way to provide a homogeneous ordered phase. Moreover, the linear coefficient depends explicitly on the density field f_0.

Linear stability of the homogeneous solutions

In this paragraph we detail the linear stability of the homogeneous solutions, Eq. (1.22) admit two homogeneous solutions. The first one is the disorder homogeneous solution for $\mu_1[f_0] < 0$, and it has been studied to establish the scaling near the onset of the transition line. The second homogeneous solution is ordered for $\mu_1[f_0] > 0$, and can be explicit as

$$\begin{aligned} f_0 &= 1 \\ |f_1| &= \sqrt{\frac{\mu_1}{\xi}} = P \end{aligned} \tag{1.23}$$

Then we study the stability of the homogeneous ordered solution to a perturbation with $f_0 = 1 + \delta f_0$ and $f_1 = P + \delta f_1$. So we introduce these fields to Eq. (1.22) and express the new system of equation as

$$\partial_t \begin{pmatrix} \delta f_0 \\ \delta f_{1,x} \\ \delta f_{1,y} \end{pmatrix} = \mathcal{M} \begin{pmatrix} \delta f_0 \\ \delta f_{1,x} \\ \delta f_{1,y} \end{pmatrix} \tag{1.24}$$

where $\mathcal{M}$ is the matrix

$$\mathcal{M} = \begin{pmatrix} 0 & -\partial_x & -\partial_y \\ -\frac{1}{2}\partial_x + P\mu_1'[1] & -2\mu_1[1] + \nu\Delta - (\kappa_1+\kappa_2)P\partial_x & (\kappa_1-\kappa_2)P\partial_y \\ -\frac{1}{2}\partial_y & -(\kappa_1-\kappa_2)P\partial_y & \nu\Delta - (\kappa_1+\kappa_2)P\partial_x \end{pmatrix} \tag{1.25}$$

Then we expand δf_0 and $\delta f_{1,x/y}$ in terms of Fourier modes for the spatial coordinates

$$\begin{aligned} \delta f_0 &= \delta f_{0,\vec{q}}\, e^{i\,\vec{q}\cdot\vec{r}} \\ \delta f_{1,x} &= \delta f_{1x,\vec{q}}\, e^{i\,\vec{q}\cdot\vec{r}} \\ \delta f_{1,y} &= \delta f_{1y,\vec{q}}\, e^{i\,\vec{q}\cdot\vec{r}} \end{aligned} \tag{1.26}$$

To characterize the linear stability, we compute the eigenvalues and eigenvectors of the matrix $\mathcal{M}$ for different values of $\vec{q}$ with the microscopic parameters fixed. We keep the highest eigenvalues of the Fourier space, if it is negative it means the solution is stable against linear perturbation and any random perturbation will decay exponentially fast. If it is positive, it means the solution is unstable and the linear perturbation will grow. We can characterize the perturbation thanks to the vector $\vec{q}$ attached to this eigenvalue. Thus, we get the direction of this perturbation and the typical wavelength.

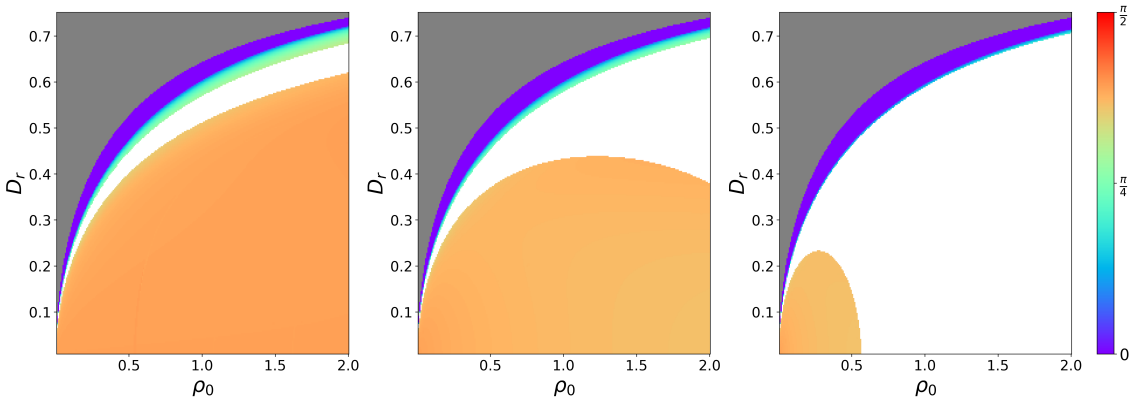

Figure 1.4: Linear stability study of the Vicsek model. Direction of the eigenvector attached to the highest eigenvalue in the plane (ρ_0, D_r) with $D_0 = 0.0$(a), $D_0 = 0.1$(b), $D_0 = 0.5$(c). The positional diffusion stabilize the homogeneous ordered phase. The instability at the onset of the transition line becomes fully longitudinal. The grey area is where the homogeneous disordered solution is stable. The white area means the homogeneous ordered solution is stable. The figure shows the importance of additional diffusion to enhance the stability of the liquid phase.

The Fig. 1.4 (a) is a typical characterization of the linear stability. If we look at the left panel, the grey part represents the limit of stability of the homogeneous disordered solution. Near the transition line, there is instability along the polar direction. This instability corresponds to the existence of bands. The white part is the stability area of the homogeneous ordered solution. Then, below the stability region, there is another instability which is called the spurious instability because it is not present at the Boltzmann level, and it is a side effects of the truncation procedure as it has been shown in [37, 38]. It is possible to add a diffusion term $D_0\Delta f$ in the Eq. (1.7) as presented in [24]. This diffusion term allows recovering the standard Vicsek diagram by removing the spurious instability thanks to the amplitude D_0. The middle and right panels show linear stability with the added positional diffusion. We see the homogeneous ordered solution is stabilized, and the spurious instability is reduced. At the onset of the transition line, the unstable mode is longitudinal, but the direction is turning when we reduce the noise with a fixed density. When there is diffusion the unstable mode becomes fully longitudinal. The Eq. (1.22) is

done at the onset of the transition line, and we can expect that modes developed at this point will continue to dominate far from the transition line. We see this is not the case, but the added positional diffusion allows us to recover the Vicsek phase diagram.

So far, we only have presented a study about homogeneous solutions. Nonetheless, inhomogeneous solutions of Eq. (1.22) exist. Indeed, if we simulate the hydrodynamic equations where the homogeneous ordered solution is unstable, near the transition line, we get bands, but these bands come from different solutions of Eq. (1.22). Solon et al have studied in [39] the existence of inhomogeneous solutions of generic Toner-Tu hydrodynamic equations. They have found three different types of solutions: periodic bands, solitonic bands, and a phase-separated profile. But there is no selection observed as in the microscopic model, to observe this selection it is needed to add noise to the equations as presented in [25].

Finally, the BGL approach introduces two important concepts. The first one is a microscopic model from which we can derive hydrodynamic equations Eq. (1.22). The second important point is a method to truncate the infinite hierarchy of PDE by expanding equations along the dominant mode at the onset of the transition line. This method is also used with different starting equations as we will show in the next section. This method is essential because it provides a qualitative agreement, by simulating equations, with the phase diagram of the Vicsek model through minor corrections. So it has been used with different models of active matter in [37, 40–45] and in different dimension [46].

1.2.3.3 Fokker-Planck approach

There are many ways to build a coarse-grained version of a microscopic model. Here we will present an approach based on the Fokker-Planck equation. The method to derive the stochastic dynamical equation for the density function has been done by Dean, and Farrell et al. in [47, 48] and has been used [49–51]. The Fokker-Planck equation is obtained by reducing the Fokker-Planck equation to the deterministic part as shown by Farrell et al. Then the next step is to use the GL truncation, as in the previous part, they get the hydrodynamic equations of the Vicsek model. We will detail the derivation of these hydrodynamic equations because it is used in the main part.

Microscopic model

The first step of this method is to consider the dynamics of a system of particles in a thermal white noise heat bath and the particles interact via a pairwise potential. Then it is possible to write a Langevin equation to describe the evolution of the particle i at time t and position $\vec{r}_i$. Here we will consider particles following a continuous time version of

the Vicsek model, the new equations are

$$\begin{aligned} \frac{\mathrm{d}\vec{r}}{\mathrm{d}t} &= v_0\vec{e}(\theta_i) \\ \frac{\mathrm{d}\theta_i}{\mathrm{d}t} &= \frac{\gamma}{\pi d_0^2}\sum_{j=1}^{N}\sin(\theta_j-\theta_i) + \sqrt{2D_r}\tilde{\xi}(t) \end{aligned} \tag{1.27}$$

where we have taken the same convention as the BGL section for the notation. v_0 is the modulus of the speed of the particles, D_r is the amplitude of the angular diffusion. Then Farrell et al. consider the density function given by $f(\vec{r},\theta,t) = \sum_{j=1}^{N}\delta(\vec{r}-\vec{r}_j)\delta(\theta-\theta_j)$, and by using the Itō calculus, according to the work of Dean, it is possible to derive the Fokker-Planck equation for the particle density function. They find

$$\begin{aligned} \partial_t f(\vec{r},\theta,t) + v_0\vec{e}(\theta)\cdot\vec{\nabla}f(\vec{r},\theta,t) = D_r\partial^2_{\theta\theta}f(\vec{r},\theta,t) - \partial_\theta\sqrt{2D_r f(\vec{r},\theta,t)}\xi \\ - \gamma\partial_\theta\left(f(\vec{r},\theta,t)\int_0^{2\pi}\mathrm{d}\theta' f(\vec{r}',\theta',t)\sin(\theta'-\theta)\right) \end{aligned} \tag{1.28}$$

One can compare the equation obtained with coarse-graining from Bertin et al. Eq. (1.7) and the one in Eq. (1.28). The first term which describes the advection of density probability is in common. Here, the second term corresponds to the angular diffusion and is different from the tumbling term in the BGL approach. There is a term of noise which is absent in the BGL coarse-graining. It is interesting because this term is multiplicative, so it matters only when the density function is nonzero. The last term relies on the interaction between particles and has a different form from the one derived in the BGL procedure. Moreover, the interaction term is computed in the mean-field approximation. Then the derivation of this equation is done under the approximation of a dense system. It is also possible to adimensionalized the Eq. (1.28) and rescale quantities as

$$t \to t/D_r \quad , \quad \vec{r} \to v_0\vec{r}/D_r \quad , \quad f \to \rho_0 f \quad , \quad \xi \to \sqrt{D_r\rho_0}\xi \tag{1.29}$$

Thus there is only one control parameter $g = \frac{\gamma\rho_0}{D_r}$.

Hydrodynamic equations

The next step, according to Farrell et al, is to perform a GL truncation and closure scheme after neglecting the noise term and taking the Fourier transform

$$\partial_t\hat{f}_k + \frac{1}{2}(\nabla\hat{f}_{k-1} + \nabla^*\hat{f}_{k+1}) = -k^2\hat{f}_k + \frac{gik}{2}\sum_{m=-\infty}^{\infty} f_{k-m}F_{-m}f_m \tag{1.30}$$

where $F_{-m} = \frac{i}{2}(\delta_{m,-1} - \delta_{m,1})$ with δ the Kronecker symbol. We perform the truncation at order $k = 2$ as BGL section, by using a similar scaling ansatz, and we get

$$\begin{aligned} \partial_t f_0 &= -\Re\left(\nabla^* f_1\right) \\ \partial_t f_1 &= \frac{g}{2}\left(f_0 - \rho_c\right) f_1 - \xi_{\text{FP}}|f_1|^2 f_1 + \nu_{\text{FP}}\Delta f_1 - \kappa_{1\text{FP}} f_1 \nabla^* f_1 - \kappa_{2\text{FP}} f_1^* \nabla f_1 - \frac{1}{2}\nabla f_0 \end{aligned} \tag{1.31}$$

Eq. (1.31) is a Toner and Tu like equation where the coefficients are given by

$$\begin{aligned} \rho_c &\equiv \frac{2}{g} & \xi_{\text{FP}} &\equiv \frac{g^2}{2} & \nu_{\text{FP}} &\equiv \frac{1}{16} \\ \kappa_{1\text{FP}} &\equiv \frac{g}{4} & \kappa_{2\text{FP}} &\equiv -\frac{g}{16} \end{aligned}$$

These coefficients allow us to recover the dependency to microscopic parameters contrary to the derivation from Toner and Tu, but in a very simple way compare to the BGL approach. Moreover, the Ginzburg-Landau coefficient behaves in the right way because the linear coefficient $\frac{g}{2}(f_0 - \rho_c)$ depends on the density and ξ_{FP} is always positive. Also, the diffusion coefficient is constant.

We can look at the homogeneous solutions of Eq. (1.31). There are two trivial solutions, the first one corresponds to the homogeneous disordered solution and the second one corresponds to the homogeneous ordered solution.

$$\begin{aligned} f_0 &= 1 \qquad f_1 = 0 \qquad \text{if } \; g < 2 \\ f_0 &= 1 \qquad |f_1| = \sqrt{\frac{(1 - \frac{2}{g})}{g}} \qquad \text{if } \; g > 2 \end{aligned} \tag{1.32}$$

The polarization of the homogeneous ordered solutions vanishes when $\rho_0 \to \infty$ because g depends on ρ_0 linearly. Here we can highlight the point that this derivation is done under the assumption of dense systems, but the homogeneous ordered phase vanishes in the limit of the dense system. This is the first problem with this approach.

The linear stability of the homogeneous ordered solution is unstable everywhere, and we can distinguish two modes. At the onset of the transition line, the instability is longitudinal but when we reduce the noise it becomes more transversal. Here, contrary to the Boltzmann approach, there is not a stable region for the homogeneous ordered solution [37]. In the Boltzmann approach, to stabilize the homogeneous ordered solution we add a positional diffusion but in that case, it has no effects on the linear stability.

Despite these issues, the hydrodynamic equation based on the coarse-grained through a Fokker-Planck equation has been used widely in the literature [9, 49, 50, 52–56] to describe different types of active matter. To conclude, we have seen that the equation derived from

the BGL approach are able to reproduce the Vicsek phase diagram contrary to the Fokker-Planck approach. Moreover, it is possible to simulate the hydrodynamic equations and find a qualitative agreement with the Vicsek model with BGL hydrodynamic equations.

1.2.4 Robustness of the Vicsek model

The Vicsek model has been presented as a limit case of active matter because it deals with identical particles which are moving at a constant speed in a homogeneous space. The model does not take into account interaction between the substrate and the particles and considers only alignment interactions. It allows describing a phase transition between a disordered phase and an ordered one even in 2D. So one can ask what is the robustness of the Vicsek model and what is the stability of the ordered phase. In real systems, the particles are not moving in a perfect substrate, or they are not perfectly identical and will perhaps interact weakly with the substrate.
So people have studied the effects of this heterogeneous media on the phenomenology of the Vicsek model. The results are the homogeneous ordered phase is changed, and the long-range order could become quasi-long range order [57–60], or it could be broken by any amount of quenched disorder [61].
A lot of active matter systems are made by biological particles and they are typically heterogeneous because their response to the environment will vary. Then it is possible to introduce systems with heterogeneous populations and study the robustness of the homogeneous ordered phase. People have studied different variation like a heterogeneous noise[62], speed inhomogeneity [63], different alignment between subpopulation [64], and subpopulation with different chirality [52, 65–67]. In all cases, they conclude, sometimes implicitly, that the ordered phase resists a finite amount of disorder.

1.3 Kuramoto model

1.3.1 General Kuramoto model

Presentation

One of the most studied systems in physics is the oscillator. One of the first oscillator studied was the pendulum which oscillates due to gravity, but today the modeling of physical systems as oscillators is ubiquitous. Huygens discovered that two identical pendulums put on the same support start to oscillate with the same frequency and phase. Nowadays, people are interested in systems where there are a large number of coupled oscillators in various fields of sciences, from physical systems such as power grids [68], chemical reactions [69], biological systems such as cardiac pacemakers cells [70] . Thus, an important question is, what is the minimal ingredient to get a frequency adjustment between coupled oscillators. The frequency adjustment is usually called synchronization [71]. This transition was first considered by Winfree in 1967 [72]. Then Yoshiki Kuramoto was interested

in such phenomena in chemical reactions and introduced a mathematical model in [73] to describe coupled oscillators. The Kuramoto model is a minimal model because it considers only a few ingredients: take into account only the phase of the oscillator. The dynamics are of the first-order derivative in time and the oscillators have a natural frequency. He has worked on this system which can be solved analytically [74]. The Kuramoto model for N oscillators can be express thanks to the following equation:

$$\frac{d\theta_i}{dt} = \omega_\alpha + K \sum_{j=1}^{N} \sin(\theta_j - \theta_i) \tag{1.33}$$

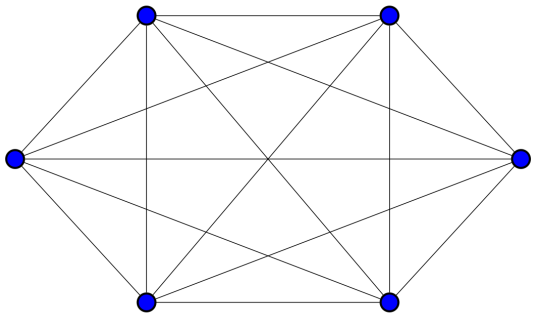

Figure 1.5: Illustration of a Kuramoto Network for $N = 6$. The links describe the existence of interaction between two oscillators.

in Eq. (1.33) ω_i is the natural frequency for each particle, and they are drawn from a distribution $g(\omega)$. K is the strength of the coupling. The coupling between oscillators runs over all the population, see illustration in Fig. 1.5. In Eq. (1.33) there is a competition between two terms, the natural frequency which forces the oscillator to oscillate at their natural frequency, and the coupling with the other oscillators. The natural frequency is fixed for each oscillator, so it plays the role of a frozen disorder. The nature of coupling is given by the sine of the difference between the phase of two oscillators. It means that synchronization coupling increases with the difference of angle until $\frac{\pi}{2}$ and decreases with the difference of angle until π. Here we see a competition between a frozen disorder and synchronization coupling. To measure the synchronization between oscillators, we have to compute the following order parameter:

$$re^{i\Psi} = \frac{1}{N} \sum_{j=1}^{N} e^{i\theta_j} \tag{1.34}$$

r measures the coherence of the oscillators and $0 \leq r \leq 1$. For a large number of oscillators, the incoherent state corresponds to a vanishing state, the synchrony state corresponds to r close to the unit. If r takes a non-zero value but far from the unit value you get a partial coherence only.

Results

The Kuramoto model can be solved exactly. We first have to consider the order parameter equation Eq. (1.34), multiply it by $e^{i\theta_\alpha}$ and keep the imaginary part. This step leads to the equation:

$$r\sin(\Psi-\theta_\alpha)=\frac{1}{N}\sum_{j=1}^{N}\sin(\theta_j-\theta_\alpha) \tag{1.35}$$

This equation allows us to replace the sum over all the oscillators with a term that involves only the difference between the phase of the current oscillator and the mean phase of oscillators. Then we can move to the rotating frame by the transformation $\theta_\alpha \to \theta_\alpha - \Omega t$ where Ω is the first moment of $g(\omega)$. By taking the limit $N \to \infty$, it allows to consider a probability density function for the oscillator and solve the equation.

In [75] Acebrón et al. present the different solutions of the standard Kuramoto model. In the case of a unimodal distribution $g(\omega) = \delta(\omega_0 - \omega)$, by moving in the rotating frame at pulsation ω_0 in 1.33 it remains only the synchronization term and there is only a synchronized phase of oscillators.
In the case of a Gaussian distribution $g(\omega)$, it is possible to define K_c as a threshold value for the Kuramoto model. Thus, for $K < K_c$ you get the incoherent phase ($r = 0$), for $K_c \leq K$ you a get a partial synchronization ($0 \leq r \leq 1$), and for $K \to \infty$ you get synchronization of the whole population of oscillators $r = 1$, see Fig. 1.6.

In the case of a bimodal distribution $g(\omega) = \frac{1}{2}\delta(\omega_0-\omega)+\frac{1}{2}\delta(\omega_0+\omega)$, according to [77–79] there is a new phase which is called standing waves. So standing waves correspond to a phase where you get a cluster of partial synchronization in both populations. So you start at low K with an incoherent phase. Then when you increase K you get the standing wave and for large K you get partial synchronization.

1.3.2 Kuramoto model under random external force

In physical situations, there are interactions that a minimal model can not catch. An easy way to take into account these perturbations is to use randomness. Then it is possible to add noise to the standard Kuramoto model 1.33 and the new equation is:

$$\frac{\mathrm{d}\theta_i}{\mathrm{d}t}=\omega_i+K\sum_{j=1}^{N}\sin(\theta_j-\theta_i)+\xi_i(t) \tag{1.36}$$

where $\xi_i(t)$ is a Gaussian white noise with $\langle\xi_i(t)=0\rangle$ and $\langle\xi_i(t)\xi_j(t')\rangle = 2D\delta(t-t')\delta_{ij}$. This noise can model random perturbations due to the environment. So there is a competition between three different terms now (frozen disorder, noise disorder, and synchronization).
In the case of unimodal distribution of natural frequencies $g(\omega) = \delta(\omega_0-\omega)$ the model 1.36 becomes the standard XY model by moving in the rotational frame rotating at pulsation

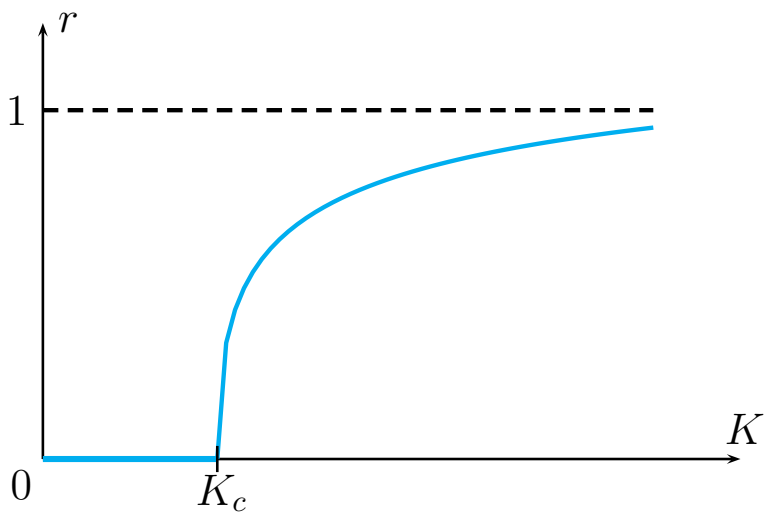

Figure 1.6: Evolution of the order parameter r for a mean field ($N \to \infty$) standard Kuramoto model with unimodal distribution [76]. Typically $g(\omega)$ could be given by a Gaussian distribution which is the only unimodal distribution with non-zero variance used in this manuscript. For a Gaussian distribution $K_c = \frac{2}{\pi g(0)}$. The figure shows a second order phase transition for a Gaussian distribution.

ω_0 [80]. The parameters can be understood as D is equivalent to the temperature T and K is the strength of the ferromagnetic interaction. The synchronization transition will correspond to the disorder-magnetization transition.
In [81] Sakaguchi studies the effects of the random force on a Gaussian distribution $g(\omega)$. He found that for limited strength of disorder D the value of K_c is larger than the standard Kuramoto 1.33 value. But there is no qualitative change in the transition from the disordered phase to the synchronization phase. For large values of D there is only a disorder phase and the study has no interest.
In the case of a bimodal distribution of natural frequencies $g(\omega) = \frac{1}{2}\delta(\omega_0 - \omega) + \frac{1}{2}\delta(\omega_0 + \omega)$, Bonilla et al. show the existence of two new phases in [82]. The first phase is called traveling waves and is always unstable. The second new phase is called standing waves and corresponds to an oscillatory order parameter $r(t)$ such as Fig. 1.7. The frequency and the amplitude of the oscillation of the order parameter change in a non-trivial way concerning the microscopic parameters. For large values of K the standing waves merge and give the standard synchronized solution.
One can conclude that the application of a random external force on the Kuramoto model does not change the qualitative behavior of the standard model.

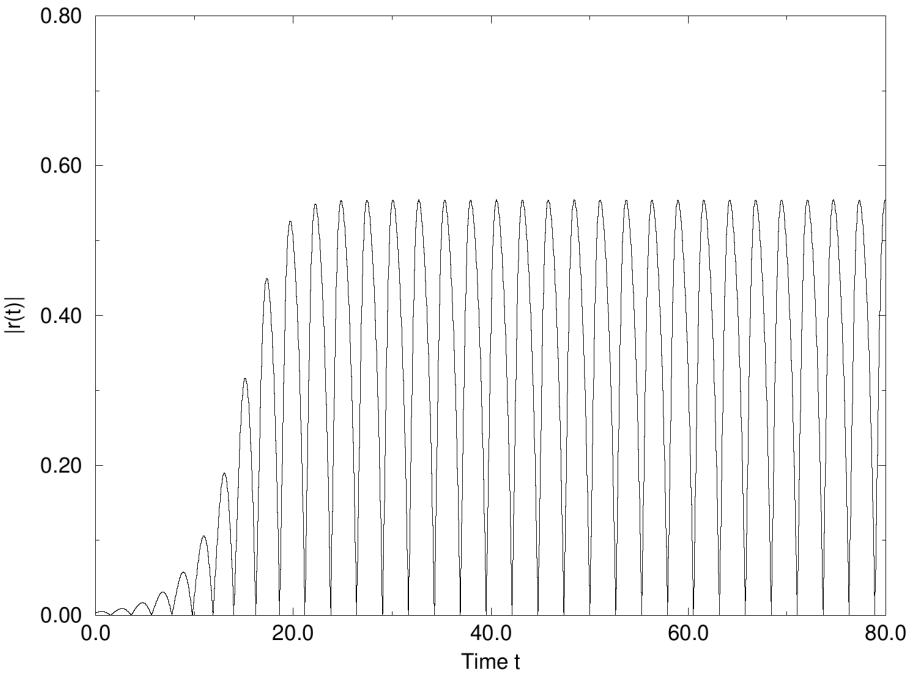

Figure 1.7: Evolution of the order parameter for the phase called standing wave. Figure from [82] with $N = 50$k, bimodal distribution of chirality $g(\omega) = \frac{1}{2}\left[\delta(\omega - \omega_0) + \delta(\omega + \omega_0)\right]$. Simulations are done with a standard Euler integration and $K = 5.1$, $D = 1$, $\omega_0 = 2$.

1.3.3 Kuramoto model in finite dimension

In the previous part, we have summarized the influence of noise which changes the competition by adding another disorder. In this part, we will study a change in the synchronization term. The standard Kuramoto is a model that relies on a fully connected network. Thus, it corresponds to coupling in infinite dimension because each oscillator will synchronize with all the other oscillators. Now we can ask what happens if we limit the interaction to only neighbors of a lattice in finite dimension. The Kuramoto model becomes

$$\frac{\mathrm{d}\theta_i}{\mathrm{d}t} = \omega_i + K \sum_{j \in \mathcal{B}} \sin\left(\theta_j - \theta_i\right) \tag{1.37}$$

where $\mathcal{B}$ corresponds to the neighborhood of i for a given lattice.
In [80] Sakaguchi et al. have studied the case of $d = 1, 2, 3$ hypercubic lattice with $g(\omega)$ a Gaussian distribution with zero mean and unit variance. They conclude that it is not possible to get a full phase synchronization for $d \leq 2$. This result has been confirmed in one dimension in [83] by Strogatz et al.. Then Hong et al. have studied [84] the Kuramoto model in finite dimension with a Gaussian distribution of natural frequency but with

larger simulations and dimension (up to $d = 6$). They show the existence of two different behaviors. In dimension above $d > 4$, the globally coupled model results are observed. In dimension, $2 < d \leq 4$, synchronization occurs in domains of finite-size. The size of these domains follows a scaling with the dimension with the coefficient $\nu = \frac{2}{d-2}$. There is no known study to the case where $g(\omega)$ is a bimodal distribution.

1.4 Work presented in this dissertation

In this section, we will do the link between the Vicsek model and the Kuramoto model. Then we will present the model called Kuramoto-Vicsek model (KVM). We will end the section with the organisation of my results.

1.4.1 Time continuous Vicsek model

A second variation of the Vicsek model is the time-continuous Vicsek model. This model can be explicit as

$$\begin{aligned} \frac{\mathrm{d}\vec{x}_i}{\mathrm{d}t} &= v_0 \vec{e}(\theta_i(t)) \\ \frac{\mathrm{d}\theta_i}{\mathrm{d}t} &= \frac{\kappa}{\mathcal{B}_i} \sum_{j \in \mathcal{B}_i} \sin\left(\theta_j(t) - \theta_i(t)\right) + \eta \xi_i(t) \end{aligned} \tag{1.38}$$

where $\mathcal{B}_i$ is the neighborhood of i in a disk of radius $R = 1$ and κ is the strength of the ferroalignment.
In the standard Vicsek model defined by Eq (1.1) the particles align instantaneously between two time steps. There is no difference in synchronization between particles with a close direction of polarization and particles with opposite directions of polarization. Now if you take into account the time-continuous limit of the update rule, according to [65, 85], you get the Eq. (1.38).
Now the interaction is no more the mean of the neighborhood polarization angle but the mean of the sine of the difference of polarization angle. It means that the strength of the interaction grows from 0 to 1 for a difference of polarization angle from 0 to $\frac{\pi}{2}$. But then the strength of the interaction decrease from 1 to 0 for a difference from $\frac{\pi}{2}$ to π. It means that if two particles have an opposite direction they almost do not interact together because they will be far away before they manage to align in the same direction. On the contrary, if two particles almost go in the same direction the alignment will be close to the standard Vicsek alignment. This simple change in the way particles interact will just describe the time needed for particles to change their direction.
There is no qualitative change in the standard Vicsek model results but here we introduce one new parameter κ. So the strength of the alignement is now governed by two parameters ρ_0 and κ, and the behavior is controled by only two dimentionless parameters.

Link between the Vicsek model and the Kuramoto model

In this paragraph, we want to highlight the existence of a link between the Kuramoto model in finite dimensions and the Vicsek model in continuous time. If we look at Eq. (1.38), the alignment term takes the form of a sum over the neighbors. Inside this sum the alignement takes the form of a sine for the difference of angles. Then if we look at Eq. (1.37), the synchronization term takes the form of a sum over the neighbors too. Moreover, the synchronization takes also the form of a sine for the phase difference. From this point, if we take the direction of the polarization as the phase of an oscillator, the two alignment/synchronization terms have the same expression.
The link between the Vicsek model and the Kuramoto model has been already established in different papers as [65]. They explicit the microscopic equations and they study the mean-field kinetic and hydrodynamic limits with two different scalings. There is a second paper from Chepizhko et al. [86] where they do the link between the nature of the phase transition (first or second order) of the Vicsek model for standard or vectorial noise, and the nature of the transition for the Kuramoto model. However, these conclusions do not remain valid due to the fact that the first claim about second order phase transition of the Vicsek model was due to finite-size effects.

1.4.2 Kuramoto-Vicsek model (KVM)

The goal of this thesis is to describe a minimal model for N chiral active particles moving at a constant speed and subject to alignment interactions. "Chiral particle" means that in a free space each particle will follow equations

$$\begin{aligned} \frac{\mathrm{d}\vec{r}_i}{\mathrm{d}t} &= v_0 \vec{e}(\theta_i) \\ \frac{\mathrm{d}\theta_i}{\mathrm{d}t} &= \omega_i \end{aligned} \tag{1.39}$$

where $\vec{r}_i$ is the position of the particle i, v_0 is the constant speed, θ_i is the direction of the polarization, thus $\vec{v}_i = (v_0 \cos(\theta_i), v_0 \sin(\theta_i))$. Also, we will denote by $g(\omega)$ the probability distribution for the chirality of the N particles.
It means that a particle i will describe a circular trajectory with a radius $r_i = \frac{v_0}{\omega_i}$ and period $T_i = 2\pi/\omega_i$. The next step of our description is to add the interaction, and this alignement interaction is taken as the continuous time limit of the Vicsek model. Now the particles obey the following equations

$$\frac{\mathrm{d}\vec{r}_i}{\mathrm{d}t} = v_0 \vec{e}(\theta_i) \tag{1.40a}$$

$$\frac{\mathrm{d}\theta_i}{\mathrm{d}t} = \omega_i + \frac{\kappa}{\mathcal{D}_i} \sum_{j \in \mathcal{D}_i} \sin(\theta_j - \theta_i) + \sqrt{2D_r}\xi_i \tag{1.40b}$$

where $\mathcal{D}_i$ is the number of particles contained in a disk of radius d_0 centered on particle i, κ is the strength of the coupling, D_r is the amplitude of the angular noise, and ξ a Gaussian white noise taken in $[-\frac{\pi}{2}, \frac{\pi}{2}]$. If we look at the update rule of the polarization angle Eq. (1.40b), we see a competition between three different terms: frozen chirality disorder, phase synchronization, and angular random noise. This is interesting because it is a 2D version of the noisy Kuramoto model Eq. (1.36) with a nonequilibrium equation. Now the difference is that oscillators are self-propelled, so the number of neighbors will change dynamically.

This new model (Eq. (1.40)) raises interesting questions. Indeed, we know that the Kuramoto model does not exhibit synchronization in 2D [84], but the Vicsek model does. Moreover, the Vicsek model does not resist a finite value of frozen disorder in given cases [61]. Does the Vicsek model resist a finite value of chirality disorder? So we will answer this question in this thesis.
We will study the Kuramoto Vicsek Model (KVM) through three different distributions. As it has been shown in the presentation of the Kuramoto model, the nature of the distribution plays an important role. In the case of the Kuramoto model, an unimodal distribution such that $\omega_i = \omega_0$ can be reduced, through a change of coordinate, to the absence of chirality. Nonetheless, in the KVM it is relevant to consider the unimodal distribution due to self-propulsion which does not allow a similar change of coordinate, because it will change the interaction between particles. Then we consider the bimodal distribution such that $g(\omega) = \frac{1}{2}\delta(\omega - \omega_0) + \frac{1}{2}\delta(\omega + \omega_0)$. Here the distribution gets a non-zero variance, and the variance plays an important role in the Kuramoto model such as governing the nature of the transition. Then we will study the Gaussian distribution such that $g(\omega) = \frac{1}{\omega_0\sqrt{2\pi}} e^{\frac{-\omega^2}{2\omega_0^2}}$. This distribution is physically important because it could model real chiral active particles which prefer to move in one direction due to a little shape deformation.

The group of Levis and Liebchen have worked on a similar model [52, 66, 67] but in their case they do not normalize the synchronization interaction. In section 2.5, we will compare the results from the two models and discuss the results of each one.

Our definition of chiral active particles is particles which describe circular trajectories. A simple definition of chirality given to people who start to learn science is: "chirality is a property of an object which is not stackable to its mirror reflection". In fact, it means there are broken symmetries. Now if we consider chiral active object, it means that the displacement of these objects will not be invariant under some symmetries. So the definition of chirality is larger than our interpretation. This property is present for biological systems such that bacteria near a wall [87], sperm cells [88], cytoskeleton at the sub-cellular scale [7, 89, 90], tissue at the multicellular scale [91]. Also, it has been studied with different kind of models [52, 66, 67, 92–98].

1.4.3 Organization of the thesis

This thesis is devoted to the study of the Kuramoto-Vicsek model (KVM). I study three different distributions which correspond to the three different parts of the manuscript.
In the first part, I study the KVM with a Gaussian distribution of chirality with zero mean and unit variance. We choose this distribution of chirality with regards to the key role played by this distribution in the Kuramoto model. I present the result of simulations at the microscopic level through a phase diagram and a study of finite-size effects. It is difficult to work analytically with this distribution of chirality, so I study simpler distributions and try to understand the link with the Gaussian distribution.
In the second part, I study the KVM with the simplest possible distribution which is the unimodal distribution. First, I perform microscopic simulations to draw the phase diagram. Then I study the stability of the different phases in the asymptotic limit and characterize the nature of their phase separation. Then I derive hydrodynamic equations with two different recipes. The first one is called the Fokker-Planck approach and the second one is called the Boltzmann Ginzburg Landau approach. To study these equations I study the linear stability of the homogeneous stationary solution and perform the simulation of these equations when it is possible.
In the next part, I study the KVM with a bimodal distribution which is composed of two unimodal distributions with opposite chirality. This bimodal distribution could be seen as a limit case of the Gaussian distribution for small values of chirality. I follow the same scheme as the previous part. First, I perform a microscopic study by numerical simulations and characterization of the different phases. Then I derive the hydrodynamic equations and study them thanks to their homogeneous stationary solutions. I finish my study by the simulation of these equations.
In the last part, I compare my results with the literature and I will focus on the close model from Levis and Liebchen.

Chapter 2

Kuramoto-Vicsek model

2.1 Introduction to microscopic simulations

In this section, I will provide the numerical details used to perform microscopic simulations of the KVM. I will also present the different considerations around phase determination.

Numerical integration

We will perform microscopic simulations by solving numerically these coupled Langevin equations Eq. (1.40). To do this, we use an Euler integration with a forward update rule:

$$\begin{aligned} \vec{r}_i(t+\Delta t) &= \vec{r}_i(t) + \Delta t\, v_0\, \vec{e}_i(\theta_i(t+\Delta t)) \\ \theta_i(t+\Delta t) &= \theta_i(t) + \Delta t\, \omega_i + \Delta t\, \frac{\kappa}{\mathcal{B}_i} \sum_{j\,\in\,\mathcal{B}_i} \sin\!\big(\theta_j - \theta_i\big) + \sqrt{2D_r \Delta t}\, \xi_i \end{aligned} \tag{2.1}$$

We choose the forward update rule to reduce the finite-size effects. In general, we use a time step $\Delta t = 0.1$ which is enough to get convergence for the standard Vicsek model. For a reasonable value of chirality this time step is small enough but for very large value of chirality it is needed to reconsider its value.

To perform the simulations, we use a rectangular system of size $L_x L_y$, but when we just specify L it means we have used a square system with $L = L_x = L_y$. The range of system sizes is from $L = 64$ to $L = 1024$, it allows us to take care about the finite-size effects.

Phase determination

There are several possibilities to determine the nature of a phase. The first one is by looking to snapshot at different time step and identify the characteristic patterns. This method is fast but qualitative. In general, the first method is used to build the phase

diagram. The second method is by looking at order parameters. We define different order parameters, the global polarization over the N particles is defined by

$$\vec{P}(t) = \frac{1}{N} \sum_{i=1}^{N} \vec{e}(\theta_i(t)) \tag{2.2}$$

The local polarization at position $\vec{x}_0$ is defined as

$$\vec{p}(t) = \frac{1}{N(\vec{x}_0)} \sum_{i \in \mathcal{B}_{\vec{x}_0}} \vec{e}(\theta_i(t)) \tag{2.3}$$

where $\mathcal{B}_{\vec{x}_0}$ is the vicinity of position $\vec{x}_0$.
In some cases there are particles with positive and negative chirality. If we restrict the sum over particles with a given sign of chirality we will add $\pm$ to the order parameter.
The chirality segregation is obtained by dividing the system in cells a of surface S_a and compute the average

$$c(t) = \left\langle \frac{1}{\omega_0} \sum_{i \in a} \frac{\omega_i}{S_a} \right\rangle_a \tag{2.4}$$

As in the standard Vicsek model, some phases are composed by well-defined phases in equilibrium with a sparse gas. There are two types of separation for this kind of phases. The first one is called microphase separation and it means that each pattern can hold a maximum number of particles. So when you increase the number of particles in a system, you will increase the number of patterns inside the systems. The other type of phase separation is called macrophase separation, it is when the number of particles held by a pattern is not fixed. In that case, when you increase the number of particles inside a system you increase the number of particles inside the pattern and not the number of pattern.

Finite size effects

The study of finite-size effects matters a lot in this kind of system, historically it leads Vicsek et al. to conclude to a second order phase transition for the Vicsek model and avoid seeing the band phase for small system size. So we take care of determining the existence of each phase asymptotically to avoid these mistakes. It is an important step because sometimes new phases seem to be discovered for a given set of parameters, but only when we perform an asymptotic study we can conclude to the existence of this new phase.

Phase diagram

We have shown the phase diagram of the Vicsek model in Fig. 1.3. The Vicsek model is modelling a competition between a noise term and an alignment term which is driven

by the density. One can conclude that if we work at a fixed density, the nature of the transition is always the same, only the value of noise where the transition happen is affected. It means we can fix the density value and vary only the noise without loosing any properties of the Vicsek model. In the time continuous model, a new parameter κ is affecting the weight of the alignment term but as for the standard model this parameter does not change the nature of the transition, and we will fix it to reduce the study to the same phase plane of the standard Vicsek model. Moreover, we remind that Chaté et al. [17] have shown that the velocity v_0 does not change the transition of the Vicsek model, then we will also fix it. So v_0, κ, ρ_0 are fixed, and we work in the phase plane (D_r,ω_0) to draw phase diagram. Thus, for $\omega_0 = 0$ we should recover the standard Vicsek model results. To characterize the different phases we will use the order parameters and summarize the results in the following Tab. 2.1. A part of this table is common to all the different phases and the Vicsek model. Along the presentation of my results, I will explain with more details and snapshots the different phases.

2.2 Gaussian distribution

In this section, we perform our computation with a Gaussian distribution of chirality. It means $g(\omega) = \frac{1}{\omega_0\sqrt{2\pi}} e^{-\frac{\omega^2}{2\omega_0^2}}$. We choose this distribution because we want to increase smoothly the chirality from the standard Vicsek case. The study of this distribution has been done through microscopic simulations.

2.2.1 Numerical Results

2.2.1.1 Phase diagram

We have drawn a phase diagram for a system of size $L = 128$, a density $\rho_0 = 1.00$, $v_0 = 1$ and a coupling strength $\kappa = 1.00$ constant. It means that we have plotted the phase diagram in the noise D_r, chirality ω_0 plane. In Fig. 2.1 the red hatch area is where the size $L_x < 4/\omega_0$, it corresponds to two times the typical radius of particle trajectory with chirality ω_0. We choose this value because there are particles with a positive chirality and a negative chirality. Thus, below this system size, phenomena observed are sure to be subjected to very strong finite-size effects and are unlikely to be representative of the asymptotic infinite-size limit. In Fig. 2.1, one can see the existence of the three standard phases of the Vicsek model: the gas phase (homogeneous disordered), the liquid phase (homogeneous ordered) and the bands phase (coexistence phase) at $\omega_0 = 0$. Now we will focus on what happen when we increase the chirality for each phase.
The disordered phase is not affected by the chirality and it remains disordered any way and the value of noise D_r where the disordered phase become unstable is not determined by the chirality.

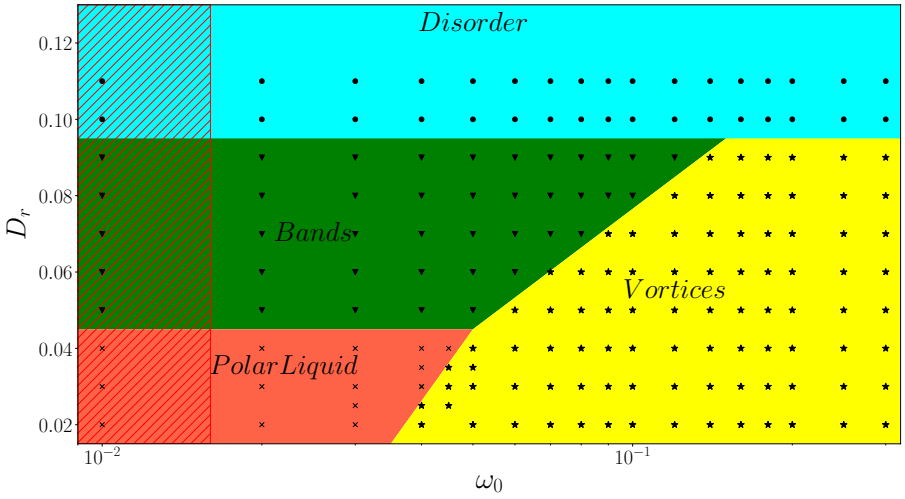

Figure 2.1: Numerical study of the phase diagram for the Gaussian distribution. Phase diagram in the plane (D_r, ω_0) for a system with parameters $L = 128$, $\rho_0 = 1$ and $\kappa = 1.00$. We put a marker for each simulation. The figure shows the existence of a new phase composed of Vortices.

The band phase remains for the small value of chirality. For larger value of ω_0 a new phase exists, see Fig. 2.2. The coarse-grained density is corresponding to the average local value of the density field for a small cell. This new phase is called vortices phase, because the density shows high dense packets where the polarization of the particles is turning aroung a center. From Fig. 2.2, we see another important feature which is the segregation between particles with positive chirality and particles with negative chirality.

Then we focus on results at the liquid noise level ($D_r = 0.3$). At zero value of chirality we get the standard liquid of the Vicsek model. Then, when we increase the chirality, the liquid phase remain until a threshold value, where the liquid disappears and forms vortices. As for the vortices at the band noise level ($D_r = 0.8$) there is a segregation between particles with positive and negative chirality.

In Fig. 2.3, we plot the difference of angle for the polarization orientation between particles with a positive chirality and negative chirality at the band noise level ($D_r = 0.8$). We see that the difference of orientation is growing with the value of chirality.
The polar liquid at zero chirality corresponds to a synchronization of all the particles. However, for non-zero value of chirality the polar liquid is different because there is a difference of polarization between particles with positive chirality and particles with negative chirality. The polarization of the two subpopulation are not pointing in the same direction and the polarization of the liquid corresponds to the mean value.

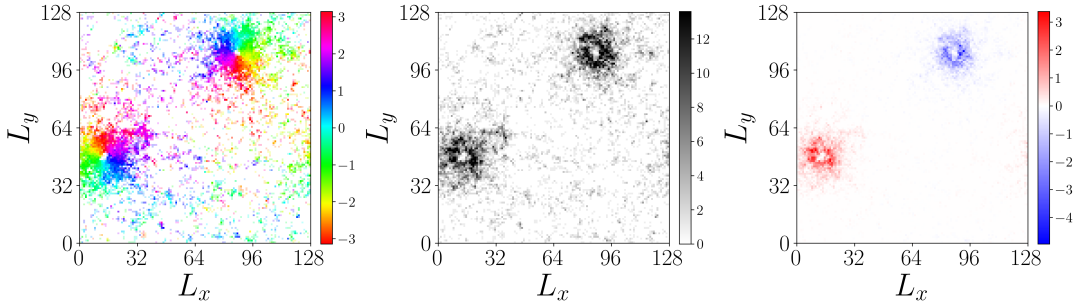

Figure 2.2: A typical snapshot of a vortex phase for a Gaussian distribution. The microscopic parameters are $\kappa = 1$,$\rho_0 = 1$, $L = 128$, $D_r = 0.03$, $v_0 = 1$ and $\omega_0 = 0.2$ The left panel shows the local coarse-grained direction of the polarization. The middle panel shows the coarse-grained density. The right panel shows the coarse-grained chirality. The figure shows the typical vortex pattern and the segregation according to the sign of their chirality.

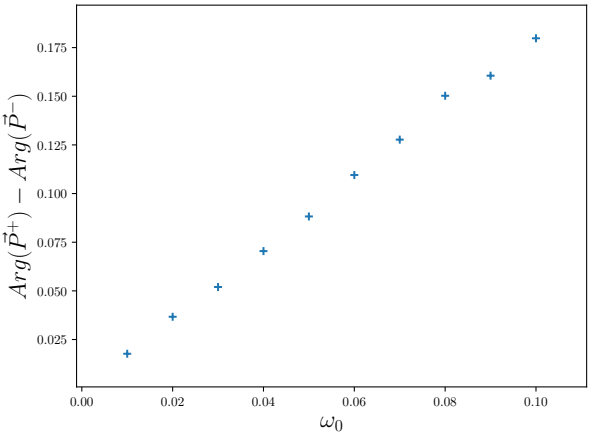

Figure 2.3: Study of the polarization inside a band phase for Gaussian distribution of chirality. It shows the difference of orientation between particles with a positive chirality and negative chirality as a function of ω_0 for the parameters $\rho_0 = 1$, $\kappa = 1$, $v_0 = 1$, $D_r = 0.8$, and $L = 128$. $\vec{P}^{\pm}$ is the total polarization of the particles with positive/negative chirality. The figure shows that the difference of polarization between particles with a positive and a negative chirality grows linearly as a function of ω_0.

So it seems that for the Kuramoto-Vicsek model with a Gaussian chirality distribution it exists only one new phase but lot of questions are open. We summarize the results for a Gaussian distribution and the later results in Tab. 2.1. To have some certainty we need to clarify the finite-size effects and the effects of initial conditions.

Phase name	Global polarization $\lvert\vec{P}\rvert$	Local polarization $\lvert\vec{p}\rvert_{\vec{x}_0}$	Global direction $Arg(\vec{P})$	Local direction $Arg(\vec{p}_{\vec{x}_0})$	Chirality segregation
Gas	Low	Low			No
Liquid	High	High	Constant	Constant	No
Bands*	Average	High	Constant	Constant	No
Rotating liquid	High	High	Rotating in time	Rotating in time	
macrodroplet*	Average	High	Rotating in time	Rotating in time	
Rotating packets*	Low	High		Rotating in time	Yes**
Vortex*	Low	High		Rotating in space	Yes**

Table 2.1: Table of the different characteristics of each phase. *:When the phase name get a star it means the phase is in equilibrium with a sparse gas. Thus, in the table we only write the local order parameters for the given pattern and not for the gas phase. Yes**: it means when it is applicable so for Gaussian or bimodal distribution of chirality.

2.2.1.2 Asymptotic behavior

Finite-size effects at liquid noise level ($D_r = 0.3$)

In this paragraph, we will study the finite-size effects at the liquid noise level. To perform this study we will plot the phase diagram in the plane size L, chirality ω_0. It will allow us to understand how evolves the boundary between two different phases with the system size. Then it allows us to determine if a phase exists in the asymptotic limit of infinite system size.

In Fig. 2.4 one can see that the liquid phase seems to disappear in the limit of infinite-size system. To be sure we will perform a quantitative study by plotting the mean value of the polarization observable $|\vec{P}|$ over time series. We plot the results in Fig 2.5. In this figure we observe a quick threshold between a value around $|\vec{P}| \sim 0.8$ to a very small value. We define the transition value using a threshold such that $|\vec{P}|^* = 0.5$. This threshold allow us to interpolate the curve and get a precise value of the transition. We plot the evolution of the transtion $\omega_0^*(L)$ in Fig 2.6.

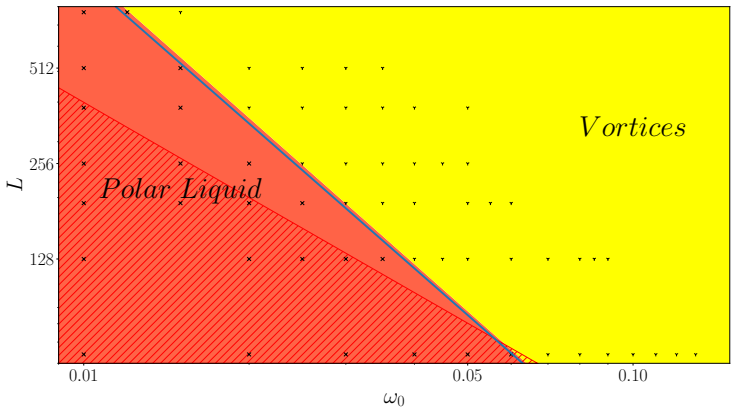

Figure 2.4: Numerical study of the asymptotic behavior for the Gaussian distribution. Phase diagram in the plane (L, ω_0) for a system with parameters $D_r = 0.030$, $v_0 = 1$, $\rho_0 = 1$ and $\kappa = 1.00$. Slope$= -1.52$ and Correlation coefficient $r = 0.977$. The figure shows that the value where the transition occurs decreases as a power law. Thus the polar liquid phase does not exist in the limit of infinite system size. Hatched area is corresponding to where we expect finite-size effects.

In Fig 2.6 we fit points by a linear regression and there is a good agreement according to the correlation coefficient. So it confirms our qualitative analysis and we can conclude that the value of chirality where the transition occurs decreases as a power law with $\omega_0^* \sim L^{-0.684}$.

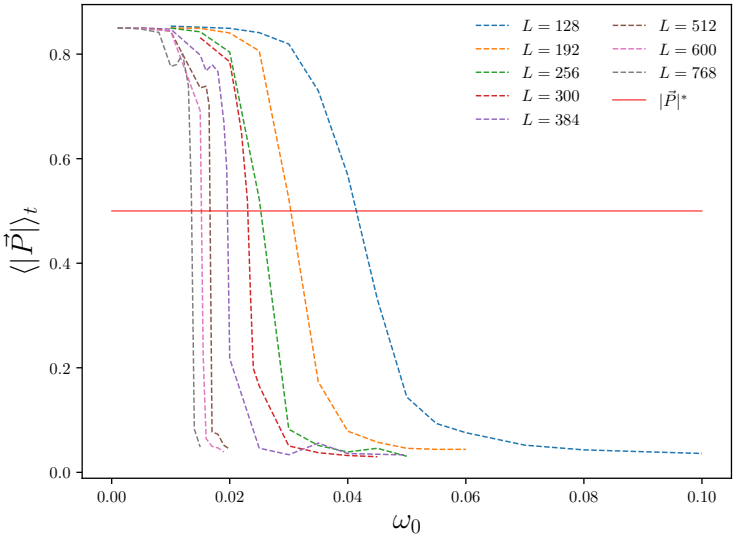

Figure 2.5: A quantitative study of the transition between polar liquid and vortices for a Gaussian distribution. Mean value of the polarization's modulus over time series as a function of the chirality ω_0 for various system sizes L. The red line marks the transition between the polar liquid phase and the vortex phase. The threshold value is $|\vec{P}|^* = 0.5$. The intersection gives the value $\omega_0^*(L)$.

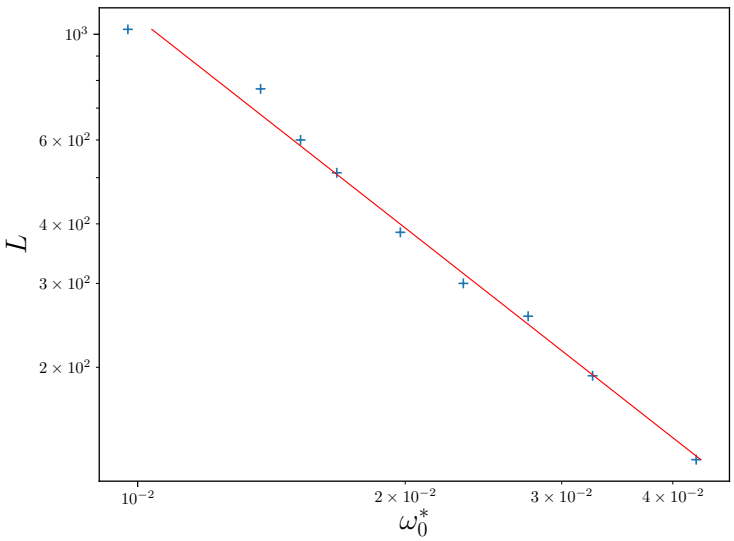

Figure 2.6: A quantitative study of the asymptotic behavior of the polar liquid phase for a Gaussian distribution. Evolution of ω_0^* as a function of L. Linear regression gives a slope of -1.462 ± 0.051 and a correlation coefficient of $r = -0.9958$. The figure shows that the value where the transition occurs decreases as a power law and thus the polar liquid does not exist in the limit of infinite system size.

Finite-size effects at band noise level ($D_r = 0.8$)

In this paragraph, we will study the finite-size effects at band noise level. To perform this study we will plot the phase diagram in the plane size L, chirality ω_0. It will allows us to understand how the boundary between two different phases evolves with the system size. Then it allows us to determine if a phase exists in the limit of infinite system size.

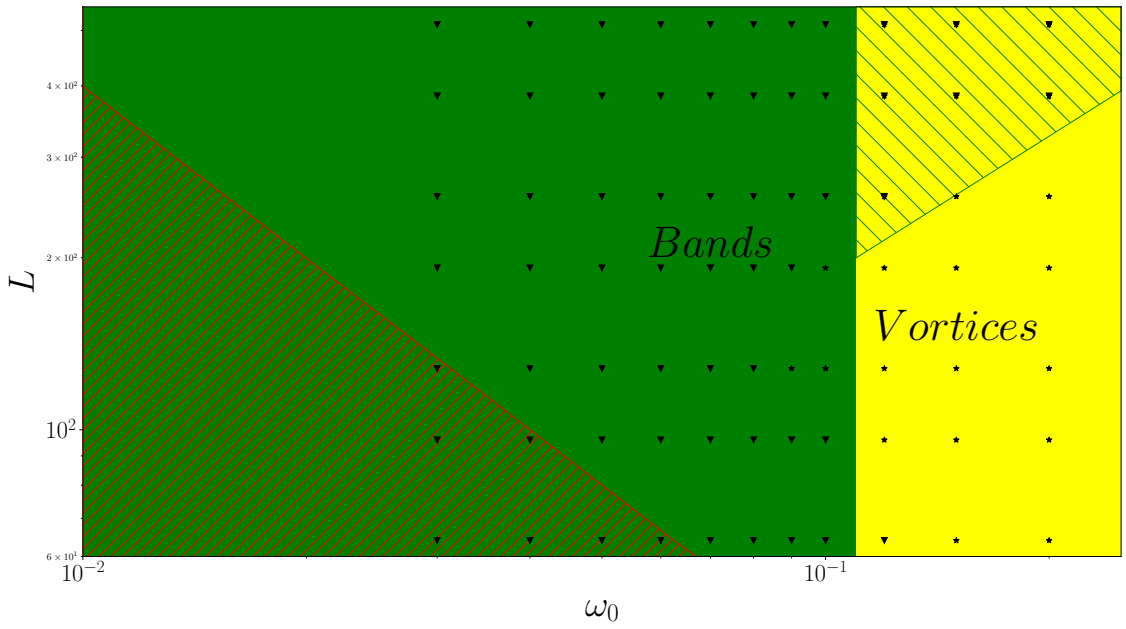

Figure 2.7: Asymptotic study of the bands phase for a Gaussian distribution. Phase diagram in the plane (L, ω_0) for a system with parameters $D_r = 0.030$, $v_0 = 1$, $\rho_0 = 1$ and $\kappa = 1.00$. The figure shows that the bands phase is stable in the limit of infinite system size.

In Fig. 2.7 one can see that the limit between bands and vortices is stable when we increase the size of the system. The red hatched area is corresponding to the place where we expect finite-size effects. Furthermore, above a given system size, it is possible to see a coexistence between bands and vortices, see Fig 2.8. In this snapshot, we see a spatial segregation between vortices with a positive chirality and vortices with a negative chirality. Also, there are lines due to the interaction with the bands.

Vortex phase: a microphase separation

We will try to determine the nature of the separation for the vortex phase. The first argument is when the system starts to become large enough we start to see a coexistence

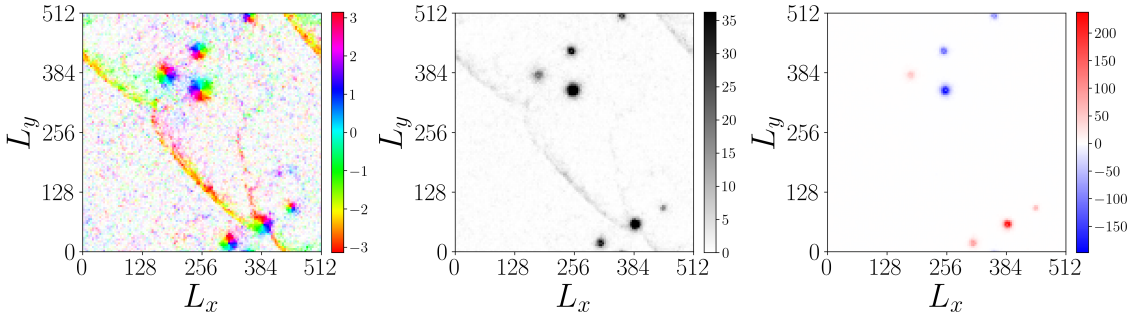

Figure 2.8: Typical snapshot of a coexistence between bands and vortices for a Gaussian distribution of chirality with parameters $L = 512$, $\omega_0 = 0.2$, $D_r = 0.070$, $v_0 = 1$, $\rho_0 = 1$ and $\kappa = 1.00$. The figure shows segregation for vortex patterns and coexistence with bands where the particles are mixed. The left panel shows the local coarse-grained direction of the polarization. The middle panel shows the coarse-grained density. The right panel shows the coarse-grained chirality.

between vortices and bands. Moreover, for small systems, there is only one vortex for each subpopulation but if the system size increases it becomes impossible to see such state even with handmade initial condition. However the situation is not clear, because if we start with a system which contains four pairs of vortices we can see a condensation up to two pairs of vortices. Up to our numerical study it seems we can conclude to a microphase separation.

Hydrodynamic considerations

In the standard Vicsek model, we have presented different possibilities to perform a coarse-graining from the miscrocopic level but in that case the particles are identical so we have to consider only one population of particles. In the case of a Gaussian distribution of chirality, each particle is different and has its own intrinsic chirality. Therefore, if we want to build a coarse-grained version we have to consider an infinite number of subpopulations which are interacting together. It is quite difficult to deal with this situation. From the Kuramoto model, we know that the different moments of the distribution play a key role. In the Gaussian case, the distribution has a zero mean and a variance given by ω_0. Now if we look for a distribution that shares these two characteristics and that is tractable at the analytical level, we propose to use the bimodal distribution which is composed by two subpopulation with an opposite unimodal distribution of chirality. So the first step will be to study the unimodal distribution of chirality and then to extend to a bimodal distribution of chirality. The study of the unimodal case will be useful at the hydrodynamic level to understand the bimodal case, but at the microscopic level the global chirality of the system is non-zero and different results are expected.

2.3 Unimodal distribution

In this section, we perform our computation with a unimodal distribution for the frozen chirality disorder. It means for all particles $\omega_i = \omega_0$ or $g(\omega) = \delta(\omega - \omega_0)$. This distribution of chirality belongs to the theoretical approach of building a hydrodynamic theory for the bimodal distribution of chirality. However, it can not be reduced to this because there is a broken symmetry for the chirality. The unimodal distribution of chirality is an important case by itself and there is experimental realization of this kind of particles such as *E. coli* [99–101], sperm cells [88, 102], magnetotatic bacteria in a rotating field [103, 104], curved polymer [96] and synthetic swimmers with a L-shape [105, 106]. So it will help us to build the hydrodynamic theory for a bimodal distribution and build a minimal model which could describe a wide range of phenomena.

2.3.1 Numerical Results

2.3.1.1 Phase diagram

According to previous explanations, we have drawn in Fig. 2.9 a phase diagram for a system of size $L = 256$, a density $\rho_0 = 1.00$, a velocity $v_0 = 1$, and a coupling strength $\kappa = 1.00$ constant. It means that we have plotted the phase diagram in the noise D_r, chirality ω_0 plane without any loss of generalities.
The red hatch area is where the size $L_x < 1/\omega_0$. This corresponds to the typical radius of the trajectory of a particle with chirality ω_0. It means if the system size is below this threshold, one chiral active particle in a free space could not describe its circular trajectory.

One can see the existence of the three standard phases of the Vicsek model: the gas phase (homogeneous disordered), the band phase, and the liquid phase (homogeneous ordered) at zero chirality value. Now we will focus on what happens when we increase the chirality for each phase.
The disordered phase is not affected by the chirality, and it remains disordered any way. What is interesting is that the noise threshold where the transition occurs is constant, so even if we increase the total disorder, the phases below this threshold are robust to this chirality frozen disorder. The band phase remains for the very small value of chirality, but for a larger value of ω_0 a new phase exists. This new phase is called vortex phase, see Fig. 2.10. In this figure, we see a dense packet in equilibrium with a sparse gas. Then, if we look at the polarization angle, we see that the polarization is turning around a center, which is land at the center of the packet. These are the reasons why we called it the vortex phase.

If one continues to increase the chirality the vortex phase becomes unstable and a new phase appears, see Fig. 2.11, which is called macrodroplet. In this new phase, there is still a dense packet in equilibrium with a sparse gas, but now the polarization is homogeneous

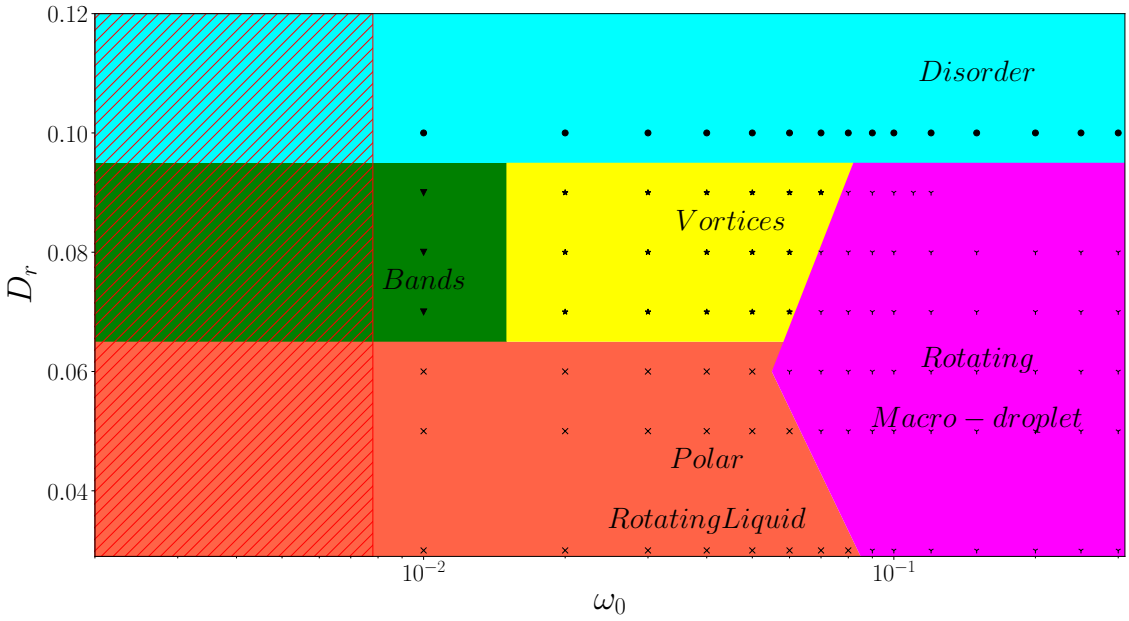

Figure 2.9: Numerical study of the phase diagram for the unimodal distribution. Phase diagram in plane (D_r, ω_0) for a system with parameters $L = 256$, $\rho_0 = 1$ and $\kappa = 1.00$. The figure shows the existence of two new phases which are called vortices and rotating Macro-droplet.

inside the dense packet. Then the polarization is rotating in time, with a frequency near to the intrinsic chirality of the particles. We called it macrodroplet because it is a macrophase separation, this point will be detailed later. Then for very large values of chirality and starting with a homogeneous initial condition, we are not able to see a macrodroplet but a multitude of rotating packets. This is not shown in Fig. 2.9 because it is due to initial conditions, and it will be studied later.

Then we focus ourselves on the liquid. When the chirality becomes non-zero the liquid starts to have rotating movement at a frequency given by the chirality ω_0. When the chirality reaches a given value, the rotating liquid phase becomes unstable, and we get the macrodroplet phase.

Up to now, it seems that the KVM with unimodal chirality distribution exhibit three new phases, but a lot of questions are open because we perform this study at a finite size. In the standard Kuramoto model, the unimodal distribution of chirality is irrelevant, but we already see that, due to self-propulsion, the unimodal distribution is relevant and shows interesting behavior. However, to have some certainty, we need to clarify the finite-size effects.

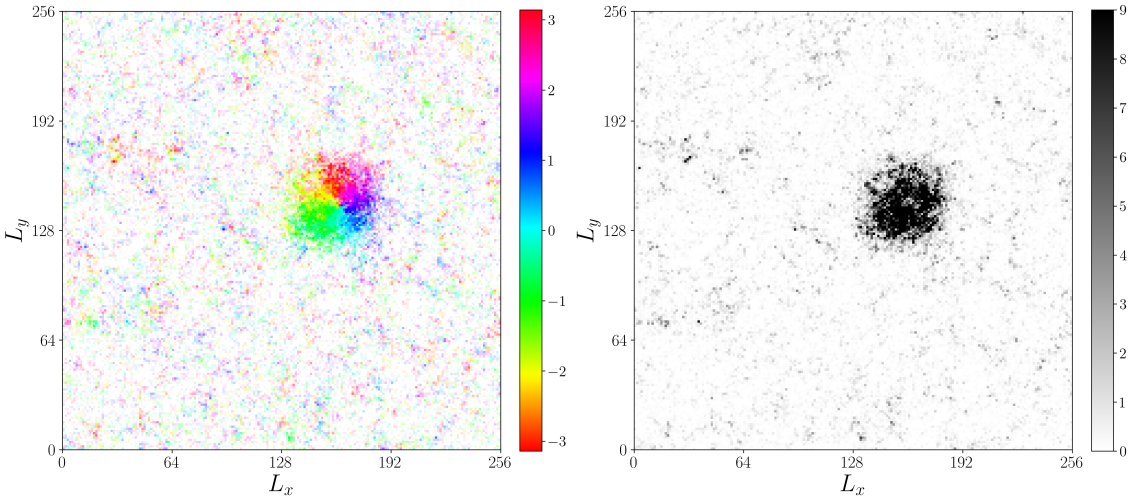

Figure 2.10: A typical snapshot of the vortex phase for a unimodal distribution. It shows a system with parameters $L = 256$, $\rho_0 = 1.0$, $D_r = 0.090$, $v_0 = 1$, $\kappa = 1.0$, and $\omega_0 = 0.060$. The figure shows the vortex pattern in equilibrium with a sparse gas. The left panel shows the local coarse-grained direction of the polarization. The right panel shows the coarse-grained density.

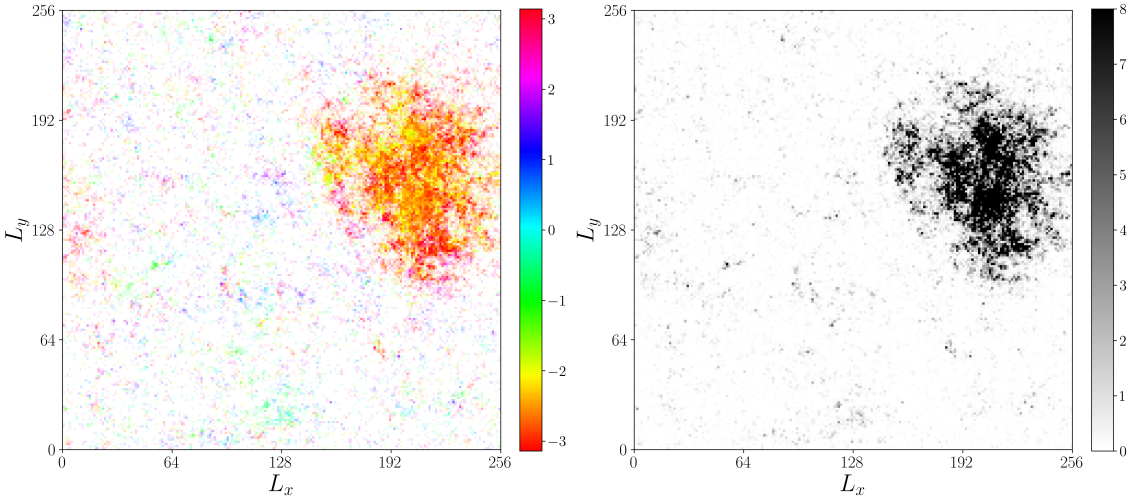

Figure 2.11: A typical snapshot of the macrodroplet phase for a unimodal distribution. It shows a system with parameters $L = 256$, $\rho_0 = 1.0$, $D_r = 0.060$, $v_0 = 1$, $\kappa = 1.0$, and $\omega_0 = 0.100$. The figure shows a rotating macrodroplet in equilibrium with a sparse gas.The left panel shows the local coarse-grained direction of the polarization. The right panel shows the coarse-grained density.

2.3.1.2 Asymptotic behavior

In this section, we will perform an asymptotic study to understand the range of the finite-size effects. The goal is to determine if all the new phases exist in the limit of infinite systems.

Finite size effects at liquid noise level ($D_r = 0.3$)

In this paragraph, we will study the finite-size effects at the liquid noise level, which means we fixed $D_r = 0.03$. To perform this study, we will plot the phase diagram in the plane size L, chirality ω_0, see Fig. 2.12. It will allow us to understand how evolves the boundary between the rotating liquid phase and the macrodroplet phase with the system size. Then it allows us to determine if a phase exists in infinite systems size limit. According to Fig. 2.12 the value where the transition occurs seems to decrease as a power law.

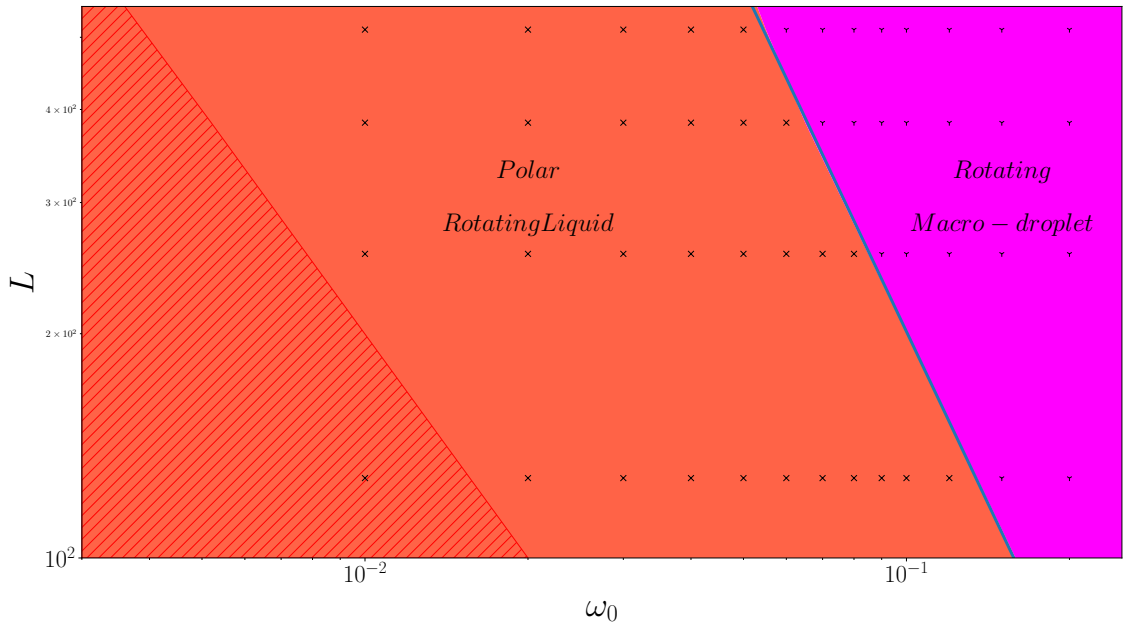

Figure 2.12: Asymptotic study of the polar liquid phase for the unimodal distribution. Phase diagram in plane (L, ω_0) for a system with parameters $D_r = 0.030$, $v_0 = 1$, $\rho_0 = 1$ and $\kappa = 1.00$. Slope $= -1.53$ and Correlation $= 0.999$. The figure shows that the value where the transition between polar liquid and rotating macrodroplet occurs diseappear in the limit of infinite system size.

Fig. 2.12 shows that the liquid phase, in the asymptotic limit, does not exist. Moreover, Fig. 2.12 shows also that value of transition evolve as a power law as $\omega_0^* \sim L^\alpha$ with

$\alpha = -0.65$. This exponent value is similar to the one found with a Gaussian distribution of chirality.

Initial condition effects at liquid noise level ($D_r = 0.3$)

In this paragraph, we will study the effects of the initial condition to be sure that our simulations are not trapped in a metastable state or if the time needed to reach the stable state is much longer than our simulation timescale.
As I mentioned earlier when we start with homogeneous and a fast ω_0 it is impossible to reach the macrodroplet state. To perform this study will take a final state of a given simulation and use it as as initial condition with a different set of parameters. Thus, we will take a macrodroplet state as the initial condition and use it with multiple rotating packet parameters. First we take a system with $L = 256$, $\kappa = 1.00$, $\rho_0 = 1.00$, $D_r = 0.030$ and $\omega_0 = 0.120$ and move it to $L = 256$, $\kappa = 1.00$, $\rho = 1.00$, $D_r = 0.030$ and $\omega_0 = 0.300$. The macrodroplet remains stable. It is possible that the time needed to form a macrodroplet is long, and faster is the ω_0, longer is the time needed to reach the macrodroplet state. This will be confirmed by the later study on the nature of the phase separation.

Finite size effects at band noise level ($D_r = 0.8$)

In this paragraph, we will study the finite-size effects to determine if the bands exist in the limit of infinite system size. To perform this study, we will plot the phase diagram in the plane size L, chirality ω_0. At this noise level, Fig. 2.13 shows that bands will not asymptotically disappear. At a given point there is a coexistence between vortices and bands. Thus, in the limit of infinite system size, there is a coexistence of bands and vortices, see Fig. 2.14
Then for large values of ω_0 the boundary between the macrodroplet phase and the vortex phase seems to be constant with the system size.
So asymptotically we can infer the coexistence of bands and vortices near the transition line and a phase transition with the macrodroplet phase at this noise level.

Initial condition effects at band noise level ($D_r = 0.8$)

In this paragraph, we will study the effects of the initial condition to be sure that our simulations are not trapped in a metastable state. We first take a vortex state $L = 256$, $\kappa = 1.00$, $\rho_0 = 1.00$, $D_r = 0.080$ and $\omega_0 = 0.050$ and move it to $\omega_0 = 0.080$. The result is that the vortex state becomes a macrodroplet. Then we take a macrodroplet $L = 256$, $\kappa = 1.00$, $\rho_0 = 1.00$, $D_r = 0.080$ and $\omega_0 = 0.080$ and move it to $\omega_0 = 0.050$.The result is that the macrodroplet becomes a vortex. So the transition between vortices and macrodroplet is well-defined.
Furthermore, at high ω_0 we start to see the macrodroplet and small packets. To be sure

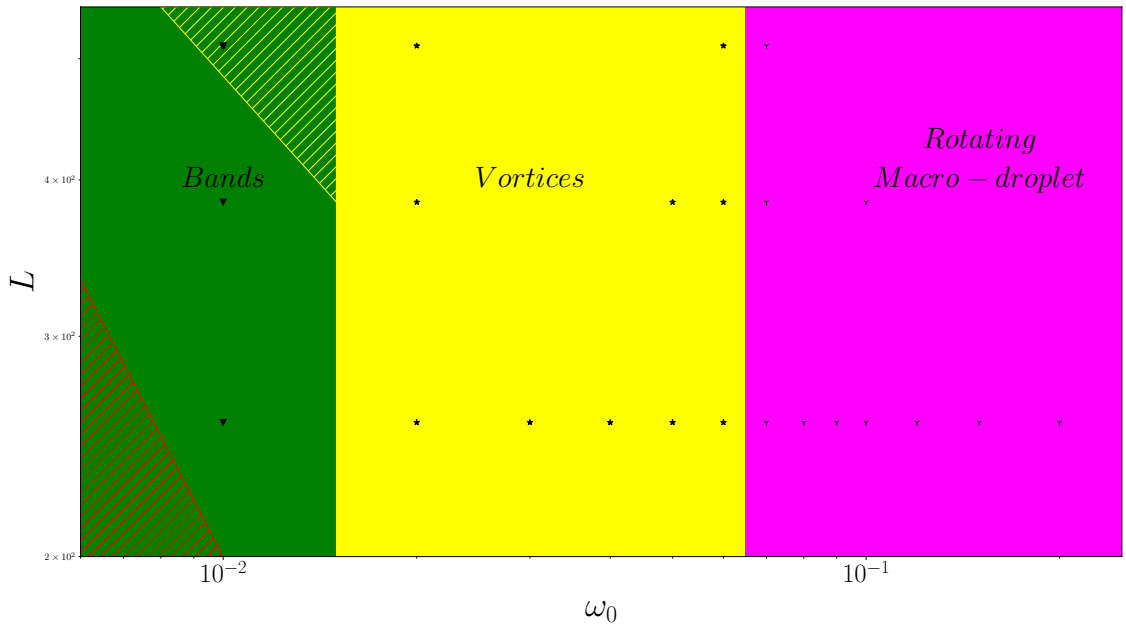

Figure 2.13: Asymptotic study of the bands phase for the unimodal distribution. Phase diagram in plane (L, ω_0) for a system with parameters $D_r = 0.080$, $v_0 = 1$, $\rho_0 = 1$ and $\kappa = 1.00$. The figure shows that the band phase is stable in the limit of infinite system size and there is a coexistence between bands and vortices (hatched area with green and yellow).

that we still are at equilibrium. We take $L = 256$, $\kappa = 1.00$, $\rho_0 = 1.00$, $D_r = 0.080$ and $\omega_0 = 0.120$ and move it to $\omega_0 = 0.250$. The macrodroplet remains. So we can conclude that the rotating packets seen at the first step were due to initial condition effects.

Macrodroplet phase: a macrophase separation

To perform this study, we take an initial state and feed it randomly in density. It means that we will take an initial condition and copy randomly a given number of particles to reach a new density and let the system evolves.
We start with the configuration $L = 512$, $\kappa = 1.00$, $\rho_0 = 1.00$, $D_r = 0.080$ and $\omega_0 = 0.100$ which is a macrodroplet. We feed it until $\rho_0 = 9.7$ where the big macrodroplet fills the entire space. In Fig. 2.15 panel (b), we plot a snapshot of the system when one side starts to interact with the opposite side. It occurs for $\rho_0 = 8.1$. So the more we increase the density, the bigger is the macrodroplet. In Fig. 2.15 panel (a), we show the algorithm used to study the evolution of the surface. First, we start with a coarse-grained grid in density, then we set the value of density to 0 or 1 by using a given threshold ρ_0^* (here $\rho_0^* = 3$). We compute the center of mass of the particle distribution, and we perform a breadth

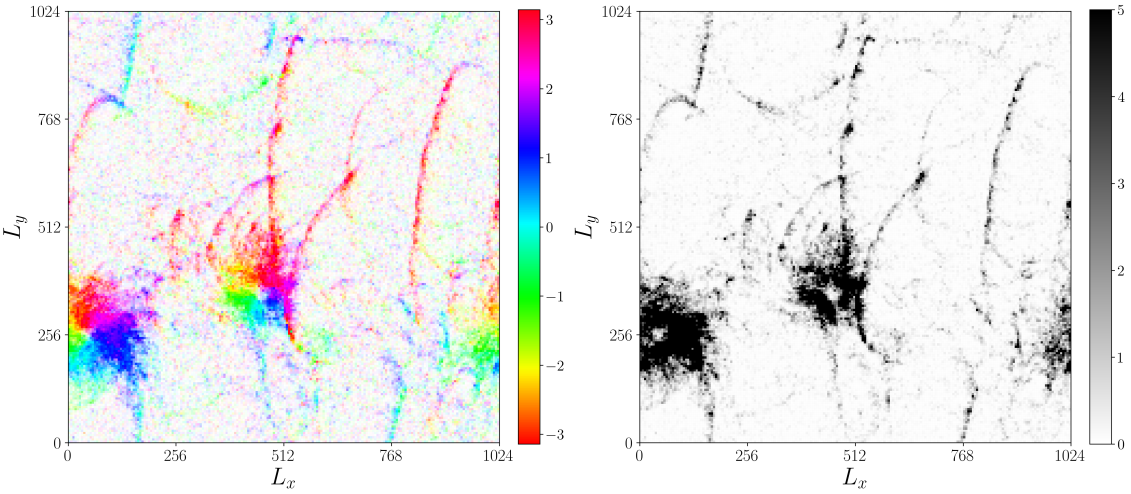

Figure 2.14: A typical snapshot of the coexistence between bands and vortices for the unimodal distribution. It shows a system with parameters $L = 1024$, $\rho_0 = 1.0$, $v_0 = 1$, $\kappa = 1.0$, $D_r = 0.080$, and $\omega_0 = 0.01$.The left panel shows the local coarse-grained direction of the polarization. The right panel shows the coarse-grained density.

first algorithm with the center of mass as a starting point. The blue square allows us to compute the surface of the macrodroplet and average over a period of time. In panel (c), we plot the evolution of the surface as a function of the density ρ_0, one can distinguish two different regimes. The first one is for low density, the surface grows linearly as a function of the density. We perform a linear regression with the seven first points and we have found a good correlation coefficient. Then, around $d = 4.0$, the surface evolution leaves the linear regime. This could be the transition between two different regimes, one where the interface dominates and the second one where the bulk dominates or simply the beginning of finite-size effects.

We also explore the behavior of the macrodroplet when we shift the chirality to understand if it breaks for large values of chirality. We take a macrodroplet phase and do a shift step in chirality and let the system relax to equilibrium. It appears that the macrodroplet remains stable very far in chirality. Thus, we have moved a configuration with $L = 256$, $\rho = 1.$, and $\omega_0 = 0.1$ to $\omega_0 = 0.54$. To explore large values of chirality need some care because we have to adapt the time step Δt.

We also tried handmade initial condition. In particular, we study how evolves a system composed of four subsystems with a macrodroplet. This configuration is not stable and after a long time, the macrodroplets finish to merge.

To summarize, we perform a shift in density, a shift in chirality, and an artificial initial

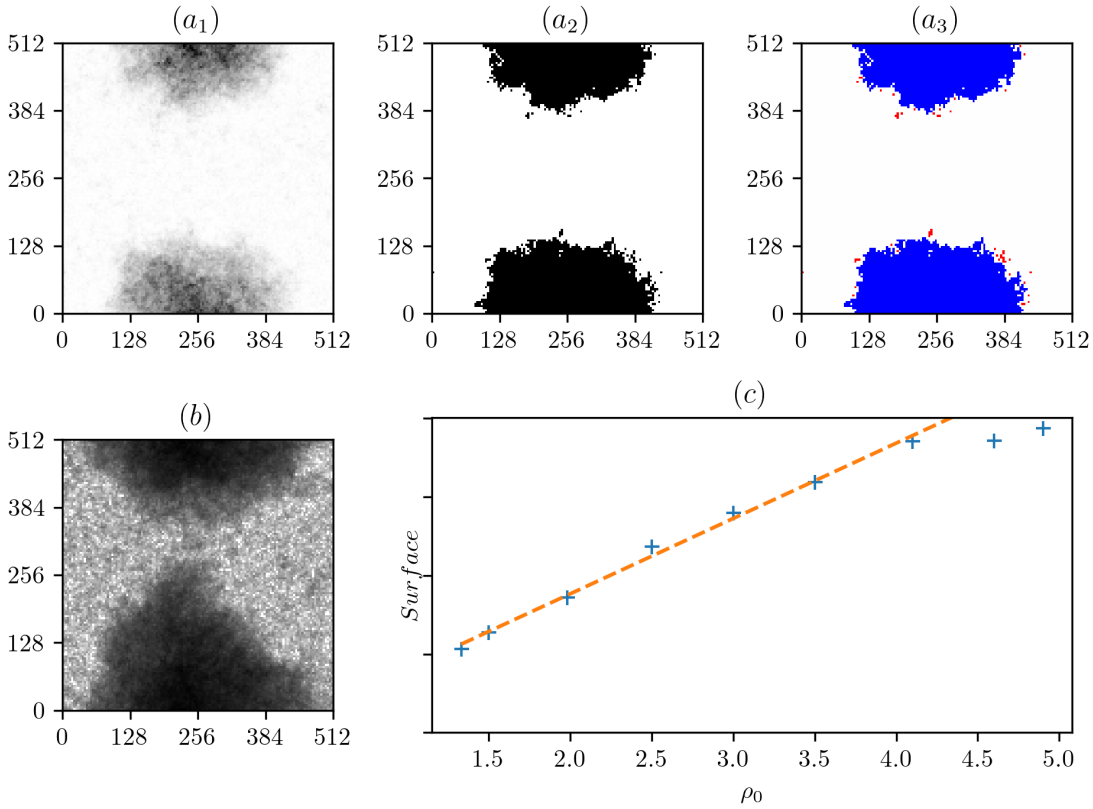

Figure 2.15: Numerical study of the macrodroplet phase as a function of the density. (a): Illustration of the algorithm used to compute the surface of macrodroplet. The microscopic parameters are $\rho_0 = 4.6$, $\kappa = 1$, $D_r = 0.8$, $v_0 = 1$, $\omega_0 = 0.1$ and $L = 512$. (a_1): Coarse-grained density of the initial state on which we apply our algorithm. (a_2): Binarized version of (a_1) with a threshold $\rho_0^* = 3$. So if $\rho(\vec{x}) < \rho_0^*$ we set to 0 otherwise we set to 1.(a_3): We apply a breadth-first algorithm with the center of mass as a starting point. Blue squares are used to compute the surface. (b): Illustration of the finite-size effects with a density $\rho_0 = 8.1$. The boundary of the macrodroplet touchs the other side.(c): Evolution of the surface as a function of the density ρ_0. We fit the seven first points with linear regression with correlation coefficient $r^2 = 0.995$. The figure shows that the macrodroplet phase is a macrophase separation.

condition. First, we conclude that rotating packets is a transient state. Second, we conclude to a macrophase separation thanks to simulations with handmade initial condition and the fact that when the density increases the surface of the macrodroplet increases too.

Vortex phase: a microphase separation

In this paragraph, we will investigate the properties of the vortex phase and show the microphase separation, it means the number of patterns grows when we increase the density. First, we will shift the vortex phase in density and study the behavior. We start with the configuration $L = 256$, $\kappa = 1.00$, $\rho_0 = 1.00$, $D_r = 0.080$ and $\omega_0 = 0.050$ which is a vortex. We feed it, as for the macrodroplet phase, until $\rho_0 = 40$ when the time needed for simulation became too long.
In Fig. 2.16 we investigate the properties of the density distribution, to do this we compute the center of mass of the vortex and then we build the density distribution $\rho(r)$ where r is the distance to the center of mass. In panel (a), we see that the maximum density ρ_{max} increases when we increase the total density ρ_0. In panel (b), we plot the normalized density for various global densities and see that the distribution obeys the same master curve. Moreover, the radius of the vortex is constant regard to our simulations. So the density diverges inside the vortex when we increase ρ_0; because it is not possible physically, it means that at a larger density the vortex should eventually split, and it results in microphase separation. In panel (c), we plot the difference between the density distribution and a value around the gas level. If we omit the curve for $\rho_0 = 30, 40$ we see that the density of the sparse gas is constant. It means that cases $\rho_0 = 30, 40$ are not in a stationary state and need a longer simulation time.

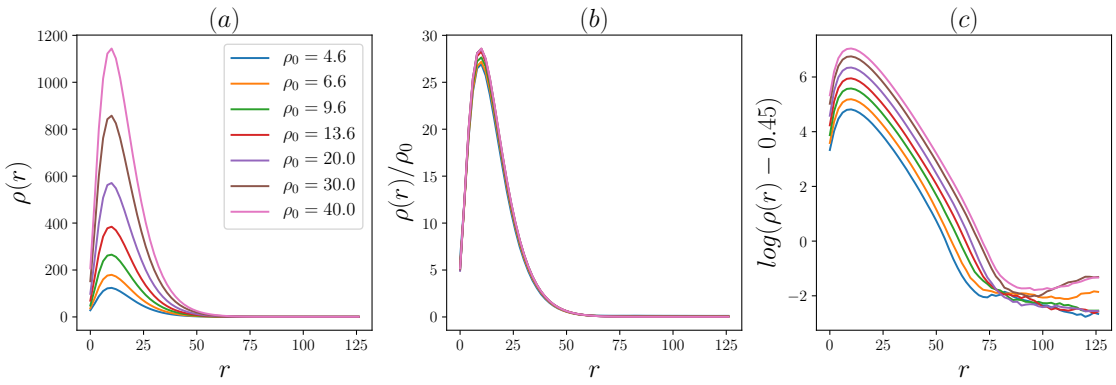

Figure 2.16: Numerical study of single vortex properties for the unimodal distribution. Center of mass centered data with parameters $L = 256$, $\omega_0 = 0.050$, $v_0 = 1$, $D_r = 0.080$ and $\kappa = 1.00$. Data are averaged over the angular coordinates. (a) The density distribution $\rho(r)$ as a function of the radius. (b) The density distribution normalized with the global density $\rho(r)/\rho_0$ as a function of the radius (c) The density distribution minus a value around the sparse gas density $\rho(r) - 0.45$ as a function of the radius. The figure shows that the density inside a vortex obeys a master curve and the gas density is constant.

In Fig. 2.17 panel (a), we want to confirm that the density diverges inside the vortex. Thus, we plot how evolves the maximum density inside the vortex as a function of the global density. We can fit with a linear curve with a very good agreement, so the maximum density ρ_{max} grows linearly with the global density ρ_0. Moreover, we have done the hypothesis that the sparse gas density is constant. We are assuming a Gaussian distribution for the vortex profile, thus it is possible to compute how evolves the half-width. So we fit the data with a function $y = a + \sqrt{b \log((x-d)/c)}$ and we get a very good agreement. So we can conclude that the level of the sparse gas is fixed and all the new particles are going inside the vortex. In panel (c), we show how evolves the momentum distribution and it seems that the evolution of the momentum is driven by the density.

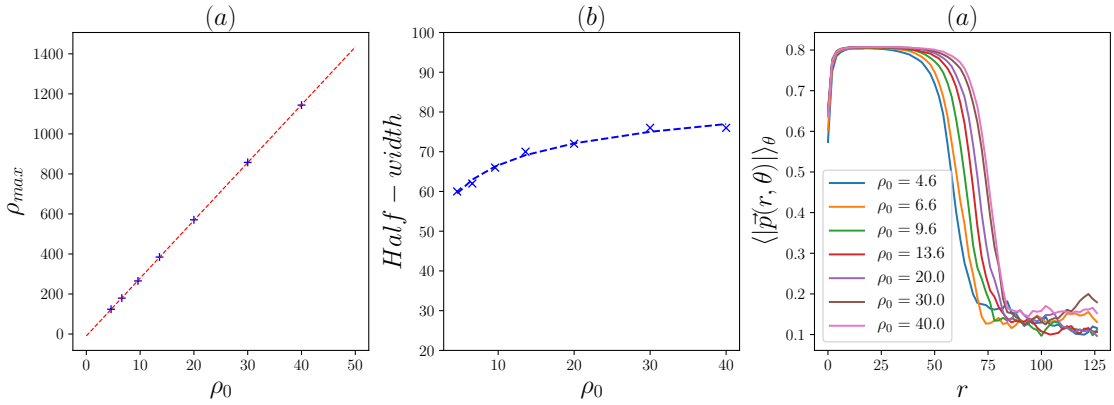

Figure 2.17: Numerical study of the vortex pattern for the unimodal distribution. Center of mass centered data with parameters $L = 256$, $\omega_0 = 0.050$, $v_0 = 1$, $D_r = 0.080$ and $\kappa = 1.00$. The data are averaged over the angular coordinates. (a)Maximum of the density distribution ρ_{max} as a function of the global density (b) Half-width of density distribution and a fit with the half-width of a Gaussian distribution (c) distribution of the momentum as a function of the radial coordinate. The figure shows that the density maximum grows linearly as a function of the global density. Then it confirms that the gas density is constant and the vortex is rotational.

In Fig. 2.17 panel (c), we plot how evolves the modulus of the local polarization average over the angle coordinate field inside the vortex. Inside a vortex, the polarization field is constant as a function of r. If we plot the direction of the local polarization as a function of the angular coordinate θ for different radius, we see that the direction of the local polarization grows linearly when we are inside the vortex, and outside the vortex, it is disordered. So the particles inside the vortex are rotating with a constant angular speed. If we plot the modulus of the local polarization field as a function of the angular coordinates for various radius. The modulus is constant along one rotation, so we can conclude that the vorticity vector is non-zero inside the vortex.

Also, to be sure that the behavior at high density does not survive when the density goes to infinity, we try to add small repulsion to see if the vortex resists a finite value of repulsion. To simulate chiral active particles with repulsion, we perform an Euler integration of the continuous equations

$$\frac{\mathrm{d}\vec{r}_i}{\mathrm{d}t} = v_0\vec{e}(\theta_i) + R_0 \sum_{j\in\mathcal{D}_i} (1-d_{ij})\vec{r}_{ij} \tag{2.5a}$$

$$\frac{\mathrm{d}\theta_i}{\mathrm{d}t} = \omega_i + \frac{\kappa}{\mathcal{D}_i} \sum_{j\in\mathcal{D}_i} \sin(\theta_j - \theta_i) + \sqrt{2D_r}\xi_i \tag{2.5b}$$

where R_0 is the repulsion strength, d_{ij} the distance between particle i and j, and $\vec{r}_{ij}$ the unit vector pointing from particle j to particle i.
First, for each density it is possible to find a finite value of repulsion where one vortex is stable. Then if we perform a shift in density for this given value of repulsion, the vortex will always burst at a given value of density according to the value of repulsion. Then we also study handmade initial conditions. We start with four or eight vortices, in the beginning, the number of vortices will decrease and the density of the remaining vortices will increase but when a vortex becomes to dense it burst. Then from the gas new vortices will be formed. This is a dynamic existence in that case.

To summarize, according to the shift in density with and without repulsion and handmade initial condition, we conclude to a microphase separation. Moreover, this point can also be inferred from the fact that bands and vortices coexist at large system sizes. If the vortex phase is macrophase separated it is incompatible with the coexistence of the two patterns.

2.3.2 Fokker-Planck approach

In this section, we will build hydrodynamic theory based on the approximation of a dense system. Thus, we will use the framework developed by Dean [47] and Farrell et al. [48], which consist of a coarse-graining of a microscopic model as presented in section 1.2.3.3.

Fokker-Planck equation

So we consider the particle distribution function $f(\vec{r},\theta,t)$ which is the probability to find a particle at position $\vec{r}$ with an orientation θ at time t. The derivation of the Fokker-Planck equation gives

$$\partial_t f(\vec{r},\theta,t) = -v_0\,\vec{e}(\theta).\vec{\nabla} f - \omega_0\partial_\theta f - \kappa\partial_\theta \int \mathrm{d}\theta' f(\vec{r},\theta')\sin(\theta'-\theta) f(\vec{r},\theta) + D_r\partial_\theta^2 f - \partial_\theta\sqrt{2f}\xi \tag{2.6}$$

where $\vec{e}(\theta) = (\cos\theta, \sin\theta)$, and ξ is a Gaussian white noise. Here the only difference with equation Eq. (1.28) is the chirality term $\omega_0\partial_\theta f$.

Then we perform the same rescaling, by setting

$$t \to t/D_r \quad , \quad \vec{r} \to v_0\vec{r}/D_r \quad , \quad f \to \rho_0 f \quad , \quad \xi \to \sqrt{D_r\rho_0}\xi \tag{2.7}$$

By taking the Fourier transform along the angular coordinate of Eq. (2.6) and neglecting the noise term it leads to

$$\dot{f}_k(\mathbf{r},t) = -\frac{1}{2}[\nabla f_{k-1} + \nabla^* f_{k+1}] + (ik\Omega_0 - k^2)f_k + \frac{igk}{2\pi}\sum_{m=-\infty}^{\infty} f_{k-m}F_{-m}f_m \tag{2.8}$$

with $F_{-m} = i\pi(\delta_{m,-1} - \delta_{m,1})$, $\Omega_0 = \frac{\omega_0}{D_r}$, $g = \frac{\rho_0\kappa}{\pi R^2 D_r}$. It means the equation is controlled by two parameters Ω_0 and g.

Hydrodynamic equations

Now if one applies the Ginzburg-Landau truncation scheme explained in section 1.2.3.2 to equation Eq. (2.8), under the complex notation, it leads to

$$\begin{aligned}
\partial_t f_0 &= -\Re\left(\nabla^* f_1\right) \\
\partial_t f_1 &= [\alpha_{\text{FP}}\left(f_0 - \rho_{c_{\text{FP}}}\right) + i\Omega_0]f_1 - \xi_{\text{FP}}|f_1|^2 f_1 + \nu_{\text{FP}}\Delta f_1 - \gamma_{\text{FP}} f_1\nabla^* f_1 - \beta_{\text{FP}} f_1^*\nabla f_1 - \frac{1}{2}\nabla f_0
\end{aligned} \tag{2.9}$$

with

$$\begin{aligned}
\alpha_{\text{FP}} &= \frac{g}{2} & \rho_{c_{\text{FP}}} &= \frac{2}{g} \\
\nu_{\text{FP}} &= \frac{(2+i\Omega_0)}{4b} & \beta_{\text{FP}} &= -\frac{g\,(2+i\Omega_0)}{4b} \\
\xi_{\text{FP}} &= \frac{g^2\,(2+i\Omega_0)}{2b} & \gamma_{\text{FP}} &= \frac{g\,(2+i\Omega_0)}{b}
\end{aligned} \tag{2.10}$$

where $b = 2(4+\Omega_0^2)$.
From the previous definition Eq. (2.10) we see that all the coefficients are complex. Now the linear stability of the homogeneous disordered phase depends on complex coefficients contrary to section 1.2.3.3, but the important point is that the stability is governed by the real part which is unchanged in that case. So we keep the same scaling ansatz from section 1.2.3.3. Moreover, Eq (2.9) has the same structure as the Vicsek hydrodynamic equations but with complex coefficients.

Homogeneous stationary solutions

The next step of the study is to find the homogeneous stationary solutions of Eq. (2.9). So the set of equations reduce to

$$\begin{aligned}
\partial_t \rho &= 0 \\
\partial_t f_1 &= [\alpha_{\text{FP}}\left(\rho - \rho_{c_{\text{FP}}}\right) + i\Omega_0]f_1 - \xi_{\text{FP}}|f_1|^2 f_1
\end{aligned}$$

It leads to $\rho = constant = 1$. Then, for f_1 we are looking for a stationary solution so $\partial_t |f_1|^2 = 0$ so $f_1 = F_{1_{\text{FP}}} e^{i\Omega_{\text{FP}} t}$. A trivial solution is $f_1 = 0$. We check if a non-trivial solution exists by solving the system of equations for the real part on one side and for the imaginary part on the other side. The derivation gives

$$\begin{aligned} F_{1_{\text{FP}}} &= \left(\alpha_{\text{FP}}(\rho_0 - \rho_{c_{\text{FP}}})/\Re(\xi_{\text{FP}})\right)^{\frac{1}{2}} \\ \Omega_{\text{FP}} &= \Omega_0 - \alpha_{\text{FP}}(\rho_0 - \rho_{c_{\text{FP}}})\Im(\xi_{\text{FP}})/\Re(\xi_{\text{FP}}) \end{aligned} \tag{2.11}$$

The solution, given by Eq. (2.11), is a homogeneous ordered solution with a polarization rotating in time. This solution corresponds to the rotating liquid defined in the section about microscopic simulation. Moreover, we have an analytical expression of the rotating pulsation which is given by Ω_{FP}.

Linear stability of the Gas solution

We call Gas solution the homogeneous isotropic state given by $\rho = 1$ and $f_1 = 0$. We will try to understand the microscopic phase diagram by studying the stability of this solution. To perform the stability analysis, we perturb the initial state by a little perturbation of the form $\rho = 1 + \delta\rho$ and $f_1 = \delta f_1$. It leads to the equations

$$\begin{aligned} \partial_t \delta\rho &= -\frac{1}{2}\left(\nabla \delta f_1^* + \nabla^* \delta f_1\right) \\ \partial_t \delta f_1 &= [\alpha_{\text{FP}}\left(1 - \rho_{c_{\text{FP}}}\right) + i\Omega_0]\delta f_1 + \nu_{\text{FP}} \Delta \delta f_1 - \frac{1}{2}\nabla \delta\rho \end{aligned}$$

Then if we expand $\delta\rho$ and $\delta f_{1,x/y}$ in terms of Fourier modes along the spatial coordinates

$$\begin{aligned} \delta\rho &= \delta\rho_{\mathbf{q}}\, e^{i\,\mathbf{q}.\mathbf{r}} \\ \delta f_{1x} &= \delta f_{1x,\mathbf{q}}\, e^{i\,\mathbf{q}.\mathbf{r}} \\ \delta f_{1y} &= \delta f_{1y,\mathbf{q}}\, e^{i\,\mathbf{q}.\mathbf{r}} \end{aligned}$$

then

$$\partial_t \begin{pmatrix} \delta\rho_{\mathbf{q}} \\ \delta f_{1x,\mathbf{q}} \\ \delta f_{1y,\mathbf{q}} \end{pmatrix} = \begin{pmatrix} 0 & -iq_x & -iq_y \\ -\frac{i}{2}q_x & \alpha_{\text{FP}}\left(1 - \rho_{c_{\text{FP}}}\right) - \Re(\nu_{\text{FP}})q^2 & -\Omega_0 + \Im(\nu_{\text{FP}})q^2 \\ -\frac{i}{2}q_y & \Omega_0 - \Im(\nu_{\text{FP}})q^2 & \alpha_{\text{FP}}\left(1 - \rho_{c_{\text{FP}}}\right) - \Re(\nu_{\text{FP}})q^2 \end{pmatrix} \begin{pmatrix} \delta\rho_{\mathbf{q}} \\ \delta f_{1x,\mathbf{q}} \\ \delta f_{1y,\mathbf{q}} \end{pmatrix}$$

So we look for the eigenvalues S of the previous matrix

$$\begin{vmatrix} -S & -iq_x & -iq_y \\ -\frac{i}{2}q_x & \alpha_{\text{FP}}\left(1 - \rho_{c_{\text{FP}}}\right) - \Re(\nu_{\text{FP}})q^2 - S & -\Omega_0 + \Im(\nu_{\text{FP}})q^2 \\ -\frac{i}{2}q_y & \Omega_0 - \Im(\nu_{\text{FP}})q^2 & \alpha_{\text{FP}}\left(1 - \rho_{c_{\text{FP}}}\right) - \Re(\nu_{\text{FP}})q^2 - S \end{vmatrix} = 0$$

It leads to the characteristic polynomial

$$\begin{aligned} &-\alpha_{_{\mathrm{FP}}} q^2 \left(1-\rho_{c_{_{\mathrm{FP}}}}\right) + \Re(\nu_{_{\mathrm{FP}}}) q^4 \\ &\left(2\left(\alpha_{_{\mathrm{FP}}}\left(1-\rho_{c_{_{\mathrm{FP}}}}\right) - \Re(\nu_{_{\mathrm{FP}}}) q^2\right)^2 + 2\left(\Omega_0 - \Im(\nu_{_{\mathrm{FP}}}) q^2\right)^2 + q^2\right) S \\ &+ 4\left(-\alpha_{_{\mathrm{FP}}}\left(1-\rho_{c_{_{\mathrm{FP}}}}\right) + \Re(\nu_{_{\mathrm{FP}}}) q^2\right) S^2 + 2S^3 = 0 \end{aligned} \tag{2.12}$$

Now if we look at the coefficients of the polynomial expression, we see that for $1 < \rho_{c_{_{\mathrm{FP}}}}$ all the coefficients are positives. So for $\rho < \rho_{c_{_{\mathrm{FP}}}}$ the homogeneous disordered phase is linearly stable against wave-like perturbations. For $1 > \rho_{c_{_{\mathrm{FP}}}}$ the real part of S becomes positive, and the homogeneous ordered solution becomes unstable against perturbations.

Linear stability of the rotating liquid solution

We call liquid solution the homogeneous rotating ordered state given by $\rho = 1$ and $f_1 = F_{1_{_{\mathrm{FP}}}} e^{i\Omega_{_{\mathrm{FP}}} t}$. This solution is a periodic solution, to properly take into account this property we should perform a Floquet analysis. Here we have done a simpler computation by doing the standard stability analysis at a given time $t = 0$. This approximation is correct if the typical time attached to the instability is much smaller than the time needed to do one rotation. In other words, if the growth rate is much bigger than $\Omega_{_{\mathrm{FP}}}$. To perform the standard stability analysis, we perturb the initial state by a little perturbation of the form $\rho = 1 + \delta\rho$ and $f_1 = F_{1_{_{\mathrm{FP}}}} e^{i\Omega_{_{\mathrm{FP}}} t} + \delta f_1$ and follow the same procedure as the previous section. We will fix the direction of the polarization by setting $t = 0$, so the polarization is along

the x-axis. After expanding in terms of Fourier modes, we get

$$
\begin{aligned}
\partial_t \delta\rho &= -\left(iq_x f_{1,x} + iq_y f_{1,y}\right) \\
\partial_t \delta f_{1,x} &= \left\{ -\frac{1}{2} iq_x + \alpha_{_{\mathrm{FP}}} F_{1_{\mathrm{FP}}} \right\} \delta\rho \\
&\quad + \Big\{ -2\alpha_{_{\mathrm{FP}}} \left(\rho_0 - \rho_{c_{\mathrm{FP}}}\right) - \Re(\nu_{_{\mathrm{FP}}}) q^2 \\
&\qquad + iF_{1_{\mathrm{FP}}} \left(-\Re(\beta_{_{\mathrm{FP}}}) q_x + \Im(\beta_{_{\mathrm{FP}}}) q_y - \Re(\gamma_{_{\mathrm{FP}}}) q_x - \Im(\gamma_{_{\mathrm{FP}}}) q_y\right) \Big\} \delta f_{1,x} \\
&\quad + \Big\{ -\Omega_0 + \Im(\nu_{_{\mathrm{FP}}}) q^2 + \Im(\xi_{_{\mathrm{FP}}}) F_{1_{\mathrm{FP}}}^2 \\
&\qquad + iF_{1_{\mathrm{FP}}} \left(-\Re(\gamma_{_{\mathrm{FP}}}) q_y + \Im(\gamma_{_{\mathrm{FP}}}) q_x + \Re(\beta_{_{\mathrm{FP}}}) q_y + \Im(\beta_{_{\mathrm{FP}}}) q_x\right) \Big\} \delta f_{1,y} \\
\partial_t \delta f_{1,y} &= -\frac{1}{2} iq_y \delta\rho \\
&\quad + \Big\{ \Omega_0 - 3\Im(\xi_{_{\mathrm{FP}}}) F_{1_{\mathrm{FP}}}^2 \delta f_{1,x} \\
&\qquad - \Im(\nu_{_{\mathrm{FP}}}) q^2 + iF_{1_{\mathrm{FP}}} \left(-\Re(\beta_{_{\mathrm{FP}}}) q_y - \Im(\beta_{_{\mathrm{FP}}}) q_x + \Re(\gamma_{_{\mathrm{FP}}}) q_y - \Im(\gamma_{_{\mathrm{FP}}}) q_x\right) \Big\} \delta f_{1,x} \\
&\quad + \Big\{ -\Re(\nu_{_{\mathrm{FP}}}) q^2 + iF_{1_{\mathrm{FP}}} \left(-\Re(\beta_{_{\mathrm{FP}}}) q_x + \Im(\beta_{_{\mathrm{FP}}}) q_y - \Re(\gamma_{_{\mathrm{FP}}}) q_x - \Im(\gamma_{_{\mathrm{FP}}}) q_y\right) \Big\} \delta f_{1,y}
\end{aligned}
\tag{2.13}
$$

We study the stability of the liquid solution by performing numerical eigenvalues analysis. So for each value of parameters and for each value of (q_x, q_y) we compute the eigenvalues of the matrix attached to Eq. (2.13). Then we keep the highest eigenvalue. If this eigenvalue is positive, the solution is unstable otherwise the solution is stable. Then we scan the Fourier space to find the highest eigenvalue of the whole Fourier space. We perform the linear stability analysis around the rotating liquid solution in Fig. 2.18.

In Fig. 2.18 we plot the highest eigenvalue on the panel (a), the modulus of the eigenvector attached to this eigenvalue in the panel (b), and the direction of the eigenvector in the right panel. One can see that the liquid solution is unstable where it is defined, but this is not a surprise. The grey part of the figure is where the liquid solution is not defined. The grey part is where the gas solution is stable. In the pure Vicsek case, see section 1.2.3.3 the liquid solution of the hydrodynamic equation based on the Fokker Planck equation is unstable everywhere.

We also plot the Fourier plane to understand the evolution of the most unstable mode in Fig 2.19. The three different points are corresponding to the white cross in Fig 2.18. We denote by q^* the most unstable vector of the Fourier space. From the Fourier space analysis, we see that at low values of Ω_0 and high values of D_r the solution is along the

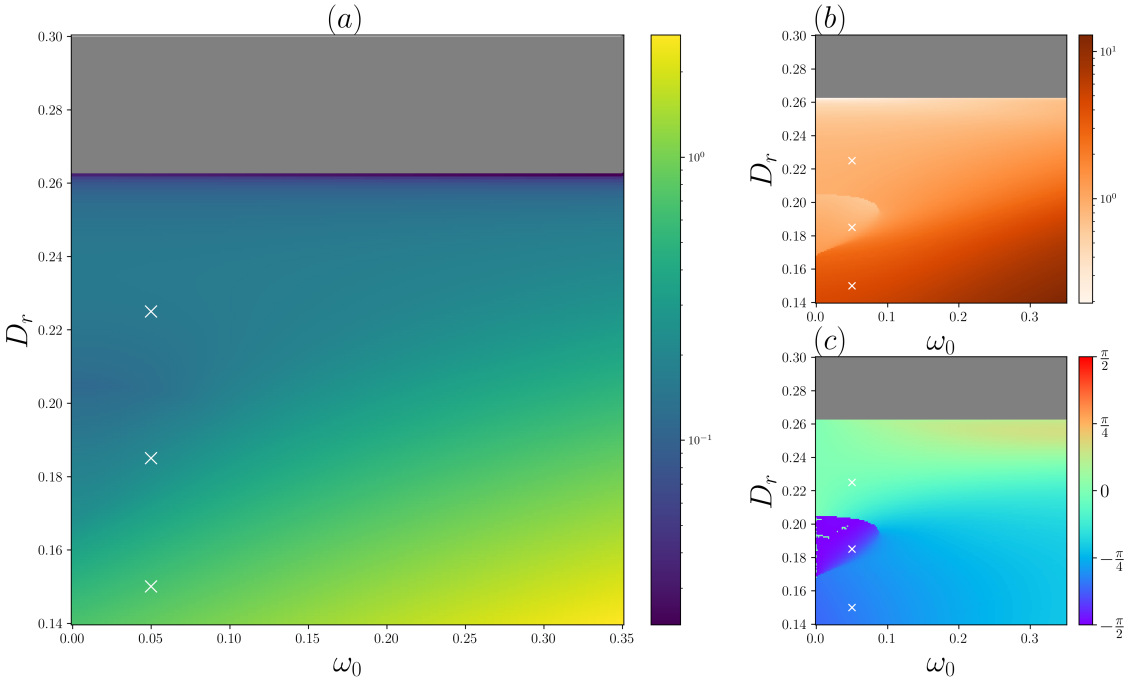

Figure 2.18: Linear stability study of the rotating liquid for the Fokker-Planck approach and unimodal distribution of chirality. Linear stability study in the plane (D_r, ω_0). The 3 white crosses are linked to Fig. 2.19. The grey part is where the liquid solution is not defined and it is the gas phase. (a): Highest eigenvalue of the Fourier space. (b): Modulus of the eigenvector attached to the highest eigenvalue of the panel (a). (c): Direction of the eigenvector attached to the highest eigenvalue of the panel (a). The figure shows that the rotating liquid is unstable everywhere.

polarization direction. So it is continuous with the Vicsek model. Now if we increase the value of Ω_0, the most unstable mode will develop a non-longitudinal component. The modulus of the most unstable mode grows very fast for low noise values and high chirality values, so if someone takes the limit $q \to 0$ in the linear stability analysis, it is possible to conclude to the stability of the rotating liquid for low value of noise.

The linear stability of the standard Vicsek model with a Fokker-Planck approach gives a liquid solution unstable everywhere. Thus, this approach does not reproduce the microscopic results at the microscopic level.
Here we have found that the rotating liquid solution is also unstable everywhere. However, to justify the fact that we have not done a Floquet analysis we need to compare the value of the growth rate with ω_0. In Fig 2.18, one can see that the growth rate and the chirality have the same order of magnitude. In other words, it is wrong to do a standard linear

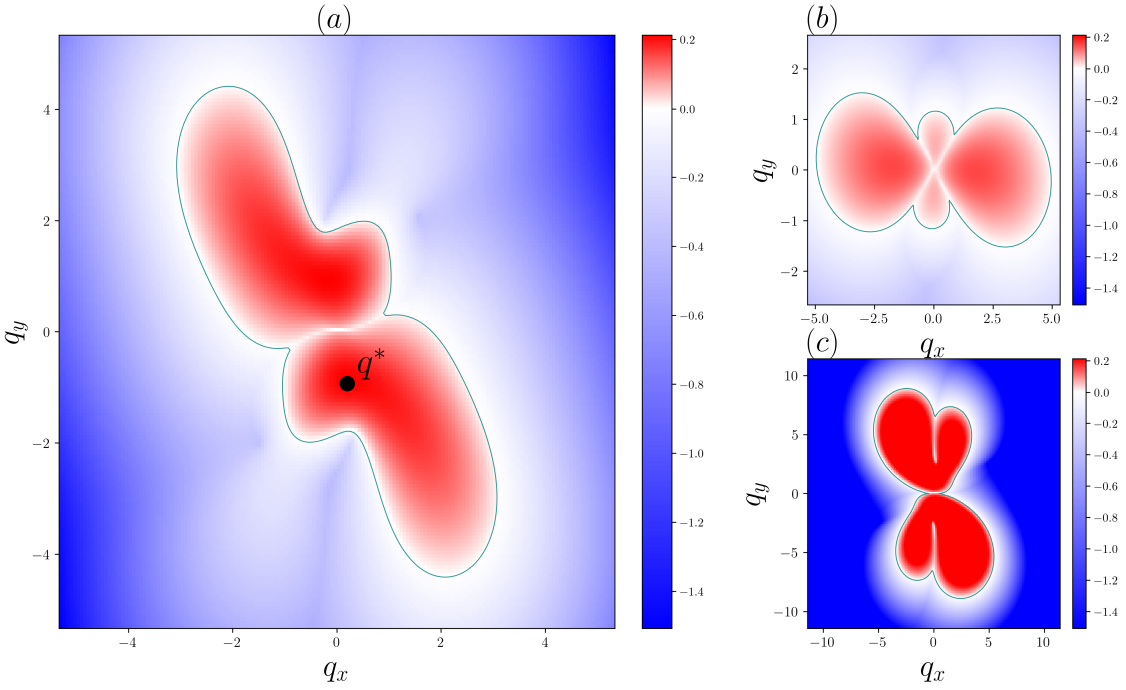

Figure 2.19: Linear stability study of the rotating liquid for the Fokker-Planck approach and unimodal distribution of chirality. Representation of the Fourier space for given set of parameters ($\rho_0 = 1.650$, $\kappa = 1.0$, $\omega_0 = 0.05$). Each panel is a white cross in Fig 2.18. (a): $D_r = 0.185$ and q^* is the highest eigenvalue in the Fourier space. The green line is the contour plot at zero value. (b): $D_r = 0.225$. (c): $D_r = 0.15$. The figure shows how evolves the most unstable mode in the Fourier space.

stability at a fix time but we should perform a Floquet analysis. Moreover, the linear stability analysis for the pure Vicsek case gives bad results with Foker-Planck approach. So it is impossible to reach a conclusion.

To summarize this section, we follow the approximation of dense systems and derive hydrodynamic equations. These equations have the same structure as the Toner-Tu equations plus a chirality term. These equations admit two homogeneous solutions, one corresponding to the disordered solution and the other one corresponding to the rotating liquid. However, the linear stability of these solutions does not permit to understand the microscopic phase diagram of the KVM with unimodal distribution because the rotating liquid is unstable like the liquid of the standard Vicsek model. In the next section, we will build a hydrodynamic description based on the approximation of dilute systems.

2.3.3 Boltzmann approach

In this section, we will adopt the BGL description, as presented in the section 1.2.3.2, because it provides a good description of the microscopic phase diagram of the Vicsek model. Thus, we will try to extend this description to the KVM.

2.3.3.1 Boltzmann approach

The first step is to write the corresponding Boltzmann equation. So we will perform the coarse-graining of the model defined in section 1.2.3.2, but now we have to take into account the chirality of the particles.
We consider $f(r,\theta,t)$ the particle distribution function. The evolution of the function in the KVM case is :

$$\frac{\partial f}{\partial t}(r,\theta,t) = \ 'free\ evolution' \ + \ 'self-diffusion\ part' \ + \ 'collision\ part'$$

The contribution of the free evolution of f is now given by $I_{fe}[f]$:

$$I_{fe}[f] = -v_0\vec{e}(\theta).\vec{\nabla}f - \omega_0\frac{\partial f}{\partial\theta}$$

The other integral terms are the same as section 1.2.3.2. It means we keep the same collision kernel. This hypothesis should remain valid for small value of chirality but for large value of chirality we should change the kernel expression and take into account the chirality.

Finally, it leads to the following Boltzmann equation

$$\begin{aligned}\frac{\partial f}{\partial t}(r,\theta,t) = -v_0\vec{e}(\theta).\vec{\nabla}f - \omega_0\partial_\theta f + \lambda((P_\sigma * f) - 1) - \int \mathrm{d}\theta' K(\theta-\theta')f(r,\theta,t)f(r,\theta',t) \\ + \iint \mathrm{d}\theta_1\,\mathrm{d}\theta_2 K(\theta_1-\theta_2)f(r,\theta_1,t)f(r,\theta_2,t)\int \mathrm{d}\xi P_\sigma(\xi)\delta_{2\pi}(\Psi(\theta_1,\theta_2)+\xi-\theta) \quad (2.14)\end{aligned}$$

with ω_0 the intrinsic chirality, P_σ a Gaussian noise distribution with variance σ, the collision kernel $K(\theta-\theta') = 4d_0v_0\sin\left(\frac{\theta-\theta'}{2}\right)$, and $\Psi(\theta_1,\theta_2) = \frac{\theta_1+\theta_2}{2}$.
Eq. (2.14) is similar to the Boltzmann equation for the Vicsek model plus a chirality term. Then we take the Fourier transform along the angular coordinate, and rescale quantities as follows

$$t \to t/\lambda, \qquad \vec{r} \to v_0\vec{r}/\lambda, \qquad \omega_0 \to \omega_0\lambda, \qquad K \to 2d_0v_0K, \qquad f \to \rho_0 f, \qquad (2.15)$$

with ρ_0 the global density and $\tilde{\rho_0} = 2d_0v_0\rho_0/\lambda$. Then it leads to

$$\partial_t f_k = -\frac{1}{2}(\nabla f_{k-1} + \nabla^* f_{k+1}) + ik\omega_0 f_k + (P_k - 1)f_k + \sum_q f_q f_{k-q}J_{k,q} \qquad (2.16)$$

with $J_{k,q} = \tilde{\rho}_0(P_k I_{k,q} - I_{0,q})$ and $I_{k,q}$ given by

$$I_{k,q} = \begin{cases} \frac{4}{\pi}\frac{1-(k-2q)(-1)^q sin(\frac{k\pi}{2})}{1-(k-2q)^2} & \text{if } |k-2q| \neq 1 \\ \frac{2}{\pi} & \text{otherwise.} \end{cases}$$

2.3.3.2 Hydrodynamic description

Now we will follow the Ginzburg-Landau truncation scheme. The first step is to determine the scaling ansatz. The procedure is to study the linear stability around the disordered solution $f_0 = 1$ and $f_k = 0$. This linear stability is governed by the same real part as section 1.2.3.2. The chirality adds a complex part to the coefficient, but it does not affect the linear stability. So the scaling ansatz of section 1.2.3.2 is unchanged.

$$f_1 \sim \varepsilon\,, \quad |f_0 - 1| \sim \varepsilon\,, \quad f_{k>0} \sim \epsilon^k\,, \quad \partial_t \sim \nabla \sim \varepsilon\,. \tag{2.17}$$

Then we expand up to order three to have a saturation term and truncate to close the system of equations. It leads to

$$\begin{aligned} \partial_t \rho &= -\frac{1}{2}\left(\nabla f_1^* + \nabla^* f_1\right) \\ \partial_t f_1 &= [\alpha_{\text{BGL}}\left(\rho - \rho_{c_{\text{BGL}}}\right) + i\omega_0] f_1 - \xi_{\text{BGL}}|f_1|^2 f_1 + \nu_{\text{BGL}}\Delta f_1 - \gamma_{\text{BGL}} f_1 \nabla^* f_1 - \beta_{\text{BGL}} f_1^* \nabla f_1 - \frac{1}{2}\nabla\rho \end{aligned} \tag{2.18}$$

with

$$\begin{aligned} \alpha_{\text{BGL}} &= J_{1,0} + J_{1,1} & \rho_{c_{\text{BGL}}} &= \frac{\lambda(1-\hat{P}_1)}{J_{1,0}+J_{1,1}} \\ \nu_{\text{BGL}} &= -\frac{1}{4}\frac{1}{\lambda(\hat{P}_2 - 1) + 2i\omega_0 + (J_{2,0}+J_{2,2})\rho} & \gamma_{\text{BGL}} &= 4\nu J_{2,1} \\ \xi_{\text{BGL}} &= -4(J_{1,-1}+J_{1,2})\nu J_{2,1} & \beta_{\text{BGL}} &= 2(J_{1,-1}+J_{1,2})\nu \end{aligned} \tag{2.19}$$

This equation is similar to Eq. (2.9). So we will follow the same development where indices X_{FP} are replaced by X_{BGL}. The structure is the same as for the Vicsek model but now all the coefficients are complex.

2.3.3.3 Homogeneous stationary equations

In the same way as Eq. (2.11) we find two solutions. One corresponding to gas phase $\rho = 1$ and $f_1 = 0$ and the second one corresponding to rotating liquid phase.

$$\begin{aligned} F_{1_{\text{BGL}}} &= \left(\alpha_{\text{BGL}}(\rho_0 - \rho_{c_{\text{BGL}}})/\Re(\xi_{\text{BGL}})\right)^{\frac{1}{2}} \\ \Omega_{\text{BGL}} &= \Omega_0 - \alpha_{\text{BGL}}(\rho_0 - \rho_{c_{\text{BGL}}})\Im(\xi_{\text{BGL}})/\Re(\xi_{\text{BGL}}) \end{aligned} \tag{2.20}$$

2.3.3.4 Linear stability analysis

Gas solution

As in the previous section 2.3.2, the linear stability is given by the sign of $1-\rho_c$. For $1-\rho_c > 0$, the gas solution is unstable and for $1-\rho_c < 0$ the gas solution is stable according to Eq. (2.12).

Rotating Liquid solution

In this paragraph, we follow the same procedure performed with Eq. (2.13). This lead to Fig. 2.20.

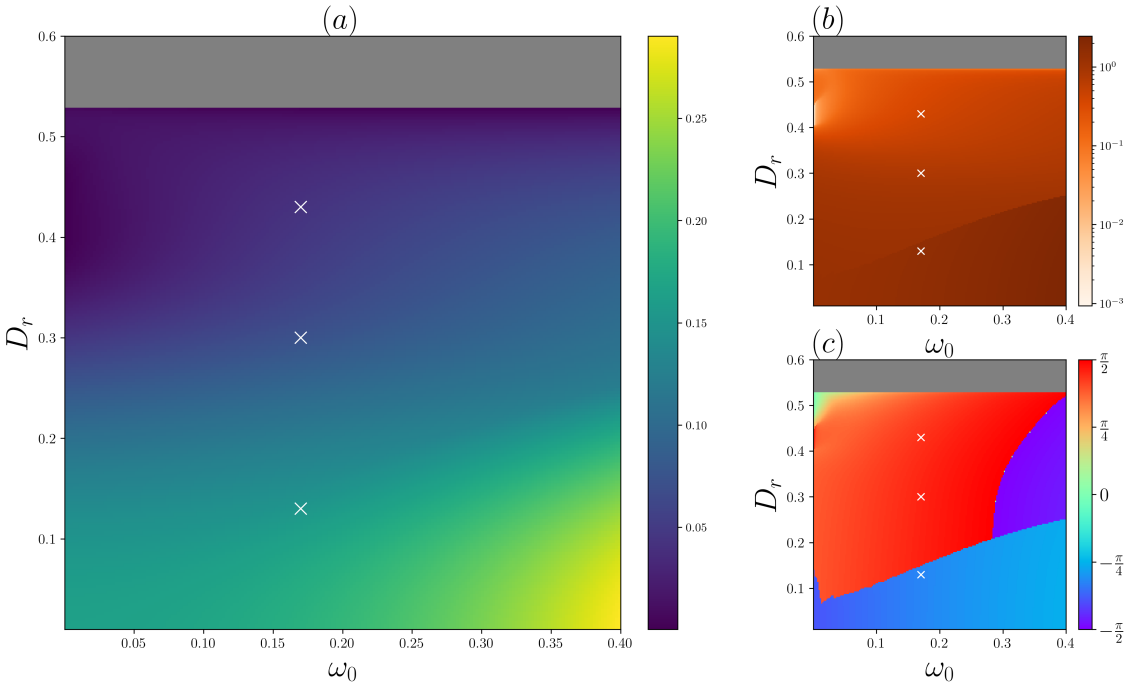

Figure 2.20: Linear stability study of the rotating liquid for the Boltzmann approach and unimodal distribution of chirality. Linear stability analysis with parameters $\rho_0 = 0.5$, $\kappa = 1.0$, and $D_0 = 0.0$. (a): Growth rate of the most unstable eigenvector (b): Modulus of the most unstable eigenvector. (c): Direction of the most unstale vector in the Fourier space. The figure shows that the rotating liquid is unstable everywhere.

Fig. 2.20 corresponds to the linear stability without diffusion. For zero chirality, panel (a) reproduces the standard linear stability for the BGL approach but it is not visible because if the chirality becomes non-zero the linear stability shows that the rotating liquid solution

is unstable everywhere. In panel (b), we show the modulus of the most unstable mode. Between $D_r \approx 0.4$ and $D_r \approx 0.5$ at low values of chirality, the modulus starts from zero but quickly increases. Below $D_r \approx 0.4$ it corresponds to the spurious instability and above $D_r \approx 0.5$ it corresponds to the band instability. Now if we look at panel (c) where the direction is shown, we see the band instability along the polarization direction at very low chirality (green color). For a non-zero value of chirality, we see a transition between two modes, one perpendicular to the polarization direction and the second one with a direction of $\frac{\pi}{4}$. We show the study in the Fourier space in Fig. 2.21 for three sets of parameters corresponding to the white crosses in Fig. 2.20. It allows us to understand how evolves the most unstable mode with the noise.
In section 1.2.3.2, we have seen that an added diffusion can stabilize the liquid phase. So we study the linear stability with an additional diffusion in Fig. 2.22.

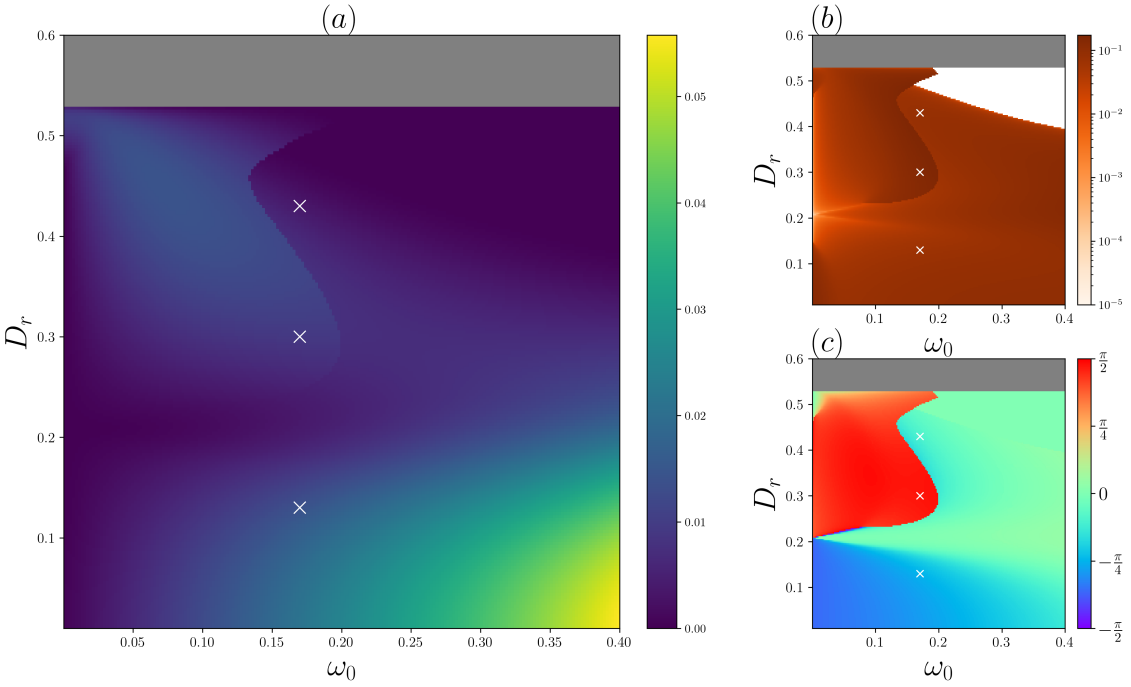

Figure 2.21: Linear stability study of the rotating liquid for the Boltzmann approach and unimodal distribution of chirality. The white crossesare linked to the Fig.2.22. Linear stability analysis with parameters $\rho_0 = 0.5$, $\kappa = 1.0$, and $D_0 = 0.5$. (a): Growth rate of the most unstable eigenvector (b): Modulus of the most unstable eigenvector. (c): Direction of the most unstable vector in the Fourier space. The figure shows that the rotating liquid solution is unstable everywhere.

Fig. 2.22 shows that, even with the diffusion, the rotating liquid phase remains unstable.

The diffusion changes the most unstable mode direction in the interesting region. So we can conclude that the rotating liquid phase is unstable at the hydrodynamic level because the growth is always positive.

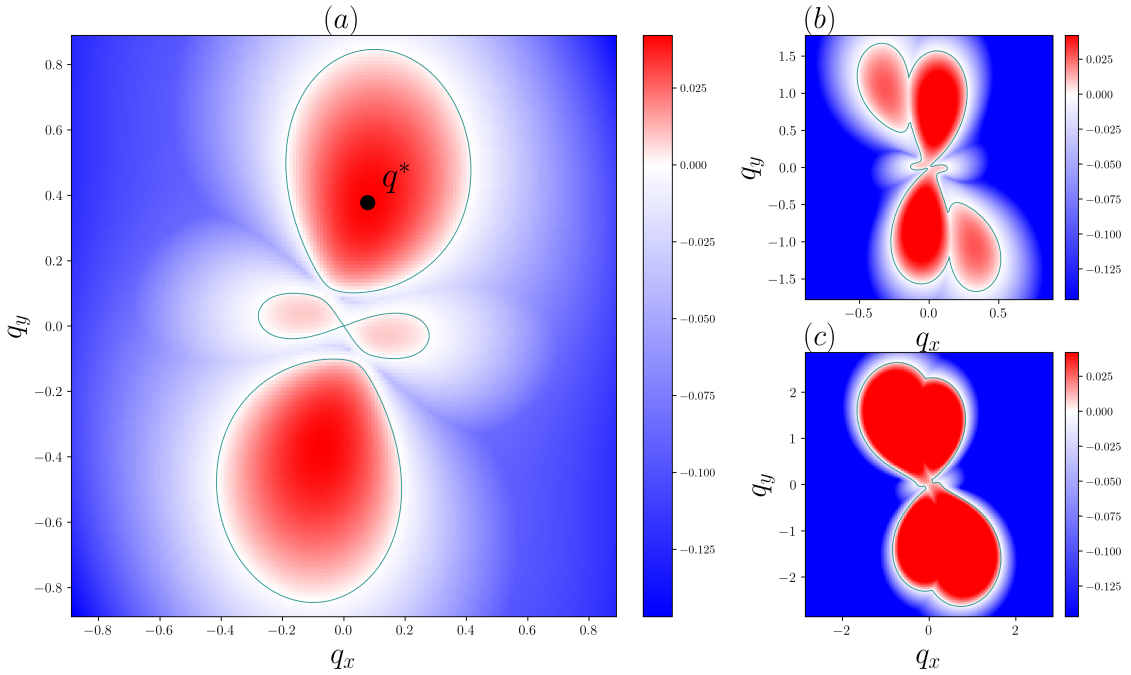

Figure 2.22: Linear stability study of the rotating liquid for the Boltzmann approach and unimodal distribution of chirality. Fourier space attached to a set of parameters with $\rho_0 = 0.5$, $\kappa = 1.0$, and $D_0 = 0.0$. (a): $D_r = 0.43$ and $\omega_0 = 0.17$ (b): $D_r = 0.3$ and $\omega_0 = 0.17$. (c): $D_r = 0.13$ and $\omega_0 = 0.17$. The figure shows how evolves the most unstable mode in the Fourier space.

In the standard Vicsek model, the BGL approach is able to reproduce the microscopic phase diagram but with a spurious instability. Here we see that the rotating liquid solution is unstable everywhere. This point means that the rotating liquid phase does not exist. So it shows a qualitative agreement with the microscopic results where the rotating liquid phase disappears in the asymptotic limit. However, in Fig. 2.20 and Fig. 2.22 one can compare the value of the growth rate with the value of the chirality ω_0 which are of the same order of magnitute. So we can not perform a standard linear stability analysis at a fixed time. Thus we will perform the Floquet stability analysis in the next part.

2.3.3.5 Floquet stability analysis of the rotating liquid solution

We have found a periodic homogeneous solution which is called the rotating liquid in Eq. (2.20). It is possible to write the general expression of a perturbation as $\rho = \rho_0 + \delta\rho$ and $f_1 = F_{1_{\text{BGL}}} e^{i\Omega_{\text{BGL}}t} + \delta f_1$. Thus if we replace this expression in Eq. (2.18) we get the following system of equations

$$\partial_t \begin{pmatrix} \delta\rho_{\mathbf{q}} \\ \delta f_{1x,\mathbf{q}} \\ \delta f_{1y,\mathbf{q}} \end{pmatrix} = L(t,\mathbf{q}) \begin{pmatrix} \delta\rho_{\mathbf{q}} \\ \delta f_{1x,\mathbf{q}} \\ \delta f_{1y,\mathbf{q}} \end{pmatrix} \tag{2.21}$$

where $L(t,\mathbf{q})$ is a T_0-periodic matrix with $T_0 = \frac{2\pi}{\Omega_{\text{BGL}}}$.

The next step is to define the evolution operator $U(t,\mathbf{q})$ such that

$$\begin{pmatrix} \delta\rho_{\mathbf{q}}(t) \\ \delta f_{1x,\mathbf{q}}(t) \\ \delta f_{1y,\mathbf{q}}(t) \end{pmatrix} = U(t,\mathbf{q}) \begin{pmatrix} \delta\rho_{\mathbf{q}}(0) \\ \delta f_{1x,\mathbf{q}}(0) \\ \delta f_{1y,\mathbf{q}}(0) \end{pmatrix} \tag{2.22}$$

Thus the evolution operator will follow the temporal partial differential equation

$$\frac{\partial}{\partial t} U(t,\mathbf{q}) = L(t,\mathbf{q}) U(t,\mathbf{q})$$

This equation is solved formally by the Dyson's formula where $\mathcal{T}\{\cdots\}$ is the time-ordered exponential

$$U(t,\mathbf{q}) = \mathcal{T}\left\{ e^{\int_0^t L(s,\mathbf{q})\,\mathrm{d}s} \right\} \tag{2.23}$$

In our case, to compute numerically the evolution operator we use the formula

$$U(t,\mathbf{q}) = \lim_{N\to\infty} \left(e^{L(N\delta t,\mathbf{q})\delta t} \cdots e^{L(2\delta t,\mathbf{q})\delta t} e^{L(1\delta t,\mathbf{q})\delta t} \right) \tag{2.24}$$

where $\delta t = \frac{t}{N}$ and numerically $N \approx 200$.

The homogeneous polar solution is periodic, so we will perform a stroboscopic analysis which is also called Floquet analysis. The idea is to compute the perturbation after one period T_0 and to see if the amplitude of the perturbation has increased or decreased. According to the Floquet theorem, any solution can be decomposed into fundamental solutions which are obtained from the eigenvalues and eigenvectors of the Floquet operator $U(T_0,\mathbf{q})$.
In practice, we compute the Floquet operator $U(T_0,\mathbf{q})$ according to Eq (2.24). To check the convergence of the integral we compute the Frobenius norm of $U(T_0,\mathbf{q})$ for $N = 100$ and then $N = 200$, if the results are different we double the number of time steps and so on. Then we compute the eigenvalues of the Floquet operator and we keep the eigenvalue

with the highest norm. If the modulus of one eigenvalue is bigger than unity the solution is unstable.

In the general case, the matrix $L(t, \mathbf{q})$ is given by

$$\begin{pmatrix} L_{00} & L_{01} & L_{02} \\ L_{10} & L_{11} & L_{12} \\ L_{20} & L_{21} & L_{22} \end{pmatrix} \tag{2.25}$$

where the coefficients L_{ij} are given in the appendix A.1.

Then we can compute numerically the Floquet operator $U(T_0, \mathbf{q})$ according to Eq. (2.24) for all the values of (q_x,q_y) of the Fourier space. Then we compute numerically the eigenvalues and eigenvectors of the Floquet operator.

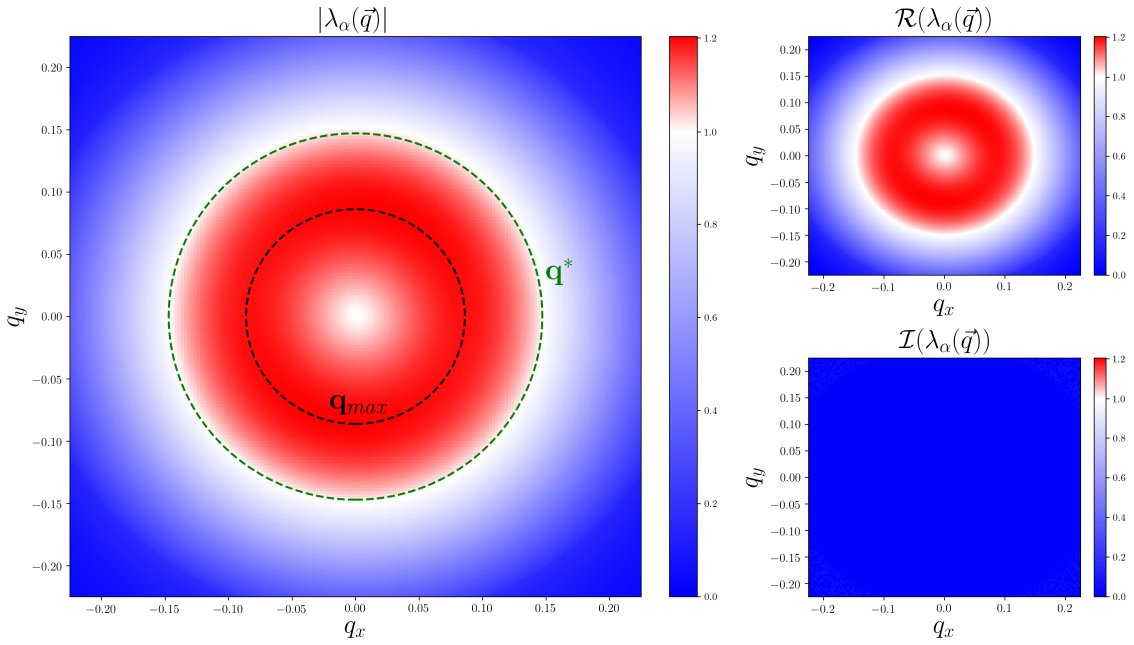

Figure 2.23: Floquet stability analysis of the rotating liquid for the Boltzmann approach and unimodal distribution of chirality. Floquet stability analysis with parameters $\rho_0 = 0.5$, $D_r = 0.5$, $\kappa = 1.0$, $\omega_0 = 0.2$ and $D_0 = 0.5$. Left: Growth rate of the most unstable eigenvector. Top right: Real part of the most unstable eigenvalues. Bottom right: Imaginary part of the most unstable eigenvalues.

In Fig 2.23, we plot the Floquet analysis in the Fourier space. The left panel shows the modulus of the Floquet multiplier $|\lambda_\alpha(\mathbf{q})|$ with the highest value. If the modulus of the Floquet multiplier is bigger than one it means the perturbation has grown after one period,

thus the solution is unstable. In the right panels, one can see the contribution from the real and imaginary part to the modulus of the Floquet multiplier. In that case, one can see that there is a wide range of values where $|\lambda_\alpha(\mathbf{q})|$ is bigger than one so the rotating polar liquid is unstable for this point of the phase space. Moreover, we see that the value with the highest Floquet multiplier is given by the black dashed line and the imaginary part is always 0.

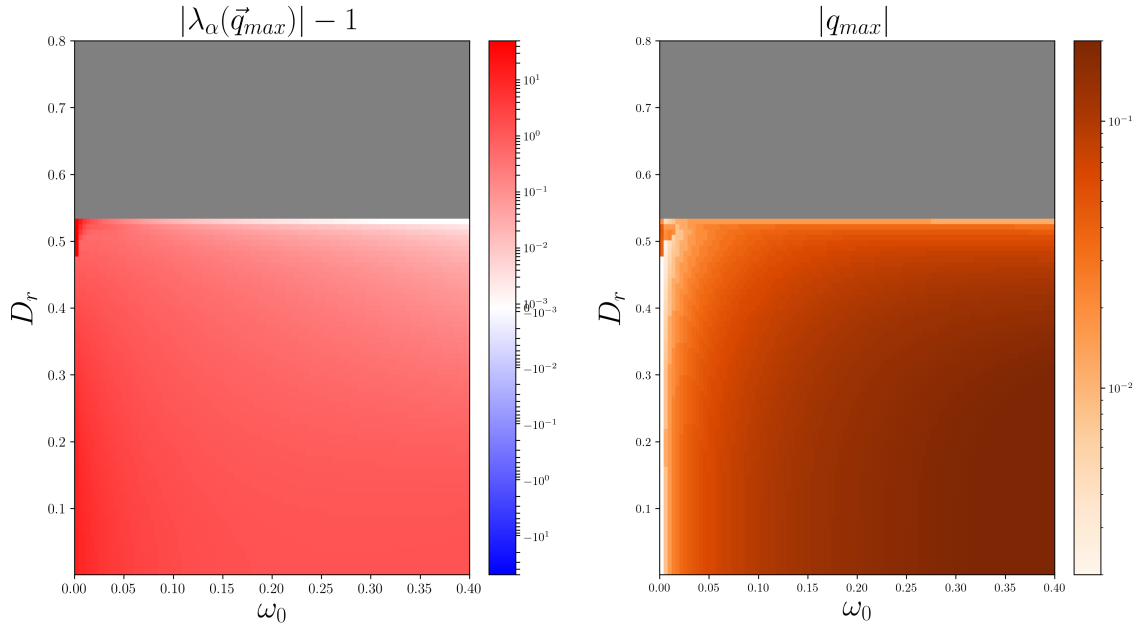

Figure 2.24: Floquet stability analysis of the rotating liquid for the Boltzmann approach and unimodal distribution of chirality. Floquet stability analysis with parameters $\rho_0 = 0.5$, $\kappa = 1.0$, and $D_0 = 0.5$. Left: Growth rate of the most unstable eigenvector. Right: Modulus of the most unstable eigenvector.

In Fig 2.24, we plot the Floquet stability analysis in the plane (ω_0, D_r). One can see that the modulus of the Floquet multiplier is always bigger than one. It means that the polar rotating liquid is unstable everywhere. Moreover, for small ω_0 values and high value of noise one can see the vestige of the band instability. In the right panel, one can see the modulus of the eigenvector attached to the Floquet multiplier.
In the next section, we show the result of the simulations of the hydrodynamic equations and the rotating polar solution exists. The existence of the rotating liquid solution is due to the finite size effects. Indeed, even if the solution is unstable you need a system bigger than the wavelength of the instability, otherwise is not possible for the instability to develop. We are always working with finite size systems so will characterize the finite size effects at the hydrodynamic level thanks to the Floquet stability analysis. It corresponds

to the green line q^* in Fig. 2.23.

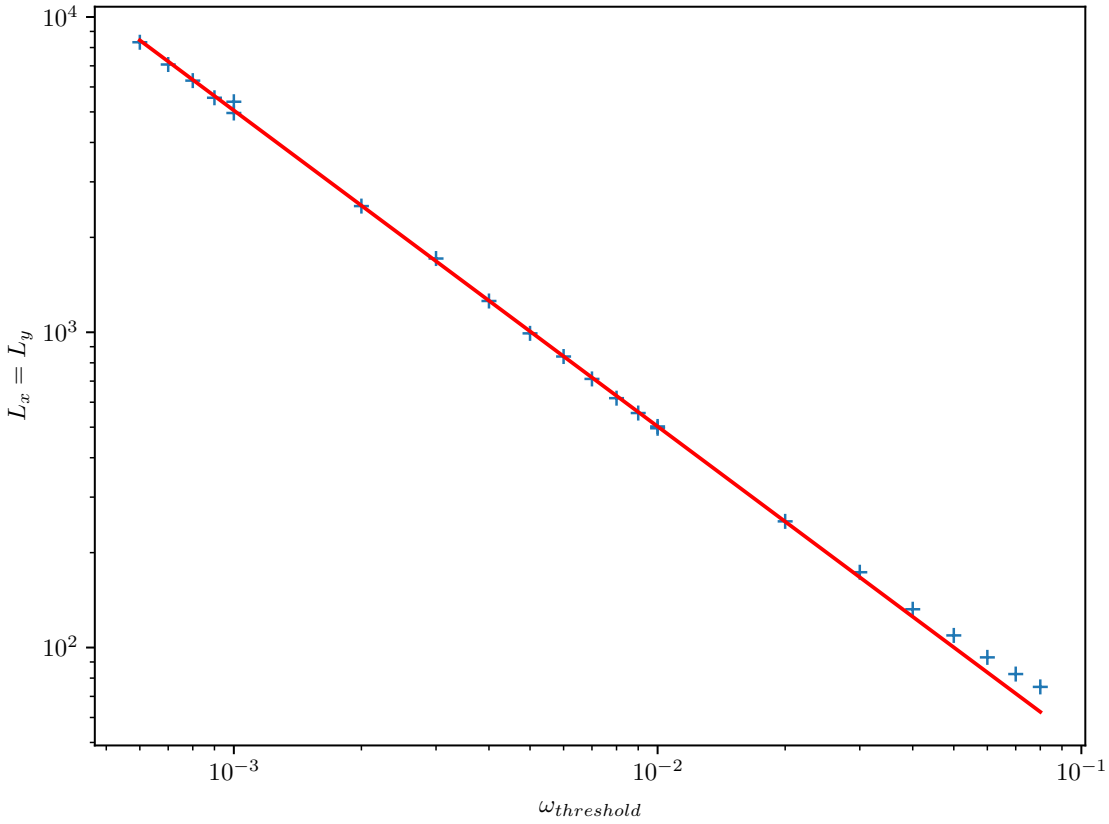

Figure 2.25: Finite-size effects characterization thanks to the Floquet stability analysis of the rotating liquid for the Boltzmann approach and unimodal distribution of chirality. System size corresponding to the wavelength of the unstable mode with the highest eigenvector modulus $\mathbf{q}^*$ as a function of ω_0. The slope of the fit is -1.002 with a correlation coefficient $R = -0.9995$.

In Fig 2.25, we plot the value of the minimal system size needed to see the instability $\frac{2\pi}{q^*}$ as a function of the chirality ω_0. We see that this value is decreasing as a power law but with a coefficient different from the one find at the microscopic level. So get a qualitative agreement only with the microscopic description. Also, we confirm the study of the finite-size effects with simulations of the hydrodynamic equations. For a size $L = 128$, we have found that the rotating liquid phase disappears for a value of $\omega_0 = 0.036$. This value is on the curve of Fig 2.25.

In Fig. 2.26, we plot the evolution of the typical size of the unstable structure as a function

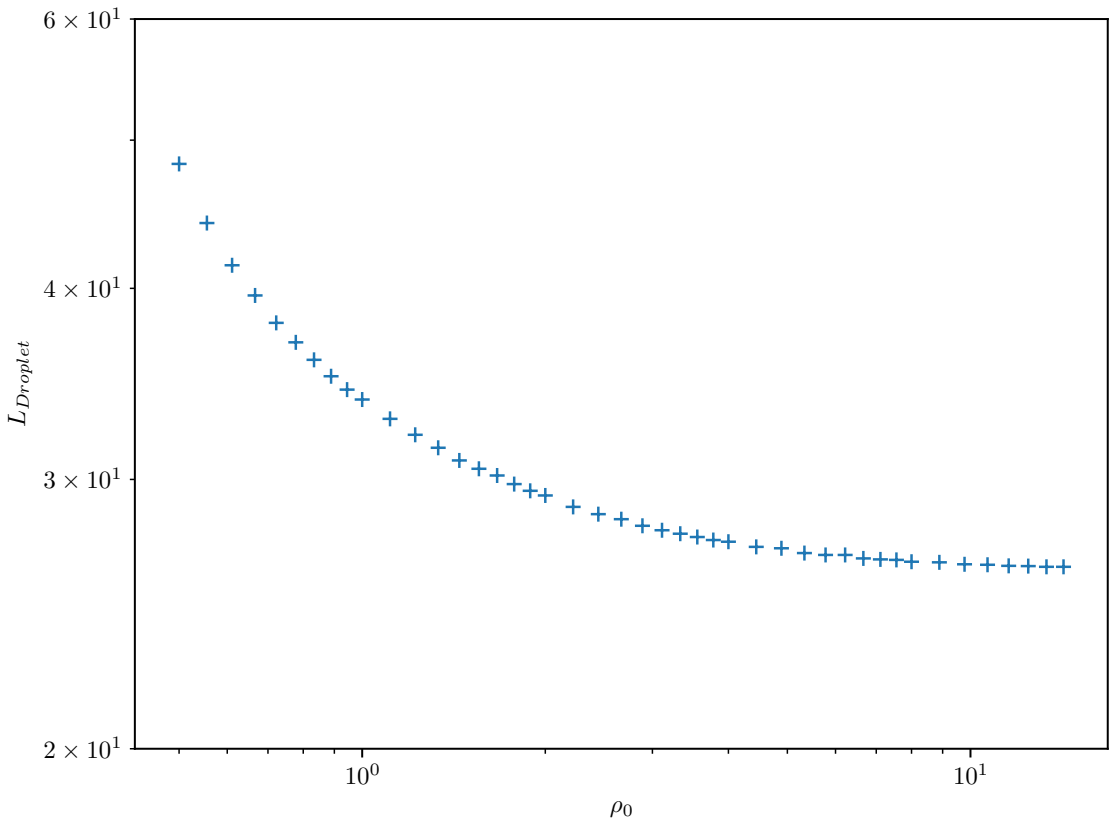

Figure 2.26: Evolution of the instability as a function of the density for the Boltzmann approach and unimodal distribution of chirality. Typical size of the unstable pattern as a function of ρ_0.

of the density ρ_0. In the microscopic simulation, we have found a macrodroplet phase but maybe the macrodroplet is just due to finite-size effects. Indeed, when the rotating liquid is unstable a pattern starts to form, then the density is increasing inside the droplet which means that the new wavelength of the instability could be different because it is now attached to a new density value. If the typical size of the unstable pattern grows when the density grows it means that the macrodroplet size is just due to finite-size effects. However in Fig. 2.26, we plot the evolution of the typical size of the unstable pattern as a function of the density and this size is decreasing and saturates to a given value. So it means that there is positive feedback in the formation of the unstable pattern and it provides a given size corresponding to a rotating packets phase. It means that the hydrodynamic theory is not able to give a simple explanation to the rotating macrodroplet state or we have made a mistake.

2.3.4 Simulations of hydrodynamic equations

In this section, I will perform numerical simulations of hydrodynamic equations to understand the solution of the hydrodynamic equations at the non-linear level. I choose to simulate Eq. (2.18) because the hydrodynamic equations provided by the BGL approach well behave and describe the band solution as in [25].

In the previous sections, we use the complex notation which is compact. Here I express the equations simulated

$$
\begin{aligned}
\partial_t \rho &= -v_0 \left(\partial_x f_{1,x} + \partial_y f_{1,y}\right) \\
\partial_t f_{1,x} &= \alpha_{\text{BGL}} \left(\rho - \rho_{c_{\text{BGL}}}\right) f_{1,x} - \omega_0 f_{1,y} - \Re(\xi_{\text{BGL}})|f_1|^2 f_{1,x} + (\Re(\nu_{\text{BGL}}) + D_0)(\partial_x^2 + \partial_y^2) f_{1,x} - \frac{v_0}{2}\partial_x \rho \\
&\quad - \Re(\gamma_{\text{BGL}}) \left[f_{1,x}(\partial_x f_{1,x} + \partial_y f_{1,y}) - f_{1,y}(\partial_x f_{1,y} - \partial_y f_{1,x})\right] \\
&\quad - \Re(\beta_{\text{BGL}}) \left[f_{1,x}(\partial_x f_{1,x} - \partial_y f_{1,y}) + f_{1,y}(\partial_x f_{1,y} + \partial_y f_{1,x})\right] \\
&\quad + \Im(\xi_{\text{BGL}})|f_1|^2 f_{1,y} - \Im(\nu_{\text{BGL}})(\partial_x^2 + \partial_y^2) f_{1,y} \\
&\quad + \Im(\gamma_{\text{BGL}}) \left[f_{1,x}(\partial_x f_{1,y} - \partial_y f_{1,x}) + f_{1,y}(\partial_x f_{1,x} + \partial_y f_{1,y})\right] \\
&\quad + \Im(\beta_{\text{BGL}}) \left[f_{1,x}(\partial_x f_{1,y} + \partial_y f_{1,x}) - f_{1,y}(\partial_x f_{1,x} - \partial_y f_{1,y})\right] \\
\partial_t f_{1,y} &= \alpha_{\text{BGL}} \left(\rho - \rho_{c_{\text{BGL}}}\right) f_{1,y} + \omega_0 f_{1,x} - \Re(\xi_{\text{BGL}})|f_1|^2 f_{1,y} + (\Re(\nu_{\text{BGL}}) + D_0)(\partial_x^2 + \partial_y^2) f_{1,y} - \frac{v_0}{2}\partial_y \rho \\
&\quad - \Re(\gamma_{\text{BGL}}) \left[f_{1,x}(\partial_x f_{1,y} - \partial_y f_{1,x}) + f_{1,y}(\partial_x f_{1,x} + \partial_y f_{1,y})\right] \\
&\quad - \Re(\beta_{\text{BGL}}) \left[f_{1,x}(\partial_x f_{1,y} + \partial_y f_{1,x}) - f_{1,y}(\partial_x f_{1,x} - \partial_y f_{1,y})\right] \\
&\quad - \Im(\xi_{\text{BGL}})|f_1|^2 f_{1,x} + \Im(\nu_{\text{BGL}})(\partial_x^2 + \partial_y^2) f_{1,x} \\
&\quad - \Im(\gamma_{\text{BGL}}) \left[f_{1,x}(\partial_x f_{1,x} + \partial_y f_{1,y}) - f_{1,y}(\partial_x f_{1,y} - \partial_y f_{1,x})\right] \\
&\quad - \Im(\beta_{\text{BGL}}) \left[f_{1,x}(\partial_x f_{1,x} - \partial_y f_{1,y}) + f_{1,y}(\partial_x f_{1,y} + \partial_y f_{1,x})\right]
\end{aligned}
\tag{2.26}
$$

We do a numerical integration using an Euler method for a system of size L_x, L_y. In general $\Delta t \in [10^{-3}; 10^{-1}]$ and $dx, dy \in [0.125; 0.5]$. We use a spectral method to compute the derivative part. Moreover, we add an extra diffusion D_0 in given cases, which allows us to stabilize the spurious instability as presented in section 1.2.3.2.

Phase overview

In the following study, we will show different phases. So we will first present an overview of the charactistic of each phases.

The first phase which is called Band is the standard Vicsek phase. There are regions with high density extended along one direction and the homogeneous polarization along the perpendicular direction. See the following phase in Fig. 2.27.

The second phase is called Liquid, and it is the standard Vicsek phase where the density

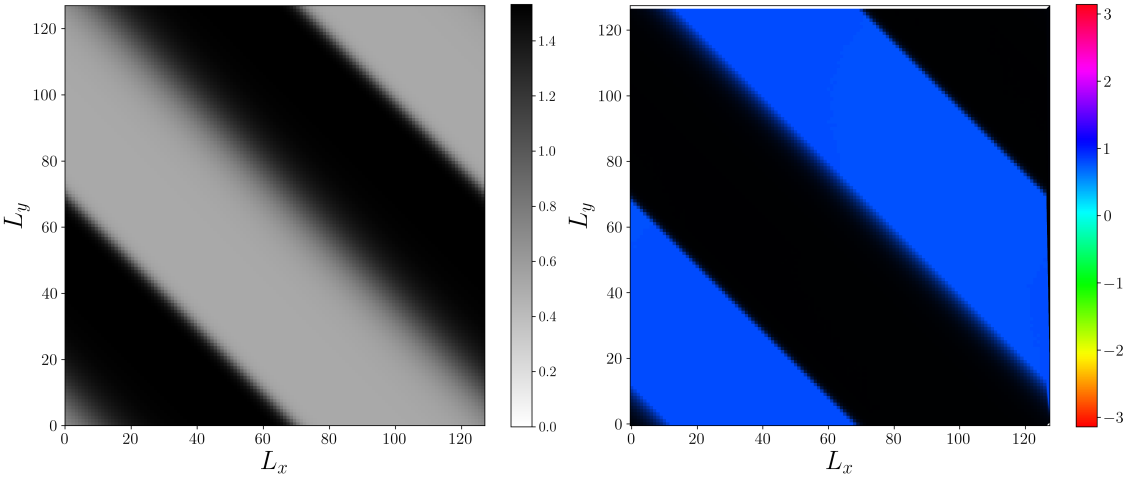

Figure 2.27: A typical snapshot of the band phase made with the hydrodynamic equations for a unimodal distribution of chirality. It shows a system with parameters $D_0 = 0.0$, $D_r = 0.5$, $\rho = 0.5$ and $\omega_0 = 0.00$. Left: Density. Right: Local polarization

is homogeneous with a global polar order.

The first new phase is called rotating liquid, and it is the previous liquid phase with a homogeneous polarization rotating in time.

The second new phase called the vortices phase shows well defined vortices. It means a bunch of disks with high density, a center with low density, and a polarization turning around their center. See snapshot below in Fig. 2.28.

The new rotating packets phase shows high-density packets rotating in time. See snapshot below in Fig. 2.29.

Non defined phase According to Fig. 2.20 the liquid is unstable without additional diffusion. If we simulate the liquid in the unstable region but not far from the stable region we get very dense patterns with negative density (red area) nearby the patterns, see Fig. 2.30.

So we perform numerical simulations with an added diffusion to avoid the non-physical phase and stabilize the rotating packets phase. One can understand this under the fact that in the center of a rotating packet there is a liquid phase, which is unstable without diffusion. In that way, the diffusion will stabilize the center of the droplet and allow the rotating packets phase. However, if we put diffusion it is not possible to observe

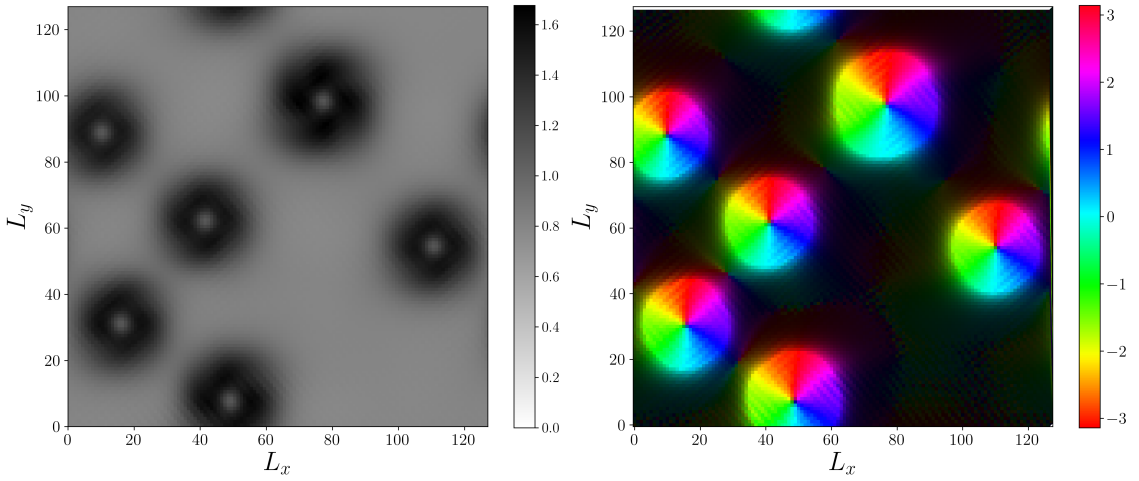

Figure 2.28: A typical snapshot of the vortices phase made with the hydrodynamic equations for a unimodal distribution of chirality. It shows a system with $D_0 = 0.0$, $D_r = 0.5$, $\rho = 0.5$ and $\omega_0 = 0.05$. Left: Density. Right: Local polarization.

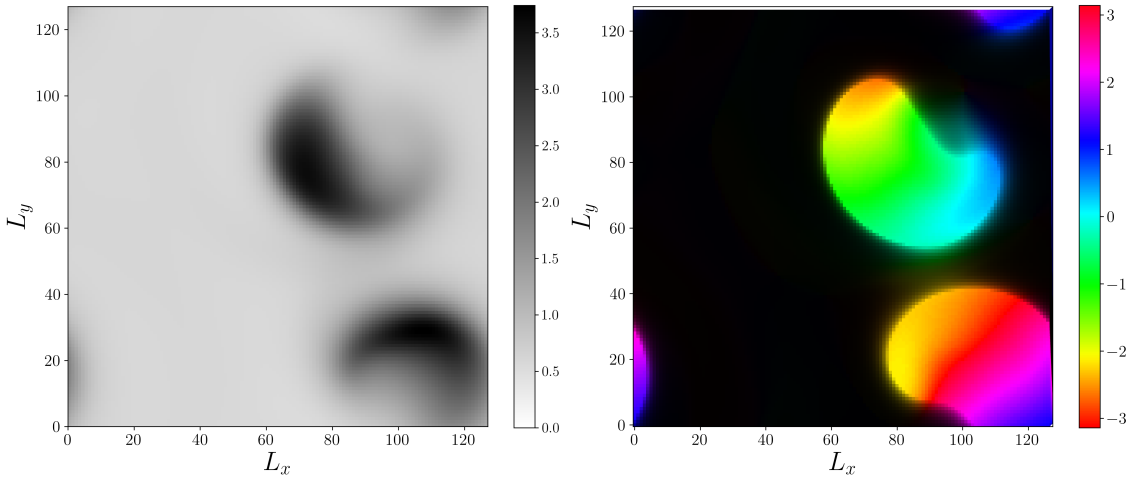

Figure 2.29: A typical snapshot of the rotating packets made with the hydrodynamic equations for a unimodal distribution of chirality. It shows a system with $D_0 = 0.5$, $D_r = 0.5$, $\rho = 0.5$ and $\omega_0 = 0.10$. Left: Density. Right: Local polarization.

spontaneously vortices but we can take a vortices state and move it smoothly in diffusion and get a stable solution. So we perform simulations with and without diffusion. Then we move smoothly the interesting solution for D_r and ω_0. The result is represented in Fig. 2.31, each point represents a solution. The size of the different regions is obtained by moving solutions.

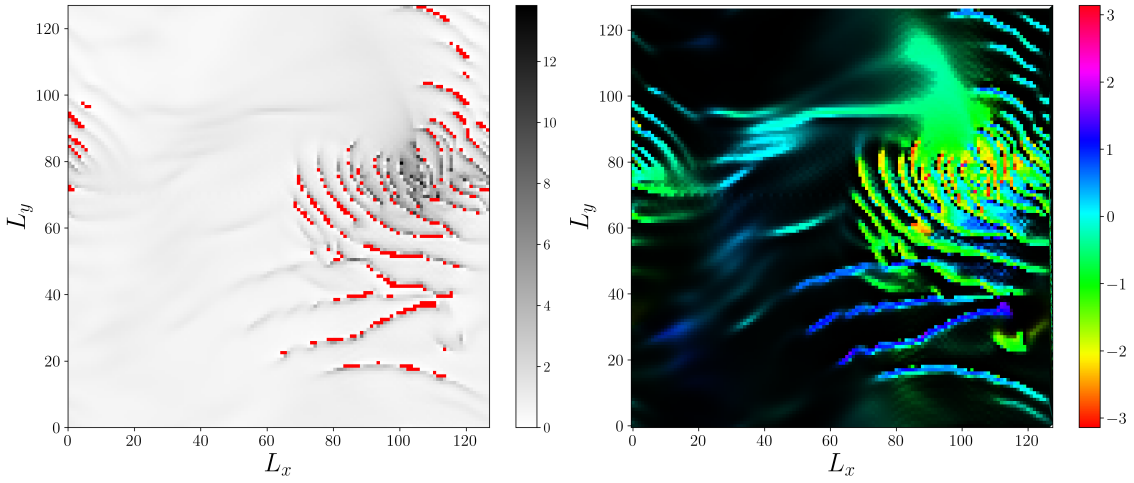

Figure 2.30: A typical snapshot of the dense patterns made with the hydrodynamic equations for a unimodal distribution of chirality. It shows a system with $D_0 = 0.0$, $D_r = 0.35$, $\rho = 0.5$ and $\omega_0 = 0.00$. Left: Density with negative density in red. Right: Local polarization.

Contrary to the microscopic phase diagram we are not able to see the macrodroplet phase which is replaced by the rotating packets phase. Otherwise, we find qualitatively the same phase diagram. The non-existence of the macrodroplet phase could be due to the truncation because we have seen that extra diffusion is needed to stabilize the rotating packets.

Now that we have an overview of the phase diagram, we can study the transition between each phase more carefully. To study carefully the transition line, we take one phase as the initial condition and move it through the transition line by little step.
We take the band phase and increase ω with $\Delta\omega = 0.004$. The band phase breaks for $\omega = 0.02$ and gives rotating packets phase. Then we take the vortices phase and decrease ω with $\Delta\omega = 0.002$. The vortices phase breaks for $\omega = 0.012$ to give something which does not stabilize in our time simulation until $\omega = 0.006$ where find again the band phase. Then we increase ω with the same $\Delta\omega$ step. At $\omega = 0.074$ we start to get rotating packets. Now let's have a look at these results with regard to the linear stability Fig. 2.22. If we start looking at $(\omega \sim 10^{-2}, D_r = 0.5)$ we see an instability along the polarization axis which can be the band instability. Then, before $\omega = 0.1$ the most unstable mode change, it should correspond to the transition from bands to vortices. For very large ω the most unstable mode change again, it should be the transition from vortices to rotating packets.

For very small ω we always get a rotating liquid. One explanation to this phenomenology is the modulus of the most unstable mode is larger than system size. So the instability does

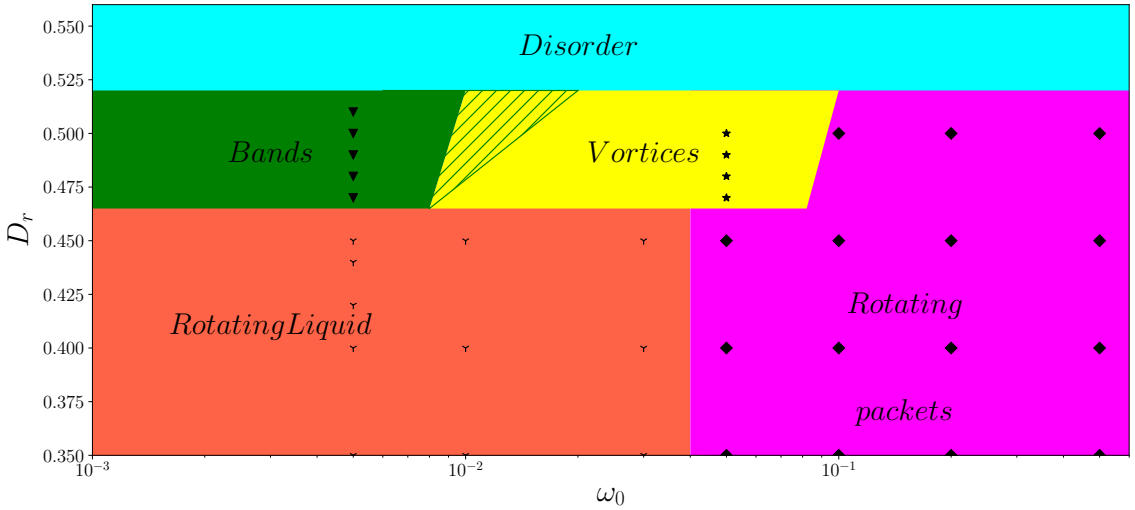

Figure 2.31: Study of the phase diagram done with simulations of the hydrodynamic equations for a unimodal distribution. Phase diagram in the plane (ω_0, D_r) with parameters $\rho_0 = 0.5$, $\kappa = 1.0$, and $L = 128$. We move each point in ω_0 to determine the transition line. The figure shows the existence of two new phase which are called vortex and rotating packets, if one replace rotating packets by rotating macrodroplet we get a qualitative agreement with the results found at the microscopic level.

not manage to develop, and we get a rotating liquid instead of vortices or rotating packets. This point will be developed in the bimodal distribution case. After these studies at the hydrodynamic level, we can conclude the qualitative agreement between our Eq. (2.26) and the microscopic model Eq. (1.40). But it shows the limit of our BGL approach and hypothesis attached to it because we have to add diffusion to compensate for some truncation effects.

2.3.5 Conclusion

In this chapter, we have studied the KVM model for a unimodal distribution of chirality. This study is cut into two parts. The first part corresponds to the microscopic simulation. In this part, we have discovered three new phases but only two are stable in the limit of infinite system size.
Then we perform a study of KVM at the hydrodynamic level by using two different approaches based on a coarse-graining of the microscopic model. These two approaches provide the same hydrodynamic equations structure, but the definitions of the coefficients are different. The Fokker-Planck approach, based on the dense system hypothesis, is not able to reproduce the phase diagram in the pure Vicsek case, so it is difficult to conclude at the linear level, even if it predicts an unstable rotating liquid. The second approach,

based on the dilute system hypothesis, is able to reproduce the phase diagram of the Vicsek model at the linear level. In the KVM model, it predicts at the linear level the instability of the rotating liquid solution. Moreover, the simulations of the full equations predict a phase diagram in a qualitative agreement with the microscopic simulations.

2.4 Bimodal distribution

In this section we perform our computation with a bimodal distribution for the frozen chirality disorder. It means $g(\omega) = \frac{1}{2}\delta(\omega+\omega_0)+\frac{1}{2}\delta(\omega-\omega_0)$. This distribution is composed by two subpopulations with unimodal distribution of opposite chirality, but it shares the two first moments of the Gaussian distribution. It will be interesting to analyze the results in the light of the previous results.

2.4.1 Numerical Results

2.4.1.1 Phase diagram

We have drawn a phase diagram for a system of size $L = 128$, a density $\rho_0 = 1.00$ and a coupling strength $\kappa = 1.00$ constant. It means that we have plotted the phase diagram in the noise, chirality plane (D_r,ω_0) without any loss of generalities.

In Fig. 2.32 the red hatch area is where the size $L_x < 4/\omega_0$, it corresponds to two times the typical radius of particle's trajectory with chirality ω_0. This is the place where we expect strong finite-size effects as explained for the Gaussian distribution.
At zero chirality we see the existence of the standard Vicsek model. Then when we increase the chirality one can see two new phases. These two new phases are the Vortex phase, where particles with a different sign of chirality segregate and form vortices, see Fig. 2.34. For larger chirality one can see the rotating packets phase, where particles segregate, to form several rotating packets, as represented in Fig. 2.33. The local polarization is homogeneous inside a packet and is rotating in time.

We can compare this phase diagram with the one found in the case of a Gaussian distribution. In that case, there is only the vortex phase and no rotating packets phase. The rotating packets phase occurs only for high value of chirality, but in a population drawn from a Gaussian distribution most of the particles have a chirality near zero. Thus there are only a little number of particles with high value of chirality and this not enough to destabilize the vortex phase.

At the first glance, the band phase is statisically identical to the pure Vicsek case without segregation between the two populations. So at zero chirality we get the standard bands of the Vicsek model, but when we start to increase the chirality there is a microscopic change compared to the standard bands because the two subpopulations start to have a different

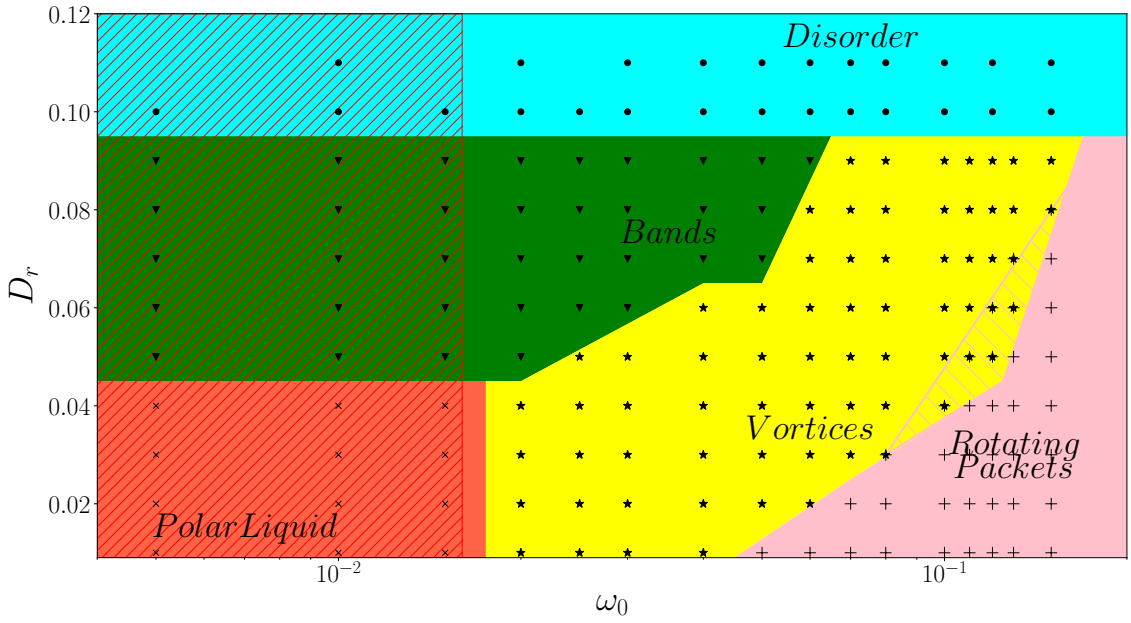

Figure 2.32: Numerical study of the phase diagram for the bimodal distribution. Phase diagram in the plane (D_r, ω_0) for a system at size $L = 128$, velocity $v_0 = 1$, density $\rho_0 = 1$ and coupling strength $\kappa = 1.00$. The figure shows two new phases which are called vortices and rotating packets.

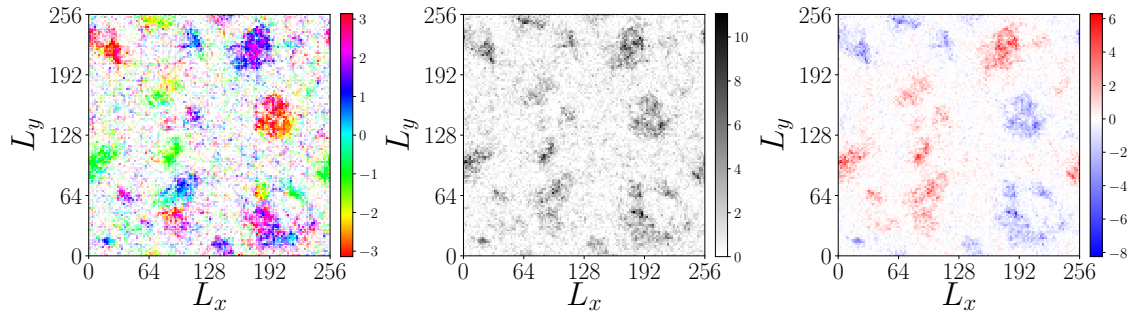

Figure 2.33: Numerical study for a bimodal distribution of chirality. Typical snapshot of the rotating packets phase with parameters $L = 256$, $\omega_0 = 0.150$, $D_r = 0.070$, $v_0 = 1$, $\rho_0 = 1$ and $\kappa = 1.00$. The left panel shows the local coarse-grained direction of the polarization. The middle panel shows the coarse-grained density. The right panel shows the coarse-grained chirality. The figure shows the segregation between particles.

direction of polarization. However this difference does not seem to have an impact on the temporal evolution of those bands. In Fig. 2.35, we plot the difference between the

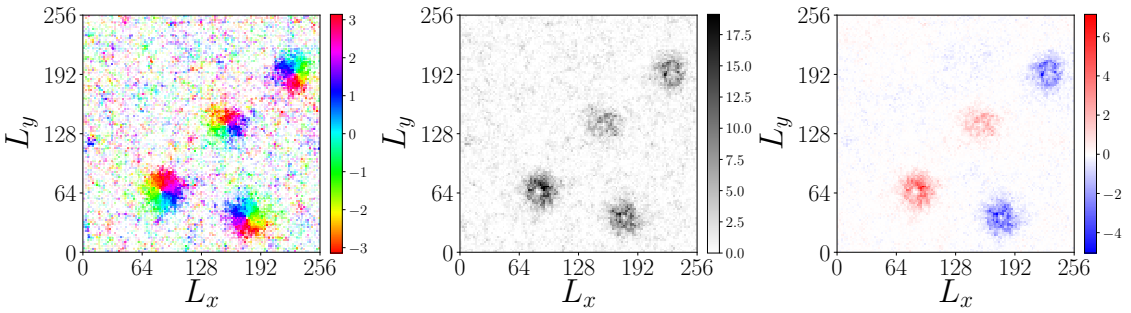

Figure 2.34: Numerical study for a bimodal distribution of chirality. Typical snapshot of the vortex phase with parameters $L = 256$, $\omega_0 = 0.070$, $D_r = 0.070$, $v_0 = 1$, $\rho_0 = 1$ and $\kappa = 1.00$.The left panel shows the local coarse-grained direction of the polarization. The middle panel shows the coarse-grained density. The right panel shows the coarse-grained chirality.The figure shows the segregation between particles.

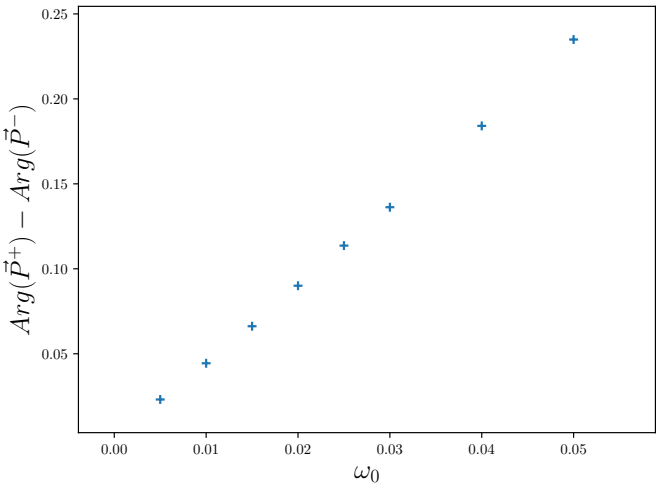

Figure 2.35: Numerical study of the bands phase for a bimodal distribution of chirality. It shows the difference of polarization direction as a function of the chirality ω_0 with parameters $\rho_0 = 1.0$, $\kappa = 1$, $v_0 = 1$, $D_r = 0.080$ and $L = 128$. The figure shows that the difference of polarization grows linearly as a function of ω_0.

global polarization of particles with positive and negative chirality as a function of the global chirality ω_0. We find that the difference of polarization increases when the chirality increases. So the band phase at non-zero values of chirality is different from the standard band phase of the Vicsek model. Moreover, the same difference holds for the liquid phase.

2.4.1.2 Asymptotic behavior

Finite size effects at liquid noise level

In this paragraph, we will study the finite-size effects. To perform this study we will plot the phase diagram in the plane (L, ω_0). It will allow us to understand how evolves the boundary between two different phases with the system size. Then it allows us to determine if a phase exists in the limit of infinite system size.

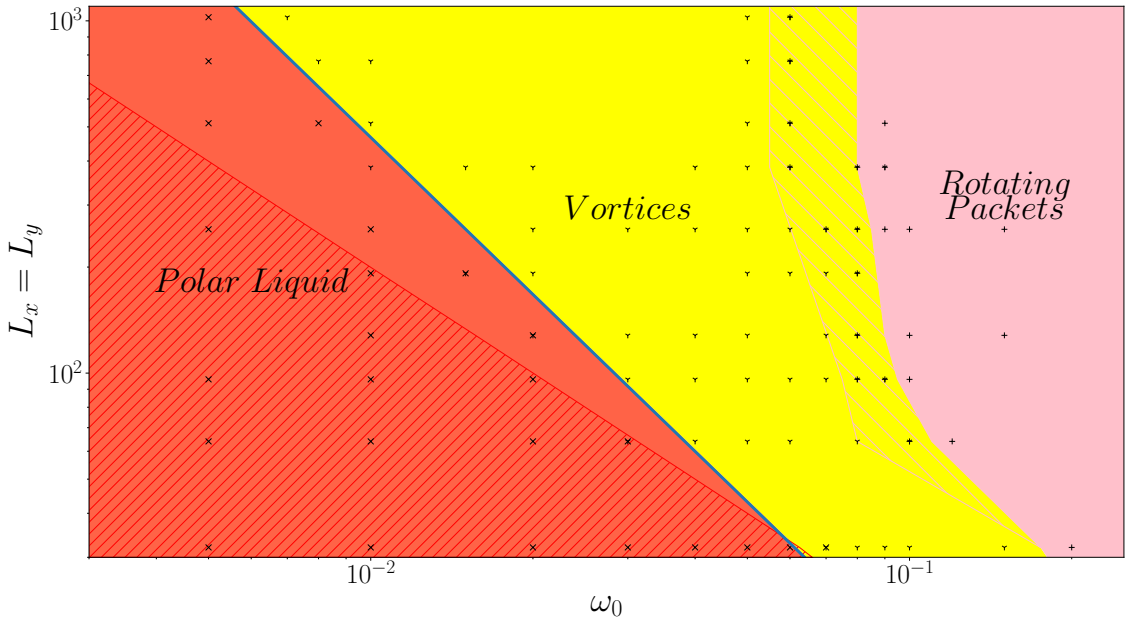

Figure 2.36: Asymptotic study of the polar liquid phase for the bimodal distribution. Phase diagram in the plane (ω_0, L) for a system with parameters $D_r = 0.030$, $v_0 = 1$, $\rho_0 = 1$ and $\kappa = 1.00$. Slope $= -1.48$ and Correlation $= 0.995$. The figure shows that the value of the transition between polar liquid and vortices decreases as a power law. Thus the polar liquid phase does not exist in the infinite system size.

Fig. 2.36 shows that the liquid phase, in the asymptotic limit, does not exist. Moreover, it shows also coexistence between vortices and rotating packets in the asymptotic limit, see Fig. 2.37.

Then we study the phase transition between liquid and vortices in a quantitative way. In Fig. 2.38 we plot the mean value of polarization for different time series. We take $|\vec{P}|_{\omega_0^*} = 0.5$ as a threshold to define the value of the transition between the liquid phase and the vortex phase.

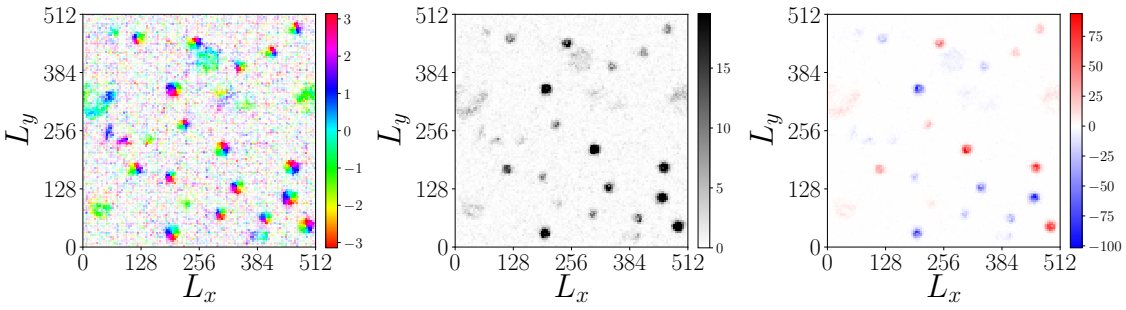

Figure 2.37: Numerical study for a bimodal distribution of chirality. Typical snapshot of the coexistence between rotating packets phase and vortex phase with parameters $L = 512$, $\omega_0 = 0.130$, $D_r = 0.070$, $v_0 = 1$, $\rho_0 = 1$ and $\kappa = 1.00$. Left: Polarization direction. Middle: Density. Right: Chirality.

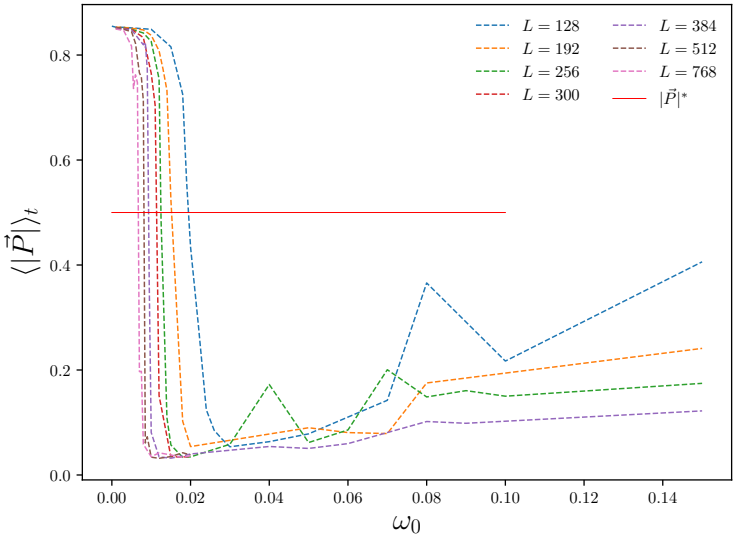

Figure 2.38: Quantitative study of the liquid-vortex transition line. It shows the mean value of polarization over time series as a function of the chirality. The threshold value is $|\vec{P}|^* = 0.5$.

In Fig. 2.39 we report the threshold values for different system sizes. One can see the law $\omega_0^* \sim L^{-0,62}$. It means the liquid phase does not exist in the infinite system size. So the quantitative study confirms the qualitative predictions. We can notice the scaling coefficient is similar to the scaling coefficients found in the previous studies.

Initial condition effects at liquid noise level

In this paragraph we test the stability of two different configurations. First, we take a rotating packets configuration at $L = 256$, $D_r = 0.030$, $\kappa = 1.0$, $\rho = 1.0$, $v_0 = 1$, $\omega_0 = 0.150$ and move it to $\omega_0 = 0.040$. The result is rotating packets disappear to give four vortices.

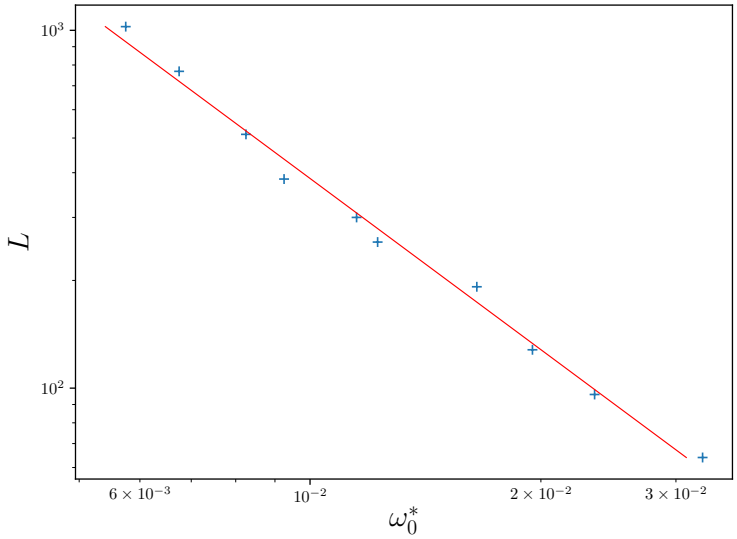

Figure 2.39: A quantitative study of the liquid-vortex transition line. We plot the threshold value as a function of the system size. The linear regression gives a slope of -1.590 ± 0.05 and a correlation coefficient of $r = -0.9960$. The figure shows that the polar liquid phase does not exist in the limit of infinite system size.

Then we do the reverse transformation and vortices disappear to give ten rotating packets. So, it is possible to get the same phase from various initial conditions, and thus there is no initial conditions effect and simulations are not trapped in a metastable state. Also, we explore the possible existence of the macrodroplet. To test the macrodroplet phase presented in the unimodal case, we take a custom initial condition, see Fig. 2.40, of two macrodroplets with opposite chirality surrounded by gas at the density of the sparse gas. It leads quickly to a rotating packets phase. It means that the macrodroplet phase doesn't resist system with particles having different values of chirality.

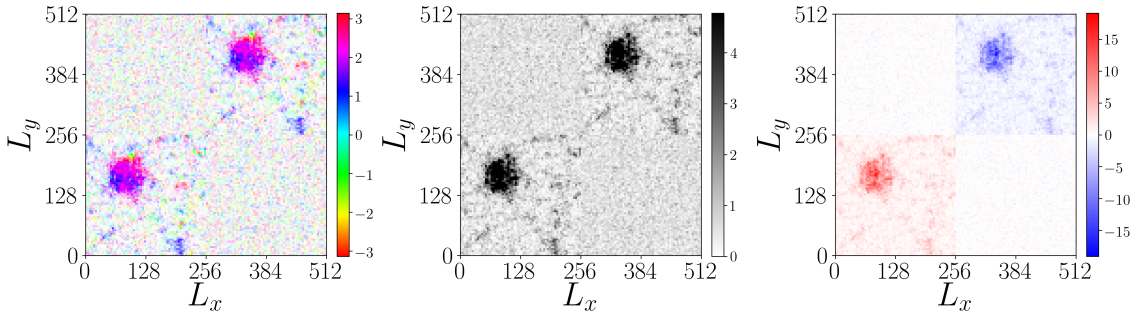

Figure 2.40: Numerical study for a bimodal distribution of chirality. Typical snapshot of the rotating packets phase with $\omega_0 = 0.150$, $D_r = 0.020$, $\rho_0 = 0.8$ and $\kappa = 1.00$ and $L = 512$. Handmade initial condition with subsystems of size $L = 256$. Left: Polarization direction. Middle: Density. Right: Chirality. The figure shows that the macrodroplets phase does not resist chirality with different signs.

Finite size effects at band noise level

In this paragraph, we will study the finite-size effects. To perform this study we will plot the phase diagram in the plane (L, ω_0).

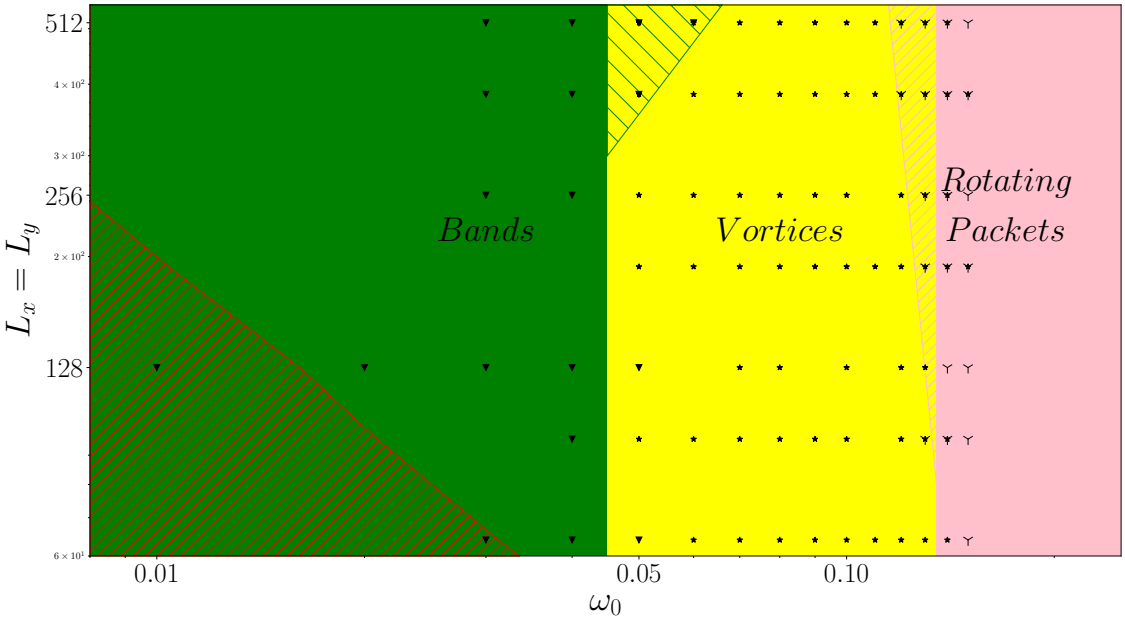

Figure 2.41: Asymptotic study of the bands phase for the bimodal distribution. Phase diagram in the plane (L, ω_0) for a system at noise $D_r = 0.070$, velocity $v_0 = 1$, density $\rho_0 = 1$ and coupling strength $\kappa = 1.00$. The figure shows that the band phase is stable with the system size.

At this noise level, Fig. 2.41 shows that bands will not asymptotically disappear. At a given point there is a coexistence between vortices and bands, see Fig 2.42. Then at larger values of ω_0 the boundary between rotating packets and vortex becomes constant with the system size. Asymptotically we can infer the existence of bands, vortices, and rotating packets.

Initial condition effects at band noise level

In this paragraph, we test the stability of three different configurations. First, we take a six rotating packets configuration at $L = 256$, $D_r = 0.070$, $\kappa = 1.0$, $\rho = 1.0$, $\omega_0 = 0.150$ and move it to $\omega_0 = 0.040$. The result is that rotating packets disappear to give two vortices. Then we do the reverse transformation and vortices disappear to give rotating packets. So one can expect a well-defined transition line between both phases.

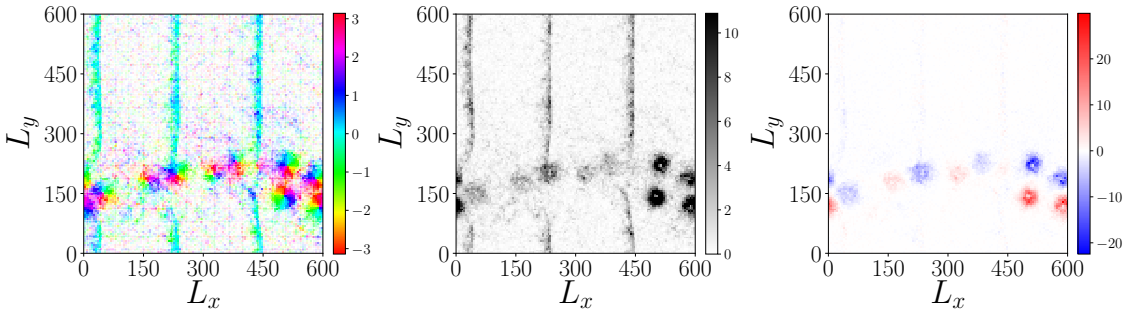

Figure 2.42: Numerical study for a bimodal distribution of chirality. Typical snapshot of the coexistence between bands phase and vortex phase with parameters $L = 600$, $\omega_0 = 0.050$, $D_r = 0.070$, $v_0 = 1$, $\rho_0 = 1$ and $\kappa = 1.00$. Left: Polarization direction. Middle: Density. Right: Chirality.

Rotating packets: a microphase separation

As explained in the previous paragraph, the rotating packets phase is a microphase separation because handmade initial conditions with macrodroplet are not stable in the bimodal case. Moreover, when we increase the system size the number of rotating packets increases and the size of the packets is stable with the system size, see snapshots in Fig.2.43. Furthermore, it is possible to observe the shape transition between a vortex and a rotating packet by looking at movies. If we start with a vortex, the density is homogeneous inside the vortex but at a given point a part of the vortex starts to deform, and due to the rotation the vortex starts to become a packet that is still rotating around the same center. We also observe the reverse phenomenon. This observation does the link between the microphase separation of the rotating packets and the microphase separation of the vortices.

Vortices: a microphase separation

The first argument is when we increase the system size, the number of vortices increases, but this could be due to initial condition effects. So, we can do a shift in density from an initial condition made of a pair of vortices. We start with a system size $L = 128$, and we feed it in density by copying randomly particles. The two vortices remain stable and repulsion is needed to break a such pattern. However, if we take a configuration with two vortices and double the system size we get height vortices. After a long time, the number of vortices stabilizes around four. From these points, we can conclude that the vortex phase is microphase separated and the finite-size effects play a strong role.

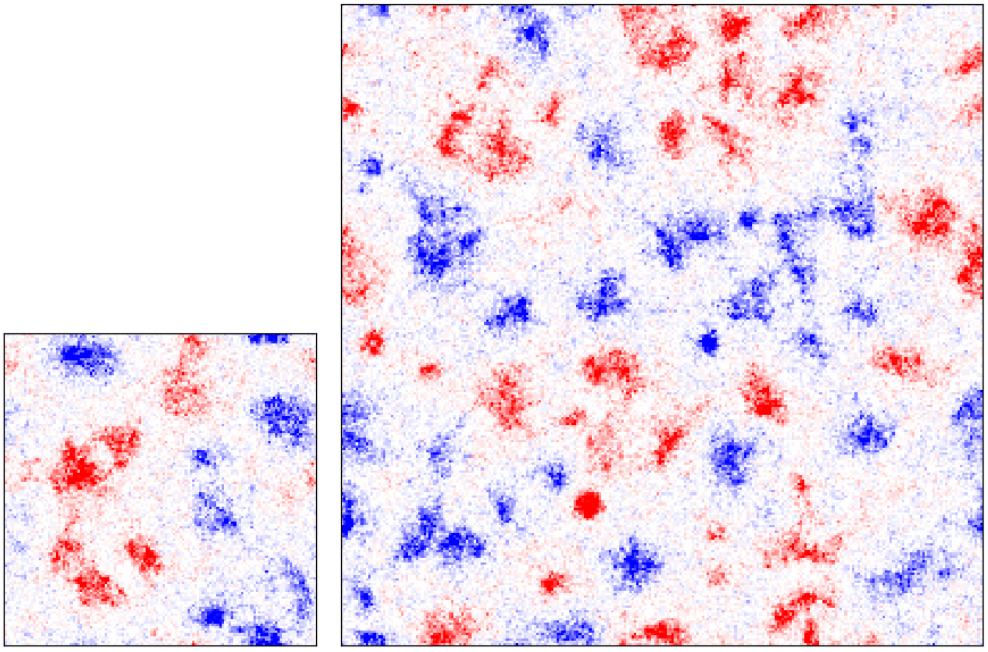

Figure 2.43: Numerical study for a bimodal distribution of chirality. Typical snapshot of the rotating packets phase with $\omega_0 = 0.150$, $D_r = 0.070$, $v_0 = 1$, $\rho_0 = 1$ and $\kappa = 1.00$. Left: $L = 256$. Right: $L = 512$. The figure shows that the size of rotating packets is constant as a function of the system size. Thus this is a macrophase separation.

2.4.2 Fokker-Planck approach

In this section, we will perform the computation under the same hypothesis as in section 2.3.2, but now we use a bimodal distribution instead of the unimodal distribution. So we will consider two populations, one with a positive chirality, one with a negative chirality. We will denote by $f(\vec{r}, \theta, t)$ the probability density function for the population with a positive chirality and by $g(\vec{r}, \theta, t)$ the probability density function for the population with a negative chirality. The main difference with section 2.3.2 is that we have to take into account the interaction between the two populations.

Evolution of the particle density function

If we follow our previous work and the paper from [47, 48]. It is possible to write the Fokker-Planck equation for the population with a positive chirality

$$\partial_t f(\vec{r},\theta,t) = -v_0\,\vec{e}(\theta).\vec{\nabla} f - \omega_0\partial_\theta f - \kappa\partial_\theta \int \mathrm{d}\theta' (f(\vec{r},\theta') + g(\vec{r},\theta'))\sin(\theta'-\theta) f(\vec{r},\theta) + D_r\partial_\theta^2 f - \partial_\theta\sqrt{2f}\xi \quad (2.27)$$

To get the temporal evolution of g we need to replace f by g and ω_0 by $-\omega_0$. In general, we will express only the equation for one population because it is easy to read from it the equation for the second population. Then we neglect the noise and perform a rescaling as follows

$$t \to t/D_r \quad , \quad \vec{r} \to v_0\vec{r}/D_r \quad , \quad f \to \tfrac{\rho_0}{2} f \quad , g \to \tfrac{\rho_0}{2} g \quad (2.28)$$

Here we make a choice to rescale f and g in the same way because we never study a case where g_0 is different from f_0. Then we take the Fourier transform along the angular coordinate, it leads to

$$\partial_t f_k = -\frac{1}{2}\left[\nabla f_{k-1} + \nabla^* f_{k+1}\right] + (ik\Omega_0 - k^2) f_k + \frac{i\bar{g}k}{2\pi}\sum_{m=-\infty}^{\infty} f_{k-m} F_{-m}(f_m + g_m) \quad (2.29)$$

with $\Omega_0 = \frac{\omega_0}{D_r}$, $\bar{g} = \frac{\rho_0\kappa}{2\pi R^2 D_r}$, and F_m is the mth Fourier coefficient of $\sin\theta$. So $F_{-1} = \frac{-1}{2i}$ and $F_1 = \frac{1}{2i}$ and $F_m = 0\ \forall\, m \notin \{-1;1\}$

Hydrodynamic equations

The next step is to follow the Ginzburg-Landau truncation scheme. First, we have to determine a scaling ansatz. We look at Eq. (2.29) and the linear stability of the homogeneous disordered solution holds under the same hypothesis of section 2.3.2, so we keep the same scaling ansatz

$$f_0 \sim 1\,, \qquad g_0 \sim 1\,, \qquad f_1 \sim g_1 \sim \partial_t \sim \nabla \sim \epsilon\,, \qquad f_k \sim g_k \sim \epsilon^k \quad \forall\ k > 1$$

Then we expand Eq. (2.29) at $k = 2$ and stop at order ϵ^2. It is possible to express f_2 and g_2 in terms of f_1 and g_1. Then we substitute f_2 and g_2 in the temporal evolution of f_1 and g_1. We get the following set of hydrodynamic equations

$$\partial_t f_1 = \left(\alpha_{\text{FP}}(f_0 - \rho_{c\text{FP}}) + i\Omega_0 - \xi_{\text{FP}}|f_1|^2\right) f_1 - \frac{1}{2}\nabla f_0 + \nu_{\text{FP}}\Delta f_1 - \beta_{\text{FP}} f_1^*\nabla f_1 - \frac{\gamma_{\text{FP}}}{2}\nabla^* f_1^2 + \alpha_{\text{FP}} f_0 g_1 - \xi_{\text{FP}}\left(|f_1|^2 g_1 + g_1^* f_1^2 + |g_1|^2 f_1\right) - \beta_{\text{FP}}\left(g_1^*\nabla f_1\right) - \frac{\gamma_{\text{FP}}}{2}\nabla^*(f_1 g_1) \quad (2.30a)$$

$$\partial_t g_1 = ... \quad (2.30b)$$

$$\partial_t f_0 = -\frac{1}{2}(\nabla f_1^* + \nabla^* f_1) \tag{2.30c}$$

$$\partial_t g_0 = -\frac{1}{2}(\nabla g_1^* + \nabla^* g_1) \tag{2.30d}$$

The first line of Eq. (2.30a) is the hydrodynamic equation found for a unimodal distribution, but now there are more terms due to the interaction with the second population. The second line of Eq. (2.30a) contains all the cross terms. Eq. (2.30b) is given by taking Eq. 2.30a and replacing f_1 by g_1 and taking the complex conjugate of all the coefficients. The last two equations are the conservation law for the density of the two populations. Now if we restrict our equation by removing all the gradient terms of non linearities ($\mathcal{O}(\nabla X_1 X_1)$ where X_1 is f_1 or g_1) we match the equations of Levis and Liebchen [66]. Their equations are written with a scalar formalism instead of our complex formalism.

2.4.2.1 Homogeneous stationary solution of the hydrodynamic equations

We are looking for a stationary solution of the previous set of equations Eq. (2.30). A trivial solution is $f_0 = g_0 = 1$ and $f_1 = g_1 = 0$, this corresponds to the disorder homogeneous phase. Then to find a possible ordered solution for the liquid we are looking for a solution with $f_1 = P$ and $g_1 = Pe^{i\phi}$. These constraints lead to

$$0 = +i\Omega_0 - 1 + \alpha_{\text{FP}}(1 + e^{i\phi}) - 2\xi_{\text{FP}}\left(P^2 + \cos\phi P^2\right)$$

which gives two different equations for real and imaginary part

$$0 = -1 + \alpha_{\text{FP}}(1 + \cos\phi) - \frac{g^2 P^2}{b}(1 + \cos\phi)$$

$$0 = \Omega_0 + \alpha_{\text{FP}}\sin\phi - \frac{g^2\Omega_0 P^2}{2b}(1 + \cos\phi)$$

then by solving these equations using *Mathematica*, it leads to

$$\begin{aligned} P^{\pm} &= \frac{\sqrt{\alpha_{\text{FP}}(4+\Omega_0^2)}}{3\alpha_{\text{FP}}\Omega_0}\sqrt{\pm\sqrt{4\alpha_{\text{FP}}^2 + 3(2\alpha_{\text{FP}} - 3)\Omega_0^2} + 3\Omega_0^2 - 2\alpha_{\text{FP}}} \\ \phi^{\pm} &= -i\ln\left(\frac{\pm(3-\alpha_{\text{FP}})\Omega_0 + i\sqrt{4\alpha_{\text{FP}}^2 + 3(2\alpha_{\text{FP}} - 3)\Omega_0^2}}{\alpha_{\text{FP}}(\Omega_0 + 2i)}\right) \end{aligned} \tag{2.31}$$

or

$$\phi^+ = \tan^{-1}\left(\frac{2\sqrt{g^4\alpha_{\text{FP}}^2\left(\Omega_0^2+4\right)^2\left(4\alpha_{\text{FP}}^2 + 6\alpha_{\text{FP}}\Omega_0^2 - 9\Omega_0^2\right)} - g^2(\alpha_{\text{FP}} - 3)\alpha_{\text{FP}}\Omega_0^2\left(\Omega_0^2+4\right)}{g^2\alpha_{\text{FP}}^2\left(\Omega_0^2+4\right)^2}, \right.$$
$$\left.\frac{\Omega_0\left(\sqrt{g^4\alpha_{\text{FP}}^2\left(\Omega_0^2+4\right)^2\left(4\alpha_{\text{FP}}^2 + 6\alpha_{\text{FP}}\Omega_0^2 - 9\Omega_0^2\right)} + 2g^2(\alpha_{\text{FP}} - 3)\alpha_{\text{FP}}\left(\Omega_0^2+4\right)\right)}{g^2\alpha_{\text{FP}}^2\left(\Omega_0^2+4\right)^2}\right)$$

The second solution corresponds to a mutual flocking phase where the two populations have the same polarization modulus but a different orientation angle ϕ. This solution corresponds to the polar liquid solution at the microscopic level.

2.4.2.2 Linear stability of the gas solution

We will study the previous gas solution and perturb it with a perturbation of the form $f_0 = 1 + \delta f_0$, $g_0 = 1 + \delta g_0$, $f_1 = \delta f_1$, and $g_1 = \delta g_1$. We replace the new expression in Eq. (2.30) and linearize the system. It leads to

$$\partial_t \delta f_1 = (\alpha_{\text{FP}}(1 - \rho_{c\text{FP}}) + i\Omega_0)\,\delta f_1 - \frac{1}{2}\nabla \delta f_0 + \nu_{\text{FP}}\Delta \delta f_1 + \alpha_{\text{FP}}\delta g_1 \tag{2.32a}$$

$$\partial_t \delta g_1 = ... \tag{2.32b}$$

$$\partial_t \delta f_0 = -\frac{1}{2}(\nabla \delta f_1^* + \nabla^* \delta f_1) \tag{2.32c}$$

$$\partial_t \delta g_0 = -\frac{1}{2}(\nabla \delta g_1^* + \nabla^* \delta g_1) \tag{2.32d}$$

where Eq. (2.32b) is given by taking Eq. 2.32a and replacing f_1 by g_1 and taking the complex conjugate of all the coefficients.
We are interested in general perturbations, and we have a system invariant by translation, thus we work in the Fourier space for Eq. (2.32) and get a system of equations that can be expressed as a 6x6 matrix. The linear stability is given by the sign of the eigenvalues of the following matrix.

$$\begin{pmatrix} 0 & -iq_x & -iq_y & 0 & 0 & 0 \\ -\frac{i}{2}q_x & \bar{\alpha}_{\text{FP}} & -\Omega_0 + \mathfrak{I}(\nu_{\text{FP}})q^2 & 0 & \alpha_{\text{FP}} & 0 \\ -\frac{i}{2}q_y & \Omega_0 - \mathfrak{I}(\nu_{\text{FP}})q^2 & \bar{\alpha}_{\text{FP}} & 0 & 0 & \alpha_{\text{FP}} \\ 0 & 0 & 0 & 0 & -iq_x & -iq_y \\ 0 & \alpha_{\text{FP}} & 0 & -\frac{i}{2}q_x & \bar{\alpha}_{\text{FP}} & \Omega_0 - \mathfrak{I}(\nu_{\text{FP}})q^2 \\ 0 & 0 & \alpha_{\text{FP}} & -\frac{i}{2}q_y & -\Omega_0 + \mathfrak{I}(\nu_{\text{FP}})q^2 & \bar{\alpha}_{\text{FP}} \end{pmatrix} \tag{2.33}$$

where $\bar{\alpha}_{\text{FP}} = \alpha_{\text{FP}}\left(1 - \rho_{c_{\text{FP}}}\right) - \mathfrak{R}(\nu_{\text{FP}})q^2$. It is possible to compute the eigenvalue exactly thanks to the characteristic polynomial attached to this matrix

$$\begin{aligned} &\left(-\frac{q^4}{4}(\alpha_{\text{FP}} - \bar{\alpha}_{\text{FP}})(\alpha_{\text{FP}} + \bar{\alpha}_{\text{FP}}) - \frac{q^4\bar{\alpha}_{\text{FP}}}{2}\right) + (q^2\bar{\alpha}_{\text{FP}}(-\alpha_{\text{FP}}^2 + \bar{\alpha}_{\text{FP}}^2 + (-q^2\mathfrak{I}(\nu_{\text{FP}}) + \Omega_0)^2))\,S \\ &\quad + \frac{1}{4}(q_x^4 + q_y^4 + 2q_x^2(q_y^2 + 2\alpha_{\text{FP}}^2 - 6\bar{\alpha}_{\text{FP}}^2 - 2(-q^2\mathfrak{I}(\nu_{\text{FP}}) + \Omega_0)^2) \\ &+ 4(-\alpha_{\text{FP}}^2 + \bar{\alpha}_{\text{FP}}^2 + (-q^2\mathfrak{I}(\nu_{\text{FP}}) + \Omega_0)^2)^2 - 4q_y^2(-\alpha_{\text{FP}}^2 + 3\bar{\alpha}_{\text{FP}}^2 + (-q^2\mathfrak{I}(\nu_{\text{FP}}) + \Omega_0)^2))S^2 \\ &\quad \bar{\alpha}_{\text{FP}}(3q^2 - 4(-\alpha_{\text{FP}}^2 + \bar{\alpha}_{\text{FP}}^2 + (-q^2\mathfrak{I}(\nu_{\text{FP}}) + \Omega_0)^2))S^3 \\ &\quad + (-q^2 - 2\alpha_{\text{FP}}^2 + 6\bar{\alpha}_{\text{FP}}^2 + 2(-q^2\mathfrak{I}(\nu_{\text{FP}}) + \Omega_0)^2)\,S^4 - 4\bar{\alpha}_{\text{FP}}S^5 + S^6 \end{aligned} \tag{2.34}$$

It is difficult to draw conclusion analytically from Eq. (2.34) but if we take the approximation $q = 0$, it is possible to compute exactly the eigenvalues which are given by $S_\pm = \alpha_{\text{FP}}\left(1-\rho_{c_{\text{FP}}}\right) \pm \sqrt{\alpha_{\text{FP}}^2 - \Omega_0^2}$. Similar to the unimodal distribution the sign of eigenvalues at $q = 0$ is controlled by the sign of $1 - \rho_{c_{\text{FP}}}$.

2.4.2.3 Linear stability of the liquid solution

We will study the Liquid solution Eq. (2.31). As for the gas solution, we expand the solution around the liquid solution Eq. (2.31).

$$\begin{aligned} f_0 &= 1 + \delta f_0 \\ f_1 &= P + \delta f_1 \\ g_0 &= 1 + \delta g_0 \\ g_1 &= Pe^{i\phi} + \delta g_1 \end{aligned}$$

then we replace in Eq. (2.30). It leads to the new set of equations in terms of $\delta f_{1,x}$,$\delta f_{1,y}$,$\delta g_{1,x}$ and $\delta g_{1,y}$

$$\partial_t \delta f_{1,x} = \mathrm{C}^{\text{FP}}_{0,0}\delta f_0 + \mathrm{C}^{\text{FP}}_{0,1}\delta g_0 + \mathrm{C}^{\text{FP}}_{0,2}\delta f_{1,x} + \mathrm{C}^{\text{FP}}_{0,3}\delta f_{1,y} + \mathrm{C}^{\text{FP}}_{0,4}\delta g_{1,x} + \mathrm{C}^{\text{FP}}_{0,5}\delta g_{1,y} \tag{2.35a}$$
$$\partial_t \delta f_{1,y} = \mathrm{C}^{\text{FP}}_{1,0}\delta f_0 + \mathrm{C}^{\text{FP}}_{1,1}\delta g_0 + \mathrm{C}^{\text{FP}}_{1,2}\delta f_{1,x} + \mathrm{C}^{\text{FP}}_{1,3}\delta f_{1,y} + \mathrm{C}^{\text{FP}}_{1,4}\delta g_{1,x} + \mathrm{C}^{\text{FP}}_{1,5}\delta g_{1,y} \tag{2.35b}$$
$$\partial_t \delta g_{1,x} = \mathrm{C}^{\text{FP}}_{2,0}\delta f_0 + \mathrm{C}^{\text{FP}}_{2,1}\delta g_0 + \mathrm{C}^{\text{FP}}_{2,2}\delta f_{1,x} + \mathrm{C}^{\text{FP}}_{2,3}\delta f_{1,y} + \mathrm{C}^{\text{FP}}_{2,4}\delta g_{1,x} + \mathrm{C}^{\text{FP}}_{2,5}\delta g_{1,y} \tag{2.35c}$$
$$\partial_t \delta g_{1,y} = \mathrm{C}^{\text{FP}}_{3,0}\delta f_0 + \mathrm{C}^{\text{FP}}_{3,1}\delta g_0 + \mathrm{C}^{\text{FP}}_{3,2}\delta f_{1,x} + \mathrm{C}^{\text{FP}}_{3,3}\delta f_{1,y} + \mathrm{C}^{\text{FP}}_{3,4}\delta g_{1,x} + \mathrm{C}^{\text{FP}}_{3,5}\delta g_{1,y} \tag{2.35d}$$

where the coefficients are expressed in Appendix A.3.

To study this system of equations we take the Fourier transform of Eq. (2.35) along the spatial coordinates, then for each set of parameters, we scan the Fourier space to find the highest eigenvalue. The sign of the eigenvalue gives information about the stability of the perturbation. Moreover, we can characterize the most unstable wavelength with its modulus and its direction. It allows us to know if the solution is stable or not by looking at the eigenvalues in the Fourier space. The results are shown in Fig. 2.44.

In Fig. 2.44 we plot the result of the numerical study of Eq. (2.35). It shows that the liquid solution is unstable everywhere and the instability is along the polarization direction. However, we have worked at a given density $\rho_0 = 4.0$ so we also plot the phase diagram in the plane (ρ_0, ω_0), see Fig. 2.45. In this figure, we see the existence of a stability region near the transition line between the gas solution to the liquid solution. This result is surprising because for the unimodal case the liquid solution is unstable everywhere. So there are two possibilities, the first one is a mistake in the computation even if the behavior seems coherent. The second one is that the truncation scheme for two populations affects the system of equations at the hydrodynamic level. However, the stability of the liquid

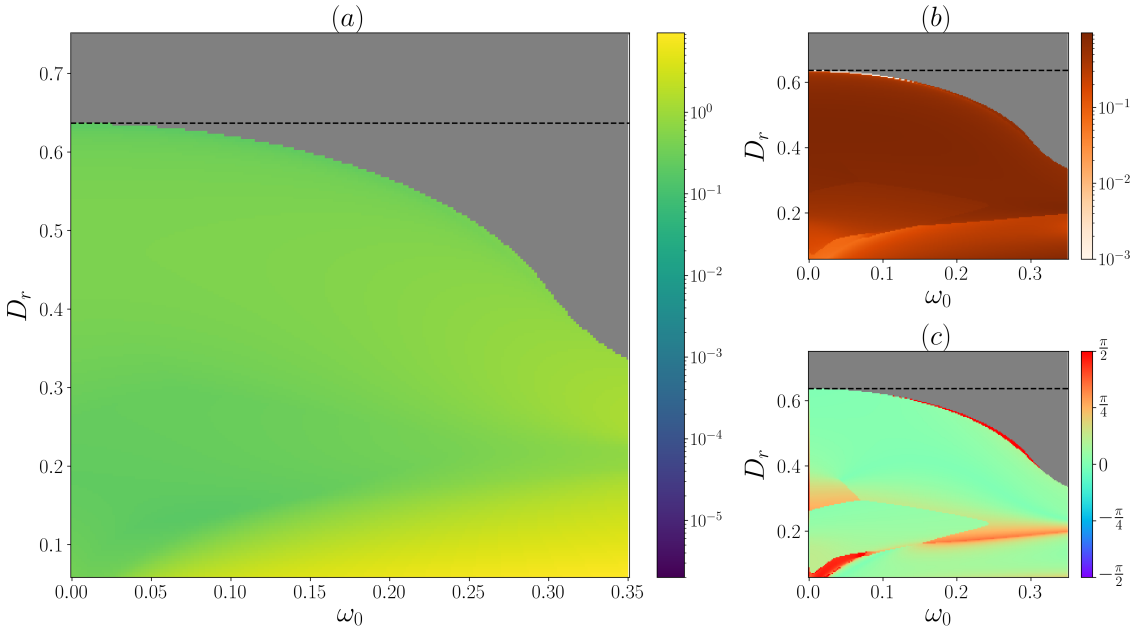

Figure 2.44: Linear stability study in the plane (D_r, ω_0) with $\rho_0 = 4.0$. The grey part is where the liquid solution is not defined. (a): Highest eigenvalue of the Fourier space. (b): Modulus of the eigenvector attached to the highest eigenvalue of the panel (a). (c): Direction of the eigenvector attached to the highest eigenvalue of the panel (a). The figure shows that the polar liquid is unstable everywhere.

solution happens on a marginal area of the phase space because it is only for small values of density but the Fokker-Planck equation is based on the assumption of dense systems.

To conclude this section, we have derived the hydrodynamic equations with a Fokker-Planck approach. Thanks to these equations we have found two homogeneous solutions which could correspond to the two homogeneous solutions found at the microscopic level. The linear stability of the gas solution seems to be the same as for the unimodal distribution of chirality. The liquid solution seems to be unstable everywhere except in a small region near the transition line between the liquid and gas solution. This point asks the question of the validity of our computation.

2.4.3 Boltzmann approach

In this section, we will perform the coarse-graining of a microscopic model under the same hypothesis as in section 2.3.3, but now we use a bimodal distribution instead of the unimodal distribution. So we will consider two populations, one with a positive chirality, one with the negative chirality, as in the previous section. We will denote by $f(\vec{r}, \theta, t)$ the

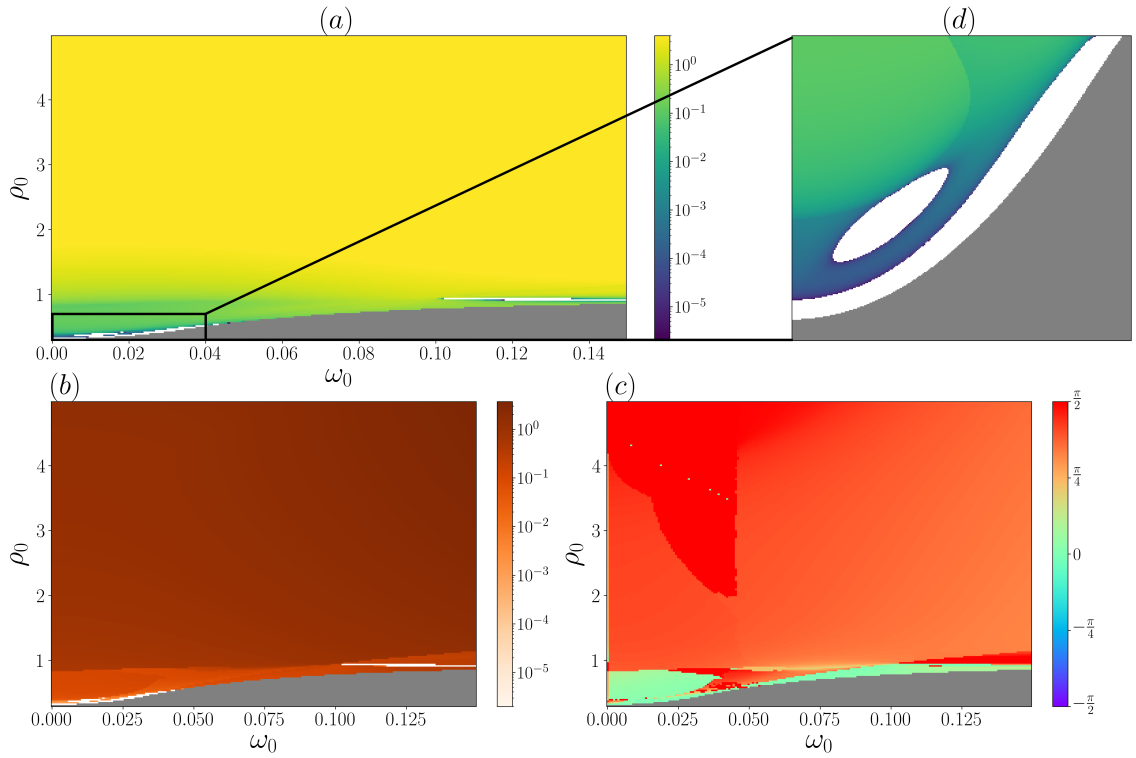

Figure 2.45: Linear stability study in the plane (ρ, ω_0) with $D_r = 0.05$. The grey part is where the liquid solution is not defined. (a): Highest eigenvalue of the Fourier space. (b): Modulus of the eigenvector attached to the highest eigenvalue of the panel (a). (c): Direction of the eigenvector attached to the highest eigenvalue of the panel (a). (d): Highest eigenvalue of the Fourier, zoom from (a) with the same colormap. The figure shows that the polar liquid is stable only in a marginal part of the phase diagram.

probability density function for the population with a positive chirality and by $g(\vec{r}, \theta, t)$ the probability density function for the population with a negative chirality. The main difference with section 2.3.3 is that we have to take into account the interaction between the two populations.

2.4.3.1 Particle distribution function in Fourier space

We consider $f(r, \theta, t)$ the particle distribution function for the first population. The evolution of the function in the Chiral-Vicsek model case is

$$\frac{\partial f}{\partial t} = \text{"free evolution"} + \text{"self-diffusion"} + \text{"collision } 1^{st} \text{ population"} + \text{"coll. } 2^{nd} \text{ population"}$$

The contribution of the free evolution, the self-diffusion, and the collision with the same

population of f is unchanged compared to the unimodal case in section 2.3.3.
The contribution of the collision between the 1^{st} population and 2^{nd} population contribute with two terms. There are the gain term and the loss term.

$$I_{fg\,coll,loss}[f] = \int_0^{2\pi} \mathrm{d}\theta' K(\theta-\theta') f(r,\theta,t) g(r,\theta',t) \tag{2.36a}$$

$$I_{fg\,coll,gain}[f] = \int_0^{2\pi}\int_0^{2\pi} \mathrm{d}\theta_1 \mathrm{d}\theta_2 K(\theta_1-\theta_2) f(r,\theta_1,t) g(r,\theta_2,t) \int_{-\infty}^{+\infty} \mathrm{d}\xi P_\sigma(\xi)\delta_{2\pi}(\Psi(\theta_1,\theta_2)+\xi-\theta) \tag{2.36b}$$

with $\Psi(\theta_1,\theta_2) = \frac{\theta_1+\theta_2}{2}$ the alignment rule and $K(\theta_1-\theta_2)$ the collision kernel. We keep the same kernel as the unimodal case 2.3.3 but the domain of validity is limited to small value of chirality. In fact, the kernel should take into account the chirality value and thus be different for collision between particles belonging to the same population and particles belonging to two different populations. We keep this kernel because it was the simplest choice. Moreover, it allows us to get a good description at the hydrodynamic level.

If we consider the particle distribution function for the second population $g(r,\theta,t)$ it will lead to the same equations with reverse chirality $-\omega_0$.

At the end we get the following Boltzmann equation for the first population

$$\begin{aligned}\frac{\partial f}{\partial t} = -v_0\vec{e}(\theta).\vec{\nabla} f - \omega_0\frac{\partial f}{\partial\theta} + \lambda\left((P_\sigma * f) - f\right) - f\int_0^{2\pi}\mathrm{d}\theta' K(\theta-\theta')\left(f(\theta')+g(\theta')\right) \\ + \iint_0^{2\pi}\mathrm{d}\theta_1\mathrm{d}\theta_2 K(\theta_1-\theta_2) f(\theta_1)\left(f(\theta_2)+g(\theta_2)\right) P_\sigma(\theta-\Psi(\theta_1,\theta_2))\end{aligned} \tag{2.37}$$

It is possible to adimensionalize Eq. (2.37)

$$t\to t/\lambda,\quad \vec{r}\to v_0\vec{r}/\lambda,\quad \omega_0\to\omega_0\lambda,\quad K\to 2d_0v_0K,\quad f\to\frac{\rho_0}{2}f,\quad g\to\frac{\rho_0}{2}g, \tag{2.38}$$

with ρ_0 the global density and $\tilde{\rho_0} = 2d_0v_0\rho_0/\lambda$. Then we take the Fourier transform along the angular coordinate, and it leads to the infinite hierarchy of PDE

$$\frac{\partial f_k}{\partial t} = -\frac{1}{2}\left(\nabla f_{k-1} + \nabla^* f_{k+1}\right) + \omega_0 ikf_k + \left(P_k-1\right)f_k + \sum_{q=-\infty}^{+\infty} J_{k,q} f_{k-q}\left(f_q+g_q\right) \tag{2.39}$$

$$\frac{\partial g_k}{\partial t} = -\frac{1}{2}\left(\nabla g_{k-1} + \nabla^* g_{k+1}\right) - \omega_0 ikg_k + \left(P_k-1\right)g_k + \sum_{q=-\infty}^{+\infty} J_{k,q} g_{k-q}\left(g_q+f_q\right) \tag{2.40}$$

with $J_{k,q} = \tilde{\rho}_0(P_kI_{k,q} - I_{0,q})$ and $I_{k,q}$ given by

$$I_{k,q} = \begin{cases} \frac{4}{\pi}\frac{1-(k-2q)(-1)^q sin(\frac{k\pi}{2})}{1-(k-2q)^2} & \text{if } |k-2q|\neq 1 \\ \frac{2}{\pi} & \text{otherwise.}\end{cases}$$

2.4.3.2 Hydrodynamic equations

To get a closed set of hydrodynamic equations we need a scaling ansatz to apply the Ginzburg-Landau truncation scheme. Thus, if we look at the linear stability of the disorder solution we will see that the first mode to become non-zero will be for $k = 1$. As for the unimodal distribution case the only coherent scaling is

$$f_1 \sim g_1 \sim \varepsilon\,, \quad |f_0 - 1| \sim |g_0 - 1| \sim \varepsilon\,, \quad f_k \sim g_k \sim \epsilon^k \;\forall\; k > 0, \quad \partial_t \sim \nabla \sim \varepsilon\,. \tag{2.41}$$

Then if we limit the expansion to order ϵ^2 for the mode $k = 2$ it is possible to slave f_2 and g_2 to f_1, and g_1 only.

$$f_2 = -2\nu\nabla f_1 + \frac{1}{2\chi}\nabla g_1 + 4\nu J_{2,1} f_1^2 - \frac{J_{2,1}}{2\chi} g_1^2 + J_{2,1}(4\nu - \frac{1}{\chi}) f_1 g_1 \tag{2.42}$$

with the new coefficients:

$$\chi = [-\left((P_2 - 1) + 2J_{2,0} + J_{2,2}\right)^2 - 4\omega_0^2 + J_{2,2}^2]/J_{2,2}$$
$$\nu = \frac{1}{4J_{2,2}\chi}\left((P_2 - 1) + 2J_{2,0} + J_{2,2} - 2i\omega_0\right)$$

If we stop the truncation at order ϵ^3 for the mode $k = 1$ and replace the expression of f_2 and g_2 by Eq. (2.42), we get the following hydrodynamic equation

$$\begin{aligned}\frac{\partial f_1}{\partial t} = &-\frac{1}{2}\nabla\rho + \left[(\mu_1[f_0, g_0] + i\omega_0) - \xi|f_1|^2\right] f_1 + \nu\Delta f_1 - \kappa_2 f_1^*\nabla f_1 - \frac{\kappa_1}{2}\nabla^* f_1^2 \\ &+ \left[\tilde{\mu}[f_0] - \tilde{\xi}|g_1|^2\right] g_1 + \tilde{\nu}\Delta g_1 - \tilde{\kappa}_2 g_1^*\nabla g_1 - \frac{\tilde{\kappa}_1}{2}\nabla^* g_1^2 \\ &+ \gamma_1|g_1|^2 f_1 + \gamma_2 f_1^* g_1^2 + \tilde{\gamma}_1|f_1|^2 g_1 + \tilde{\gamma}_2 g_1^* f_1^2 + \delta_1\nabla^*(f_1 g_1) + \delta_2 f_1^*\nabla g_1 + \tilde{\delta}_2 g_1^*\nabla f_1 \end{aligned} \tag{2.43a}$$

$$\partial_t g_1 = ... \tag{2.43b}$$

$$\partial_t f_0 = -\frac{1}{2}(\nabla^* f_1 + \nabla f_1^*) \tag{2.43c}$$

$$\partial_g g_0 = -\frac{1}{2}(\nabla^* g_1 + \nabla g_1^*) \tag{2.43d}$$

with the coefficients defined in the appendix A.4.
The first line of Eq. (2.43a) corresponds to the BGL hydrodynamic equations for the standard Vicsek model, and it is the evolution of the polarization due to the first population. The second line of this equation has also the form of a standard Toner-Tu equation without the pressure term and corresponds to the evolution due to the second population. The last line gathers the terms coupling f_1 and g_1. To get the temporal evolution of g_1, one should take Eq. (2.43a) and exchange $f_1 \leftrightarrow g_1$ and take the complex conjugate of all the coefficients. The two last equations Eq. (2.43c) and (2.43d) are the exact conservation laws.

2.4.3.3 Homogeneous stationary equations

We are looking for the homogeneous stationary solution of Eq. (2.43). So we neglect all gradients terms and the temporal derivative. It leads to a system of six coupled equations (after expanding into real and imaginary part)

$$\partial_t f_0 = 0 \tag{2.44a}$$

$$\partial_t g_0 = 0 \tag{2.44b}$$

$$\begin{aligned}\frac{\partial f_1}{\partial t} = 0 = \mu_1[f_0, g_0]f_1 + i\omega_0 f_1 - \xi f_1|f_1|^2 + \tilde{\mu}[f_0]g_1 \\ + \gamma_2 f_1^* g_1^2 + \tilde{\gamma}_2 g_1^* f_1^2 + \tilde{\gamma}_1|f_1|^2 g_1 - \tilde{\xi} g_1|g_1|^2 + \gamma_1|g_1|^2 f_1\end{aligned} \tag{2.44c}$$

$$\frac{\partial g_1}{\partial t} = ... \tag{2.44d}$$

The first trivial solution is $f_0 = cst = g_0 = 1$ and $f_1 = g_1 = 0$.
Then we look for a solution with $f_0 = cst = g_0 = 1$ and $f_1 = P$ and $g_1 = Pe^{i\Omega}$ which correspond to the microscopic solution for the liquid phase. Then we replace in Eq. (2.44c) and we get a new equation which can be written formally

$$0 = P^2 * B + A \tag{2.45}$$

It is not possible to solve analytically the equation. Then if we use the condition that $P \in \mathbb{R}^+$ we have to solve $\mathfrak{Im}(AB^*) = 0$ and $\mathfrak{Re}(-AB^*) > 0$ to get a value for P. The condition $\mathfrak{Im}(AB^*) = 0$ gives an equation of the form:

$$0 = c_0 + c_1 cos(\Omega) + c_2 cos(2\Omega) + s_1 sin(\Omega) + s_2 sin(2\Omega) \tag{2.46}$$

with the coefficients written in the appendix. We solve these equations numerically in the following part where we perform simulations. However, we know the limit $\Omega \xrightarrow[\omega_0 \to 0]{} 0$. To get an exact expression of Ω for small chirality we can expand at order 1 the equation 2.46. We get

$$\Omega = -\frac{c_0 + c_1 + c_2}{s_1 + 2s_2} \tag{2.47}$$

In Fig. 2.46, we plot the relative error between Eq. (2.47) and the exact expression solved numerically with respect to ω_0. We conclude that the error is very small for the interesting range of ω_0.

To summarize, in this paragraph we have found the existence of two homogeneous stationary solutions. The homogeneous ordered solution corresponds to the microscopic polar liquid and the disordered phase corresponds to the gas phase. Now we will study the stability of these two phases.

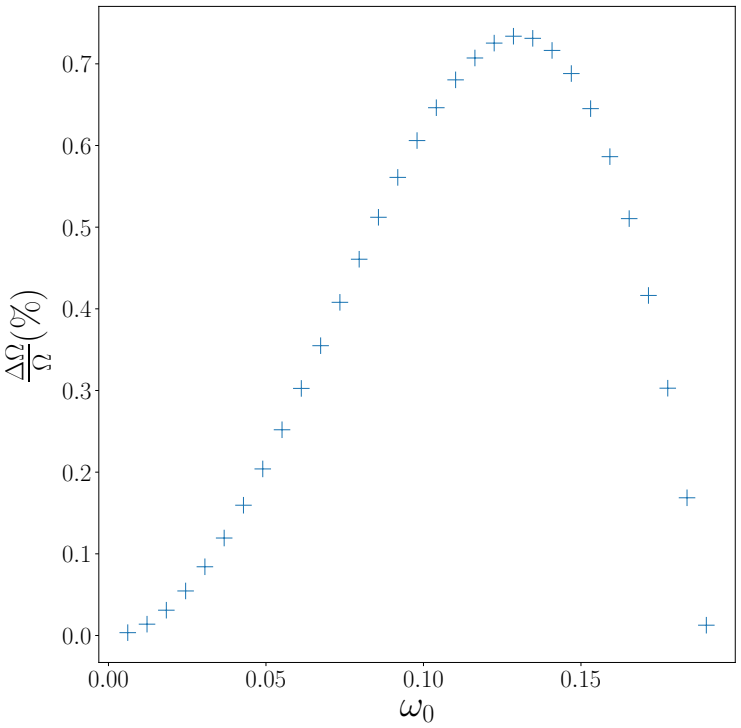

Figure 2.46: Comparison between the exact expression of Ω and the expansion at order one. We plot the relative error in % as a function of the chirality.

2.4.3.4 Linear stabilty of the gas solution

To study the linear stability of the gas solution we perturb this solution as follows

$$f_0 = 1 + \delta f_0 \qquad f_1 = \delta f_1 \tag{2.48a}$$

$$g_0 = 1 + \delta g_0 \qquad g_1 = \delta g_1 \tag{2.48b}$$

We get the new system of equations after removing terms of order ϵ^2

$$\partial_t \delta f_1 = -\frac{1}{2}\nabla\delta\rho + (\mu_1[1,1] + i\omega_0)\delta f_1 + \nu\Delta\delta f_1 + \tilde{\mu}[1]\delta g1 + \tilde{\nu}\Delta\delta g_1 \tag{2.49a}$$

$$\partial_t \delta g_1 = ... \tag{2.49b}$$

$$\partial_t \delta f_0 = -\frac{1}{2}(\nabla^*\delta f_1 + \nabla\delta f_1^*) \tag{2.49c}$$

$$\partial_g \delta g_0 = -\frac{1}{2}(\nabla^*\delta g_1 + \nabla\delta g_1^*) \tag{2.49d}$$

We are interested in the dynamic of a general perturbation, thus we take the Fourier transform of Eq. (2.49) and get a system of equations which can be expressed as a 6x6

matrix. The linear stability is given by the sign of the eigenvalues of the following matrix.

$$\begin{pmatrix} 0 & -iq_x & -iq_y & 0 & 0 & 0 \\ -\frac{i}{2}q_x & \mu_1[1,1]-\Re(\nu)q^2 & -\omega_0+\Im(\nu)q^2 & 0 & \tilde{\mu}[1]-\tilde{\nu}q^2 & 0 \\ -\frac{i}{2}q_y & \omega_0-\Im(\nu)q^2 & \mu_1[1,1]-\Re(\nu)q^2 & 0 & 0 & \tilde{\mu}[1]-\tilde{\nu}q^2 \\ 0 & 0 & 0 & 0 & -iq_x & -iq_y \\ 0 & \tilde{\mu}[1]-\tilde{\nu}q^2 & 0 & -\frac{i}{2}q_x & \mu_1[1,1]-\Re(\nu)q^2 & \omega_0-\Im(\nu)q^2 \\ 0 & 0 & \tilde{\mu}[1]-\tilde{\nu}q^2 & -\frac{i}{2}q_y & -\omega_0+\Im(\nu)q^2 & \mu_1[1,1]-\Re(\nu)q^2 \end{pmatrix} \tag{2.50}$$

We do not try to solve it analytically. So we explore the Fourier space (q_x, q_y) for each value of parameters (D_r, ω_0, ρ_0). The result is the linear stability of the disordered solution is given by the sign of $\mu_1[1,1]$ as for the unimodal distribution.

2.4.3.5 Linear stability of the liquid solution

We will study the linear stability of the liquid solution against a wave like perturbation. We develop around the liquid solution, so we use

$$f_0 = 1 + \delta f_0 \qquad f_1 = P + \delta f_1 \tag{2.51a}$$
$$g_0 = 1 + \delta g_0 \qquad g_1 = Pe^{i\Omega} + \delta g_1 \tag{2.51b}$$

Then we use Eq. (2.51) to replace the expression of f_0, g_0, f_1 and g_1 in Eq. (2.43). We remove terms of order ϵ^2 or higher and we get the following system of equations

$$\partial_t \delta f_{1,x} = C^{\text{BGL}}_{0,0}\delta f_0 + C^{\text{BGL}}_{0,1}\delta g_0 + C^{\text{BGL}}_{0,2}\delta f_{1,x} + C^{\text{BGL}}_{0,3}\delta f_{1,y} + C^{\text{BGL}}_{0,4}\delta g_{1,x} + C^{\text{BGL}}_{0,5}\delta g_{1,y} \tag{2.52a}$$
$$\partial_t \delta f_{1,y} = C^{\text{BGL}}_{1,0}\delta f_0 + C^{\text{BGL}}_{1,1}\delta g_0 + C^{\text{BGL}}_{1,2}\delta f_{1,x} + C^{\text{BGL}}_{1,3}\delta f_{1,y} + C^{\text{BGL}}_{1,4}\delta g_{1,x} + C^{\text{BGL}}_{1,5}\delta g_{1,y} \tag{2.52b}$$
$$\partial_t \delta g_{1,x} = C^{\text{BGL}}_{2,0}\delta f_0 + C^{\text{BGL}}_{2,1}\delta g_0 + C^{\text{BGL}}_{2,2}\delta f_{1,x} + C^{\text{BGL}}_{2,3}\delta f_{1,y} + C^{\text{BGL}}_{2,4}\delta g_{1,x} + C^{\text{BGL}}_{2,5}\delta g_{1,y} \tag{2.52c}$$
$$\partial_t \delta g_{1,y} = C^{\text{BGL}}_{3,0}\delta f_0 + C^{\text{BGL}}_{3,1}\delta g_0 + C^{\text{BGL}}_{3,2}\delta f_{1,x} + C^{\text{BGL}}_{3,3}\delta f_{1,y} + C^{\text{BGL}}_{3,4}\delta g_{1,x} + C^{\text{BGL}}_{3,5}\delta g_{1,y} \tag{2.52d}$$

where the coefficients are expressed in appendix A.5.

The first step is to compute numerically the domain of existence of the liquid solution. Then to study the stability we take the Fourier transform of Eq. (2.52), and for each set of parameters we scan the Fourier space to determine the highest eigenvalue, so the stability of the solution.

We represent the result in Fig. 2.47. We see in this figure that the liquid solution is unstable everywhere. In this figure we can see clearly the link with the linear stability of the liquid phase in the Vicsek model, see Fig. 1.4. Indeed, for $D_r > 0.45$ and zero chirality the growth rate is already non-zero value and the direction of the instability is along the polarization direction as for the band instability of the standard Vicsek model.

For $0.37 < D_r < 0.45$ and zero chirality value the growth rate is starting from zero and it increases when we increase the chirality value.
For $D_r < 0.37$ and zero chirality value the growth rate is already positive, it correspond to the spurious instability.

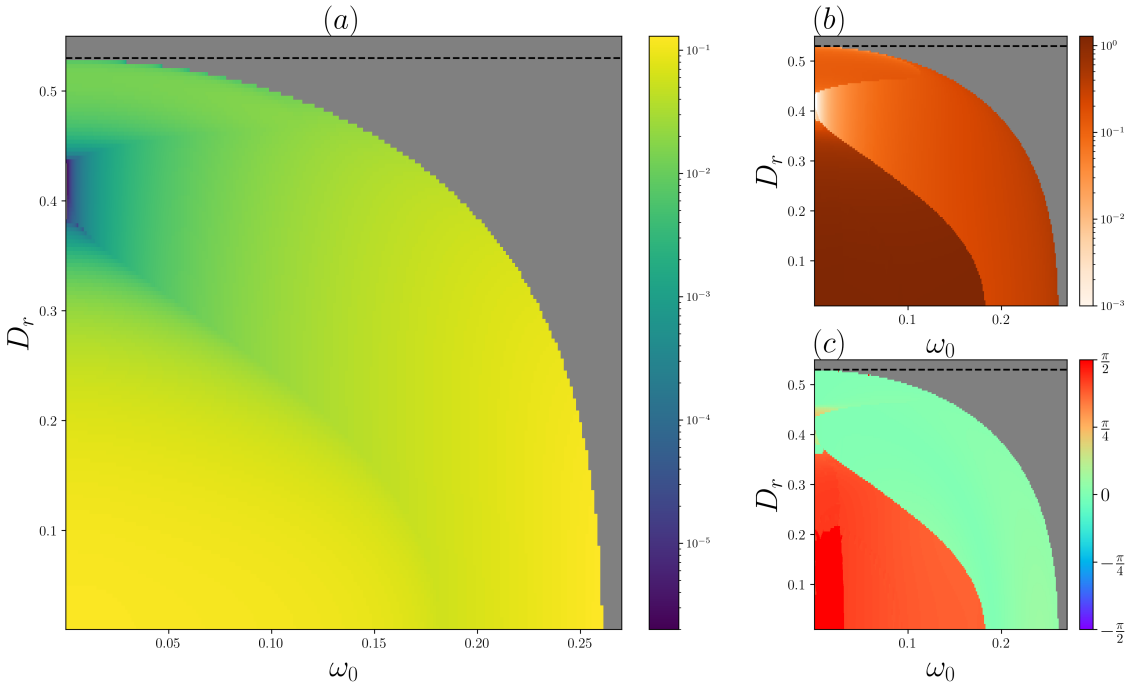

Figure 2.47: Linear stability study in the plane (D_r, ω_0) with $\rho_0 = 0.5$, $\kappa = 1.0$ and $D_0 = 0.0$. The grey part is where the liquid solution is not defined. The black dashed line is the limit of stability of the disordered solution. (a): Highest eigenvalue of the Fourier space. (b): Modulus of the eigenvector attached to the highest eigenvalue of the panel (a). (c): Direction of the eigenvector attached to the highest eigenvalue of the panel (a). The figure shows that the polar liquid is unstable everywhere without diffusion.

In the introduction we show that it is possible to take into account an additional diffusion to remove the spurious instability, so we also study the previous equations with $\nu\Delta f_k \to (\nu + D_0)\Delta f_k$. In Fig. 2.48, we plot the linear stability in the same plane as Fig. 2.47 but with $D_0 = 0.5$. We see that the region for $D_r > 0.45$ is not affected, the growth rate is already positive for zero chirality values. The region for $D_r < 0.37$ is strongly affected because the growth rate start from zero for zero chirality value now. There is also a change in the direction of the most unstable vector, in Fig. 2.47 the spurious instability is perpendicular to the polarization direction and now it leaves room to two modes, one along the perpendicular direction and the other one along a direction of $\frac{\pi}{4}$. In Fig. 2.47

we have found that the liquid solution is unstable everywhere but even after removing the spurious instability the liquid solution is still unstable everywhere.

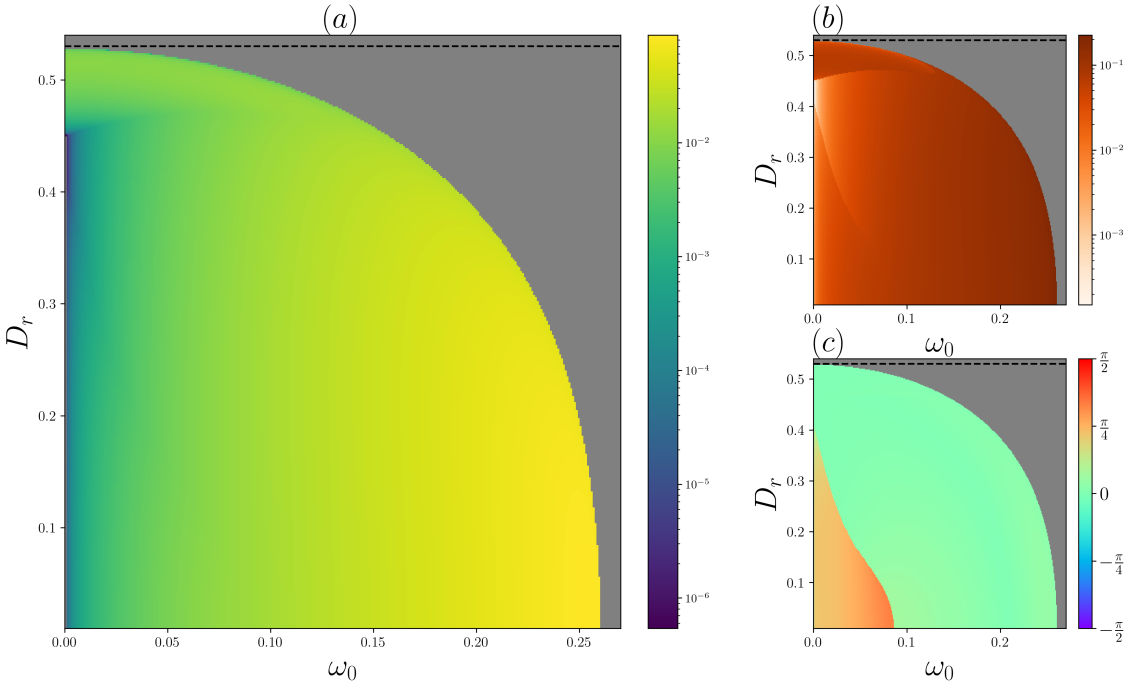

Figure 2.48: Linear stability study in the plane (D_r, ω_0) with $\rho_0 = 0.5$, $\kappa = 1.0$ and $D_0 = 0.5$. The grey part is where the liquid solution is not defined. The balck dashed line is the limit of stability of the disordered solution. (a): Highest eigenvalue of the Fourier space. (b): Modulus of the eigenvector attached to the highest eigenvalue of panel (a). (c): Direction of the eigenvector attached to the highest eigenvalue of panel (a). The figure shows that the polar liquide is unstable everywhere even with an additional diffusion.

In the Fokker-Planck approach, we have found marginal stability region when we work in the plane (ρ_0,ω_0). So in Fig. 2.49, we plot the linear stability with diffusion in the plane (ρ_0, ω_0). We found that the growth rate starts at zero value for zero chirality value and becomes positive when we increase the chirality.

2.4.3.6 Finite size effects at the linear level

In section 2.4.1.2, we have performed a numerical study of the finite-size effects. We have plotted the evolution of the transition line between bands and vortices as a function of the system size. We have seen that the polar liquid is stable at finite-size, but the value where the transition occurs decreases as a power law with the size of the system. We will

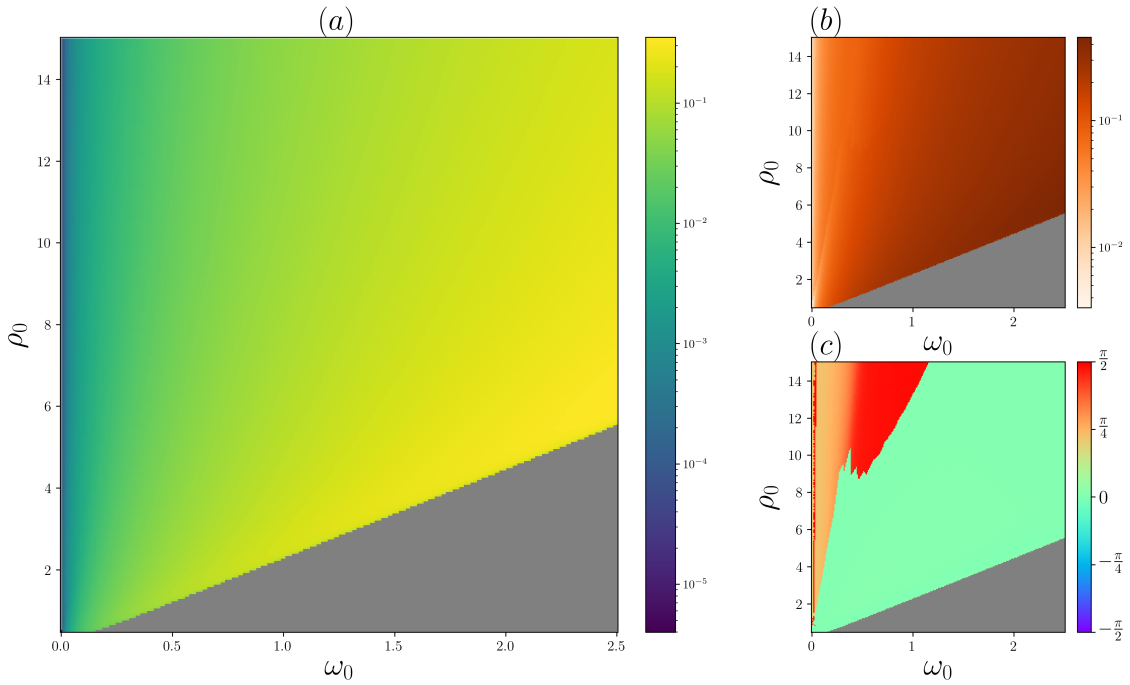

Figure 2.49: Linear stability study in the plane (ρ_0, ω_0) with $D_r = 0.45$, $\kappa = 1.0$ and $D_0 = 0.5$. The grey part is where the liquid solution is not defined. (a): Highest eigenvalue of the Fourier space. (b): Modulus of the eigenvector attached to the highest eigenvalue of panel (a). (c): Direction of the eigenvector attached to the highest eigenvalue of panel (a). The figure shows that the polar liquid is unstable everywhere even with an additional diffusion.

try to understand this result thanks to the linear stability of the liquid solution presented in the previous section 2.4.3.5.
To study the linear stability of the liquid solution we study the sign of the eigenvalue whatever is the modulus of the eigenvector attached to it. This point is equivalent to study infinite system size limit because we do not care about the size needed to get the instability pattern. Thus, to check the stability, we keep the mode with the highest eigenvalue in the Fourier space.
Here, we are looking for a positive eigenvalue with the highest modulus. The liquid phase is unstable at the linear level, but we are working with finite system size. The instability will develop only if the wavelength is smaller than the system size. So we have recorded the value of the unstable mode with the highest modulus $q^\dagger$ as a function of the chirality with the other parameters fixed in Fig. 2.50.

In Fig. 2.50 we see that the value attached to $q^\dagger$ decreases as a power law with $\omega_0 \sim L^{\dagger - \alpha^\dagger}$

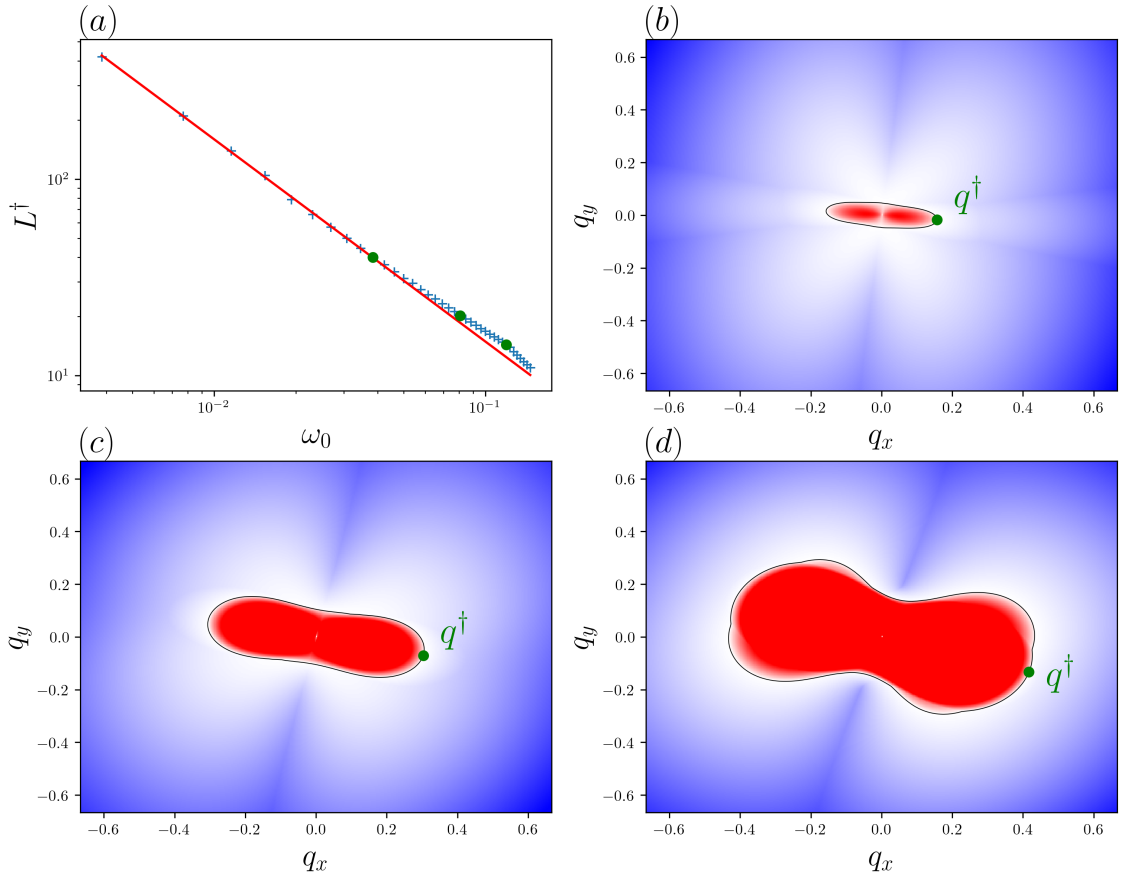

Figure 2.50: Finite-size effects study with parameters $D_0 = 0.5$, $\rho_0 = 0.5$, $\kappa = 1.0$, $D_r = 0.4$. (a): System size $L^\dagger$ needed to observe the instability as a function of the chirality. The green dots are (b,c,d) in the Fourier space. The linear regression gives: -1.002 ± 0.001 with a correlation coefficient $r^2 = 0.999$ (b): Fourier space for $\omega_0 = 0.03846$ with a characterization of $q^\dagger$. (c): Fourier space for $\omega_0 = 0.08077$. (d): Fourier space for $\omega_0 = 0.11923$. The direction of the unstable mode is tilted because the $q_x = 0$ direction corresponds to the polarization direction of the f population, the global polarization has an angle $-\frac{\Omega}{2}$ with the q_x direction. The figure shows that the hydrodynamic description allows us to get a qualitative agreement with the finite size effects at the microscipic level.

with $\alpha^\dagger \approx 1$. First, we find that the value of ω_0 at the transition decreases as a power law, like the result at the microscopic level. However, the exponent is different from the result at the microscopic level. The difference of exponent could be due to non-linear effects or due to the Ginzburg-Landau truncation scheme.

2.4.4 Simulations of the hydrodynamic equations

In this section, we will perform the numerical study of Eq. (2.43). In the previous section, we have studied this equation at the linear level, but now we are insterested in the non-linear solutions of the equations.

Numerical setup

We perform the numerical simulation of Eq. (2.43) by using an Euler integration with $\Delta t \sim 10^{-3}$ and $\mathrm{d}x$, $dy \in [0.125, 0.25]$ and we use a spectral method to compute the derivative terms. As we have seen with the linear stability, for low value of noise there is a spurious instability. Thus, when we perform numerical simulation for low noise we get weird patterns with negative density, which is physically impossible. To regularize the spurious instability we add an extra diffusion, as presented for the linear stability in Sec. 2.4.3.5. So, we will always work with an additional diffusion, $\nu\Delta f_k \to (\nu + D_0)\Delta f_k$, in Eq. (2.43). The microscopic model defined for the coarse graining already generate effective diffusion due to the discretization and the angular noise.

Overview of observed phase

We have explored the phase space, and we have identified four different phases. In this paragraph, we will give an overview of the four phases.

The first phase that we call bands is the standard Band phase in the limit of $\omega_0 = 0$, see Fig. 2.51. In this phase, we get the standard band shape for the density field but inside the band, each population has a different polarization. The population with a positive chirality has a polarization that forms a positive angle with the global polarization inside the band phase. The population with a negative chirality has a polarization that forms a negative angle with the global polarization inside the band phase.

The second phase is called Liquid and is the standard liquid phase in the limit $\omega_0 = 0$. In this phase, we get a homogeneous density field for each population. The polarization field between each population is different and form an angle Ω.

The third new phase is the vortex phase and it shows vortices with an elongated shape in one direction but when we increase the value of D_0 this shape regularizes. In this phase we see segregation between the population with a positive chirality and the population with a negative chirality as for the microscopic simulations, see Fig 2.52.

The last phase is called the rotating packets phase and it shows packets for each population and the segregation between the two populations hold, see Fig. 2.53. In the rotating

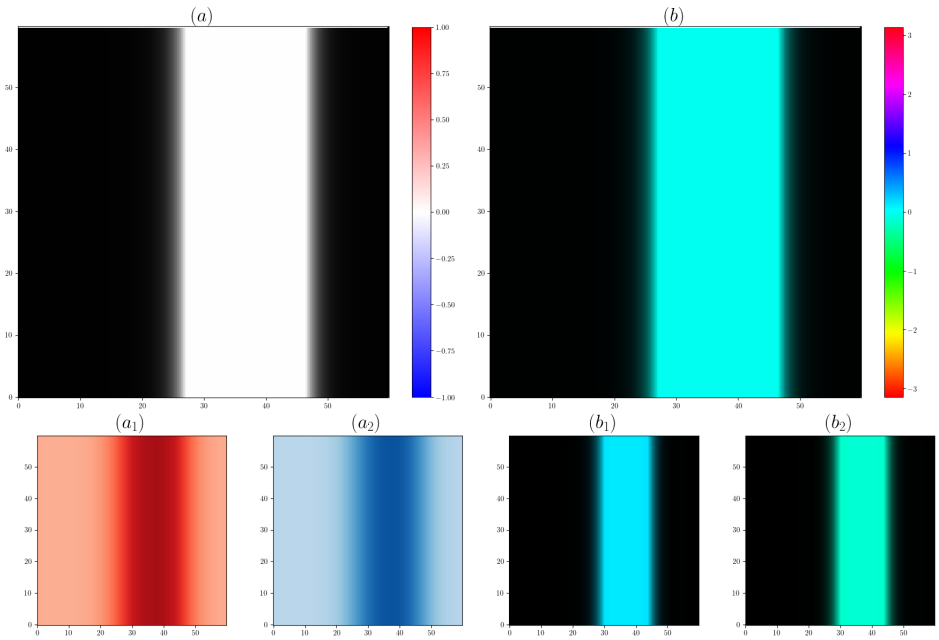

Figure 2.51: Simulation of the hydrodynamic equation for a bimodal distribution. Typical snapshot of the band phase for $\rho_0 = 0.5$, $\omega_0 = 0.0$ with $D_r = 0.4$, $\kappa = 1.0$ and $D_0 = 0.5$. (a): Chirality of the two populations. (b): Local direction of the polarization $Arg(\vec{p})$. (a_1): Density of the population with a positive chirality (a_2): Density of the population with negative chirality. (b_1): Local direction of polarization for the population with a positive chirality, (b_2): Local direction of the polarization for the population with a negative chirality. The symmetry axis of the eigenvalues is doing an angle with the x-direction because the x-direction is the direction along the polarization of the first population f_1. The figure shows the difference in polarization between the two populations inside the band.

packets phase, we see homogeneous packets in density and almost homogeneous in direction of the local polarization vector which is rotating in time. If one looks carefully at the figure we can see the position of the center of rotation which is on the boundary of each packet.

Phase diagram of the hydrodynamic equations

We plot the phase diagram in the plane (D_r, ω_0) to be able to compare it with the microscopic phase diagram of the KVM. In Fig. 2.54 we plot the phase diagram, for large values of noise we get a disordered phase. Then when we reduce the noise value at low chirality we start to see the band. As mentioned earlier, for $\omega_0 = 0$ we get the standard band but when we increase the chirality the two populations start to have different values of polarization angle, this point could be seen on the snapshot of Fig. 2.51. This property

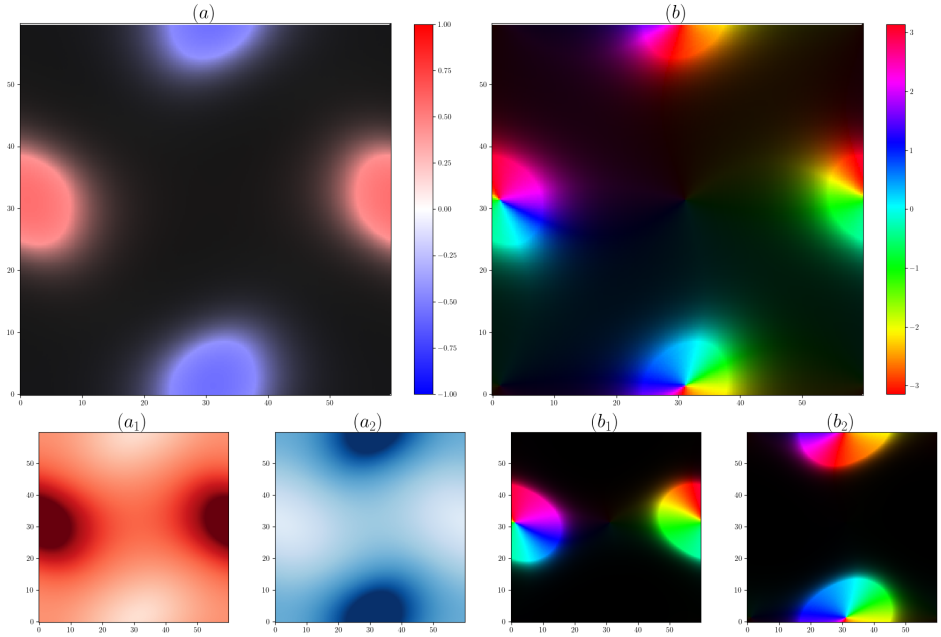

Figure 2.52: Simulation of the hydrodynamic equation for a bimodal distribution. Typical snapshot of the vortex phase for $\rho_0 = 0.5$, $\omega_0 = 0.10$ with $D_r = 0.4$, $\kappa = 1.0$ and $D_0 = 0.5$. (a): Chirality of the two populations. (b): Local direction of the polarization $Arg(\vec{p})$. (a_1): Density of the population with a positive chirality (a_2): Density of the population with negative chirality. (b_1): Local direction of polarization for the population with a positive chirality, (b_2): Local direction of the polarization for the population with a negative chirality. The figure shows the vortex pattern and the segregation between particles with positive and negative chirality.

is shared with the microscopic model. Then for larger values of chirality, we see the vortex phase. In that case, there is always a coexistence between bands and vortices but for $D_0 = 0$ there is a part of the phase diagram where there are only vortices. If one continues to increase the chirality value the vortices move on to rotating packets.

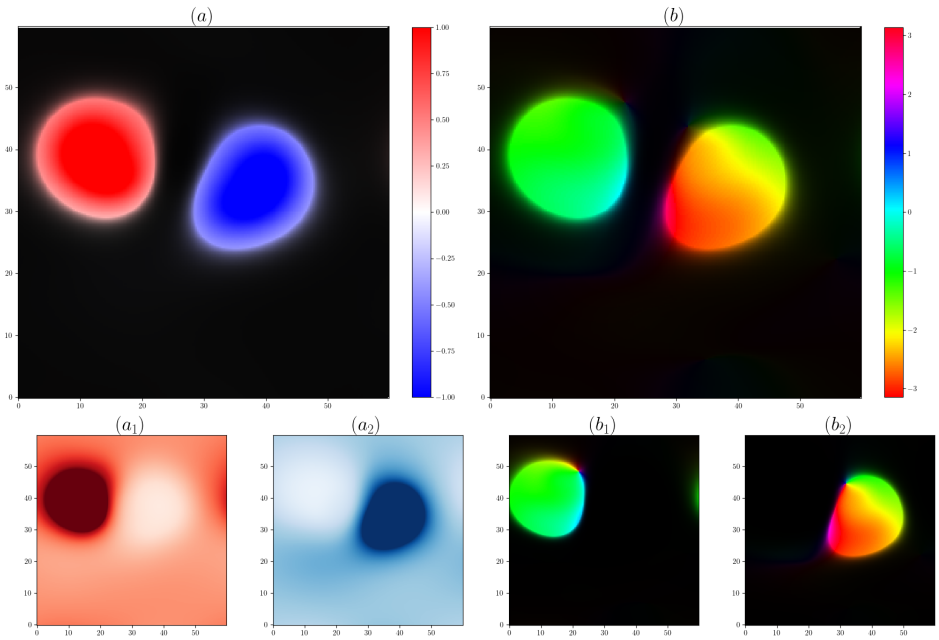

Figure 2.53: Simulation of the hydrodynamic equation for a bimodal distribution. Typical snapshot of the rotating packets phase for $\rho_0 = 0.5$, $\omega_0 = 0.30$ with $D_r = 0.4$, $\kappa = 1.0$ and $D_0 = 0.5$. (a): Chirality of the two populations. (b): Local direction of the polarization $Arg(\vec{p})$. (a_1): Density of the population with a positive chirality (a_2): Density of the population with negative chirality. (b_1): Local direction of polarization for the population with a positive chirality, (b_2): Local direction of the polarization for the population with a negative chirality. The figure shows the rotating packets pattern and the segregation between particles with a positive and negative chirality.

For low values of noise and low values of chirality, we can see the rotating liquid which should disappear in the limit of infinite system size according to the linear study. Here, we see that the domain of existence of the polar liquid goes above the red dashed line but this point will be commented in the next paragraph. Then for larger values of chirality, we have found the rotating packets phase.

Link between the phase diagram and the linear stability

Here we will first remind the reader of the difference between a spinodal curve and a binodal curve. The spinodal curve is the limit between the region where the solution is stable and where it is not. However, it does not mean that the spinodal curve is corresponding to the line of the transition. The binodal curve is delimiting the existence of the coexistence region.

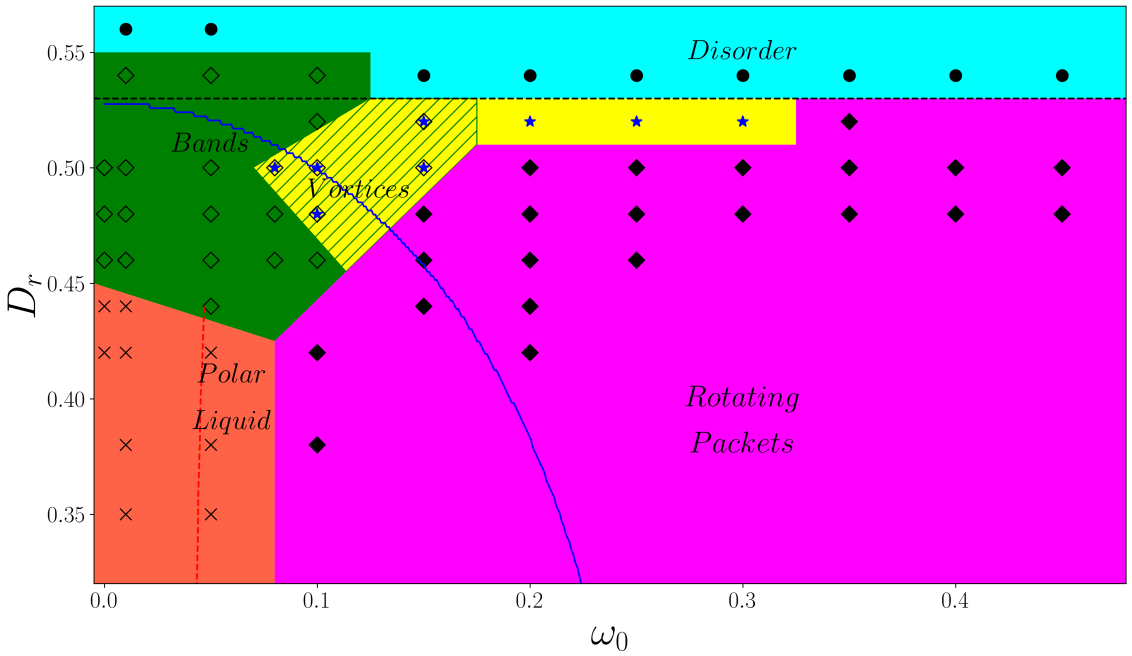

Figure 2.54: Phase diagram of the hydrodynamic equations for a bimodal distribution of chirality in the plane (D_r, ω_0), with parameters $\rho_0 = 0.5$, $\kappa = 1.0$, $L = 64$ and $D_0 = 0.5$. The black dashed line is the limit of the linear stability of the disordered homogeneous solution. The red dashed line is the ω_0 value attached to $q^\dagger$ for $L = 64$. The blue line is the analytical limit of existence for the homogeneous ordered solution. The figure shows the qualitative agreement between the phase diagram at the hydrodynamic level and the phase diagram at the microscopic level.

If one compares the phase diagram obtained at the hydrodynamic level with the one obtained at the microscopic level, we see a qualitative agreement because all the phases are present in both and the relative position of the phase is respected. Now we can compare the difference between the linear study and the non-linear study of equations Eq. (2.43). To do this we plot the linear stability with the phase diagram attached to hydrodynamic equations in Fig. 2.55. Moreover, we add the linear stability of the homogeneous disorder with a dashed black line and the red dashed limit line is where we expect finite-size effects thanks to the study at the linear level. First, if we look at the polar liquid phase we see that it corresponds to a small wavevector but we are able to see the polar liquid phase for larger ω_0 than expected by the study of $q^\dagger$. Then, we see the wavevector corresponding to the band instability. The domain of bands, which is the coexistence phase, is delimited by the bimodal curve which is at a higher value of noise than the spinodal curve, see the blue line in Fig 2.54. The maximum chirality value where we can see bands and polar liquid are close probably because bands could be seen as a polar liquid phase in the middle, if

this solution is no more defined it means the bands will break. For larger chirality, the vortex phase straddles the domain of existence of the polar liquid solution and outside. The rest of the phase space is occupied by rotating packets but it is not possible to explain the transition between vortices into rotating packets with our study.

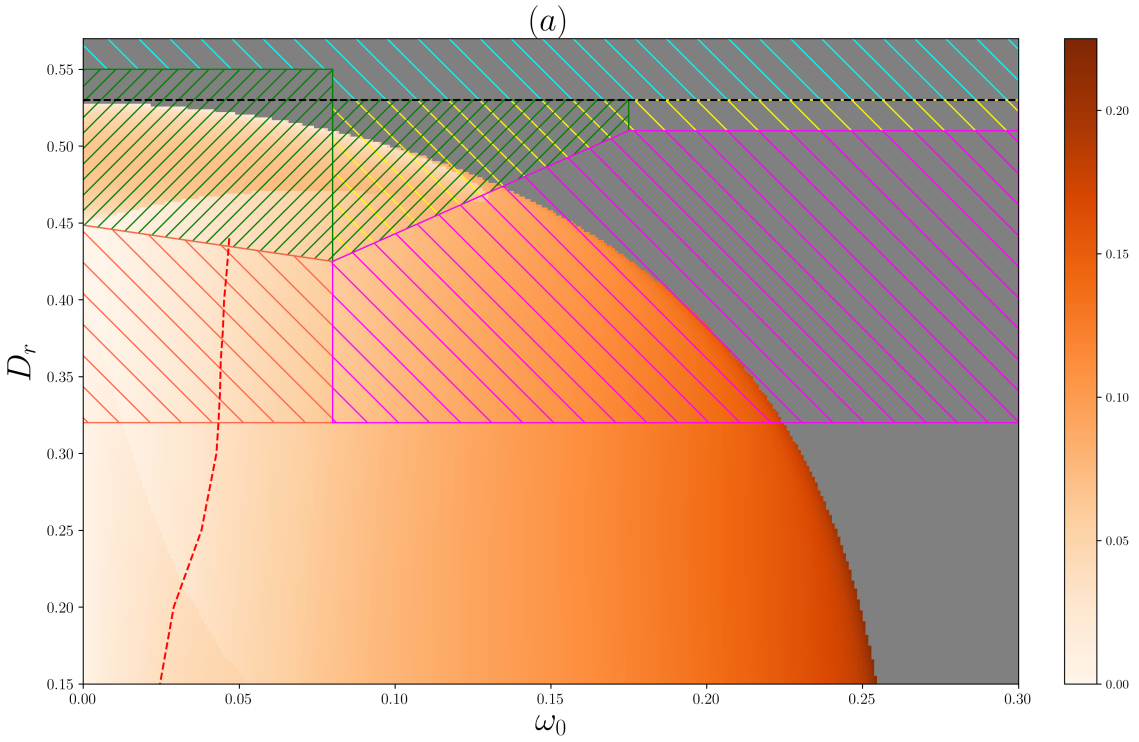

Figure 2.55: Comparison between the linear stability and the phase diagram from the hydrodynamic equations. Modulus of the most unstable wavevector in the plane (D_r, ω_0) with parameters $\rho_0 = 0.5$, $\kappa = 1.0$ and $D_0 = 0.5$. The black dashed line is corresponding to the linear stability of the homogeneous disordered phase. The red dashed line is corresponding the ω_0 attached to $q^\dagger$ for $L = 64$. We add the phase diagram at the hydrodynamic level with the same colormap as Fig. 2.54. The figure shows the link between the band phase and the instability. We see also the link between the existence domain of the polar liquid phase and the finite-size effects.

2.4.5 Conclusion

We have studied the KVM for a bimodal distribution of chirality through microscopic simulations and hydrodynamic equations obtained by the coarse-graining of a microscopic model. The numerical simulations at the microscopic level show two new phases which are called vortex phase and rotating packets phase. Also, the liquid phase, which is the

phase where particles are fully synchronized, disappears in the asymptotic limit of infinite system size. Thus, the chirality disorder breaks the synchronization in 2D.
Then we build two sets of hydrodynamic equations, the first one is based on a Fokker-Planck equation. This model allows finding the two homogeneous solutions seen at the microscopic level. Moreover, the linear stability shows that the liquid solution is unstable except in a marginal part of the phase space. The second set of hydrodynamic equations is based on the Boltzmann equation. It provides the two homogeneous solutions observed at the microscopic level too. In that case, the linear stability shows that the liquid solution is unstable everywhere and it helps to understand the finite size effect even if the scaling exponent is different from the microscopic one.
In the last part, we explore the hydrodynamic equations based on the Boltzmann equation at the non-linear level thanks to numerical simulations. So, we can find the two other phases which are the vortex phase and the rotating packet phase. Furthermore, the phase diagram obtained at the hydrodynamic level is qualitatively in agreement with the one obtained at the microscopic level. So we can conclude that the Boltzmann approach provides a good framework to understand the KVM model for a bimodal distribution of chirality.

2.5 Position of our results in the litterature

In the introduction, we have presented the framework for DADAM and the Kuramoto model. Due to the rise of interest in chiral active matter, other people have studied models close to the KVM. Here we provide a detailed description of their results and how it is possible to interpret their conclusion with regards to our results. Thus we will mainly focus on the work from Denk et al [96], the work from Levis and Liebchen [52, 66, 67], and the work from Liao and Klapp [107].

J. Denk et al., "Active Curved Polymers form Vortex Patterns on Membranes", Physical Review Letters 116, 178301 (2016)

The first work is the paper from Denk et al [96]. In this paper, they have studied the pattern formation for curved polymer in 2D where each polymer is described as an inextensible wormlike chain of length L and intrinsic curvature κ_0. The polymers are propelled with a tangential velocity and the interaction is given by a repulsive truncated Lennard-Jones potential and each polymer has the possibility to bend. The first step was to perform Brownian dynamics simulations. This allows them to draw a phase diagram in the plane (density, noise). At fixed noise, when they increase the density, they observe a phase transition from a gas state at low-density values to a vortex state for an intermediate value of density and a trains state where the curved polymer form a cluster that travels in an irregular fashion. To model these simulations they consider a microscopic model similar to the one describe in the section about the unimodal distribution of chirality, see Sec. 2.3.3. Then they follow the same BGL approach to get the same set of hydrodynamic

equations as Eq. (2.18). They use these hydrodynamic equations to compute the homogeneous rotating ordered phase. Moreover, they have simulated the Boltzmann equation and found rotating spots of high density, aka polar rotating packets (see Fig. 2.56 panel (c)). Then they have performed the linear stability analysis of the homogeneous rotating ordered solution at the Boltzmann level and in the rotating frame. They found that the homogeneous ordered solution expressed in the rotating frame is unstable at the onset of the transition line between disordered phase and ordered phase but stable far from this transition line (see Fig. 2.56 panel (b)). Moreover, they draw a phase diagram of this model by solving the Boltzmann equation numerically and found that when the homogeneous ordered phase is unstable it lets place to a phase of swirls which are callled polar rotating packets in this manuscript (see Fig. 2.56 panel (a)). These results are important because I have studied the same hydrodynamic equations with Eq. (2.18) but I have not done the same work because I mainly work at the hydrodynamic level while they have performed their study at the Boltzmann level. Thus the comparison is interesting because the only difference is the truncation step.

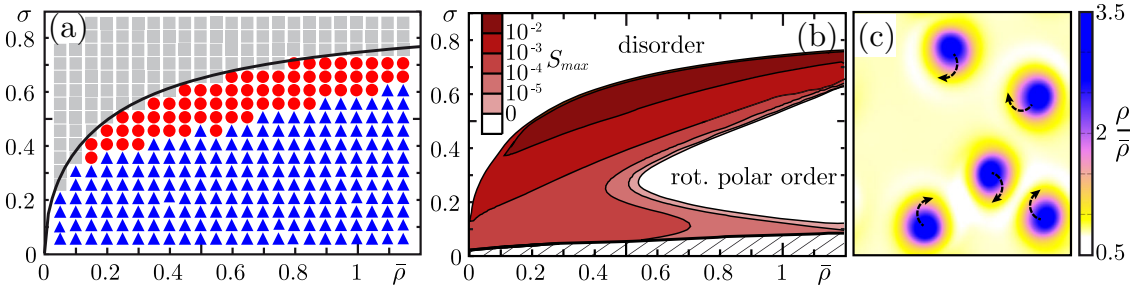

Figure 2.56: Figure taken from [96]. (a) Phase diagram at the Boltzmann level. grey square are disordered states. Red dots are rotating packets. Blue triangle are ordered states.(b) Linear stability of the homogeneous ordered state. (c) Result of a simulation performed at the Boltzmann level in the swirls phase.

First, we compare our microscopic results from section 2.3.1 with the results from Denk et al. [96]. We can also identify the two new phases, despite they were simulating different objects. In particular, they are simulating bend polymers and the interactions between polymers (via repulsion) are totally different from our particles interactions (via ferromagnetic alignment). The first phase is called vortices and the other phase is called train states. Here one can identify their vortex phase with our vortex phase. The second phase which is called train states seems to be badly understood but if we look at the movie referred to in their paper, we can draw some conclusions. In their movie, the particles have a tendency to aggregate together in one big packet but the packet interacts with itmself due to the periodic boundary condition. This first point is the sign of strong finite-size effects. Moreover, the global movement of the aggregate seems to be a rotation. It means that our macrodroplet phase is perhaps similar to their train phase but to make a decision

further studies of finite-size effects in their simulations are needed.
Secondly, they have studied the linear stability of the KVM at the Boltzmann level and they have found a stability area contrary to what we found at the microscopic level and then at the hydrodynamic level. We highlight the point that they have done the linear stability in the rotating frame contrary to us (we should have done a Floquet analysis). Their linear stability results show a region of stability for high density and low noise. In our case, as soon as we add chirality the homogeneous ordered solution becomes unstable. So here we see the first difference. Then, they performed the numerical simulation of the Boltzmann equation and found swirls, this phase corresponds to the vortex phase found in our hydrodynamic simulation. Also, we have found rotating packets for low noise or high chirality value, according to their phase diagram, they have found the homogeneous ordered phase instead. This difference is relevant and calls for further studies because our simulation of hydrodynamic equations are partially in agreement with our microscopic simulation but contradict the results at the Boltzmann level.

With this comparison, we can see that chiral active matter, with a unimodal distribution of chirality, seems to share characteristic features which are not sensitive to the way it is implemented. Moreover, our work seems to catch all the physical phases (vortex and macrodroplet phase) according to the previous comparison. The second point is that finite-size effects play an important role, which is reasonable because, historically, it leads to a controversy in the case of the Vicsek model.

Work from Levis, Liebchen

This work is split into two papers [52, 67]. They have studied a microscopic model which is the KVM but without normalization. So it is a Vicsek model in continuous time limit without normalization of the interaction plus a chirality term. Each particle follows the equations

$$\begin{aligned} \frac{d\vec{r}_i}{dt} &= v_0 \vec{e}(\theta_i) \\ \frac{d\theta_i}{dt} &= \omega_i + \frac{\kappa}{\pi d_0^2} \sum_{j \in B_i} \sin\big(\theta_j - \theta_i\big) + \sqrt{2D_r}\xi_i \end{aligned} \tag{2.53}$$

They have studied the case with a unimodal, bimodal, and Gaussian distribution of chirality. We will distinguish the three cases.

Unimodal distribution of chirality

In that case, there is only one population with a fixed chirality $\omega_i = \omega_0 \quad \forall\, i$ as in section 2.3. They have studied their microscopic model with numerical simulations and analytical approximations. Thus, they have drawn a phase diagram presented in Fig. 2.57 panel (a), the transition line are based on the linear stability approach at the hydrodynamic

level and confirmed by around ten microscopic simulations. In this figure, we see two new phases, the first one is called rotating macrodroplet (see panel (b)) and corresponds to a dense polar domain inside which polarization rotate. The second one is called microflock pattern (see panel (c)) and corresponds to a multitude of small rotating packets with a homogeneous order inside. Then, they use the Fokker-Planck approach to derive hydrodynamic equations, and from them, they have found the two homogeneous solutions. The first homogeneous solution corresponds to the disordered phase and the second homogeneous solution is ordered and rotating in time aka the rotating liquid. They characterize the stability of this periodic solution by performing a standard linear stability analysis instead of the Floquet analysis.

In the paper [52], they have studied the linear stability of the liquid solution of Eq. (2.9) by making strong hypothesis because they set $q_x = 0$ or $q_y = 0$. Then they take $\Omega = 0$ and expand the dispersion relation to second order around respectively $q_y = 0$ and $q_x = 0$. They had found an instability along the polarization direction for $2 < g\rho_0 < 22/7$. Also, they had found an instability perpendicular to the flocking direction for $2 < g\rho_0 < 82/21$. Then, they had taken the limit $\Omega \to 0$ and expand the dispersion relation to second order in Ω and q_y or q_x. In that case, their linear stability analysis shows a short wavelength instability. They have also performed various expansions in the linear stability analysis to plot the red and blue line of their phase diagram in panel (a) of Fig. 2.57. The red line is composed of two parts. The first one is $\Omega > 2\sqrt{\frac{2}{7}}$, which is obtained by the expansion up to order two in q_y and in $g\rho_0$ with $q_x = 0$. The second part is obtained with an expansion to order one in q_y and order three in $g\rho_0$. The blue line is also composed of two parts. The horizontal line is given by $g\rho_0 > 10/3$ which is got with an expansion at order two in Ω and q_x with $q_y = 0$. The other part is obtained by an expansion at order two in q_y and three in $g\rho_0$.

In their paper, they have never shown and commented on the density distribution. To well understand their state, we redo their simulations, and we represent a typical snapshot of their simulations in Fig. 2.58. The left panel shows the polarization and we can distinguish different packets. The right panel shows the density field. If someone looks at the packet in the center with a purple polarization, we can see a strange behavior because this packet is composed of three packets on the density map. If one looks carefully at the work presented in Fig 2.61 panel (c), for a bimodal distribution of chirality, we observe such pathological behavior. Moreover, one can see that the density distribution diverges inside a packet because all the particles are in only one or two cells of our coarse-graining, see right panel Fig 2.58. Here we can add that this pathological condensation is strongly affected by the numerical implementation. Indeed, a backward update rule will lead to denser packets compared to a forward update rule. The finite time-step Δt leads to the introduction of spatial diffusion and in the limit $\Delta t \to 0$ the packets have a tendency to converge to a singular object. It leads to instability when the number of particles is large enough.

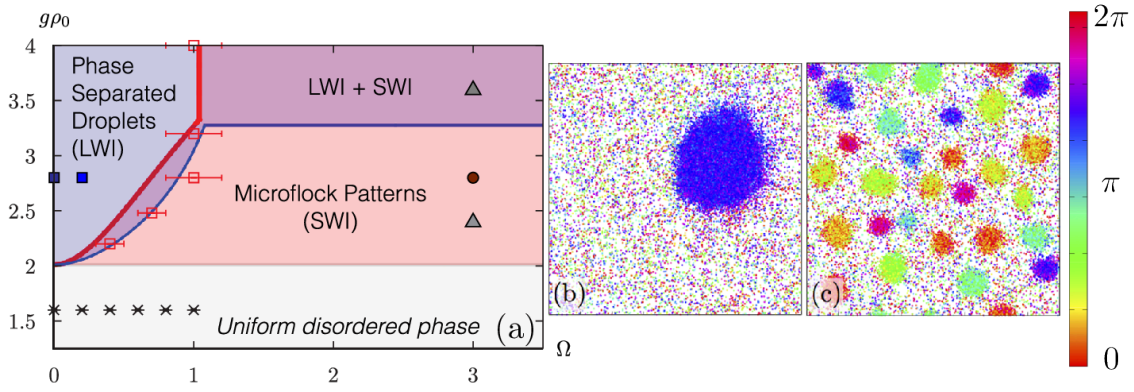

Figure 2.57: Figure taken from [52].(a) Phase diagram from linear stability in the plane (Ω, $g\rho_0$). There are two new phases with a part of the phase diagram where there is coexistence between them. Color in (b) and (c) represent the direction of the polarization for particles. (b) Snapshot of the macrodroplet phase. (c) Snapshot of the microflocks phase.

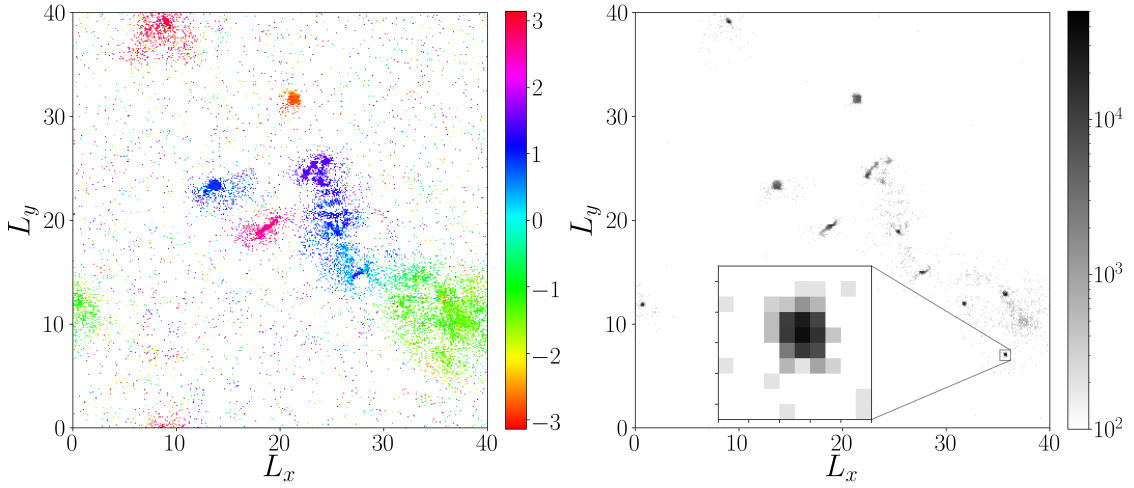

Figure 2.58: Unimodal distribution. Typical snapshot of the simulation based on the model from Levis et al. with parameters $D_r = 0.5$, $\omega_0 = 1.5$, $\kappa = 0.22$, and $\rho_0 = 20$.

We can compare the results from their simulations with our simulations. In that case, the comparison could have been consistent because we study the same kind of particle-based model where the only difference is the normalization in the interaction part of Eq. (1.40). The first new phase is the rotating macrodroplet which is in agreement with our results. The second new phase is rotating packets. At the early stage of our numerical study, we

also found rotating packets, but after exploring the finite-size effects we conclude to an initial condition effect, where the convergence time to reach macrodroplet becomes too long.
How to understand their results? They have done simulations in the dense regime (usually $\rho_0 = 20$) because they want to compare their results with the hydrodynamic theory based on the Fokker-Planck approach which is based on the hypothesis of a dense system. But the problem with the dense regime is, you can not simulate large systems. Thus, they had to deal with strong finite-size effects. Moreover, they choose not to normalize the interaction by the number of neighbors. So it creates a positive feedback loop where the dense packets get a stronger interaction without any upper limit. It leads to pathological behavior. They probably miss the vortex phase due to the finite-size effects, but because simulating systems in their configuration is costly in terms of CPU we do not even try to find the vortex phase. We can also mention the fact that when we increase the density, the area of bands domain decreases for the Vicsek model, so it is harder to find them.

Then we can compare their study of the linear stability of the rotating liquid solution with our numerical study of this linear instability, see Fig. 2.60. In this figure, we plot our full numerical study of the linear stability in panels (a_1 & a_2) and we add the line corresponding to their separation with the same color code as Fig. 2.57 panel (a). Then in panels (b_1 & b_2) we plot the linear stability if we restrict the study to the direction of the polarization ($q_y = 0$). In panels (c_1 & c_2), we restrict the study to the direction perpendicular to the polarization direction, so we set $q_x = 0$. Panels x_1 are corresponding to the growth and panels x_2 are corresponding to the modulus of the wavevector attached to the growth rate of panels x_1, where $x \in \{a, b, c\}$.
First, they have studied the case where $\Omega = 0$ and they claim the existence of a long wavelength instability along the polarization direction if $2 < g\rho_0 < 22/7$. If we look at panel (b_2), there is an instability with a relatively long-wavelength for $2 < g\rho_0 < 22/7$. There is also a long wavelength instability perpendicular to the polarization direction according to panel (c_2). So our numerical results are in agreement with their results at $\Omega = 0$. Then they study the case where $\Omega \neq 0$, they have found the existence of a short wavelength instability and give the line corresponding to this limitation. If we look at our results we do not see any region where there is only a short wavelength instability. However, if we look at panel (c_2) we see a short wavelength instability for $g\rho_0 = 2$ and $\Omega = 0$. The line doing the transition between the region where there is only short wavelength and coexistence between short and long wavelength is corresponding to a change according to panel (b_2), we plot the blue dashed line to indicate these results. Unfortunately, the long wavelength is overwhelming the whole phase plane for large Ω. Our numerical results seem to agree with their results for $\Omega = 0$ but diverging for $\Omega \neq 0$. First, we can question ourselves about the validity of the numerical implementation. However, the difference does not seems to come from numerical mistakes because the code gives good results for $\Omega = 0$ and the results about the Boltzmann approach, which are done with the same code with only different coefficients, are coherent. On the other side, to avoid numerical computation

they have expanded the dispersion relation around $g\rho_0 = 2$ and $q_{x,y} = 0$ which is not true according to the values found numerically.

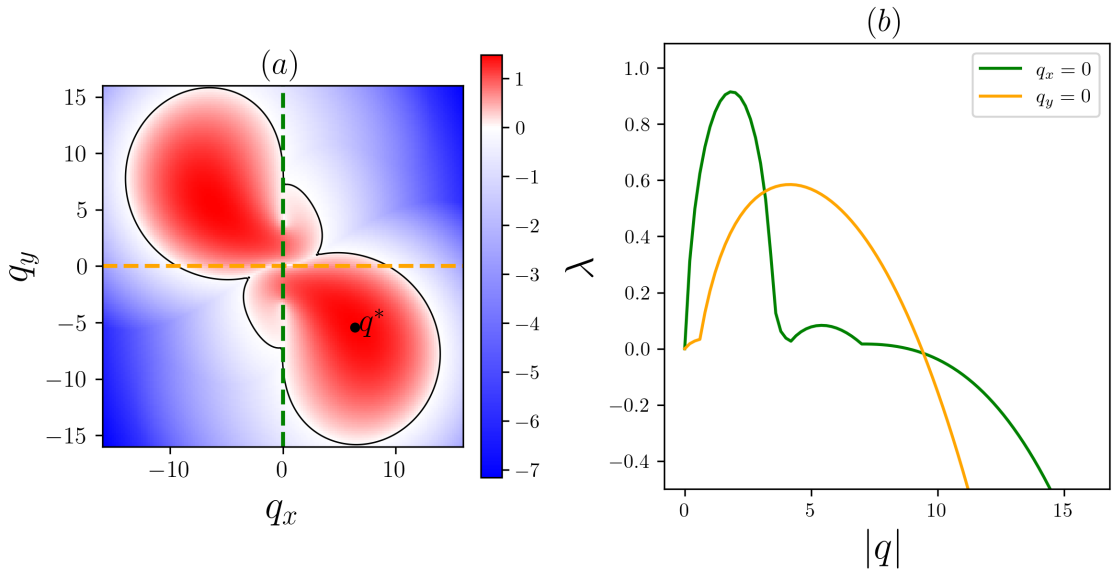

Figure 2.59: Unimodal distribution. Typical snapshot of the Fourier space with parameters $D_r = 0.16$, $\omega_0 = 0.32$, $\kappa = 1.0$, and $\rho_0 = 1.650$. (a) The snapshot of the Fourier space with the most unstable mode pointed. (b) Growth rate as a function of the modulus of the wave vector. The green curve is for an instability perpendicular to the polarization direction. The orange curve is for instability along the polarization direction.

Also, we want to highlight another limitation of the Levis and Liebchen's approach. In Fig. 2.59, we plot the data for a point that is in the coexistence region between short and long wavelength instabilities. In panel (a), we plot the Fourier space attached to this point. In panel (b), we plot the real part of the growth rate as a function of the modulus of the wave vector if we restrict the study to the case $q_x = 0$ & $q_y = 0$. We see an instability along $q_x = 0$ and an instability along $q_y = 0$ according to panel (b). However, if we look at the Fourier space we can see only one unstable mode for a direction around $-\frac{\pi}{4}$, thus the instability along $q_x = 0$ and $q_y = 0$ give a wrong interpretation of the physics. We have seen in Fig. 2.18 that the direction of the most unstable mode is different from $q_x = 0$ or $q_y = 0$ in a wide region of the phase space, thus this argument explains why we expect different results between the Levis and Liebchen approach and the numerical study.

To summarize the comparison about the unimodal distribution of chirality, we have found the vortex phase and we thought that the rotating packets are due to initial conditions contrary to their results. Moreover, their numerical simulations seem to get some trouble

due to the lack of normalization in the interaction rule. Then their linear stability catches only a little part of the linear stability results found with a numerical study.

In the paper [107], Liao and Klapp have written conclusions from the results of Levis and Liebchen. In the light of our new results, we can now read their previous conclusions. First, let me introduce this work, they have studied a model of chiral active matter where the particles are interacting via long-range dipolar interaction instead of the usual short-range ferro-alignment. The particles are subjected to translational self-propulsion and rotational self-propulsion. Thus they are following the same behavior of particles in the KVM with a unimodal distribution of chirality in an empty system. Then, the interaction between particles is composed of two terms. The first term is describing the steric repulsion between particles via a Weeks-Chandler-Andersen potential, while the second term is describing the dipole-dipole interaction. They have found a phase diagram where there are two new phases composed of different types of vortices. It is not possible to distinguish these two types of vortices for polar particles. In the conclusion, they compare their results with those obtained by Levis and Liebchen. In particular, they have said that there are no vortex structures in the case of ferroalignment interaction contrary to dipole-dipole interaction. In the light of our results, it is possible to get vortices structures with a ferroalignment interaction. Dipole-dipole interaction tends to align the dipolar particles, thus, an alignment interaction and a rotational self-propulsion seem to be enough to get the vortex pattern.

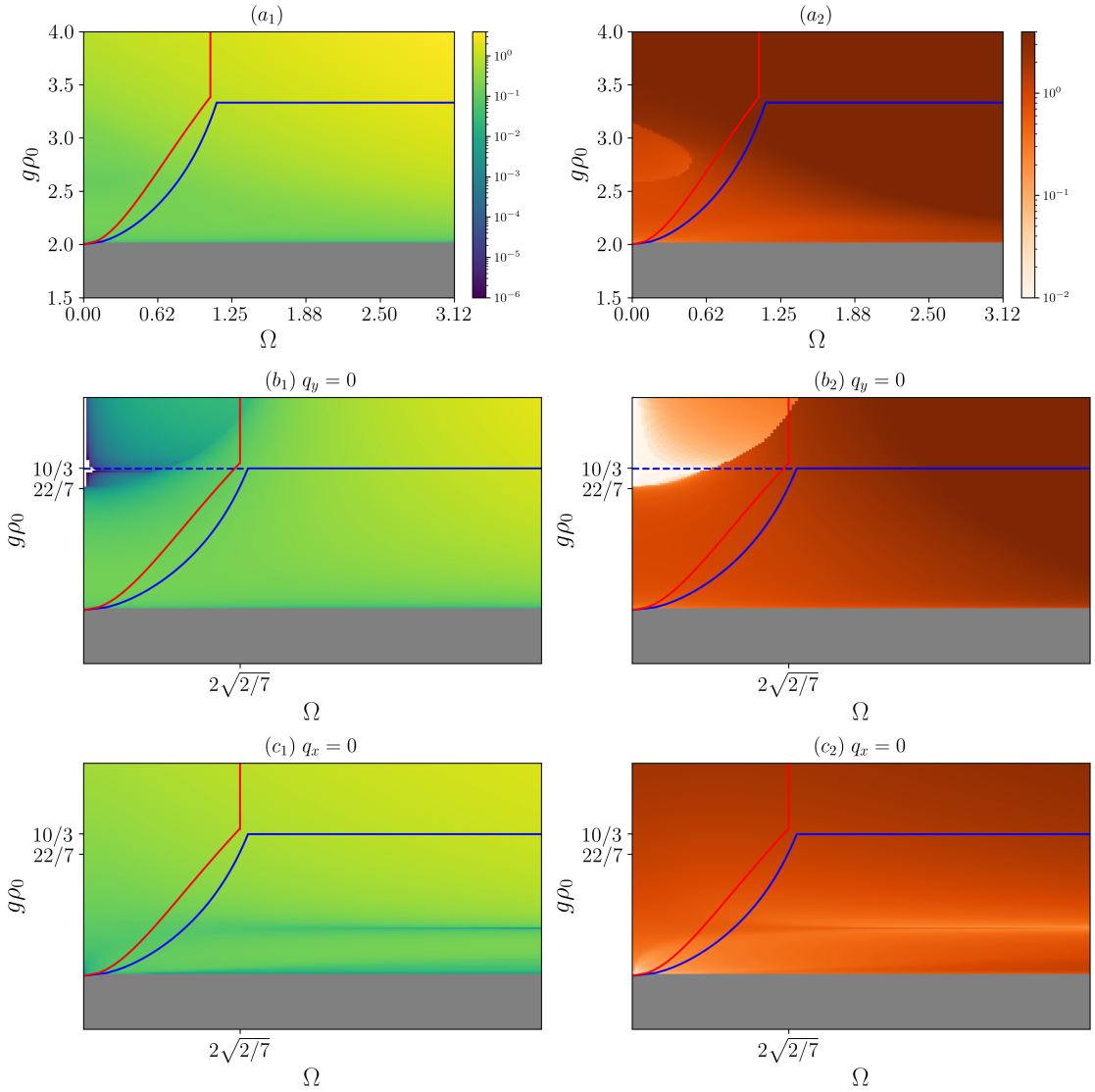

Figure 2.60: Unimodal distribution. Linear stability in the plane $(g\rho_0, \Omega)$. The red and blue lines are taken from Fig. 2.57 panel (a). The red line is obtained by expanding the dispersion relation in q_y and in $g\rho_0$, and the blue line by expanding in q_x and in $g\rho_0$. The grey part is where the rotating liquid solution is not defined. (a_1) The growth rate of the full linear stability. (a_2) Modulus of the most unstable wavevector. (b_1) The growth rate of the linear stability along the polarization direction $(q_y = 0)$. (b_2) Modulus of the most unstable wavevector along the polarization direction. (c_1) The growth rate of the linear stability along the direction perpendicular to the polarization direction $(q_x = 0)$. (c_2) Modulus of the most unstable wavevector along the direction perpendicular to the polarization direction.

Bimodal distribution of chirality

Levis and Liebchen have also studied the case of a bimodal distribution for chirality in [66, 67]. It means there are two populations, one with chirality $\omega_i = +\omega_0$ and the other one with chirality $\omega_i = -\omega_0$. They found the phase diagram in Fig. 2.61. They get the phase diagram thanks to the study of the domain of existence of the liquid phase and the linear stability of the disordered homogeneous phase. So the ordered phase of the Vicsek model lets place to mutual flocking which is a homogeneous ordered phase where the polarization of each species forms an angle. They characterize this angle at the microscopic level and at the hydrodynamic level and they have found a good agreement between numerical values and analytical predictions. If the value ω_0 continues to increase the mutual flocking phase lets place to a new phase where there is segregation between the two populations. Each population forms a rotating packet in equilibrium with a sparse gas, the population with $+\omega_0$ form a packet rotating counterclockwise, and the population with $-\omega_0$ form a packet rotating clockwise. They claim that the cluster grows linearly with the number of particles, in other words, it is a macrophase separation. Also, they derive hydrodynamic equations following the Fokker-Planck approach. They found the homogeneous ordered solution where the two polarizations of the two populations formed an angle and provide an analytical expression for this angle. Then they perform the linear stability of the homogeneous disordered solution and show it is unstable above a threshold. To conclude, they claim the existence of a new active matter phase, aka the mutual flocking, in which there is long-range order even in presence of chirality disorder.

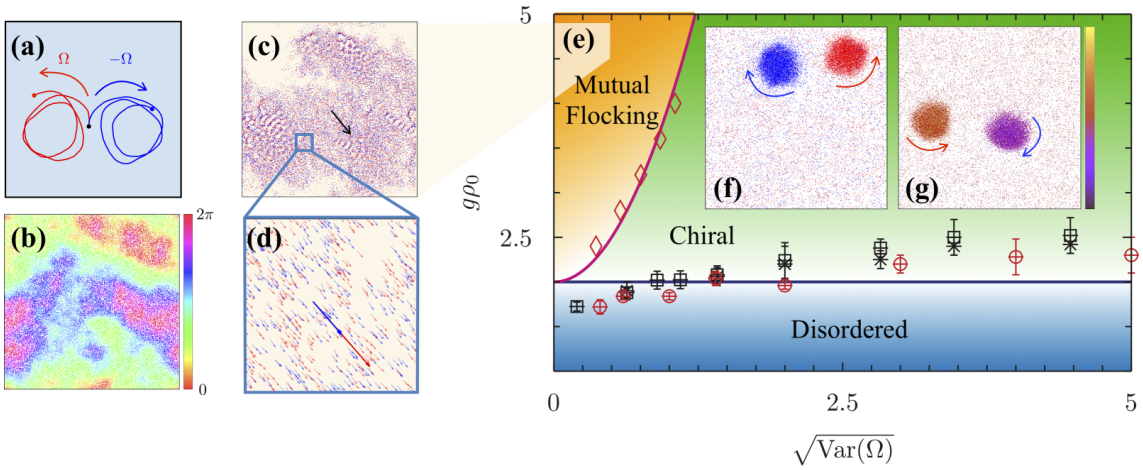

Figure 2.61: The figure is taken from [66]. (a) Illustration of the chirality in the case of a bimodal distribution of chirality. (b,c,d) Illustration of the mutual flocking phase. (e) Phase diagram in the plane $(\Omega, g\rho_0)$. The red line is obtained by computing the existence domain of the mutual flocking phase in the limit $\Omega \to 0$. The blue line is the result of the linear stability of the disordered homogeneous solution.

First, at the microscopic level, we have found that the mutual flocking phase disappears in the limit of infinite system size. They claim the existence of mutual flocking, which can be viewed as finite-size effects from our point of view. Then, they have not shown the bands phase which should be here because it shows the same difference in the polarization angle as the mutual flocking. Moreover, this model shows bands for $\omega_0 = 0$ according to snapshot in [52]. This lack of bands is a strong issue because at the same noise level there is the vortex phase, which is also lacking in their results. Also, the vortex phase is usually the phase that needs the highest number of time steps to appear. Then for large values of ω_0 we have found the rotating packets phase which is also present in their numerical simulation. But there is still a difference in our simulations we have shown that the rotating packets phase is a microphase separation contrary to their claim of a macrophase separation. For the unimodal distribution, we have found that the density is diverging in the center of the packets. We want to highlight the fact that they are using a dot representation for the particles, this representation is attractive but could hide details. Moreover, they never represent the density map of the simulation which makes it difficult to read their snapshots. The temporal discretization introduces a diffusion, it would be interesting to plot how behaves the typical lengthscale with the value of the timestep.

Secondly, at the hydrodynamic level, they have performed the linear stability of the disordered solution. Also, we notice the fact that they have written hydrodynamic equations based on the Fokker-Planck approach but they do not keep all the terms which are gradients and nonlinear. If we restrict our hydrodynamic equations Eq. (2.30) in the same way, we get the following equations in a complex formalism

$$\partial_t f_1 = \left(\alpha_{\text{FP}}(f_0 - \rho_{c\text{FP}}) + i\Omega_0 - \xi_{\text{FP}}|f_1|^2\right) f_1 - \frac{1}{2}\nabla f_0 + \nu_{\text{FP}}\Delta f_1 + \alpha_{\text{FP}} f_0 g_1 - \xi_{\text{FP}}\left(|f_1|^2 g_1 + g_1^* f_1^2 + |g_1|^2 f_1\right) \tag{2.54a}$$

$$\partial_t g_1 = \left(\alpha_{\text{FP}}(g_0 - \rho_{c\text{FP}}) - i\Omega_0 - \xi_{\text{FP}}|g_1|^2\right) g_1 - \frac{1}{2}\nabla g_0 + \nu_{\text{FP}}\Delta g_1 + \alpha_{\text{FP}} f_1 - \xi_{\text{FP}}\left(|g_1|^2 f_1 + f_1^* g_1^2 + |f_1|^2 g_1\right) \tag{2.54b}$$

$$\partial_t f_0 = -\frac{1}{2}(\nabla f_1^* + \nabla^* f_1) \tag{2.54c}$$

$$\partial_t g_0 = -\frac{1}{2}(\nabla g_1^* + \nabla^* g_1) \tag{2.54d}$$

This additional truncation does not affect the analytical expression of the liquid solution, so we get the same expression. Then they perform the linear stability of the disordered solution which is not affected by this extra truncation. They found that, as for the unimodal distribution, the linear stability of the disordered solution is governed by the

sign of $1-\rho_c$ (written with our formalism). But they do not perform the linear stability of the mutual flocking phase contrary to us, we have found that the mutual flocking phase is unstable and we are also able to characterize the finite-size effects. However, they have not worked on the same equations because they have made an extra truncation. So we have performed the linear stability of the new equations Eq. (2.54) by doing a small perturbation around the liquid solution and it leads to the new system of equations

$$\partial_t \delta f_{1,x} = \bar{\mathrm{C}}^{\mathrm{FP}}_{0,0}\delta f_0 + \bar{\mathrm{C}}^{\mathrm{FP}}_{0,1}\delta g_0 + \bar{\mathrm{C}}^{\mathrm{FP}}_{0,2}\delta f_{1,x} + \bar{\mathrm{C}}^{\mathrm{FP}}_{0,3}\delta f_{1,y} + \bar{\mathrm{C}}^{\mathrm{FP}}_{0,4}\delta g_{1,x} + \bar{\mathrm{C}}^{\mathrm{FP}}_{0,5}\delta g_{1,y} \tag{2.55a}$$

$$\partial_t \delta f_{1,y} = \bar{\mathrm{C}}^{\mathrm{FP}}_{1,0}\delta f_0 + \bar{\mathrm{C}}^{\mathrm{FP}}_{1,1}\delta g_0 + \bar{\mathrm{C}}^{\mathrm{FP}}_{1,2}\delta f_{1,x} + \bar{\mathrm{C}}^{\mathrm{FP}}_{1,3}\delta f_{1,y} + \bar{\mathrm{C}}^{\mathrm{FP}}_{1,4}\delta g_{1,x} + \bar{\mathrm{C}}^{\mathrm{FP}}_{1,5}\delta g_{1,y} \tag{2.55b}$$

$$\partial_t \delta g_{1,x} = \bar{\mathrm{C}}^{\mathrm{FP}}_{2,0}\delta f_0 + \bar{\mathrm{C}}^{\mathrm{FP}}_{2,1}\delta g_0 + \bar{\mathrm{C}}^{\mathrm{FP}}_{2,2}\delta f_{1,x} + \bar{\mathrm{C}}^{\mathrm{FP}}_{2,3}\delta f_{1,y} + \bar{\mathrm{C}}^{\mathrm{FP}}_{2,4}\delta g_{1,x} + \bar{\mathrm{C}}^{\mathrm{FP}}_{2,5}\delta g_{1,y} \tag{2.55c}$$

$$\partial_t \delta g_{1,y} = \bar{\mathrm{C}}^{\mathrm{FP}}_{3,0}\delta f_0 + \bar{\mathrm{C}}^{\mathrm{FP}}_{3,1}\delta g_0 + \bar{\mathrm{C}}^{\mathrm{FP}}_{3,2}\delta f_{1,x} + \bar{\mathrm{C}}^{\mathrm{FP}}_{3,3}\delta f_{1,y} + \bar{\mathrm{C}}^{\mathrm{FP}}_{3,4}\delta g_{1,x} + \bar{\mathrm{C}}^{\mathrm{FP}}_{3,5}\delta g_{1,y} \tag{2.55d}$$

where the coefficients are expressed in Appendix A.2.

The result of the linear stability for the full equations Eq. (2.35) we find that the mutual flocking phase is unstable everywhere except in a marginal part of the phase space. In Fig. 2.62 we plot the result of the numerical study of Eq. (2.55) which is without gradient of nonlinear terms. We perform the same kind of study as for the full equations. The figure shows that the liquid solution is not unstable everywhere because there is an area of the phase space where the highest eigenvalue is zero. This point shows the consequence of the extra truncation. Thus, if one wants to provide a comprehensive study it is needed to take into account all the terms provided by the Ginzburg-Landau truncation. Also, Levis and Liebchen have computed the limit line of the existence of the liquid solution under the approximation of low chirality values, it is represented with a red line in our figure, see Fig 2.62. Indeed, for low intrinsic frequency values, their criteria hold, but quickly the domain of existence is larger than their definition. They have used this criterion to plot their phase diagram, but for larger values of ω_0 the solution is a bad approximation, so their domain drawn in the phase diagram is wrong.

To summarize we have found two more phases (bands phase & vortex phase) and we have concluded to the existence of mutual flocking only in finite size. Then we have shown that their phase diagram is wrong because the mutual flocking solution is unstable everywhere. Moreover, an extra truncation could deeply change the linear stability behavior of the mutual flocking phase.

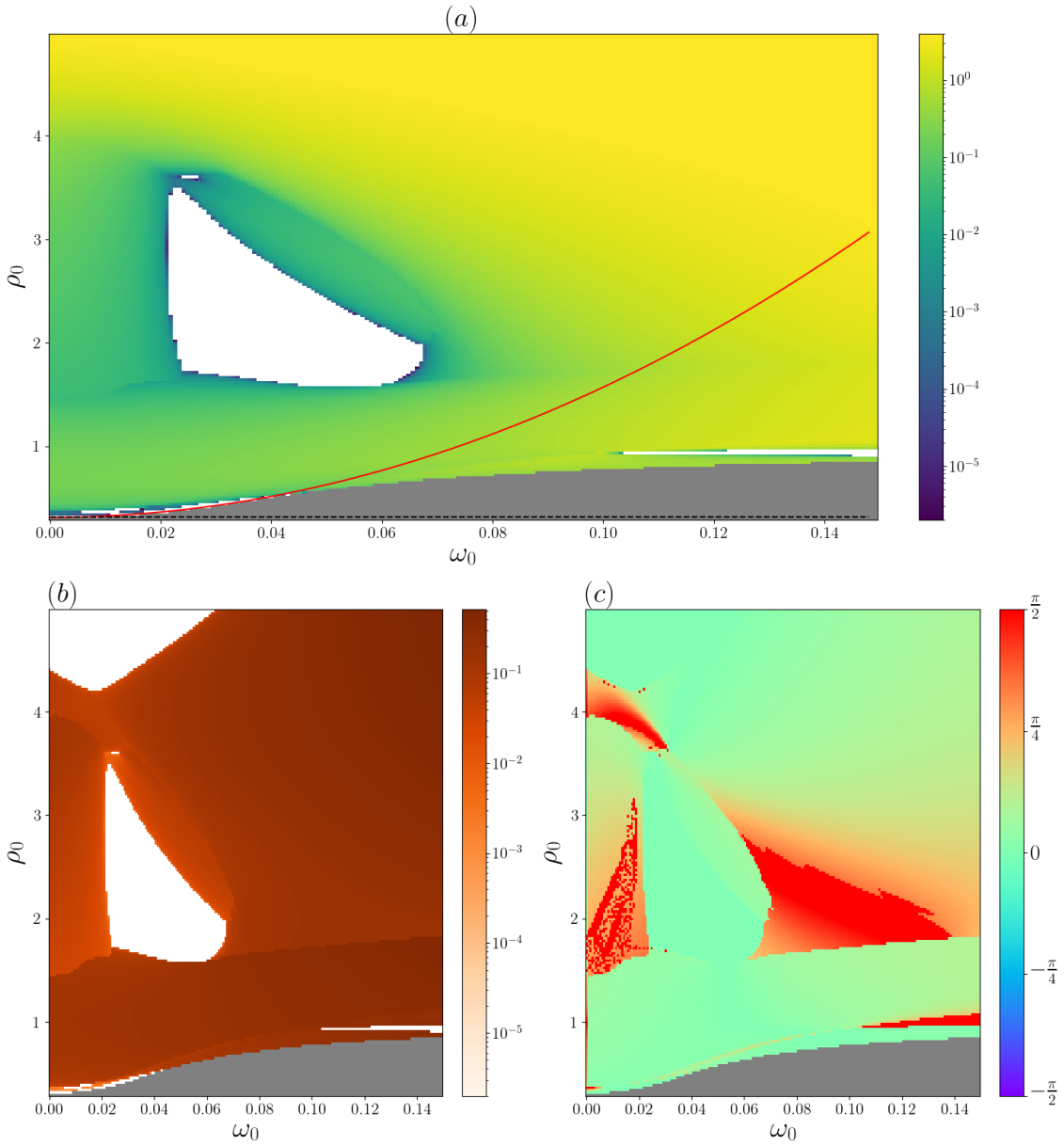

Figure 2.62: Bimodal distribution. Linear stability study in the plane (ρ, ω_0) with $D_r = 0.05$. The red line is the criteria used by Liebchen and Levis. The grey part is where the liquid solution is not defined. (a): Highest eigenvalues of the Fourier space. (b): Modulus of the eigenvectors attached to the highest eigenvalues of the panel (a). (c): Direction of the eigenvectors attached to the highest eigenvalues of the panel (a).

Gaussian distribution of chirality
They study the case of a Gaussian distribution of chirality where the chirality are drawn according to $g(\omega) = \frac{1}{\omega_0\sqrt{2\pi}} e^{-\frac{\omega^2}{2\omega_0^2}}$. They claim that they get the same results as for the bimodal distribution for the microscopic simulation. Thus, they claim that the stability threshold for the homogeneous disordered solution is the same as for the bimodal case. Then they have the mutual flocking phase and the rotating packet phase.

We can confirm the point that the threshold value for the disordered phase is not affected by the nature of the distribution studied. In our simulation, we have found the bands phase, the mutual flocking phase, and the vortex phase. Like for the bimodal case, they do not found bands, which is weird because they show some bands in a snapshot for the unimodal distribution at zero chirality. Then for large ω_0 we have only found vortices even though we have performed simulations for very large values of chirality (until $\omega_0 = 0.5$ which is far from the vortex-band transition). So they have found the mutual flocking phase and the rotating packet phase which are finite-size effects or not existing in our simulations.

Finally, they claim the existence of a long-range polarization order for a Gaussian distribution of chirality which contradicts our results.

Chapter 3

General Conclusion

We have explained that the Vicsek model can be seen as a limit case to model DADAM with ferroalignment. This model describes a phase transition between a disordered phase and an ordered phase even in 2D. It plays the role of a starting point to understand the ubiquitous property of collective motion in active matter. However, people had tried to extend the Vicsek model by changing step by step each ingredient in its rules. They asked about the robustness of the Vicsek model and found that the synchronized phase is not always resistant to small modifications. For instance, the synchronized phase does not resist the introduction of a frozen spatial disorder [61].
Our goal was to introduce a model to describe chiral active matter, which is the active matter with a tendency to describe rotation in free space. Thus, the new model introduced can be seen as the Vicsek model plus a frozen chirality disorder in a way similar to the Kuramoto disorder, or a Kuramoto model in finite dimension plus the self-propulsion of the oscillators. This is interesting because the Kuramoto model in finite dimension does not exhibit synchronization in 2D whereas the Vicsek model does. So our goal was to understand if there is synchronization and if the KVM is able to reproduce the different phases of chiral active matter such as vortex, rotating pattern.

In the first part, we study the KVM for a Gaussian distribution of chirality. At the microscopic level, we have found the segregation between positive and negative chirality. In particular, we have shown the existence of a new phase called the vortex phase. Then, the synchronized phase does not resist the chirality disorder in the limit of infinite system size.

In the second part, we study the simplest possible distribution for the chirality which is a unimodal distribution. We study this distribution thanks to numerical simulations at the microscopic scale, then we build a hydrodynamic theory by following two different approaches. The numerical simulations show two new phases which are a phase composed of vortices and another phase composed of a droplet of rotating liquid. Moreover, the full synchronized phase disappears in the limit of big systems. It means the synchronized

phase is not robust to the introduction of a chirality. Then we use a theoretical approach based on the Fokker-Planck equation which does not allow us to do clear conclusions. On the contrary, the theoretical approach based on the Boltzmann equation allows us to understand the linear instability of the synchronized phase. Moreover, it allows to qualitatively describe the microscopic phase diagram of the KVM via simulation of the hydrodynamic equations.

In the last part, we study another distribution with a zero mean and a non-zero variance. We use a bimodal distribution where half of the particles have a positive chirality, and the other half have the opposite chirality. At the microscopic level, we found a segregation between particles with a positive chirality and particles with a negative chirality. Thus, there is no more droplet of rotating liquid which is replaced by a phase of rotating packets composed of only one species. Also, the synchronized phase does not resist the introduction of chirality in the limit of infinite system size. As in the previous part, the theoretical approach based on the Fokker-Planck equation does not provide any clear conclusion. Furthermore, the theoretical approach based on the Boltzmann equation qualitatively describes the microscopic phase diagram again.

These results prove the non-existence of long-range polar order for chiral active matter. Moreover, they are in contradiction with the work of Levis and Liebchen in [52, 66].

Finally, our KVM model is a starting point to study chiral active matter. The main result is the non-existence of the synchronized phase whatever the distribution is. We have seen a better agreement with the theoretical approach based on the Boltzmann equation. It is possible to continue the study of the KVM in several ways. For instance, the first way could be to improve our hydrodynamic description by taking into account the chirality in the collisions kernel. Another possibility is to simulate the KVM equations at the Boltzmann level. We can also try to extend our hydrodynamic description to the nematic alignment because it seems some features at the microscopic level are commons with the ferroalignment as presented in [108]. It has been shown that the Kuramoto model does not exhibit synchronization in 2D but a partial frequency synchronization in 3D. Another important point could be to extend the KVM in 3D.

Appendix A

Exact expression of the coefficients

A.1 Coefficient attached to the Floquet analysis

$$L_{00} = 0 \tag{A.1a}$$

$$L_{01} = -iq_x \tag{A.1b}$$

$$L_{02} = -iq_y \tag{A.1c}$$

$$L_{10} = -\frac{iq_x}{2} + F_1\alpha_{\text{BGL}}\cos(\Omega t) \tag{A.1d}$$

$$\begin{aligned} L_{11} = &-\mu_1 - q^2\Re(\nu) - F_1^2\Re(\xi)\cos(2\Omega t) + F_1^2\Im(\xi)\sin(2\Omega t) \\ &+ iq_xF_1(-\Re(\beta)\cos(\Omega t) - \Re(\gamma)\cos(\Omega t) - \Im(\beta)\sin(\Omega t) + \Im(\gamma)\sin(\Omega t)) \\ &+ iq_yF_1(\Im(\beta)\cos(\Omega t) - \Im(\gamma)\cos(\Omega t) - \Re(\beta)\sin(\Omega t) - \Re(\gamma)\sin(\Omega t)) \end{aligned} \tag{A.1e}$$

$$\begin{aligned} L_{12} = &-\omega_0 + q^2\Im(\nu) + 2F_1^2\Im(\xi) - F_1^2\Im(\xi)\cos(2\Omega t) - F_1^2\Re(\xi)\sin(2\Omega t) \\ &+ iq_yF_1(\Re(\beta)\cos(\Omega t) - \Re(\gamma)\cos(\Omega t) + \Im(\beta)\sin(\Omega t) + \Im(\gamma)\sin(\Omega t)) \\ &+ iq_xF_1(\Im(\beta)\cos(\Omega t) + \Im(\gamma)\cos(\Omega t) - \Re(\beta)\sin(\Omega t) + \Re(\gamma)\sin(\Omega t)) \end{aligned} \tag{A.1f}$$

$$L_{20} = -\frac{iq_y}{2} + F_1\alpha_{\text{BGL}}\sin(\Omega t) \tag{A.1g}$$

$$\begin{aligned} L_{21} = &-q^2\Im(\nu) - 2F_1^2\Im(\xi) + \omega_0 - F_1^2\Im(\xi)\cos(2\Omega t) - F_1^2\Re(\xi)\sin(2\Omega t) \\ &+ iq_yF_1(-\Re(\beta)\cos(\Omega t) + \Re(\gamma)\cos(\Omega t) - \Im(\beta)\sin(\Omega t) - \Im(\gamma)\sin(\Omega t)) \\ &+ iq_xF_1(-\Im(\beta)\cos(\Omega t) - \Im(\gamma)\cos(\Omega t) + \Re(\beta)\sin(\Omega t) - \Re(\gamma)\sin(\Omega t)) \end{aligned} \tag{A.1h}$$

$$\begin{aligned} L_{22} = &-\mu_1 - q^2\Re(\nu) + F_1^2\Re(\xi)\cos(2\Omega t) - F_1^2\Im(\xi)\sin(2\Omega t) \\ &+ iq_xF_1(-\Re(\beta)\cos(\Omega t) - \Re(\gamma)\cos(\Omega t) - \Im(\beta)\sin(\Omega t) + \Im(\gamma)\sin(\Omega t)) \\ &+ iq_yF_1(\Im(\beta)\cos(\Omega t) - \Im(\gamma)\cos(\Omega t) - \Re(\beta)\sin(\Omega t) - \Re(\gamma)\sin(\Omega t)) \end{aligned} \tag{A.1i}$$

A.2 Expression of the coefficients for the study without gradient terms in paragraph 2.5

In this section we express the coefficient of Eq. (2.55) in the following table

$$
\begin{aligned}
\bar{C}^{FP}_{0,0} &= \alpha_{FP} P(1+\cos\phi) - \tfrac{1}{2}\partial_x \\
\bar{C}^{FP}_{0,1} &= 0 \\
\bar{C}^{FP}_{0,2} &= -1 + \alpha_{FP} + \tfrac{1}{4b}(\partial_x^2+\partial_y^2) - \tfrac{2g^2P^2}{b}(1+\cos\phi) \\
\bar{C}^{FP}_{0,3} &= -\Omega_0 - \tfrac{\Omega_0}{8b}(\partial_x^2+\partial_y^2) + \tfrac{g^2P^2\Omega_0}{2b}(1+\cos\phi) - \tfrac{g^2P^2}{b}\sin\phi \\
\bar{C}^{FP}_{0,4} &= \alpha_{FP} - \tfrac{g^2P^2}{b}(1+\cos\phi) \\
\bar{C}^{FP}_{0,5} &= -\tfrac{g^2P^2}{b}\sin\phi
\end{aligned}
$$

$$
\begin{aligned}
\bar{C}^{FP}_{1,0} &= \alpha_{FP} P\sin\phi - \tfrac{1}{2}\partial_y \\
\bar{C}^{FP}_{1,1} &= 0 \\
\bar{C}^{FP}_{1,2} &= \Omega_0 + \tfrac{\Omega_0}{8b}(\partial_x^2+\partial_y^2) - \tfrac{g^2\Omega_0P^2}{b}(1+\cos\phi) \\
\bar{C}^{FP}_{1,3} &= -1 + \alpha_{FP} + \tfrac{1}{4b}(\partial_x^2+\partial_y^2) - \tfrac{g^2P^2}{b}(1+\cos\phi) - \tfrac{g^2\Omega_0P^2}{2b}\sin\phi \\
\bar{C}^{FP}_{1,4} &= -\tfrac{g^2\Omega_0P^2}{2b}(1+\cos\phi) \\
\bar{C}^{FP}_{1,5} &= \alpha_{FP} - \tfrac{g^2\Omega_0P^2}{2b}\sin\phi
\end{aligned}
$$

$$
\begin{aligned}
\bar{C}^{FP}_{2,0} &= 0 \\
\bar{C}^{FP}_{2,1} &= \alpha_{FP} P(1+\cos\phi) - \tfrac{1}{2}\partial_x \\
\bar{C}^{FP}_{2,2} &= \alpha_{FP} - \tfrac{g^2P^2}{b}(\cos\phi+\cos^2\phi) - \tfrac{g^2\Omega_0P^2}{2b}(\sin\phi+\cos\phi\sin\phi) \\
\bar{C}^{FP}_{2,3} &= -\tfrac{g^2\Omega_0P^2}{2b}\sin^2\phi - \tfrac{g^2P^2}{b}\cos\phi\sin\phi \\
\bar{C}^{FP}_{2,4} &= -1 + \alpha_{FP} + \tfrac{1}{4b}(\partial_x^2+\partial_y^2) - \tfrac{g^2P^2}{b}(1+2\cos\phi+\cos^2\phi) - \tfrac{g^2\Omega_0P^2}{2b}(\sin\phi+\sin\phi\cos\phi) \\
\bar{C}^{FP}_{2,5} &= \Omega_0 + \tfrac{\Omega_0}{8b}(\partial_x^2+\partial_y^2) - \tfrac{g^2P^2}{b}\cos\phi\sin\phi - \tfrac{g^2\Omega_0P^2}{2b}(1+\cos\phi+\sin^2\phi)
\end{aligned}
$$

$$
\begin{aligned}
\bar{C}^{FP}_{3,0} &= 0 \\
\bar{C}^{FP}_{3,1} &= \alpha_{FP} P\sin\phi - \tfrac{Pe}{2}\partial_y \\
\bar{C}^{FP}_{3,2} &= -\tfrac{g^2P^2}{b}(\sin\phi+\cos\phi\sin\phi) + \tfrac{g^2P^2}{2b}(\cos\phi+\cos^2\phi) \\
\bar{C}^{FP}_{3,3} &= \alpha_{FP} + \tfrac{g^2\Omega_0P^2}{2b}\cos\phi\sin\phi - \tfrac{g^2P^2}{b}\sin^2\phi \\
\bar{C}^{FP}_{3,4} &= -\Omega_0 - \tfrac{\Omega_0}{8b}(\partial_x^2+\partial_y^2) - \tfrac{g^2P^2}{b}(\sin\phi+\sin\phi\cos\phi) + \tfrac{g^2\Omega_0P^2}{2b}(1+2\cos\phi+\cos^2\phi) \\
\bar{C}^{FP}_{3,5} &= -1 + \alpha_{FP} + \tfrac{Pe^2}{4b}(\partial_x^2+\partial_y^2) - \tfrac{g^2P^2}{b}(1+\cos\phi+\sin^2\phi) + \tfrac{g^2\Omega_0P^2}{2b}\cos\phi\sin\phi
\end{aligned}
$$

A.3 Expression of the coefficients for the study with gradient terms in paragraph 2.3.2

In this section we express the coefficient of Eq. (2.35) in the following table

$$
\begin{aligned}
\mathrm{C}^{\mathrm{FP}}_{0,0} &= \alpha_{\mathrm{FP}} P(1+\cos\phi) - \tfrac{1}{2}\partial_x \\
\mathrm{C}^{\mathrm{FP}}_{0,1} &= 0 \\
\mathrm{C}^{\mathrm{FP}}_{0,2} &= -1 + \alpha_{\mathrm{FP}} + \tfrac{1}{4b}(\partial_x^2+\partial_y^2) - \tfrac{2g^2P^2}{b}(1+\cos\phi) \\
&\quad + \tfrac{gP}{8b}\left((-6-2\cos\phi+3\Omega_0\sin\phi)\partial_x + (-5\Omega_0 - 3\Omega_0\cos\phi - 2\sin\phi)\partial_y\right) \\
\mathrm{C}^{\mathrm{FP}}_{0,3} &= -\Omega_0 - \tfrac{\Omega_0}{8b}(\partial_x^2+\partial_y^2) + \tfrac{g^2P^2\Omega_0}{2b}(1+\cos\phi) - \tfrac{g^2P^2}{b}\sin\phi \\
&\quad + \tfrac{gP}{8b}\left((3\Omega_0 + \Omega_0\cos\phi + 6\sin\phi)\partial_x + (-10 - 6\cos\phi + \Omega_0\sin\phi)\partial_y\right) \\
\mathrm{C}^{\mathrm{FP}}_{0,4} &= \alpha_{\mathrm{FP}} - \tfrac{g^2P^2}{b}(1+\cos\phi) - \tfrac{gP}{8b}(4\partial_x + 2\Omega_0\partial_y) \\
\mathrm{C}^{\mathrm{FP}}_{0,5} &= -\tfrac{g^2P^2}{b}\sin\phi + \tfrac{gP}{8b}(2\Omega_0\partial_x - 4\partial_y)
\end{aligned}
$$

$$
\begin{aligned}
\mathrm{C}^{\mathrm{FP}}_{1,0} &= \alpha_{\mathrm{FP}} P\sin\phi - \tfrac{1}{2}\partial_y \\
\mathrm{C}^{\mathrm{FP}}_{1,1} &= 0 \\
\mathrm{C}^{\mathrm{FP}}_{1,2} &= \Omega_0 + \tfrac{\Omega_0}{8b}(\partial_x^2+\partial_y^2) - \tfrac{g^2\Omega_0P^2}{b}(1+\cos\phi) \\
&\quad + \tfrac{gP}{8b}\left((-3\Omega_0 - \Omega_0\cos\phi - 6\sin\phi)\partial_x + (10 + 6\cos\phi - \Omega_0\sin\phi)\partial_y\right) \\
\mathrm{C}^{\mathrm{FP}}_{1,3} &= -1 + \alpha_{\mathrm{FP}} + \tfrac{1}{4b}(\partial_x^2+\partial_y^2) - \tfrac{g^2P^2}{b}(1+\cos\phi) - \tfrac{g^2\Omega_0P^2}{2b}\sin\phi \\
&\quad + \tfrac{gP}{8b}\left((-6-2\cos\phi+3\Omega_0\sin\phi)\partial_x + (-5\Omega_0 - 3\Omega_0\cos\phi - 2\sin\phi)\partial_y\right) \\
\mathrm{C}^{\mathrm{FP}}_{1,4} &= -\tfrac{g^2\Omega_0P^2}{2b}(1+\cos\phi) + \tfrac{gP}{8b}(-2\Omega_0\partial_x + 4\partial_y) \\
\mathrm{C}^{\mathrm{FP}}_{1,5} &= \alpha_{\mathrm{FP}} - \tfrac{g^2\Omega_0P^2}{2b}\sin\phi + \tfrac{gP}{8b}(-4\partial_x - 2\Omega_0\partial_y)
\end{aligned}
$$

$$
\begin{aligned}
\mathrm{C}^{\mathrm{FP}}_{2,0} &= 0 \\
\mathrm{C}^{\mathrm{FP}}_{2,1} &= \alpha_{\mathrm{FP}} P(1+\cos\phi) - \tfrac{1}{2}\partial_x \\
\mathrm{C}^{\mathrm{FP}}_{2,2} &= \alpha_{\mathrm{FP}} - \tfrac{g^2P^2}{b}(\cos\phi+\cos^2\phi) - \tfrac{g^2\Omega_0P^2}{2b}(\sin\phi+\cos\phi\sin\phi) \\
&\quad + \tfrac{gP}{8b}\left((-4\cos\phi - 2\Omega_0\sin\phi)\partial_x + (2\Omega_0\cos\phi - 4\sin\phi)\partial_y\right) \\
\mathrm{C}^{\mathrm{FP}}_{2,3} &= -\tfrac{g^2\Omega_0P^2}{2b}\sin^2\phi - \tfrac{g^2P^2}{b}\cos\phi\sin\phi \\
&\quad + \tfrac{gP}{8b}\left((-2\Omega_0\cos\phi + 4\sin\phi)\partial_x + (-4\cos\phi - 2\Omega_0\sin\phi)\partial_y\right) \\
\mathrm{C}^{\mathrm{FP}}_{2,4} &= -1 + \alpha_{\mathrm{FP}} + \tfrac{1}{4b}(\partial_x^2+\partial_y^2) - \tfrac{g^2P^2}{b}(1+2\cos\phi+\cos^2\phi) - \tfrac{g^2\Omega_0P^2}{2b}(\sin\phi+\sin\phi\cos\phi) \\
&\quad + \tfrac{gP}{8b}\left((-2-6\cos\phi - 5\Omega_0\sin\phi)\partial_x + (3\Omega_0 + 5\Omega_0\cos\phi - 6\sin\phi)\partial_y\right) \\
\mathrm{C}^{\mathrm{FP}}_{2,5} &= \Omega_0 + \tfrac{\Omega_0}{8b}(\partial_x^2+\partial_y^2) - \tfrac{g^2P^2}{b}\cos\phi\sin\phi - \tfrac{g^2\Omega_0P^2}{2b}(1+\cos\phi+\sin^2\phi) \\
&\quad + \tfrac{gP}{8b}\left((-\Omega_0 - 3\Omega_0\cos\phi + 10\sin\phi)\partial_x + (-6 - 10\cos\phi - 3\Omega_0\sin\phi)\partial_y\right)
\end{aligned}
$$

$$
\begin{aligned}
\mathrm{C}^{\mathrm{FP}}_{3,0} &= 0 \\
\mathrm{C}^{\mathrm{FP}}_{3,1} &= \alpha_{\mathrm{FP}} \sin\phi - \tfrac{1}{2}\partial_y \\
\mathrm{C}^{\mathrm{FP}}_{3,2} &= -\tfrac{g^2P^2}{b}(\sin\phi + \cos\phi\sin\phi) + \tfrac{g^2P^2}{2b}(\cos\phi + \cos^2\phi) \\
&\quad + \tfrac{gP}{8b}\left((2\Omega_0\cos\phi - 4\sin\phi)\partial_x + (4\cos\phi + 2\Omega_0\sin\phi)\partial_y\right) \\
\mathrm{C}^{\mathrm{FP}}_{3,3} &= \alpha_{\mathrm{FP}} + \tfrac{g^2\Omega_0P^2}{2b}\cos\phi\sin\phi - \tfrac{g^2P^2}{b}\sin^2\phi \\
&\quad + \tfrac{gP}{8b}\left((-4\cos\phi - 2\Omega_0\sin\phi)\partial_x + (2\Omega_0\cos\phi - 4\sin\phi)\partial_y\right) \\
\mathrm{C}^{\mathrm{FP}}_{3,4} &= -\Omega_0 - \tfrac{\Omega_0}{8b}(\partial_x^2 + \partial_y^2) - \tfrac{g^2P^2}{b}(\sin\phi + \sin\phi\cos\phi) + \tfrac{g^2\Omega_0P^2}{2b}(1 + 2\cos\phi + \cos^2\phi) \\
&\quad + \tfrac{gP}{8b}\left((\Omega_0 + 3\Omega_0\cos\phi - 10\sin\phi)\partial_x + (6 + 10\cos\phi + 3\Omega_0\sin\phi)\partial_y\right) \\
\mathrm{C}^{\mathrm{FP}}_{3,5} &= -1 + \alpha_{\mathrm{FP}} + \tfrac{1}{4b}(\partial_x^2 + \partial_y^2) - \tfrac{g^2P^2}{b}(1 + \cos\phi + \sin^2\phi) + \tfrac{g^2\Omega_0P^2}{2b}\cos\phi\sin\phi \\
&\quad + \tfrac{gP}{8b}\left((-2 - 6\cos\phi - 5\Omega_0\sin\phi)\partial_x + (3\Omega_0 + 5\Omega_0\cos\phi - 6\sin\phi)\partial_y\right)
\end{aligned}
$$

A.4 Exact expression of the coefficients of Eq. 2.43

In this appendix we give the exact expression of the different coefficients involve in Eq. 2.43. The three first intermediate coefficients are given by

$$
\begin{aligned}
\zeta &= J_{1,-1} + J_{1,2} \\
\chi &= J_{2,2}/[-\left((P_2 - 1) + 2J_{2,0} + J_{2,2}\right)^2 - 4\omega_0^2 + J_{2,2}^2] \\
\nu &= \frac{\chi}{4J_{2,2}}\left((P_2 - 1) + 2J_{2,0} + J_{2,2} - 2i\omega_0\right)
\end{aligned}
$$

The coefficients of Eq. (2.43a) are given by

$$
\begin{aligned}
&\mu_1[f_0, g_0] = P_1 - 1 + f_0(J_{1,1} + J_{1,0}) + g_0 J_{1,0} \qquad \kappa_1 = 4\nu J_{2,1} \qquad \kappa_2 = 2\nu\zeta - \tfrac{1}{2}J_{1,2}\chi \\
&\xi = -J_{2,1}(4\nu\zeta - \tfrac{1}{2}J_{1,2}\chi) \qquad \tilde{\mu}[f_0] = J_{1,1}f_0 \qquad \tilde{\xi} = \frac{J_{1,-1}J_{2,1}J_{2,2}}{\chi} \\
&\tilde{\nu} = -\tfrac{1}{4}\chi \qquad \tilde{\kappa}_2 = -\tfrac{1}{4}J_{1,-1}\chi \qquad \tilde{\kappa}_1 = -J_{2,1}\chi \\
&\tilde{\gamma}_1 = J_{2,1}(4\nu^* J_{1,2} + 4\nu\zeta - \frac{\zeta J_{2,2}}{\chi}) \qquad \gamma_1 = J_{1,-1}J_{2,1}(4\nu - \chi) \qquad \gamma_2 = J_{2,1}(4\nu^* J_{1,2} - \zeta\chi) \\
&\tilde{\gamma}_2 = 4\nu J_{1,-1}J_{2,1} \qquad \delta_1 = \frac{J_{2,1}}{2}(-4\nu + \chi) \qquad \delta_2 = -2\nu^* J_{1,2} + \tfrac{1}{2}\chi \\
&\tilde{\delta_2} = -2\nu J_{1,-1}
\end{aligned}
$$

A.5 Exact expression of coefficients for the linear stability of the liquid solution

In this section we express the exact expression of the coefficients of Eq. (2.52). To maintain the notation short we will use the notation $\Re(X) \equiv X_r$, $\Im(X) \equiv X_i$ and $\mu[1,1] \equiv \mu$.

Also, we denote by $\alpha \equiv (J_{1,1} + J_{1,0})$

$$
\begin{aligned}
C^{\text{BGL}}_{0,0} = \;& P(\alpha + J_{1,1}\cos(\Omega)) - \tfrac{1}{2}\partial_x \\
C^{\text{BGL}}_{0,1} = \;& J_{1,0}P \\
C^{\text{BGL}}_{0,2} = \;& \nu_r\Delta + \mu_1 \\
& + P^2\left(\gamma_{1,r} - 3\xi_r + 2\cos(\Omega)(\tilde{\gamma}_{1,r} + \tilde{\gamma}_{2,r}) + \gamma_{2,r}\cos(2\Omega) + 2\sin\Omega(\tilde{\gamma}_{2,i} - \tilde{\gamma}_{1,i}) - \gamma_{2,i}\sin(2\Omega)\right) \\
& + P\left(-\kappa_{2,r} + \cos(\Omega)(\tilde{\delta}_{2,r} + \delta_{1,r}) + \sin\Omega(\tilde{\delta}_{2,i} - \delta_{1,i})\right)\partial_x \\
& + P\left(\kappa_{2,i} - \kappa_{1,i} + \cos(\Omega)(\delta_{1,i} - \tilde{\delta}_{2,i}) + \sin\Omega(\tilde{\delta}_{2,r} + \delta_{1,r})\right)\partial_y \\
C^{\text{BGL}}_{0,3} = \;& -\nu_i\Delta - \omega_0 \\
& - P^2\left(-\gamma_{1,i} + \xi_i - 2\tilde{\gamma}_{2,i}\cos(\Omega) + \gamma_{2,i}\cos(2\Omega) + 2\tilde{\gamma}_{2,r}\sin\Omega + \gamma_{2,r}\sin(2\Omega)\right) \\
& + P\left(\kappa_{2,i} + \kappa_{1,i} - \cos(\Omega)(\tilde{\delta}_{2,i} - \delta_{1,i}) + \sin\Omega(\tilde{\delta}_{2,r} - \delta_{1,r})\right)\partial_x \\
& + P\left(\kappa_{2,r} - \kappa_{1,r} + \cos(\Omega)(\delta_{1,r} - \tilde{\delta}_{2,r}) - \sin\Omega(\tilde{\delta}_{2,i} - \delta_{1,i})\right)\partial_y \\
C^{\text{BGL}}_{0,4} = \;& \tilde{\nu}\Delta + J_{1,1}\tfrac{\rho_0}{2} \\
& + P^2\left(\tilde{\gamma}_{1,r} + \tilde{\gamma}_{2,r} - 2\tilde{\xi} + 2\cos(\Omega)(\gamma_{2,r} + \gamma_{1,r}) + a_{4,r}\cos(2\Omega) - 2\gamma_{2,i}\sin\Omega P\right) \\
& + P\left(\delta_{2,r} + \delta_{1,r} - \tilde{\kappa}_2\cos(\Omega)\right)\partial_x + P\left(-\delta_{2,i} + \delta_{1,i} - \tilde{\kappa}_2\sin\Omega\right)\partial_y \\
C^{\text{BGL}}_{0,5} = \;& P^2\left(-\tilde{\gamma}_{1,i} + \tilde{\gamma}_{2,i} - 2\gamma_{2,i}\cos(\Omega) + 2\sin\Omega(\gamma_{1,r} - \gamma_{2,r}) - \tilde{\xi}\sin(2\Omega)\right) \\
& + P\left(-\delta_{2,i} - \delta_{1,i} - \tilde{\kappa}_2\sin\Omega\right)\partial_x + P\left(-\delta_{2,r} + \delta_{1,r} + \cos(\Omega)(-\tilde{\kappa}_1 + \tilde{\kappa}_2)\right)\partial_y
\end{aligned}
$$

$$
\begin{aligned}
C^{\text{BGL}}_{1,0} = \;& -\tfrac{1}{2}\partial_y + J_{1,1}P\sin\Omega \\
C^{\text{BGL}}_{1,1} = \;& 0 \\
C^{\text{BGL}}_{1,2} = \;& \nu_i\Delta + \omega_0 + P^2\left(-3\xi_i + 2\cos(\Omega)(\tilde{\gamma}_{1,i} + \tilde{\gamma}_{2,i}) + \cos(\Omega)^2(\gamma_{2,i} + \gamma_{1,i})\right. \\
& \left. + 2\sin\Omega(\tilde{\gamma}_{1,r} - \tilde{\gamma}_{2,r} + \gamma_{2,r}\cos(\Omega)) + \sin^2\Omega(\gamma_{1,i} - \gamma_{2,i})\right) \\
& + P\left(-\kappa_{2,i} + \cos(\Omega)(\tilde{\delta}_{2,i} + \delta_{1,i}) + \sin\Omega(\delta_{1,r} - \tilde{\delta}_{2,r})\right)\partial_x \\
& + P\left(-\kappa_{2,r} + \kappa_{1,r} + \cos(\Omega)(\tilde{\delta}_{2,r} - \delta_{1,r}) + \sin\Omega(\tilde{\delta}_{2,i} + \delta_{1,i})\right)\partial_y \\
C^{\text{BGL}}_{1,3} = \;& \nu_r\Delta + \mu_1 + P^2\left(-\xi_r + 2\tilde{\gamma}_{2,r}\cos(\Omega) + \cos(\Omega)^2(\gamma_{1,r} - \gamma_{2,r})\right. \\
& \left. + 2\sin\Omega(\tilde{\gamma}_{2,i} + \gamma_{2,i}\cos(\Omega)) + \sin^2\Omega(\gamma_{2,r} + \gamma_{1,r})\right) \\
& + P\left(-\kappa_{2,r} - \kappa_{1,r} + \cos(\Omega)(\tilde{\delta}_{2,r} + \delta_{1,r}) + \sin\Omega(\tilde{\delta}_{2,i} - \delta_{1,i})\right)\partial_x \\
& + P\left(\kappa_{2,i} - \kappa_{1,i} + \cos(\Omega)(\delta_{1,i} - \tilde{\delta}_{2,i}) + \sin\Omega(\tilde{\delta}_{2,r} + \delta_{1,r})\right)\partial_y \\
C^{\text{BGL}}_{1,4} = \;& P^2\left(\tilde{\gamma}_{1,i} + \tilde{\gamma}_{2,i} + 2\cos(\Omega)(\gamma_{2,i} + \gamma_{1,i}) + 2\gamma_{2,r}\sin\Omega - 2\tilde{\xi}\cos(\Omega)\sin\Omega\right) \\
& + P\left(\delta_{2,i} + \delta_{1,i} + \sin\Omega(-\tilde{\kappa}_1 + \tilde{\kappa}_2)\right)\partial_x \\
& + P\left(\delta_{2,r} - \delta_{1,r} + \cos(\Omega)(-\tilde{\kappa}_2 + \tilde{\kappa}_1)\right)\partial_y \\
C^{\text{BGL}}_{1,5} = \;& \tilde{\nu}\Delta + J_{1,1}\tfrac{\rho_0}{2} \\
& + P^2\left(\tilde{\gamma}_{1,r} - \tilde{\gamma}_{2,r} + 2\gamma_{2,r}\cos(\Omega) - \tilde{\xi}\cos(\Omega)^2 + 2\sin\Omega(\gamma_{1,i} - \gamma_{2,i}) - 3\tilde{\xi}\sin^2\Omega\right) \\
& + P\left(\delta_{2,r} + \delta_{1,r} + \cos(\Omega)(-\tilde{\kappa}_2 - \tilde{\kappa}_1)\right)\partial_x \\
& + P\left(-\delta_{2,i} + \delta_{1,i} + \sin\Omega(-\tilde{\kappa}_2 - \tilde{\kappa}_1)\right)\partial_y
\end{aligned}
$$

$$
\begin{aligned}
C^{\text{BGL}}_{2,0} = \;& J_{1,1} P \cos(\Omega) \\
C^{\text{BGL}}_{2,1} = \;& J_{1,1} P - \tfrac{1}{2}\partial_x + P\alpha\cos(\Omega) \\
C^{\text{BGL}}_{2,2} = \;& \tilde{\nu}\Delta + J_{1,1}\tfrac{\rho_0}{2} \\
& + P^2\left(\tilde{\gamma}_{1,r} - 3\tilde{\xi} + 2\cos(\Omega)(\gamma_{2,r}+\gamma_{1,r}) + \tilde{\gamma}_{2,r}\cos(2\Omega) + 2\sin\Omega(\gamma_{1,i}-\gamma_{2,i}) + \tilde{\gamma}_{2,i}\sin(2\Omega)\right) \\
& + P\left(-\tilde{\kappa}_2 + \cos(\Omega)(\delta_{2,r}+\delta_{1,r}) + \sin\Omega(\delta_{1,i}-\delta_{2,i})\right)\partial_x \\
& + P\left(\cos(\Omega)(\delta_{2,i}-\delta_{1,i}) + \sin\Omega(\delta_{2,r}+\delta_{1,r})\right)\partial_y \\
C^{\text{BGL}}_{2,3} = \;& P^2\left(\tilde{\gamma}_{1,i} + 2\gamma_{2,i}\cos(\Omega) - \tilde{\gamma}_{2,i}\cos(2\Omega) + 2\gamma_{2,r}\sin\Omega + \tilde{\gamma}_{2,r}\sin(2\Omega)\right) \\
& + P\left(\cos(\Omega)(\delta_{2,i}+\delta_{1,i}) + \sin\Omega(\delta_{2,r}-\delta_{1,r})\right)\partial_x \\
& + P\left(\tilde{\kappa}_2 - \tilde{\kappa}_1 + \cos(\Omega)(\delta_{1,r}-\delta_{2,r}) + \sin\Omega(\delta_{2,i}+\delta_{1,i})\right)\partial_y \\
C^{\text{BGL}}_{2,4} = \;& \nu_r\Delta + \mu_1 \\
& + P^2\left(\gamma_{2,r}+\gamma_{1,r} - 2\xi_r + 2\cos(\Omega)(\tilde{\gamma}_{1,r}+\tilde{\gamma}_{2,r}) - \xi_r\cos(2\Omega) + 2\tilde{\gamma}_{2,i}\sin\Omega + -\xi_i\sin(2\Omega)\right) \\
& + P\left(\tilde{\delta}_{2,r} + \delta_{1,r} - \kappa_{2,r}\cos(\Omega) - (-\kappa_{2,i}+\kappa_{1,i})\sin\Omega\right)\partial_x \\
& + P\left(\tilde{\delta}_{2,i} - \delta_{1,i} + (-\kappa_{2,i}+\kappa_{1,i})\cos(\Omega) + -\kappa_{2,r}\sin\Omega\right)\partial_y \\
C^{\text{BGL}}_{2,5} = \;& \nu_i\Delta + \omega_0 \\
& + P^2\left(-\gamma_{2,i}+\gamma_{1,i} - 2\xi_i + 2\tilde{\gamma}_{2,i}\cos(\Omega) + \xi_i\cos(2\Omega) + 2\sin\Omega(\tilde{\gamma}_{1,r} - 2\tilde{\gamma}_{2,r}) + -\xi_r\sin(2\Omega)\right) \\
& + P\left(\tilde{\delta}_{2,i} + \delta_{1,i} + (-\kappa_{2,i}-\kappa_{1,i})\cos(\Omega) + -\kappa_{2,r}\sin\Omega\right)\partial_x \\
& - P\left(\tilde{\delta}_{2,r} - \delta_{1,r} + (-\kappa_{2,r}+\kappa_{1,r})\cos(\Omega) - (-\kappa_{2,i}-\kappa_{1,i})\sin\Omega\right)\partial_y
\end{aligned}
$$

$$
\begin{aligned}
C^{\text{BGL}}_{3,0} = \;& J_{1,1} P \sin\Omega \\
C^{\text{BGL}}_{3,1} = \;& P\alpha\sin\Omega - \tfrac{1}{2}\partial_y \\
C^{\text{BGL}}_{3,2} = \;& P^2\left(-\tilde{\gamma}_{1,i} - 2\cos(\Omega)(\gamma_{2,i}+\gamma_{1,i}) - \tilde{\gamma}_{2,i}\cos(2\Omega) + 2\sin\Omega(\gamma_{1,r}-\gamma_{2,r}) + \tilde{\gamma}_{2,r}\sin(2\Omega)\right) \\
& + P\left(-\cos(\Omega)(\delta_{2,i}+\delta_{1,i}) + \sin\Omega(\delta_{1,r}-\delta_{2,r})\right)\partial_x \\
& + P\left(-\tilde{\kappa}_2 + \tilde{\kappa}_1 + \cos(\Omega)(\delta_{2,r}-\delta_{1,r}) - \sin\Omega(\delta_{2,i}+\delta_{1,i})\right)\partial_y \\
C^{\text{BGL}}_{3,3} = \;& \tilde{\nu}\Delta + J_{1,1}\tfrac{\rho_0}{2} \\
& + P^2\left(\tilde{\gamma}_{1,r} - \tilde{\xi} + 2\gamma_{2,r}\cos(\Omega) - \tilde{\gamma}_{2,r}\cos(2\Omega) - 2\gamma_{2,i}\sin\Omega - \tilde{\gamma}_{2,i}\sin(2\Omega)\right) \\
& + P\partial_x\left(-\tilde{\kappa}_2 - \tilde{\kappa}_1 + (\delta_{2,r}+\delta_{1,r})\cos(\Omega) + (-\delta_{2,i}+\delta_{1,i})\sin\Omega\right) \\
& + P\partial_y\left((\delta_{2,i}-\delta_{1,i})\cos(\Omega) + (\delta_{2,r}+\delta_{1,r})\sin\Omega\right) \\
C^{\text{BGL}}_{3,4} = \;& -\nu_i\Delta - \omega_0 \\
& + P^2\left(-\gamma_{2,i} - \gamma_{1,i} + 2\xi_i - 2\cos(\Omega)(\tilde{\gamma}_{1,i}-\tilde{\gamma}_{2,i}) + \xi_i\cos(2\Omega) + 2\tilde{\gamma}_{2,r}\sin\Omega - \xi_r\sin(2\Omega)\right) \\
& - P\left(\tilde{\delta}_{2,i} + \delta_{1,i} + -\kappa_{2,i}\cos(\Omega) + (-\kappa_{2,r}+\kappa_{1,r})\sin\Omega\right)\partial_x \\
& + P\left(\tilde{\delta}_{2,r} - \delta_{1,r} + (-\kappa_{2,r}+\kappa_{1,r})\cos(\Omega) + \kappa_{2,i}\sin\Omega\right)\partial_y \\
C^{\text{BGL}}_{3,5} = \;& \nu_r\Delta + \mu_1[\tfrac{\rho_0}{2}, \tfrac{\rho_0}{2}] \\
& + P^2\left(-\gamma_{2,r} + \gamma_{1,r} - 2\xi_r + 2\tilde{\gamma}_{2,r}\cos(\Omega) - -\xi_r\cos(2\Omega) + 2\sin\Omega(\tilde{\gamma}_{2,i}-\tilde{\gamma}_{1,i}) + \xi_i\sin(2\Omega)\right) \\
& + P\left(\tilde{\delta}_{2,r} + \delta_{1,r} + (-\kappa_{2,r}-\kappa_{1,r})\cos(\Omega) + \kappa_{2,i}\sin\Omega\right)\partial_x \\
& + P\left(\tilde{\delta}_{2,i} - \delta_{1,i} + (-\kappa_{2,i}+\kappa_{1,i})\cos(\Omega) + (-\kappa_{2,r}-\kappa_{1,r})\sin\Omega\right)\partial_y
\end{aligned}
$$

Appendix B

Hydrodynamic Simulations

In this Appendix, we provide the details of the hydrodynamic equations simulations performed in section 2.3.4 & 2.4.4. We present the result using Eq. 2.9.
First, we consider a system of size $L_x * L_y$ with a spatial step dx along the x-direction and dy along the y-direction. We compute the terms with a derivative part by taking the discrete Fourier transform along the spatial coordinates (2D) with the library *FFTW*, $f_{1,\frac{x}{y}}(x,y) \rightarrow \hat{f}_{1,\frac{x}{y}}(q_x,q_y)$. This allow us to compute the different terms

$-q^2\hat{f}_{1,x}$	$\rightarrow$	$\Delta f_{1,x}$
$-q^2\hat{f}_{1,y}$	$\rightarrow$	$\Delta f_{1,y}$
$iq_x\hat{f}_{1,x}$	$\rightarrow$	$\partial_x f_{1,x}$
$iq_x\hat{f}_{1,x}$	$\rightarrow$	$\partial_y f_{1,x}$
$iq_x\hat{f}_{1,y}$,	$\rightarrow$	$\partial_x f_{1,y}$
$iq_y\hat{f}_{1,y}$	$\rightarrow$	$\partial_y f_{1,y}$
$iq_x\rho$	$\rightarrow$	$\partial_x\rho$
$iq_y\rho$	$\rightarrow$	$\partial_y\rho$

To avoid the effect of introducing aliasing errors due to nonlinearities in the numerical solution, we apply the two-thirds rule introduced by Orszag [109].

$$\hat{f}(q_x,q_y,t) = \begin{cases} \hat{f}(q_x,q_y,t) & \text{if } q_x < \frac{2}{3}q_x^{max} \text{ and } q_y < \frac{2}{3}q_y^{max} \\ 0 \quad \text{else} \end{cases}$$

Then we perform an Euler integration of Eq. 2.26 as follows

$$
\begin{aligned}
\tfrac{\rho(t+\Delta t)}{\Delta t} &= \tfrac{\rho(t)}{\Delta t} + \left(\partial_x f_{1,x}(t) + \partial_y f_{1,y}(t)\right) \\
\tfrac{f_{1,x}(t+\Delta t)}{\Delta t} &= \tfrac{f_{1,x}(t)}{\Delta t} + \alpha_{\text{BGL}}\left(\rho(t) - \rho_{c_{\text{BGL}}}\right) f_{1,x}(t) - \omega_0 f_{1,y}(t) - \Re(\xi_{\text{BGL}})|f_1(t)|^2 f_{1,x}(t) \\
&+ (\Re(\nu_{\text{BGL}}) + D_0)\Delta f_{1,x}(t) - \frac{1}{2}\partial_x \rho(t) \\
&- \Re(\gamma_{\text{BGL}})\left[f_{1,x}(t)(\partial_x f_{1,x}(t) + \partial_y f_{1,y}(t)) - f_{1,y}(t)(\partial_x f_{1,y}(t) - \partial_y f_{1,x}(t))\right] \\
&- \Re(\beta_{\text{BGL}})\left[f_{1,x}(t)(\partial_x f_{1,x}(t) - \partial_y f_{1,y}(t)) + f_{1,y}(t)(\partial_x f_{1,y}(t) + \partial_y f_{1,x}(t))\right] \\
&+ \Im(\xi_{\text{BGL}})|f_1(t)|^2 f_{1,y}(t) - \Im(\nu_{\text{BGL}})\Delta f_{1,y}(t) \\
&+ \Im(\gamma_{\text{BGL}})\left[f_{1,x}(t)(\partial_x f_{1,y}(t) - \partial_y f_{1,x}(t)) + f_{1,y}(t)(\partial_x f_{1,x}(t) + \partial_y f_{1,y}(t))\right] \\
&+ \Im(\beta_{\text{BGL}})\left[f_{1,x}(t)(\partial_x f_{1,y}(t) + \partial_y f_{1,x}(t)) - f_{1,y}(t)(\partial_x f_{1,x}(t) - \partial_y f_{1,y}(t))\right] \\
\tfrac{f_{1,y}(t+\Delta t)}{\Delta t} &= \tfrac{f_{1,y}(t)}{\Delta t} + \alpha_{\text{BGL}}\left(\rho(t) - \rho_{c_{\text{BGL}}}\right) f_{1,y}(t) + \omega_0 f_{1,x}(t) - \Re(\xi_{\text{BGL}})|f_1(t)|^2 f_{1,y}(t) \\
&+ (\Re(\nu_{\text{BGL}}) + D_0)\Delta f_{1,y}(t) - \frac{1}{2}\partial_y \rho(t) \\
&- \Re(\gamma_{\text{BGL}})\left[f_{1,x}(t)(\partial_x f_{1,y}(t) - \partial_y f_{1,x}(t)) + f_{1,y}(t)(\partial_x f_{1,x}(t) + \partial_y f_{1,y}(t))\right] \\
&- \Re(\beta_{\text{BGL}})\left[f_{1,x}(t)(\partial_x f_{1,y}(t) + \partial_y f_{1,x}(t)) - f_{1,y}(t)(\partial_x f_{1,x}(t) - \partial_y f_{1,y}(t))\right] \\
&- \Im(\xi_{\text{BGL}})|f_1(t)|^2 f_{1,x}(t) + \Im(\nu_{\text{BGL}})\Delta f_{1,x}(t) \\
&- \Im(\gamma_{\text{BGL}})\left[f_{1,x}(t)(\partial_x f_{1,x}(t) + \partial_y f_{1,y}(t)) - f_{1,y}(t)(\partial_x f_{1,y}(t) - \partial_y f_{1,x}(t))\right] \\
&- \Im(\beta_{\text{BGL}})\left[f_{1,x}(t)(\partial_x f_{1,x}(t) - \partial_y f_{1,y}(t)) + f_{1,y}(t)(\partial_x f_{1,y}(t) + \partial_y f_{1,x}(t))\right]
\end{aligned}
\tag{B.1}
$$

where the time step $\Delta t \sim 10^{-3}$ and $\mathrm{d}x$,$\mathrm{d}y \sim 0.125$. This range of integration parameters is needed because it is hard to resolve the front of the band, the center of vortices and boundaries of rotating packets.

Appendix C

Résumé de la thèse en français

C.1 Introduction à la matière active et la synchronisation

C.1.1 Qu'est que la matière active?

Pendant longtemps, la physique statistique s'est intéressée à l'étude des propriétés collectives des systèmes à l'équilibre. On considère qu'un système est à l'équilibre lorsque les différentes grandeurs ont le temps de relaxer et que le comportement du système obéit à la loi des grands nombres. On sait qu'un système est à l'équilibre lorsque certaines propriétés sont vérifiées telles que le théorème de fluctuation-dissipation ou le bilan détaillé. Malheureusement, l'ensemble des systèmes à l'équilibre ne concernent qu'une toute petite partie des systèmes qui nous entourent. Ainsi, pour un système, il y a plusieurs façons d'être hors équilibre. Une première façon simple est de prendre un système à l'équilibre et de le déplacer de son point d'équilibre. Alors, le système va relaxer vers un nouvel équilibre [1]. Pendant cette période, le système se trouve hors équilibre. Une seconde façon de faire est de mettre un système dans un état stationnaire hors équilibre, tel qu'un système en contact avec deux thermostats à des températures différentes. Ce système va alors être traversé par un flux d'énergie qui le placera hors équilibre. Une autre possibilité est que le système soit maintenu hors équilibre en son sein par des réactions chimiques. Ce dernier cas de figure est celui qui est important pour tous les systèmes vivants qui nous entourent. C'est aussi celui qui nous intéresse, car la matière active rentre dans cette catégorie.
Une définition communément admise de la matière active est : un système maintenu hors équilibre par une consommation d'énergie à l'échelle de ses constituants, de façon à les mettre en mouvement. Ainsi, le flux d'énergie est à l'échelle des constituants. Cette sous-classe de systèmes hors équilibre est intéressante, car ces systèmes partagent une propriété majeure, qui est l'existence de mouvements collectifs. De plus, cela se produit dans différentes dimensions et à différentes échelles. On peut, par exemple, citer les bancs de poissons [3], les murmurations d'oiseaux en trois dimensions [2]. En deux dimensions, on va trouver les troupeaux d'animaux [4], les colonies de bactéries [5, 6]. À une seule dimension, on peut citer les systèmes composés de moteurs moléculaires. Cependant, il

existe aussi des systèmes synthétiques composés, par exemple, de grains vibrants [8] ou de particules colloïdales [9–11].
Il y a plusieurs façons de classer les différents systèmes de la matière active, mais certaines distinctions sont fondamentales. Dans un premier temps, on va différencier les systèmes où les constituants interagissent avec le fluide environnant et les autres où l'interaction y est négligeable. En effet, les particules se déplaçant dans un fluide vont le mettre en mouvement et ainsi interagir à longue portée avec les autres particules. Lorsque ces interactions sont négligeables, on dit que le système est *sec*. Dans le cas contraire, on dit que le système est *mouillé*. Dans cette thèse, nous allons uniquement nous intéresser aux systèmes dits sec. Parmi ces systèmes où l'interaction est uniquement locale, il y a deux grandes catégories d'interaction. Le premier cas est lorsque les particules interagissent uniquement par répulsion, on appelle cela des systèmes de particules browniennes actives. On a alors une séparation de phase induite par la mobilité. De l'autre côté, il y a les particules qui interagissent uniquement par alignement. Cette dernière catégorie de système est appelée DADAM pour Dry, Aligning, Dilute, Active Matter [13]. Dans cette catégorie, il y a deux types d'alignements possibles. Le premier type est l'alignement polaire, alors deux particules vont tendre à aligner leur vitesse de façon à avoir le même vecteur vitesse. Le second type est l'alignement nématique, alors les deux particules vont avoir tendance à mettre leur vecteur vitesse parallèle.
Historiquement, l'étude théorique de la matière active est née en 1995 avec l'introduction du modèle de Vicsek [16] et ensuite les équations de Toner et Tu [18, 20, 29, 33]. Le modèle de Vicsek est un modèle minimal qui correspond au cas limite DADAM avec un alignement polaire pur. Maintenant, nous avons compris dans quel paysage s'inscrit cette thèse, nous allons rapidement présenter les résultats du modèle de Vicsek, car ils sont la base de ce travail.

C.1.2 Le modèle de Vicsek

Comme nous l'avons évoqué précédemment, le modèle de Vicsek est un cas limite. Dans ce modèle, on considère un système composé de N particules autopropulsées à vitesse constante v_0. De plus, ces particules vont localement s'aligner. Cet alignement s'effectue avec la direction moyenne des particules dans leur voisinage plus un bruit qui modélise que les particules ne s'alignent pas parfaitement à chaque pas de temps. On définit le voisinage d'une particule comme toutes les particules contenues dans un disque de rayon R centré sur cette même particule. Donc, le modèle de Vicsek est basé sur une compétition entre l'alignement et le bruit.
Le modèle de Vicsek est un modèle remarquable, car en deux dimensions, il permet de décrire une transition de phase entre une phase désordonnée où les particules se comportent comme dans un gaz et une phase ordonnée où les particules se déplacent toutes dans la même direction. Cela est impossible pour un système à l'équilibre d'après le théorème de Mermin-Wagner. Historiquement, cette transition de phase a été présentée comme une transition de phase du second ordre par Vicsek et ses collaborateurs. Cependant, après

les publications de Hugues Chaté et collaborateurs [17], la transition de phase du modèle de Vicsek est maintenant comprise comme une transition du premier ordre. Il y a donc trois phases : la phase désordonnée dit gaz, la phase ordonnée dit liquide, et la phase de coexistence. Cette phase de coexistence est particulière, car il y a coexistence entre un gaz et une phase ordonnée qui se présente sous forme de bandes. Dans ces bandes, les particules sont synchronisées avec une direction perpendiculaire à la direction d'élongation de la bande. Ainsi, la phase de bande et la phase de liquide ne présentent pas les mêmes symétries. Cela se traduit dans le diagramme des phases par l'absence de point critique, on peut voir cela comme l'envoi du point critique à l'infini.

Dans le précédent paragraphe, nous avons décrit le modèle de Vicsek historique qui est un modèle à temps discret. Cette thèse se base sur une autre formulation du modèle de Vicsek, qui est le modèle de Vicsek en temps continu. Ainsi, les équations se formulent différemment, mais les résultats restent exactement les mêmes.

Le modèle de Vicsek est un modèle microscopique qui décrit les règles d'évolutions des différents constituants. Cependant, lorsque le nombre de constituants devient très grand, il devient difficile de raisonner à l'échelle d'un individu et il est bien plus commode de traiter le problème comme s'il s'agissait d'un milieu continu. C'est exactement l'approche adoptée en hydrodynamique. Ainsi, je vais vous présenter trois manières de passer d'un modèle discret à un modèle continu. De manières générales, il y a deux façons de faire. La première façon de faire est de réfléchir à partir des symétries du problème. La seconde façon est de réaliser un maillage grossier d'un modèle microscopique.

Ainsi, en 1995 Toner et Tu ont écrit les premières équations hydrodynamiques du modèle de Vicsek [18, 20, 29, 33]. Pour ce faire, ils ont écrit des équations génériques qui répondent aux symétries du problème. Ensuite, ils ont utilisé les outils du groupe de renormalisation pour effectuer un certain nombre de prédictions. Malheureusement, lorsqu'ils ont écrit leurs équations, ils ont oublié un terme. Cependant, leurs premières prédictions restent qualitativement valables. Ainsi, ils ont prédit l'existence d'une transition de phase vers une phase ordonnée en deux dimensions. Néanmoins, cette approche présente deux problèmes. Le premier est qu'il n'y a aucun lien entre les paramètres des équations et les paramètres microscopiques. Le second, est le fait qu'il ne soit pas possible de prédire la nature de la transition avec ces outils.

Les deux dernières approches sont basées sur le maillage grossier d'un modèle microscopique. Dans un premier temps, nous allons présenter l'approche dite de Boltzmann-Ginzburg-Landau (BGL). Cette approche considère un modèle légèrement différent du modèle de Vicsek, mais appartenant à la même classe d'universalité [22, 23]. Dans ce cas, on considère un modèle de N particules. Les particules évoluent en ligne droite et peuvent subir une diffusion et une collision. À partir de ce modèle, il est possible d'écrire une équation de Boltzmann en effectuant deux hypothèses. La première hypothèse est

que le système est dilué, et qu'il n'y a que des collisions entre deux particules. La seconde hypothèse est celle de chaos moléculaire, cela implique l'absence de corrélations entre les particules. Une fois l'équation de Boltzmann écrite, il est possible d'écrire une équation hydrodynamique en suivant une approche à la Ginzburg-Laudau. On obtient des équations hydrodynamiques qui possèdent la même forme que les équations de Toner et Tu. Cependant, avec l'approche de BGL, on connaît parfaitement la dépendance des coefficients des équations en fonction des paramètres microscopiques. Ainsi, il est possible de les étudier dans le même espace des phases que le modèle microscopique. Moyennant quelques considérations, l'approche de BGL permet de retrouver qualitativement le diagramme des phases du modèle de Vicsek. Donc, il est prédit une transition de phase du premier ordre et les différentes phases (gaz, liquide, bandes).

La dernière approche est basée sur une équation de Fokker-Planck. Le modèle microscopique est le suivant : on considère des particules subissant un bruit blanc et interagissant via une interaction potentielle de la même forme que le modèle de Vicsek en temps continu. Ensuite, sous l'hypothèse d'un système dense [47, 48], il est possible d'écrire une équation de Fokker-Planck. Une fois que l'équation est écrite, il suffit de négliger le terme de bruit et de suivre la méthode de Ginzburg-Landau. On obtient alors des équations hydrodynamiques ayant la même structure que les équations de Toner-Tu et BGL, mais avec des coefficients différents. Cette approche étant basée sur un maillage grossier, nous gardons le lien entre les paramètres microscopiques et les coefficients. Malheureusement, on ne retrouve pas le diagramme des phases du modèle de Vicsek avec cette méthode.

Jusqu'ici, nous avons présenté les connaissances générales autour du modèle de Vicsek. Nous avons vu que le modèle de Vicsek est un modèle minimal permettant de décrire la transition de phase vers un mouvement collectif. Cependant, la plupart des systèmes ne peuvent pas être modélisés par le modèle de Vicsek. C'est pourquoi il est intéressant de voir comment se comporte le modèle de Vicsek lorsque l'on rajoute des ingrédients. Dans cette étude, ce qui nous intéresse est la robustesse du modèle de Vicsek face à différents désordres. Dans l'article de Yu Duan [61], ils étudient l'effet d'un désordre spatial sur le modèle de Vicsek et ils montrent que la robustesse du modèle de Vicsek dépend de la forme du désordre.

Maintenant que nous avons resitué le contexte de notre étude et les différentes méthodes qui permettent d'obtenir des équations hydrodynamiques, nous allons nous intéresser à l'étude de la synchronisation.

C.1.3 Le modèle de Kuramoto

Le modèle de Kuramoto est un modèle introduit pour étudier la synchronisation des oscillateurs [73]. C'est aussi un modèle minimal, car il ne considère que deux ingrédients : la fréquence propre des oscillateurs et un terme de couplage entre les oscillateurs. Il

s'énonce simplement: l'évolution temporelle de la phase des oscillateurs est donnée par la fréquence propre des oscillateurs plus un terme de couplage avec les autres oscillateurs en fonction de leur différence de phase. Il y a donc une compétition entre le désordre gelé de chiralité et le terme de synchronisation. De plus, tous les oscillateurs interagissent entre eux, cela signifie que le modèle est en dimension infinie. Aussi, c'est un modèle remarquable, car il est possible de le résoudre analytiquement [74]. Ainsi, il permet de décrire une transition de phase entre une phase désordonnée et une phase où une fraction macroscopique des oscillateurs sont en phase. La nature de la transition de phase va dépendre de la distribution des fréquences propres. Dans notre problème, seulement trois distributions de fréquences propres vont nous intéresser. La première est la distribution unimodal où tous les oscillateurs ont la même fréquence propre. Dans le cadre du modèle de Kuramoto, cette distribution ne présente aucun intérêt car un changement de coordonnées permet alors de supprimer le terme de fréquence propre et il n'y a qu'une phase synchronisée. La seconde distribution est la distribution Gaussienne, alors le modèle de Kuramoto décrit une transition entre une phase désordonnée et une phase où une partie macroscopique des oscillateurs sont en phase. Dans ce cas de figure, la transition se trouve être du second ordre. La troisième distribution est la distribution bimodale, où il y a deux populations ayant chacune une fréquence propre donnée, et il y a une nouvelle phase appelée onde stationnaire. Dans cette nouvelle phase, il y a une synchronisation partielle dans chaque sous-population. Lorsque l'on continue d'augmenter le couplage, ces deux groupes d'oscillateurs synchronisés fusionnent.

Le modèle de Kuramoto est un modèle minimal qui permet de décrire la synchronisation d'oscillateurs et trouve de nombreuses situations d'application. Néanmoins, on peut lui rajouter des ingrédients pour essayer d'étendre son domaine d'application. Ainsi, si on ajoute un terme de bruit, cela permet de prendre en compte des aspects difficile à décrire à l'échelle microscopique tel que des oscillateurs légèrement non-identique dans leur couplage. Dans ce cas de figure, si le bruit reste raisonnable, les résultats du modèle de Kuramoto restent inchangés.

De plus, nous avons vu que le modèle de Kuramoto est énoncé en dimension infinie. Si maintenant, on se place en dimension finie, c'est-à-dire que l'on considère un réseau et qu'à chaque nœud du réseau on place un oscillateur. Alors, les oscillateurs ne vont interagir qu'avec les nœuds voisins [84]. Dans ce cas de figure, il n'est pas possible d'obtenir de synchronisation en dimensions $d \leq 2$. On obtient une synchronisation de domaine de taille finie pour $2 < d \leq 4$. Pour $d > 4$, on retrouve les résultats du modèle global.

C.1.4 Matière active chirale

Dans ce paragraphe, nous allons présenter succinctement ce qu'est la matière active chirale et pourquoi cela présente un intérêt. Dans notre étude, la matière active chirale désigne

des particules actives qui vont décrire des cercles dans un espace vide où il n'y a aucune interaction. Ces particules se différencient des particules actives dans le modèle de Vicsek, qui elles vont en ligne droite. Cela présente un intérêt, car il existe des situations expérimentales où les particules présentent ce comportement.

C.2 Le modèle de Kuramoto-Vicsek

C.2.1 Présentation du modèle de Kuramoto-Vicsek

Dans cette section, nous allons présenter ce que l'on appelle le modèle de Kuramoto-Vicsek (KVM). L'objectif est d'avoir un modèle simple qui permette de décrire le comportement des particules actives chirales. Ainsi, on peut se poser la question comment modifier le modèle de Vicsek de façon à décrire le comportement de ces particules. Une possibilité est de changer la règle pour la mise à jour de l'orientation des particules. Pour ce faire, il suffit d'ajouter une pulsation propre à chaque particule, ce qui aboutit à une compétition entre trois termes : la pulsation propre de la particule, l'alignement sur ses plus proches voisins, et le terme de bruit. La pulsation propre joue le rôle du désordre gelé de chiralité. Il prend la même forme que dans le modèle de Kuramoto.
Il existe une seconde interprétation. Dans le modèle de Kuramoto, on considère la pulsation des oscillateurs, mais on souhaite adapter ce modèle à des particules actives chirales. Pour cela, il suffit d'assimiler la phase d'un oscillateur à la direction de sa polarisation et d'ajouter l'équation d'auto-propulsion.
Ainsi, le KVM peut être vu comme un modèle de Vicsek avec un désordre gelé de chiralité ou comme un modèle de Kuramoto avec auto-propulsion. Cela soulève plusieurs questions intéressantes. Ainsi, nous savons que le modèle de Vicsek permet une synchronisation des vitesses en deux dimensions, contrairement au modèle de Kuramoto. Donc est-il possible d'avoir une synchronisation des vitesses avec le KVM? Ensuite, la matière active chirale montre de nouvelles phases tel que des vortex. Donc est-ce que le KVM est-il un modèle minimal capable de reproduire la phénoménologie de la matière active chirale?

Pour répondre à toutes ces questions, nous avons étudié trois distributions différentes. L'étude est découpée principalement en deux approches, la première se fait à travers des simulations des équations microscopiques et la seconde à travers une approche hydrodynamique.

C.2.2 Résultats du KVM pour une distribution de chiralité gaussienne

Dans cette section, nous allons présenter les résultats pour une distribution de chiralité suivant une loi Gaussienne. Le désordre de chiralité caractérise alors l'écart type de la loi

Gaussienne. Nous allons nous limiter aux résultats numériques, car les approches analytique basées sur un maillage grossier se trouvent être beaucoup plus difficiles à appliquer dans le cas d'une distribution continue.
Pour une chiralité nulle nous trouvons les résultats du modèle de Vicsek standard. Lorsque l'on augmente la valeur de la chiralité la phase de liquide résiste. Si l'on continue d'augmenter la chiralité, pour une valeur donnée, on observe une transition vers une phase de vortex avec ségrégation des particules en fonction du signe de leur chiralité. Lorsque l'on se place à un niveau de bruit correspondant à la phase de bande, on observe que lorsque l'on augmente la chiralité les bandes résistent jusqu'à une valeur non négligeable. Ensuite, la phase de bandes laisse place à une phase de vortex. Dans le cas de cette disribution, nous n'observons jamais de paquets tournants, cela est compréhensible car, dans le cas d'une distribution bimodale, on observe ces paquets tournants pour les grandes valeurs de chiralité. Dans une distribution Gaussienne, la plus grande partie des particules possèdent une chiralité proche de zéro. Aussi, une étude plus approfondie, nous apprend que les bandes et les vortex coexistent. L'étude des effets de taille finie nous apprend que la valeur de la transition entre le liquide et les vortex décroît en loi puissance. On peut donc dire que dans la limite des grands systèmes, la phase de synchronisation n'existe plus.

C.2.3 Résultats du KVM pour une distribution de chiralité unimodale

C.2.3.1 Résultats à l'échelle microscopique

Dans ce paragraphe, nous allons présenter les résultats de simulations à l'échelle microscopique, c'est-à-dire à l'échelle de nos particules actives chirales. Nous avons simulé des systèmes avec un grand nombre de particules pour une distribution unimodal. Donc toutes les particules possèdent la même pulsation propre. À chiralité nulle, nous retrouvons le modèle de Vicsek, ce qui est rassurant quant à notre implémentation numérique de la chiralité. Ensuite, lorsqu'on augmente la valeur de la chiralité, on remarque que la phase liquide devient tournante, c'est-à-dire que la polarisation du liquide tourne dans le temps. Cela est normal et correspond à un liquide si on effectue un changement de coordonnées dans un référentiel tournant. Cependant, lorsque l'on continue d'augmenter la chiralité, on voit apparaître une nouvelle phase constituée d'une goutte de liquide tournant en équilibre avec un gaz dilué. De plus, après une étude plus approfondie, il apparaît que la séparation de phase est macrophase, c'est-à-dire que lorsque l'on augmente le nombre de particules dans le système, la taille de la goutte de liquide augmente et non le nombre de goutte. Si maintenant, on se place au niveau de bruit qui correspond à une phase de bandes, lorsque l'on augmente la chiralité les bandes résistent dans un premier temps. Cependant, passé un certain point elles laissent place à une phase de vortex. Les vortex sont des structures globalement circulaires dans lesquels la direction de la polarisation tourne autour d'un centre correspondant au centre de la structure. Ensuite, on peut encore continuer à augmenter la chiralité et la phase de vortex laisse place à la phase de goutte de liquide. Après

des études plus approfondies, on comprend que les vortex sont une séparation microphase et qu'il y a une zone de coexistence entre les bandes et les vortex. De plus, la phase de désordre n'est pas affectée par la chiralité. Il nous reste un dernier point à étudier. En effet, historiquement Vicsek a prétendu avoir découvert une transition du second ordre à cause des effets de taille finie. Dans notre cas, une étude plus fine des effets de taille finie nous montre que le liquide tournant n'existe pas dans la limite des grands systèmes. En effet, la valeur à laquelle la transition se produit décroît en loi puissance avec la taille du système. Ainsi, la phase de synchronisation ne résiste pas à l'introduction d'un désordre gelé de chiralité en deux dimensions.

C.2.3.2 Approche de Fokker-Planck

Nous avons détaillé précédemment au paragraphe C.1.2 comment passer d'un modèle microscopique à une description en terme d'équations hydrodynamiques. Ici, nous allons utiliser la méthode basée sur l'écriture d'une équation de Fokker-Planck. Ainsi, nous trouvons une équation ayant la même structure que l'équation de Toner et Tu. Or, tous les coefficients sont complexes et dépendent des coefficients microscopiques, la partie imaginaire est pilotée par la chiralité. Ensuite, nous avons étudié la stabilité linéaire de la phase homogène désordonnée et ordonnée. Nous trouvons que la stabilité linéaire de la phase désordonnée dépend du signe d'un des coefficients des équations et change de signe en fonction de la valeur de la densité. Cela est similaire au cas Vicsek pur. Pour le cas de la phase homogène ordonnée, on trouve qu'elle est instable partout. Il est difficile de conclure quoique ce soit, car c'est aussi le cas pour le modèle de Vicsek pur alors que la phase liquide existe bien microscopiquement. Ainsi, cette approche ne nous permet pas de conclure précisément.

C.2.3.3 Approche de BGL

Après avoir détaillé les résultats de l'approche basée sur l'équation de Fokker-Planck. Nous allons nous intéresser aux résultats basés sur l'écriture d'une équation de Boltzmann. Nous suivons l'approche expliquée dans le paragraphe C.1.2 pour écrire les équations hydrodynamiques. Nos équations ont la même structure que les équations hydrodynamiques pour le cas Vicsek mais comme dans C.2.3.2 les coefficients sont maintenant complexes avec une dépendance aux paramètres microscopiques. Ici aussi, la partie imaginaire est pilotée par la chiralité. Ensuite, nous nous sommes intéressés à la stabilité linéaire des solutions homogènes. Dans ce cas de figure, cela est plus pertinent, car cette approche est capable de reproduire le diagramme des phases microscopiques du modèle de Vicsek. Pour la phase homogène désordonnée, la stabilité est toujours pilotée par le changement de signe d'un coefficient en fonction de la densité. On retrouve le même comportement que pour le cas Vicsek pur. Ensuite, la solution de liquide tournant n'est par contre jamais stable lorsque

l'on met la moindre chiralité. Contrairement au cas du liquide pour le modèle de Vicsek, qui présente une zone de stabilité. On retrouve donc le comportement du KVM au niveau microscopique.
De plus, on peut étudier les solutions non-linéaires des équations en les simulant numériquement. En simulant ces équations, on trouve bien la phase de vortex, et aussi une phase de paquets tournants. Néanmoins, nous ne sommes pas capables de trouver une goutte de liquide tournant, cela est peut-être dû au maillage grossier du modèle microscopique. Si on assimile la phase de paquets tournant à la goutte de liquide tournant, il est possible de retrouver qualitativement le diagramme des phases du KVM. Ainsi, cette approche basée sur l'écriture d'une équation de Boltzmann, permet de retrouver qualitativement le comportement du KVM.

C.2.4 Résultats du KVM pour une distribution de chiralité bimodale

C.2.4.1 Résultats à l'échelle microscopique

Nous allons maintenant nous intéresser aux résultats microscopiques dans le cas d'une distribution bimodale de chiralité, c'est-à-dire que la moitié des particules possèdent une chiralité positive et l'autre moitié la chiralité opposée. Pour une chiralité nulle, nous retrouvons bien le modèle de Vicsek avec une phase de gaz, de bandes, et de liquide. Lorsque l'on commence à augmenter la chiralité, la phase de liquide persiste pendant un moment. Cependant, une fois que l'on dépasse une certaine valeur une nouvelle phase apparaît. Dans cette nouvelle phase, il y a une ségrégation entre les particules de chiralité positive et les particules de chiralité négative. De plus, dans cette nouvelle phase, les particules forment des paquets tournants en équilibre avec un gaz dilué. Si maintenant, on se place au niveau du bruit correspondant à la phase de bandes, lorsque l'on augmente la chiralité les bandes résistent un certain temps. Après une certaine valeur, les bandes laissent place à une phase de vortex en équilibre avec un gaz dilué. De même, lorsque l'on continue d'augmenter la chiralité, les vortex laissent place à la phase de paquets tournants. De plus, la phase de désordre n'est pas affectée par la chiralité.
Des études plus fines nous permettent de conclure que la phase de vortex, et de paquets tournants sont des séparations microphases. De plus, on peut voir une certaine coexistence entre les vortex et les bandes. Aussi, il existe une coexistence entre les vortex et les paquets tournants au niveau de la frontière.
Si on se penche sur les effets de taille finie, on se rend compte que la phase de liquide décroît lorsque la taille du système augmente. La valeur de la frontière décroît en suivant une loi puissance. Ainsi, dans la limite des grands systèmes la phase de liquide où les particules sont synchronisées n'existe pas.

C.2.4.2 Approche de Fokker-Planck

Pour cette distribution bimodale, nous devons maintenant considérer le cas de deux populations en interaction. Il est donc possible d'écrire deux équations de Fokker-Planck couplées et d'en déduire un système de six équations hydrodynamiques couplées. Les coefficients sont toujours complexes et l'on retrouve une première partie de l'équation pour la polarisation qui possède une structure à la Toner et Tu puis une seconde partie de l'équation qui regroupe des termes croisés entre les deux populations. De même que pour le cas d'une distribution unimodale, on retrouve une stabilité linéaire du gaz gouvernée par le même coefficient et une phase de liquide qui est instable. Cependant, il est difficile de tirer plus de conclusions au vu des résultats de cette approche pour le cas Vicsek standard.

C.2.4.3 Approche de BGL

À présent, nous allons présenter l'écriture des équations hydrodynamiques pour la distribution bimodale en suivant l'approche de BGL. Il faut, dans un premier temps, écrire deux équations de Boltzmann couplées. Ensuite, on applique la méthode de Ginzburg-Landau. On obtient ainsi un système de six équations couplées. Les équations sur la polarisation peuvent être séparées en deux parties : une première partie qui a une structure à la Toner Tu, et une seconde partie qui correspond aux termes croisés entre les deux populations. On peut noter qu'il y a une différence dans les coefficients et dans les termes croisés entre l'approche de BGl et l'approche de Fokker-Planck. Donc pour une distribution bimodale nous avons des équations avec une structure différente à l'échelle non-linéaire uniquement. Ensuite, on effectue la stabilité linéaire pour les solutions homogènes. Pour la solution désordonnée, on trouve le même résultat que pour la distribution unimodale. Pour la solution ordonnée, on trouve que la solution est instable dès qu'il y a un désordre de chiralité. De plus, nous avons essayé de caractériser les effets de taille finie à l'aide de la stabilité linéaire. Ainsi, nous avons effectivement trouvé que la valeur de la frontière de l'existence du liquide décroît en loi puissance. Néanmoins, nous avons trouvé un exposant différent par rapport aux résultats microscopiques. Cela peut venir de plusieurs choses. La première possibilité est que la valeur de l'exposant est déterminée par des effets non-linéaire. Une seconde possibilité est que le maillage grossier permettant d'écrire des équations hydrodynamiques efface certaines dépendances. Pour résumer, l'étude au niveau linéaire permet de comprendre la stabilité du gaz et l'absence de stabilité du liquide.
Ensuite, nous avons poursuivi notre étude au niveau non-linéaire en effectuant les simulations des équations hydrodynamiques. Ces simulations nous ont permis de retrouver la phase de vortex et de paquets tournants. Il est aussi possible de retrouver qualitativement le diagramme des phases microscopique. Encore une fois, l'approche de BGL permet d'obtenir une description qualitative du KVM et de comprendre les résultats numériques.

C.3 Conclusion

Dans cette thèse, nous avons présenté le modèle de Vicsek qui peut être vu comme un cas limite de la matière active. Ce modèle permet de décrire une transition de phase entre une phase désordonnée et une phase synchronisée, même en deux dimensions. Ce modèle est crucial car il joue le rôle de point de départ pour étudier les propriétés des mouvements collectifs dans la matière active. Ainsi, différents groupes ont essayé d'étendre la portée du modèle de Vicsek en apportant des modifications à celui-ci. En particulier, certaines personnes ont essayé d'ajouter un désordre spatial fixe. Dans ce cas, la phase de synchronisation des particules ne résiste pas toujours à l'introduction de ce désordre.
Notre but était d'étudier la matière active chirale, pour laquelle les constituants décrivent des cercles dans un espace vide. Pour ce faire, nous avons introduit un nouveau modèle qui peut être vu comme un modèle de Vicsek où l'on ajoute du désordre gelé dans l'esprit du modèle de Kuramoto. Un autre point de vue est que notre modèle est un modèle de Kuramoto où l'on rajoute l'auto-propulsion des oscillateurs. Ce nouveau modèle appelé modèle de Kuramoto-Vicsek est très intéressant, car le modèle de Kuramoto ne permet pas d'avoir une phase synchronisée en deux dimensions. Une des problématiques était de comprendre si le KVM présentait une phase synchronisée. De plus, nous avons cherché à comprendre si le modèle permettait de retrouver des structures présentent dans la matière active chirale tel que les vortex ou des structures tournantes dans le temps.

Dans la première partie, nous avons étudié une distribution de chiralité Gaussienne avec une moyenne nulle. Pour cette distribution, nous avons effectué uniquement une étude au niveau microscopique à l'aide de simulations. Certains résultats sont similaires à l'étude de la distribution bimodale comme la ségrégation des particules en fonction du signe de leur chiralité. Ainsi, nous trouvons que la phase synchronisée disparaît dans la limite des grands systèmes. Ici, nous ne sommes capables d'observer qu'une seule nouvelle phase qui est la phase de vortex.

Dans une seconde partie, nous nous sommes intéressé à la distribution la plus simple possible qui est une distribution unimodale où toutes les particules possèdent la même chiralité. Nous l'avons étudié à l'aide de simulations numériques à l'échelle microscopique. Ces simulations nous ont permis de découvrir de nouvelles phases qui sont une phase de vortex et une phase de goutte de liquide tournante. Néanmoins, après une étude plus fine nous avons conclu que la phase liquide, aussi appelée phase synchronisée, disparaît dans la limite des systèmes de grandes tailles. Pour essayer de comprendre les résultats microscopiques, nous avons écrit des équations hydrodynamiques en effectuant un maillage grossier de deux modèles microscopiques différents. Le premier modèle basé sur l'écriture d'une équation de Fokker-Planck ne nous a pas permis de faire des conclusions très utiles. Le second modèle basé sur l'écriture d'une équation de Boltzmann a conduit à des résultats plus intéressants. En effet, il permet de comprendre que la phase synchronisée n'est pas stable au niveau linéaire. De plus, il permet aussi de décrire qualitativement le diagramme

des phases microscopiques.

Dans une dernière partie, nous avons travaillé sur une distribution bimodale, c'est-à-dire que la moitié des particules possèdent une chiralité et l'autre moitié possèdent la chiralité opposée. Ainsi, nous avons étudié cette distribution à l'aide de simulations numériques et le premier résultat est que l'on observe une ségrégation entre les particules avec une chiralité positive et celles qui ont une chiralité négative. Avec cette distribution ce n'est plus possible d'observer la phase de goutte de liquide tournant, à la place on observe une phase composée de plusieurs paquets tournants. Aussi, la phase de vortex persiste. Cependant, comme pour la distribution précédente la phase de liquide disparaît dans la limite des systèmes des grandes tailles. Notre approche théorique basée sur l'écriture d'une équation de Foker-Planck de ne permet pas de faire des conclusions claires contrairement à l'approche basée sur l'écriture d'une équation de Boltzmann. En effet, avec la seconde approche nous sommes capables de reconstituer le diagramme des phases microscopiques de façon qualitative.

De manière générale, nous voyons que la phase synchronisée du modèle de Vicsek ne résiste pas à l'introduction d'un désordre gelé de chiralité à la Kuramoto. Cependant, le modèle permet de retrouver différentes phases que l'on observe dans des systèmes de matière active chirale. Pour poursuivre l'étude de ce modèle on peut avancer certains points. On peut améliorer notre description continue en prenant en compte la chiralité dans notre noyau de collision ou étudier le système d'équations avant la troncation. De plus, nous avons étudié uniquement l'alignement ferro-magnétique alors qu'il semble que l'alignement nématique présente aussi la disparition de la phase liquide. Ainsi, on pourrait dériver des équations hydrodynamiques pour le cas nématique. Ensuite, nous avons présenté le modèle de Kuramoto qui ne permet pas d'observer une phase synchronisée en 2D, cependant en 3D il y a une synchronisation partielle des fréquences qui est observée. Ainsi, il serait pertinent d'écrire et d'étudier un modèle de KVM en 3D.

Bibliography

[1] J. R. Gomez-Solano, A. Petrosyan, S. Ciliberto, and C. Maes, "Fluctuations and response in a non-equilibrium micron-sized system", Journal of Statistical Mechanics: Theory and Experiment **2011**, P01008 (2011).

[2] A. Cavagna, A. Cimarelli, I. Giardina, G. Parisi, R. Santagati, F. Stefanini, and M. Viale, "Scale-free correlations in starling flocks", Proceedings of the National Academy of Sciences **107**, 11865–11870 (2010).

[3] J. Gautrais, C. Jost, M. Soria, A. Campo, S. Motsch, R. Fournier, S. Blanco, and G. Theraulaz, "Analyzing fish movement as a persistent turning walker", Journal of Mathematical Biology **58**, 429–445 (2009).

[4] J. Buhl, D. J. T. Sumpter, I. D. Couzin, J. J. Hale, E. Despland, E. R. Miller, and S. J. Simpson, "From Disorder to Order in Marching Locusts", Science **312**, 1402–1406 (2006).

[5] D. Nishiguchi, K. H. Nagai, H. Chaté, and M. Sano, "Long-range nematic order and anomalous fluctuations in suspensions of swimming filamentous bacteria", Physical Review E **95**, 020601 (2017).

[6] H. P. Zhang, A. Be'er, E. L. Florin, and H. L. Swinney, "Collective motion and density fluctuations in bacterial colonies", Proceedings of the National Academy of Sciences **107**, 13626–13630 (2010).

[7] Y. Sumino, K. H. Nagai, Y. Shitaka, D. Tanaka, K. Yoshikawa, H. Chaté, and K. Oiwa, "Large-scale vortex lattice emerging from collectively moving microtubules", Nature **483**, 448–452 (2012).

[8] J. Deseigne, O. Dauchot, and H. Chaté, "Collective Motion of Vibrated Polar Disks", Physical Review Letters **105**, 098001 (2010).

[9] A. Bricard, J.-B. Caussin, N. Desreumaux, O. Dauchot, and D. Bartolo, "Emergence of macroscopic directed motion in populations of motile colloids", Nature **503**, 95–98 (2013).

[10] A. Bricard, J.-B. Caussin, D. Das, C. Savoie, V. Chikkadi, K. Shitara, O. Chepizhko, F. Peruani, D. Saintillan, and D. Bartolo, "Emergent vortices in populations of colloidal rollers", Nature Communications **6**, 7470 (2015).

[11] V. Narayan, S. Ramaswamy, and N. Menon, "Long-Lived Giant Number Fluctuations in a Swarming Granular Nematic", Science **317**, 105–108 (2007).

[12] M. Rubenstein, A. Cornejo, and R. Nagpal, "Programmable self-assembly in a thousand-robot swarm", Science **345**, 795–799 (2014).

[13] H. Chaté, "Dry Aligning Dilute Active Matter", Annual Review of Condensed Matter Physics **11**, 189–212 (2020).

[14] O. A. Igoshin, R. Welch, D. Kaiser, and G. Oster, "Waves and aggregation patterns in myxobacteria", Proceedings of the National Academy of Sciences **101**, 4256–4261 (2004).

[15] O. A. Igoshin, D. Kaiser, and G. Oster, "Breaking symmetry in myxobacteria", Current Biology **14**, R459–R462 (2004).

[16] T. Vicsek, A. Czirók, E. Ben-Jacob, I. Cohen, and O. Shochet, "Novel Type of Phase Transition in a System of Self-Driven Particles", Physical Review Letters **75**, 1226–1229 (1995).

[17] H. Chaté, F. Ginelli, G. Grégoire, and F. Raynaud, "Collective motion of self-propelled particles interacting without cohesion", Physical Review E **77**, 046113 (2008).

[18] J. Toner and Y. Tu, "Long-Range Order in a Two-Dimensional Dynamical XY Model: How Birds Fly Together", Physical Review Letters **75**, 4326–4329 (1995).

[19] N. D. Mermin and H. Wagner, "Absence of Ferromagnetism or Antiferromagnetism in One- or Two-Dimensional Isotropic Heisenberg Models", Physical Review Letters **17**, 1133–1136 (1966).

[20] J. Toner and Y. Tu, "Flocks, herds, and schools: A quantitative theory of flocking", Physical Review E **58**, 4828–4858 (1998).

[21] G. Grégoire and H. Chaté, "Onset of Collective and Cohesive Motion", Physical Review Letters **92**, 025702 (2004).

[22] E. Bertin, M. Droz, and G. Grégoire, "Boltzmann and hydrodynamic description for self-propelled particles", Physical Review E **74**, 022101 (2006).

[23] E. Bertin, M. Droz, and G. Grégoire, "Hydrodynamic equations for self-propelled particles: microscopic derivation and stability analysis", Journal of Physics A: Mathematical and Theoretical **42**, 445001 (2009).

[24] E. Bertin, F. Ginelli, and H. Chaté, "Boltzmann-Ginzburg-Landau approach for continuous descriptions of generic Vicsek-like models", The European Physical Journal Special Topics **223**, 10.1140/epjst/e2014-02193-y (2014).

[25] A. P. Solon, H. Chaté, and J. Tailleur, "From Phase to Micro-Phase Separation in Flocking Models: The Essential Role of Non-Equilibrium Fluctuations", Physical Review Letters **114**, 068101 (2015).

[26] A. Czirók, H. E. Stanley, and T. Vicsek, "Spontaneously ordered motion of self-propelled particles", Journal of Physics A: Mathematical and General **30**, 1375–1385 (1997).

[27] D. Martin, H. Chaté, C. Nardini, A. Solon, J. Tailleur, and F. Van Wijland, "Fluctuation-Induced Phase Separation in Metric and Topological Models of Collective Motion", Physical Review Letters **126**, 148001 (2021).

[28] F. Ginelli and H. Chaté, "Relevance of Metric-Free Interactions in Flocking Phenomena", Physical Review Letters **105**, 168103 (2010).

[29] J. Toner, Y. Tu, and S. Ramaswamy, "Hydrodynamics and phases of flocks", Annals of Physics, Special Issue **318**, 170–244 (2005).

[30] Z. Csahók and A. Czirók, "Hydrodynamics of bacterial motion", Physica A: Statistical Mechanics and its Applications **243**, 304–318 (1997).

[31] R. Aditi Simha and S. Ramaswamy, "Hydrodynamic Fluctuations and Instabilities in Ordered Suspensions of Self-Propelled Particles", Physical Review Letters **89**, 058101 (2002).

[32] R. A. Simha and S. Ramaswamy, "Statistical hydrodynamics of ordered suspensions of self-propelled particles: waves, giant number fluctuations and instabilities", Physica A: Statistical Mechanics and its Applications, Invited Papers from the 21th IUPAP International Conference on St Atistical Physics **306**, 262–269 (2002).

[33] J. Toner, "Reanalysis of the hydrodynamic theory of fluid, polar-ordered flocks", Physical Review E **86**, 031918 (2012).

[34] T. Hanke, C. A. Weber, and E. Frey, "Understanding collective dynamics of soft active colloids by binary scattering", Physical Review E **88**, 052309 (2013).

[35] E. Carlen, P. Degond, and B. Wennberg, "Kinetic limits for pair-interaction driven master equations and biological swarm models", Mathematical Models and Methods in Applied Sciences **23**, 1339–1376 (2013).

[36] E. Carlen, R. Chatelin, P. Degond, and B. Wennberg, "Kinetic hierarchy and propagation of chaos in biological swarm models", Physica D: Nonlinear Phenomena **260**, 90–111 (2013).

[37] B. Mahault, "Outstanding problems in the statistical physics of active matter", PhD thesis (2018).

[38] A. Peshkov, "Boltzmann-ginzburg-landau approach to simple models of active matter", PhD thesis (2013).

[39] A. P. Solon, J.-B. Caussin, D. Bartolo, H. Chaté, and J. Tailleur, "Pattern formation in flocking models: A hydrodynamic description", Physical Review E **92**, 062111 (2015).

[40] B. Mahault, A. Patelli, and H. Chaté, "Deriving hydrodynamic equations from dry active matter models in three dimensions", Journal of Statistical Mechanics: Theory and Experiment **2018**, 093202 (2018).

[41] B. Mahault and H. Chaté, "Long-Range Nematic Order in Two-Dimensional Active Matter", Physical Review Letters **127**, 048003 (2021).

[42] E. Bertin, H. Chaté, F. Ginelli, S. Mishra, A. Peshkov, and S. Ramaswamy, "Mesoscopic theory for fluctuating active nematics", New Journal of Physics **15**, 085032 (2013).

[43] A. Peshkov, I. S. Aranson, E. Bertin, H. Chaté, and F. Ginelli, "Nonlinear Field Equations for Aligning Self-Propelled Rods", Physical Review Letters **109**, 268701 (2012).

[44] A. Peshkov, E. Bertin, F. Ginelli, and H. Chaté, "Boltzmann-Ginzburg-Landau approach for continuous descriptions of generic Vicsek-like models", The European Physical Journal Special Topics **223**, 1315–1344 (2014).

[45] S. Ngo, A. Peshkov, I. S. Aranson, E. Bertin, F. Ginelli, and H. Chaté, "Large-Scale Chaos and Fluctuations in Active Nematics", Physical Review Letters **113**, 038302 (2014).

[46] B. Mahault, X.-c. Jiang, E. Bertin, Y.-q. Ma, A. Patelli, X.-q. Shi, and H. Chaté, "Self-Propelled Particles with Velocity Reversals and Ferromagnetic Alignment: Active Matter Class with Second-Order Transition to Quasi-Long-Range Polar Order", Physical Review Letters **120**, 258002 (2018).

[47] D. S. Dean, "Langevin equation for the density of a system of interacting Langevin processes", Journal of Physics A: Mathematical and General **29**, L613–L617 (1996).

[48] F. D. C. Farrell, M. C. Marchetti, D. Marenduzzo, and J. Tailleur, "Pattern Formation in Self-Propelled Particles with Density-Dependent Motility", Physical Review Letters **108**, 248101 (2012).

[49] R. Großmann, L. Schimansky-Geier, and P. Romanczuk, "Self-propelled particles with selective attraction–repulsion interaction: from microscopic dynamics to coarse-grained theories", New Journal of Physics **15**, 085014 (2013).

[50] R. Großmann, P. Romanczuk, M. Bär, and L. Schimansky-Geier, "Vortex Arrays and Mesoscale Turbulence of Self-Propelled Particles", Physical Review Letters **113**, 258104 (2014).

[51] R. Großmann, P. Romanczuk, M. Bär, and L. Schimansky-Geier, "Pattern formation in active particle systems due to competing alignment interactions", The European Physical Journal Special Topics **224**, 1325–1347 (2015).

[52] B. Liebchen and D. Levis, "Collective Behavior of Chiral Active Matter: Pattern Formation and Enhanced Flocking", Physical Review Letters **119**, 058002 (2017).

[53] A. P. Solon, J. Stenhammar, R. Wittkowski, M. Kardar, Y. Kafri, M. E. Cates, and J. Tailleur, "Pressure and Phase Equilibria in Interacting Active Brownian Spheres", Physical Review Letters **114**, 198301 (2015).

[54] A. P. Solon, J. Stenhammar, M. E. Cates, Y. Kafri, and J. Tailleur, "Generalized thermodynamics of motility-induced phase separation: phase equilibria, Laplace pressure, and change of ensembles", New Journal of Physics **20**, 075001 (2018).

[55] A. P. Solon, J. Stenhammar, M. E. Cates, Y. Kafri, and J. Tailleur, "Generalized thermodynamics of phase equilibria in scalar active matter", Physical Review E **97**, 020602 (2018).

[56] J. Stenhammar, R. Wittkowski, D. Marenduzzo, and M. E. Cates, "Light-induced self-assembly of active rectification devices", Science Advances **2**, e1501850 (2016).

[57] O. Chepizhko, E. G. Altmann, and F. Peruani, "Optimal Noise Maximizes Collective Motion in Heterogeneous Media", Physical Review Letters **110**, 238101 (2013).

[58] O. Chepizhko and F. Peruani, "Active particles in heterogeneous media display new physics", The European Physical Journal Special Topics **224**, 1287–1302 (2015).

[59] J. Toner, N. Guttenberg, and Y. Tu, "Swarming in the Dirt: Ordered Flocks with Quenched Disorder", Physical Review Letters **121**, 248002 (2018).

[60] J. Toner, N. Guttenberg, and Y. Tu, "Hydrodynamic theory of flocking in the presence of quenched disorder", Physical Review E **98**, 062604 (2018).

[61] Y. Duan, B. Mahault, Y.-q. Ma, X.-q. Shi, and H. Chaté, "Breakdown of Ergodicity and Self-Averaging in Polar Flocks with Quenched Disorder", Physical Review Letters **126**, 178001 (2021).

[62] G. Ariel, O. Rimer, and E. Ben-Jacob, "Order–Disorder Phase Transition in Heterogeneous Populations of Self-propelled Particles", Journal of Statistical Physics **158**, 579–588 (2015).

[63] K. Copenhagen, D. A. Quint, and A. Gopinathan, "Self-organized sorting limits behavioral variability in swarms", Scientific Reports **6**, 31808 (2016).

[64] A. M. Menzel, "Collective motion of binary self-propelled particle mixtures", Physical Review E **85**, 021912 (2012).

[65] P. Degond, G. Dimarco, and T. B. N. Mac, "Hydrodynamics of the Kuramoto-Vicsek model of rotating self-propelled particles", Mathematical Models and Methods in Applied Sciences **24**, 277–325 (2014).

[66] D. Levis, I. Pagonabarraga, and B. Liebchen, "Activity induced synchronization: Mutual flocking and chiral self-sorting", Physical Review Research **1**, 023026 (2019).

[67] D. Levis and B. Liebchen, "Simultaneous Phase Separation and Pattern Formation in Chiral Active Mixtures", Physical Review E **100**, 012406 (2019).

[68] A. E. Motter, S. A. Myers, M. Anghel, and T. Nishikawa, "Spontaneous synchrony in power-grid networks", Nature Physics **9**, 191–197 (2013).

[69] I. Z. Kiss, Y. Zhai, and J. L. Hudson, "Emerging Coherence in a Population of Chemical Oscillators", Science **296**, 1676–1678 (2002).

[70] A. T. Winfree, *The Geometry of Biological Time*, Second, Interdisciplinary Applied Mathematics (Springer-Verlag, New York, 2001).

[71] A. Pikovsky, M. Rosenblum, and J. Kurths, *Synchronization: A Universal Concept in Nonlinear Sciences*, First (Cambridge University Press, Oct. 2001).

[72] A. T. Winfree, "Biological rhythms and the behavior of populations of coupled oscillators", Journal of Theoretical Biology **16**, 15–42 (1967).

[73] Y. Kuramoto, "Self-entrainment of a population of coupled non-linear oscillators", in International Symposium on Mathematical Problems in Theoretical Physics, edited by H. Araki, Lecture Notes in Physics (1975), pp. 420–422.

[74] Y. Kuramoto, *Chemical Oscillations, Waves, and Turbulence*, Springer Series in Synergetics (Springer-Verlag, Berlin Heidelberg, 1984).

[75] J. A. Acebrón, L. L. Bonilla, C. J. Pérez Vicente, F. Ritort, and R. Spigler, "The Kuramoto model: A simple paradigm for synchronization phenomena", Reviews of Modern Physics **77**, 137–185 (2005).

[76] S. H. Strogatz and R. E. Mirollo, "Collective synchronisation in lattices of nonlinear oscillators with randomness", **21**, L699–L705 (1988).

[77] B. Pietras, N. Deschle, and A. Daffertshofer, "First-order phase transitions in the Kuramoto model with compact bimodal frequency distributions", Physical Review E **98**, 062219 (2018).

[78] E. A. Martens, E. Barreto, S. H. Strogatz, E. Ott, P. So, and T. M. Antonsen, "Exact results for the Kuramoto model with a bimodal frequency distribution", Physical Review E **79**, 026204 (2009).

[79] J. D. Crawford, "Amplitude expansions for instabilities in populations of globally-coupled oscillators", Journal of Statistical Physics **74**, 1047–1084 (1994).

[80] H. Sakaguchi, S. Shinomoto, and Y. Kuramoto, "Local and Grobal Self-Entrainments in Oscillator Lattices", Progress of Theoretical Physics **77**, 1005–1010 (1987).

[81] H. Sakaguchi, "Cooperative Phenomena in Coupled Oscillator Systems under External Fields", Progress of Theoretical Physics **79**, 39–46 (1988).

[82] L. Bonilla, C. Pérez Vicente, and R. Spigler, "Time-periodic phases in populations of nonlinearly coupled oscillators with bimodal frequency distributions", Physica D: Nonlinear Phenomena **113**, 79–97 (1998).

[83] S. H. Strogatzt, "Collective synchronisation in lattices of non-linear oscillators with randomness", 10.

[84] H. Hong, H. Chaté, H. Park, and L.-H. Tang, "Entrainment Transition in Populations of Random Frequency Oscillators", Physical Review Letters **99**, 184101 (2007).

[85] A. A. Chepizhko, V. L. Kulinskii, Y. Holovatch, B. Berche, N. Bogolyubov, and R. Folk, "The kinetic regime of the Vicsek model", in STATISTICAL PHYSICS: MODERN TRENDS AND APPLICATIONS: The 3rd Conference on Statistical Physics Dedicated to the 100th Anniversary of Mykola Bogolyubov (2009), pp. 25–33.

[86] A. A. Chepizhko and V. L. Kulinskii, "On the relation between Vicsek and Kuramoto models of spontaneous synchronization", Physica A: Statistical Mechanics and its Applications **389**, 5347–5352 (2010).

[87] E. Lauga, W. R. DiLuzio, G. M. Whitesides, and H. A. Stone, "Swimming in circles: Motion of bacteria near solid boundaries", Biophysical Journal **90**, 400–412 (2006).

[88] I. H. Riedel, "A Self-Organized Vortex Array of Hydrodynamically Entrained Sperm Cells", Science **309**, 300–303 (2005).

[89] Y. H. Tee, T. Shemesh, V. Thiagarajan, R. F. Hariadi, K. L. Anderson, C. Page, N. Volkmann, D. Hanein, S. Sivaramakrishnan, M. M. Kozlov, and A. D. Bershadsky, "Cellular chirality arising from the self-organization of the actin cytoskeleton", Nature Cell Biology **17**, 445–457 (2015).

[90] M. Loose and T. J. Mitchison, "The bacterial cell division proteins FtsA and FtsZ self-organize into dynamic cytoskeletal patterns", Nature Cell Biology **16**, 38–46 (2014).

[91] L. Q. Wan, K. Ronaldson, M. Park, G. Taylor, Y. Zhang, J. M. Gimble, and G. Vunjak-Novakovic, "Micropatterned mammalian cells exhibit phenotype-specific left-right asymmetry", Proceedings of the National Academy of Sciences **108**, 12295–12300 (2011).

[92] Y. Yang, F. Qiu, and G. Gompper, "Self-organized vortices of circling self-propelled particles and curved active flagella", Physical Review E **89**, 012720 (2014).

[93] A. Kaiser and H. Löwen, "Vortex arrays as emergent collective phenomena for circle swimmers", Physical Review E **87**, 032712 (2013).

[94] M. Mijalkov and G. Volpe, "Sorting of chiral microswimmers", Soft Matter **9**, 6376 (2013).

[95] B. Liebchen, M. E. Cates, and D. Marenduzzo, "Pattern formation in chemically interacting active rotors with self-propulsion", Soft Matter **12**, 7259–7264 (2016).

[96] J. Denk, L. Huber, E. Reithmann, and E. Frey, "Active Curved Polymers form Vortex Patterns on Membranes", Physical Review Letters **116**, 178301 (2016).

[97] J. M. Moore, M. A. Glaser, and M. D. Betterton, "Chiral self-sorting of active semiflexible filaments with intrinsic curvature", Soft Matter **17**, 4559–4565 (2021).

[98] M. Fruchart, R. Hanai, P. B. Littlewood, and V. Vitelli, "Non-reciprocal phase transitions", Nature **592**, 363–369 (2021).

[99] W. R. DiLuzio, L. Turner, M. Mayer, P. Garstecki, D. B. Weibel, H. C. Berg, and G. M. Whitesides, "Escherichia coli swim on the right-hand side", Nature **435**, 1271–1274 (2005).

[100] E. Lauga, W. R. DiLuzio, G. M. Whitesides, and H. A. Stone, "Swimming in Circles: Motion of Bacteria near Solid Boundaries", Biophysical Journal **90**, 400–412 (2006).

[101] R. Di Leonardo, D. Dell'Arciprete, L. Angelani, and V. Iebba, "Swimming with an Image", Physical Review Letters **106**, 038101 (2011).

[102] B. M. Friedrich and F. Julicher, "Chemotaxis of sperm cells", Proceedings of the National Academy of Sciences **104**, 13256–13261 (2007).

[103] K. Ērglis, Q. Wen, V. Ose, A. Zeltins, A. Sharipo, P. A. Janmey, and A. Cēbers, "Dynamics of Magnetotactic Bacteria in a Rotating Magnetic Field", Biophysical Journal **93**, 1402–1412 (2007).

[104] A. Cēbers, "Diffusion of magnetotactic bacterium in rotating magnetic field", Journal of Magnetism and Magnetic Materials **323**, 279–282 (2011).

[105] F. Kümmel, B. ten Hagen, R. Wittkowski, I. Buttinoni, R. Eichhorn, G. Volpe, H. Löwen, and C. Bechinger, "Circular Motion of Asymmetric Self-Propelling Particles", Physical Review Letters **110**, 198302 (2013).

[106] B. ten Hagen, F. Kümmel, R. Wittkowski, D. Takagi, H. Löwen, and C. Bechinger, "Gravitaxis of asymmetric self-propelled colloidal particles", Nature Communications **5**, 4829 (2014).

[107] G.-J. Liao and S. H. L. Klapp, "Emergent vortices and phase separation in systems of chiral active particles with dipolar interactions", Soft Matter **17**, 6833–6847 (2021).

[108] B. Ventejou, H. Chaté, R. Montagne, and X.-q. Shi, "Susceptibility of Orientationally-Ordered Active Matter to Chirality Disorder", arXiv:2107.14106 [cond-mat] (2021).

[109] S. A. Orszag, "On the elimination of aliasing in finite-difference schemes by filtering high-wavenumber components", Journal of Atmospheric Sciences **28**, 1074–1074 (1971).

université PARIS-SACLAY
ÉCOLE DOCTORALE
Physique en l'Île-de-France (PIF)

Titre: Synchronisation de la matière active chirale en 2D.

Mots clés: Physique statistique hors équilibre, matière active, mouvements collectifs, synchronisation

Résumé: La matière active est une classe de systèmes hors-équilibres où les constituants consomment de l'énergie pour affecter leur mouvement. Cette thèse considère l'effet de la chiralité sur les mouvements collectifs dans la matière active, cherchant en particulier à savoir si ces mouvements peuvent résister à un « désordre chiral ». Pour ce faire, des variations du modèle de Vicsek à deux dimensions ont été étudiées, dans lesquelles les particules actives sont dotées d'une chiralité individuelle qui confère une courbure moyenne à leurs trajectoires. Dans les cas où elles étaient accessibles, les théories hydrodynamiques correspondantes ont été dérivées et étudiées.
Une distribution gaussienne centrée de chiralité a d'abord été considérée. On a montré que la phase ordonnée homogène du modèle pur était brisée par un désordre arbitrairement faible, contrairement à la phase de bandes qui résiste à un degré fini de chiralité. Sour l'effet du désordre, ces phases laissent place à une phase de vortex que nous avons caractérisée comme résultant d'une séparation en microphases.
Le cas gaussien se prêtant mal aux théories hydrodynamiques, nous avons ensuite considéré une distribution bimodale de chiralité facilitant l'approche théorique. Dans ce cas, le modèle particulaire se comporte comme dans le cas gaussien, à l'exception de l'émergence d'une phase supplémentaire de 'paquets polaires tournants'. La théorie hydrodynamique dérivée via une approche de type Boltzmann rend compte qualitativement de la phénoménologie microscopique : la phase ordonnée homogène est linéairement instable dans tout son domaine d'existence, et les phases 'chirales' (vortex et paquets tournants) sont des solutions de la théorie.
Le cas d'une distribution unimodale, brisant donc explicitement la chiralité globale, a aussi été étudiée. Là encore la phase ordonnée homogène (tournante dans ce cas) est instable tant au niveau particulaire qu'hydrodynamique, alors que les bandes du modèle de Vicsek peuvent résister à une chiralité finie.

Title: Synchronization of 2D chiral active matter

Keywords: Nonequilibrium statistical physics, active matter, collective motion, synchronization

Abstract: Active matter designates a class of out of equilibrium systems made of components spending energy to displace themselves. This dissertation considers the effect of chirality on collectively moving active matter, investigating in particular whether such collective motion can survive 'chirality disorder'. To this aim, we study variants of the 2D Vicsek model in which self-propelled particles are endowed with some individual chirality conferring a mean curvature to their trajectories. In addition, whenever possible, corresponding hydrodynamic theories were derived and their solutions investigated.
A zero-mean Gaussian distribution of individual chiralities was first examined. The homogeneous ordered phase of the pure Vicsek model was found broken by any amount of chirality disorder, in contrast with the traveling bands of the coexistence phase, which survive a finite amount. Under the effect of chirality disorder these states give place to a vortex phase, which we characterized as resulting from microphase separation.
The Gaussian does not allow easily for the derivation of hydrodynamic theories. We thus the considered instead the case of a bimodal chirality distribution still with zero mean. The particle model then display the same phenomenology as in the Gaussian case, except for the emergence of an additional phase of 'rotating polar packets'. A hydrodynamic theory derived via a Boltzmann approach was found to account qualitatively for the collective phenomena found at microscopic level: the homogeneous ordered phase is linearly unstable in all its domain of existence, and the 'chiral' phases (vortices and rotating packets) were observed as solutions of the hydrodynamic theory.
The case of a unimodal distribution, breaking explicitly global chirality, was also considered. Here again the homogeneous order (rotating) solution is unstable in both the particle model and at hydrodynamic level, whereas the Vicsek bands resist a finite amount of chirality.

Université Paris-Saclay
Espace Technologique / Immeuble Discovery
Route de l'Orme aux Merisiers RD 128 / 91190 Saint-Aubin, France